博 士 論 文

光応答性ジアリールエテンを用いた光操作可能な

新機能性材料の創生

Creation of new photo-operatable functional materials

using photoresponsive diarylethenes

龍谷大学大学院　理工学研究科

博士後期課程　物質化学専攻

Graduate School of Science and Technology

Ryukoku University

Ｔ２０Ｄ００１　　中川　優磨

Yuma Nakagawa

Contents

Chapter 1

General Introduction

Chapter 2

Photoinduced cytotoxicity and cell killing mechanism of photochromic diarylethene

Chapter 3

Photomechanical behavior of diarylethene crystals and their manipulation by light

Chapter 4

Phototunable golden luster microcrystalline film of photochromic diarylethene

Chapter 5

Chapter 1

General Introduction

1.1 Photochromism

Photochromism is defined as ''a reversible transformation of a single chemical species being induced in one or both direction by absorption of electromagnetic radiation between two states having different distinguishable absorption spectra.''[1] The molecules that exhibit such phenomena are called photochromic molecules. Typical photochromic compounds include azobenzene, spiropyran, hexaarylbiimidazole (HABI), fulgide, diarylethene (DAE), phenoxynaphthacenequinone, and others (Figure 1.1). The azobenzene, spiropyran, and HABI are known to be thermally unstable in the isomers formed by UV light irradiation, and these isomers are reverted by heat (called ''T-type'').[2] In contrast, it is known that the isomers of fulgide, DAE, and others formed by UV light irradiation are thermally stable, and revert to their original structure when irradiated with light of different wavelengths (called P-type).[2] In particular, the DAEs usually generate isomers in a highly sensitive and reversible manner. Its both isomers generally have high thermal stability and reversibility.[3,4] Owing to these excellent properties, the DAE has a possibility to apply for various scientific and industrial field such as optical memory, photo-switch, photo-actuator, bioimaging and so on.
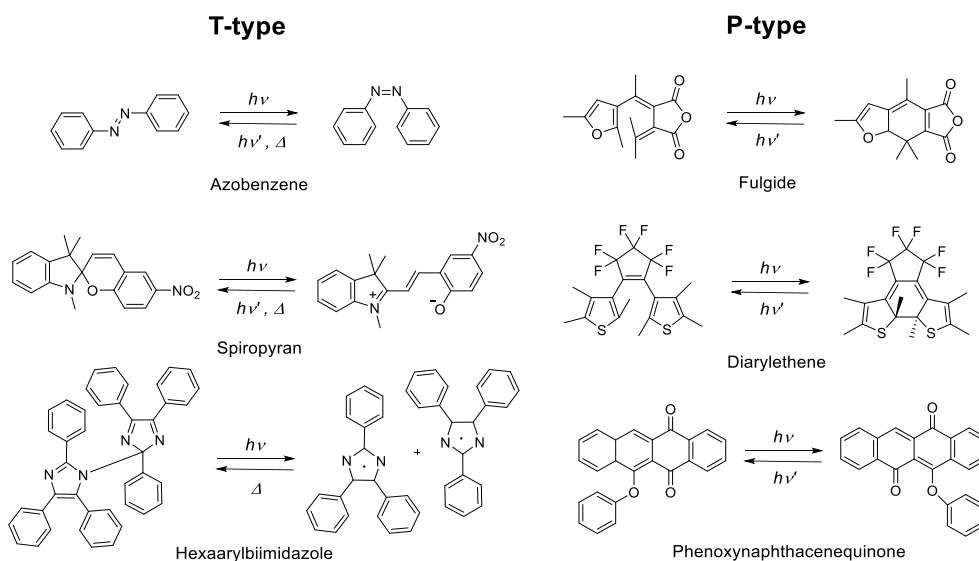
Figure 1.1 Molecular structures of typical thermally stable (P-Type: light) and unstable (T-type: left) Photochromic compounds.

The structural formula of a typical DAE molecule in Scheme 1.1. Here, X and Y are heteroatoms and R_1-R_6 are substituents such as alkyl groups. T The characteristics of these molecule, such as the absorption spectra of both isomers and quantum yields of the photochromic reactions change depending on the type of substituent or heteroatom and the substituted positions of the heterocyclic ring to the ethene moiety.[5,6]
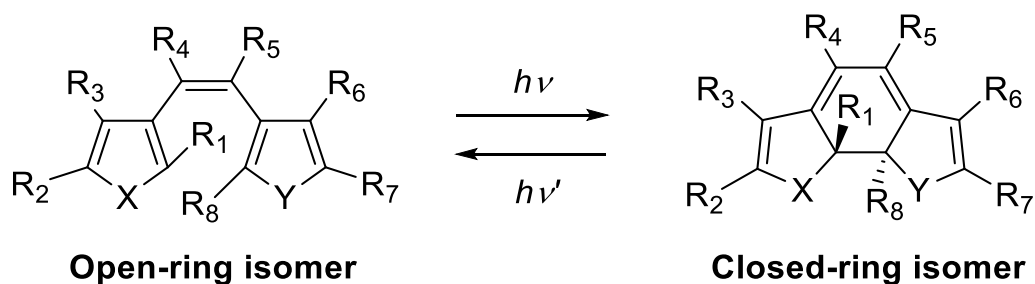
Scheme 1.1 photochromism of a typical diarylethene molecule.

1.2 Photochromic reactions in the crystalline state of a diarylethene

In photochromic compounds, DAE and some photoresponsive molecules can react not only in solution but also in the solid state.[7-14] In order to undergo photochromic reactions in crystalline state, two conditions must be achieved. One is the distance between two photo-reactive carbon atoms. In 1971, Schmidt reported the experimentally observed limit of center-to-center distance of double bonds of photo-dimerized coumarin monomers in the crystalline state.[15] From the results, the photo-reactive distance between the double bonds was found to be 4.2 Å > d > 3.5 Å. In addition, Irie and co-workers have reported the relationship between the reactivity and distance between the reactive carbon atoms of DAE derivatives in the crystalline state.[16,17] The results show that the DAE molecules with perfluorocyclopentene in the ethene moiety undergo a photocyclization reaction in the crystalline state when the reactive carbons distance is less than 4.2 Å (Figure 1.2). Therefore, photochromic reactions can occur in the solid phase if the distance between the reacting atoms or bonds is less than 4.2 Å. The other is that the structural changes accompanied with photoisomerization are acceptable in crystalline state.[18,19] Spiropyran and azobenzene, which are typical photochromic compounds similar to DAE, generally do not show photochromism in crystalline state. This is because the structural changes that occur during isomerization are so large that there is no local free volume in the crystal to allow the reaction.[18]
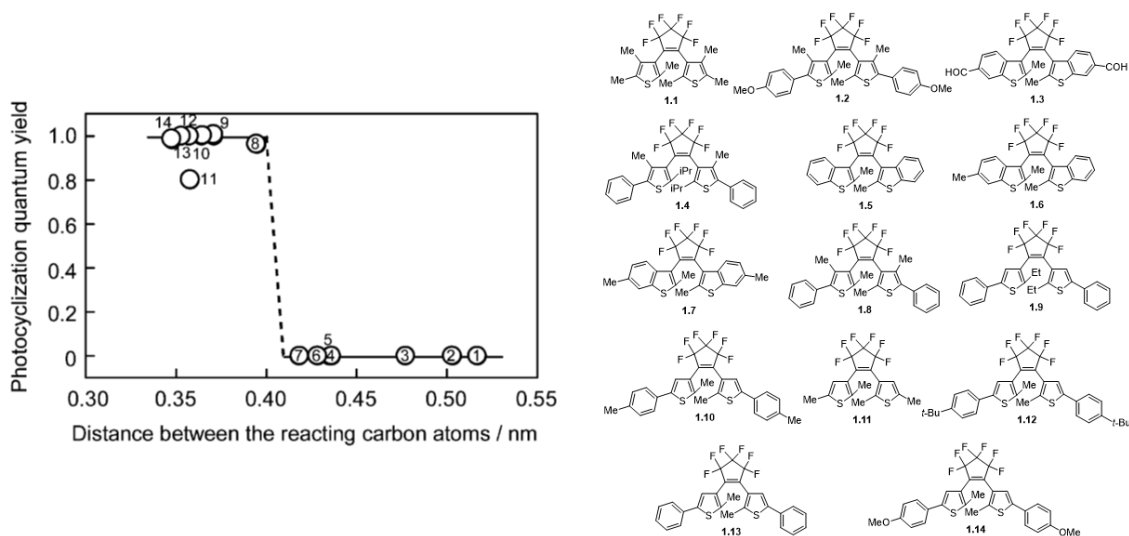
Figure 1.2 Relationship between the photocyclization quantum yield and the distance between the reacting carbons. 1: **1.1**, 2: **1.2**, 3: **1.3**, 4: **1.4**, 5: **1.5**, 6: **1.6**, 7: **1.7**, 8: **1.8**, 9: **1.9**, 10: **1.10**, 11: **1.11**, 12: **1.12**, 13: **1.13**, 14: **1.14**.[16]

The open-ring isomers of DAE exist in two conformations in solution,[20-22] one parallel (mirror symmetry) orientation in which the two aryl rings are aligned parallel to each other, and the other antiparallel (C2 symmetry) one in which the two aryl rings are aligned in opposite directions (Figure 1.3). Since they are in equilibrium in solution, either conformation is possible. In addition, the photocyclization proceeds only from the antiparallel conformation. Irie and co-workers synthesized a derivative of 1,2-bis(2-methylbenzo[b]thiophen-3-yl)perfluorocyclopentene with two terminal carboxyl groups.[23] This derivative is locked in a parallel conformation in cyclohexane due to the formation of intramolecular hydrogen bonds by the carboxyl group. The photocyclization reaction did not proceed even when irradiated with UV light in this state. This is the same in the crystalline state as well as in solution. Irie and co-workers reported the DAE crystal showing different photo-reactivity between the two crystals polymorphism having antiparallel and parallel conformations (Figure 1.4).[24] The **1.15o-α** Crystal changes from colorless to green upon UV light irradiation, and returns to colorless upon visible light irradiation. This is due to the antiparallel conformation of the **1.15o** in the crystal (Figure 1.4 (b): left). Whereas, the **1.15o-β** crystal is packed in parallel conformation to the **1.15o** (Figure 1.4 (b): right). Therefore, it cannot undergo photocyclization reaction. From this result, the conformation of the molecule is important for the photocyclization reaction.
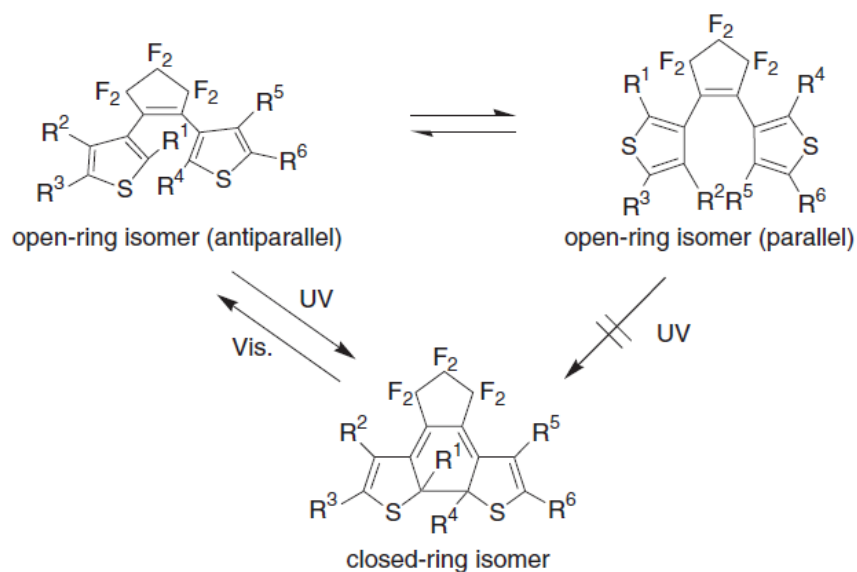
Figure 1.3 Photochromic reaction of diarylethene. Two conformers in open-ring isomers in equilibrium.[22]
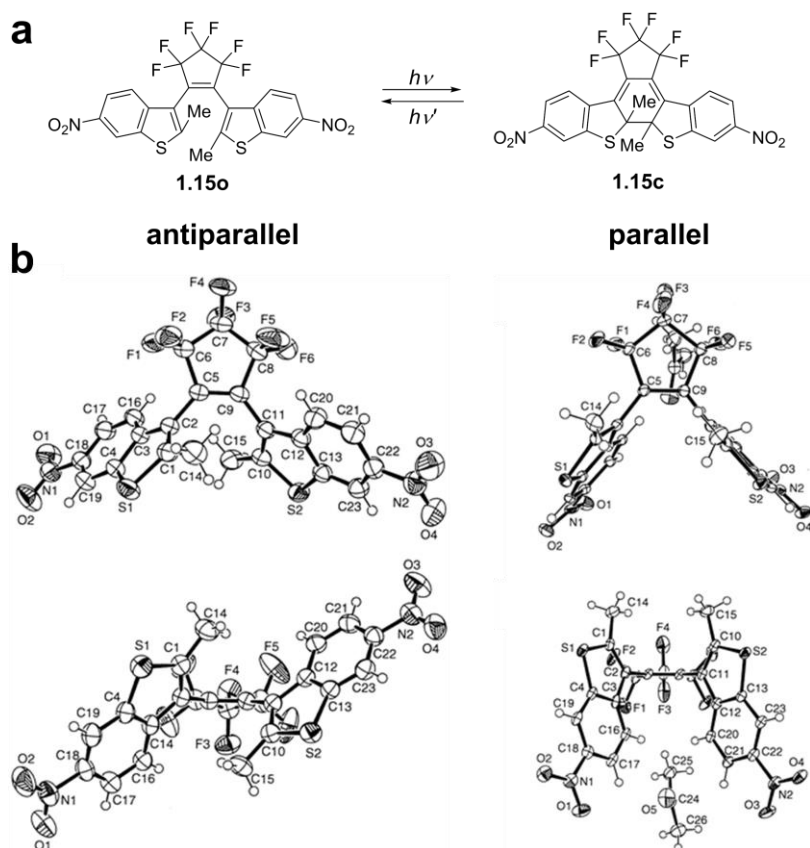
Figure 1.4 (a) Molecular structure of the open- and closed-ring isomers of **1.15**. (b) ORTEP drawings of top (above) and side (below) views of **1.15o-α** (left) and **1.15o-β** (right).[24]

1.3 Photoinduced shape change of diarylethene crystals

In 2007, Irie and co-workers reported that reversible shape of a single crystals of **1.9o** and **1.16o** upon alternate irradiation with alternating UV and visible light.[25] In addition, the rod-like crystal of **1.16o** was bent to the direction of the light source when irradiated with UV light, and returned to its original columnar form upon subsequent irradiation with visible light. Then, by repeated bending and stretching, the gold particle heavier than the rod-like crystal was lifted and moved about 30 μm (Figure 1.5).
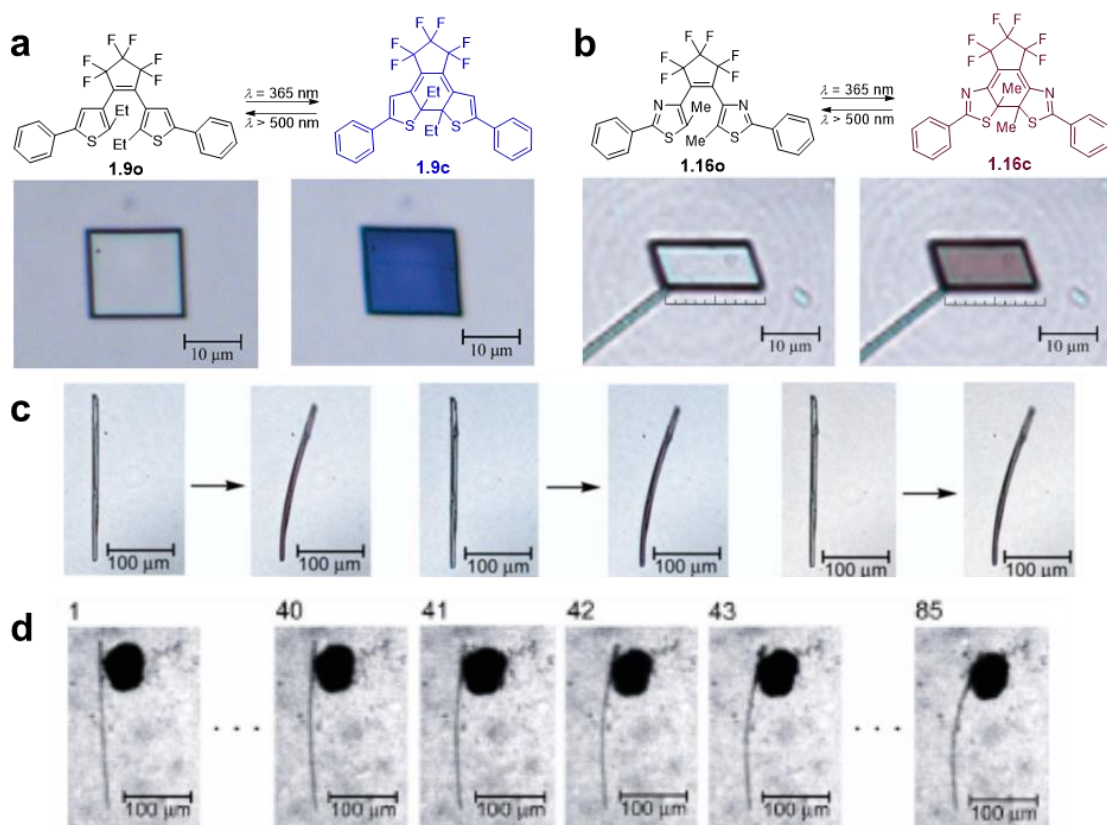
Figure 1.5 (a, b) Molecular structures of the open- and closed-ring isomers of the two compounds along with images illustrating the deformation of their single crystals on irradiation with UV ($\lambda = 365$ nm) and visible ($\lambda > 500$ nm) light. (a) A square single crystal of **1.9** with corner angles of 88 and 92 ° reversibly changed to a lozenge shape with corner angles of 82 and 98 °. (b) A rectangular single crystal of **1.16** reversibly contracted and expanded as much as 7%. The thickness of the crystal was 330 nm. (c) Reversible bending of a rod-like crystal of **1.16** upon alternate irradiation with UV and visible light. (d) Movement of a gold micro-particle by the rod-like crystal of **1.16o** upon UV light irradiation.[25]

Due to the high concentration of dye in the molecularly aggregated crystal, most of the light is absorbed at the irradiated surface and does not reach the other side. This causes the crystals to have a bimetallic-like structure[26] upon UV light irradiation due to the formation of a closed-form on the surface. The layer of closed-form produced in this process has a different crystal lattice volume than the layer of the open-ring isomer, so it bends. In other words, bending is caused by differences in the stacking of open and closed ring molecules.

The direction of bending can be explained by the bending behavior of the cocrystal of **1.17o** and perfluoronaphthalene (FN), reported by Irie and co-workers.[27] By irradiating the needle-like crystal of **1.17o** with UV light, a photocyclization reaction occurs in the surface layer lined by open-ring isomers in the *c*-axis direction, and the structure of the generated closed-ring isomers becomes longer in the *b*-axis direction. Therefore, the surface layer of the needle crystal extends in the *b*-axis direction and bends away from the UV light due to the length difference from the *b*-axis direction of the open- and closed-ring isomers (Figure 1.6). In other words, the length in the long axis direction of the crystal bends away from the light source when the layer consists of only open-ring isomers < the layer containing closed-ring isomers, and closer to the light source when the layer consists of only open-ring isomers > the layer containing closed-ring isomers.
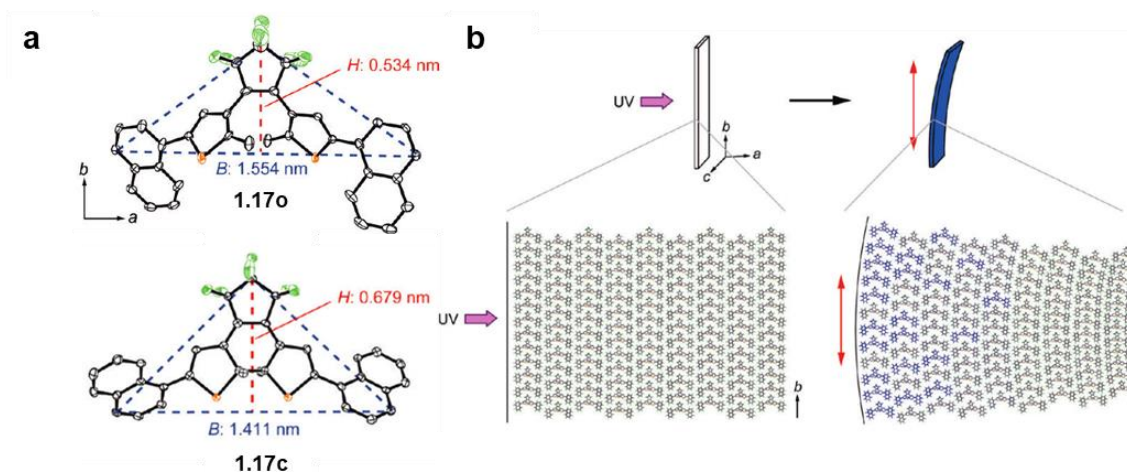
Figure 1.6 (a) ORTEP drawings of **1.17o** in the cocrystal of **1.17o·FN** and **1.17c** in the crystal of the isolated and independently recrystallized closed-ring isomer. (b) Schematic illustration of the photoinduced bending. The blue molecules are photogenerated closed-ring isomers in the crystal. The red arrow indicates the direction of the anisotropic elongation of the crystal, which is parallel to the *b*-axis, upon UV irradiation.[27]

After that, photoinduced crystal bending of many DAEs has been reported up to now.[28-45] During this time, photoinduced bending behavior of DAE has been reported, including quantitative evaluation,[28-31] specific bending motions such as twisting[32,33] and multi-step bending[34,35], and response to polarized light.[36] Therefore, the mechanism of photoinduced bending behavior is almost completely understood. Recently, this bending behavior has been applied to light-driven actuators such as cantilever motion,[27] gearwheel rotation,[39] current switching,[40] and material transport.[44]

1.4 Photosalient effect of diarylethene crystals

It has been reported that external stimuli such as heat, light, and mechanical shock in molecular assemblies such as crystals,[27,39,40,44,46-50] polymers,[51-54] and gels[54-60] can cause changes in the micro-scale molecular structure, leading to macroscopic response changes in many systems. Especially, the light is an excellent tool to activate locally, remotely, and instantly on the target, and thus can be applied in various environments. Among these, the "photosalient effect" has been attracting much attention as a phenomenon in which microscopic changes using light produce macroscopic changes.[61-69] The photosalient effect shows the phenomenon of crystals scattering or jumping apart when exposed to light. The photosalient phenomenon is similar to the bending behavior described above, but differs greatly in that it generates an instantaneous force that causes the crystal to jump. This is due to the changes in the molecular conformation of the crystal caused by light irradiation, which results in the accumulation of strain in the crystal. Then the strain energy accumulated inside the crystal is released all at once to the outside at a certain moment, causing the crystal to jump or disperse, or some other behavior.

In 2013, Naumov and co-workers reported that when excited with strong UV light, μm- to mm-sized prismatic crystals (**1.18N**) of cobalt coordination compounds suddenly hop off the surface and travel up to several tens of centimeters, that is, 10^2-10^5 times their own length (Figure 1.7).[64] They called this photo-functional phenomenon the "photosalient effect".

Figure 1.7 (a) The intramolecular linkage isomerization of nitropentaamminecobalt(III) complexes by UV light irradiation. (b, c) Series of snapshots and sketches of the five kinematic effects of UV-excited crystals of **1.18N**: splitting of a crystal into two pieces of nearly equal size (1), separation of a small piece off the crystal that propels the remaining part into a spinning or linear motion (2), crystal explosion (3), minor repositioning without lift off the base and apparent splitting or separation of debris (4), and rolling or flipping of the crystal (5).[64]

It has been reported that the photosalient effect is also observed in DAE crystals.[39,41,70-72] In 2007 and 2012, Irie and co-workers reported a jumping and peeling (:the crystal surface is peeled off) phenomenon in DAE crystals having a thiazole rings upon UV light irradiation (Figure 1.8).[41,70]

Naumov et al. compiled the characteristics of the crystal structures common to Salient active molecules as follows[46]: (1) The crystal structures before and after the salient effect are very similar to each other, with only minor changes in the relative spatial conformations of the molecules. Therefore, the space group remains the same and the change in the V/Z values of the crystal parameters ($\Delta_{V/Z}$) is very small ($\Delta_{V/Z} < 25$ Å^3). Here, V is the volume per lattice and Z is the number of molecules per lattice. (2) An anisotropic change in the size of the crystal lattice occurs, with a very small expansion of the lattice constant in certain directions and a very small contraction of other lattice constants. Therefore, the small strains generated locally by the change in molecular conformation are released to the outside without canceling each other out as a whole.

Recently, the application of photosalient phenomena has been reported for the hybrid material of an electrical fuse link[69] and for hollow-crystal scattering inclusions[72].
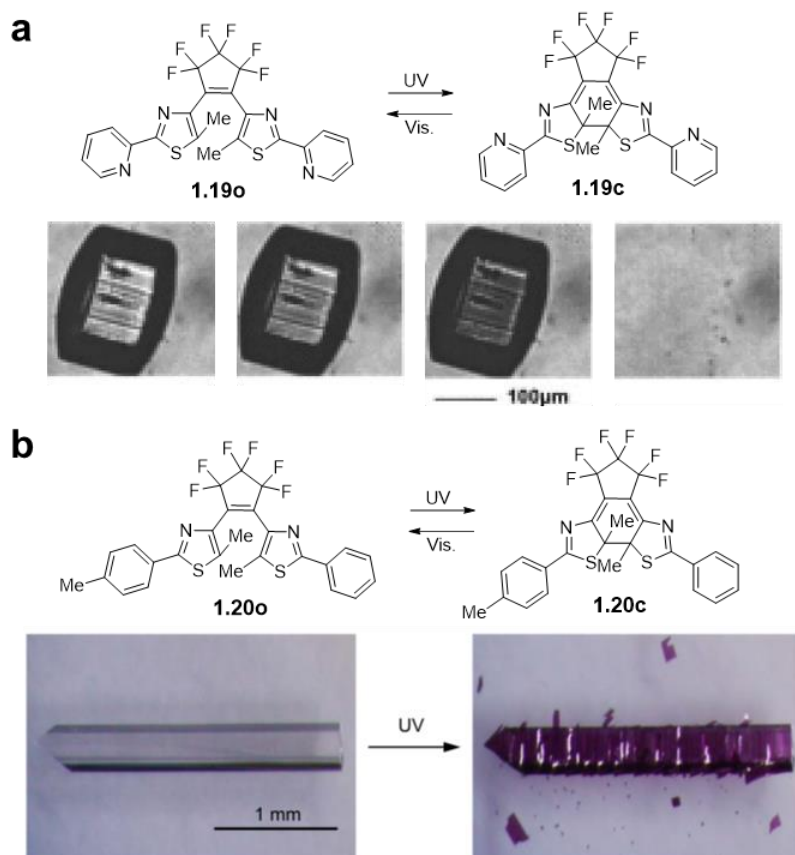
Figure 1.8 (a) Molecular structures of open- and closed-ring isomers of **1.19**, and photoinduced jumping of **1.19o** crystal upon UV light irradiation.[70] (b) Molecular structures of open- and closed-ring isomers of **1.20**, and photoinduced peeling of **1.20o** crystal upon UV light irradiation.[39]

1.5 The application of photochromic diarylethene

Photochromic compounds have been studied as on-off switches to change the optical,[73-77] optoelectronics[77,78], biological,[79-90] wetting,[91-94] aggregation,[95-105] and biomimetics[72,91,93,106-109] properties of various systems by their molecular motion, polarity change, and absorption change though the photoisomerization. In particular, DAE is expected to have a wide range of applications because both isomers are generally thermally stable.

Matsuda and co-workers have reported reversible macroscopic changes between colorless microspheres and colored fibers due to photoisomerization of amphiphilic DAE derivatives (Figure 1.9).[100] The amphiphiles of **1.21o** with a nonyloxy chain as a hydrophobic group on one side and two triethylene glycol units as hydrophilic groups on

the other side form supramolecular structures in water to form microspheres of several micrometers in size. Upon UV light irradiation of the formed colorless microspheres, their division was observed and colored fibers of **1.21c** were formed. In addition, upon visible light irradiation of the colored fibers, they return to the microspheres in their original position. This transformation of the supramolecular structures was also observed upon changing the temperature. Thus, photoisomerization of the photochromic moiety can completely switching the structures of the aggregates.
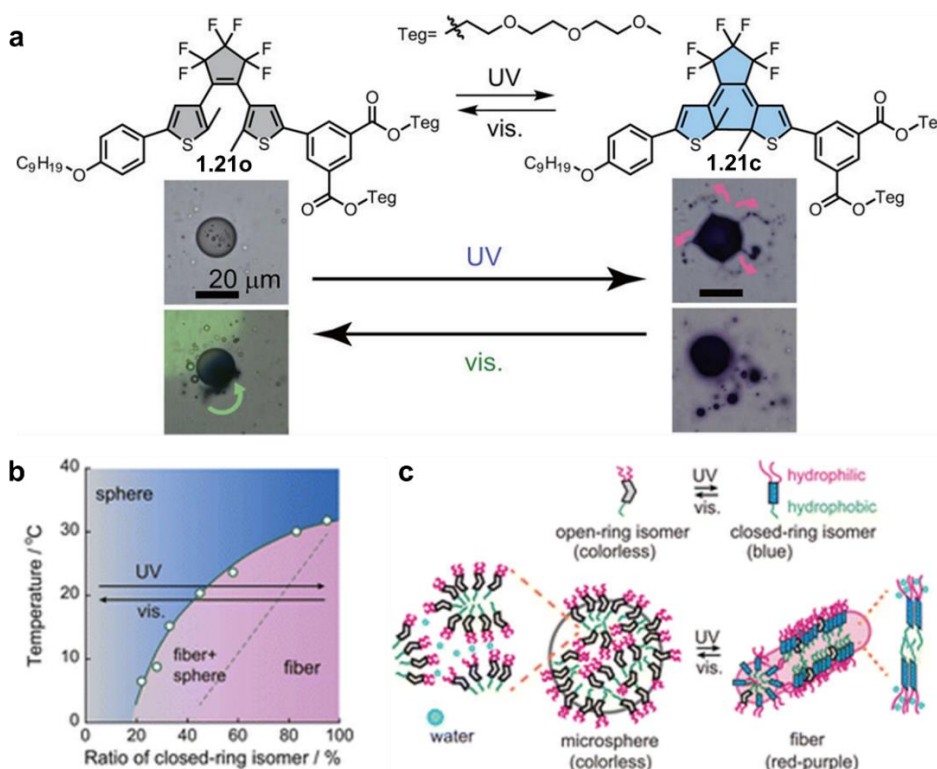
Figure 1.9 (a) Molecular structures and photochromism of open- and closed-ring isomers of **1.21**, and reversible morphological changes of microspheres and fibers upon light irradiation. (b) Phase diagram of the mixture of **1.21o** and **1.21c**. The transition temperatures were obtained from the turbidity change upon cooling (green open circle). (c) Schematic illustration of the photoinduced morphological transformation of the supramolecular assembly.[100]

Gamez and co-workers have reported the preparation of complexes consisting of DAE and anticancer metal complexes, which showed different cytotoxic activities in open- and closed-ring isomers (Figure 1.10).[89] This difference in cytotoxic activity is likely due to differences in the intracellular behavior of the open- and closed-forms. The Pt/**1.22c** complex has been observed to co-localize with the nucleus of A375 cells, suggesting that

its cytotoxicity may be related to its ability to reach the nucleus. Comparatively, the Pt/**1.22o** complex, which is much less active than the Pt/**1.22c** complex against A375 cells, is not found in the nucleus. This has potential applications in photoactivated chemotherapy (PACT).
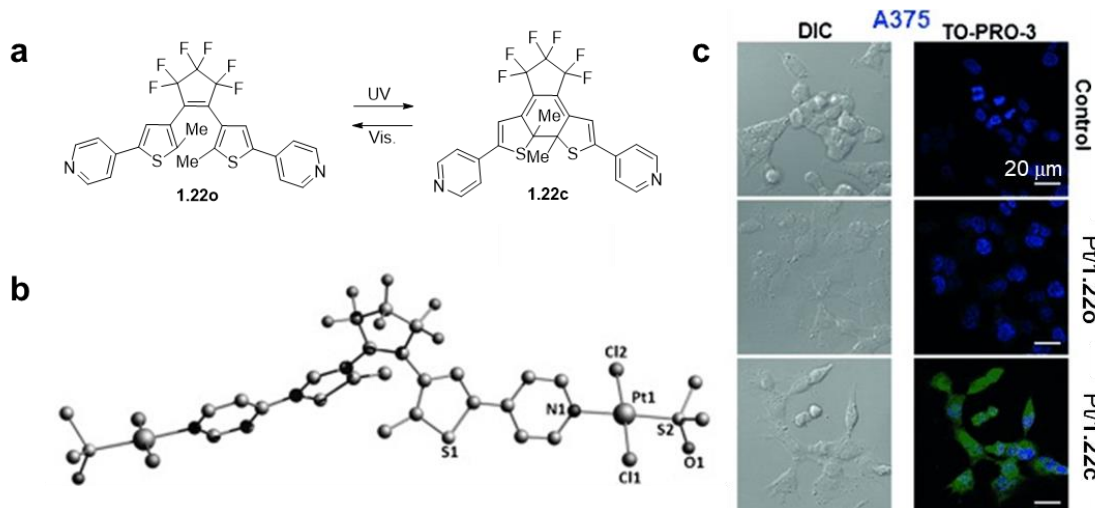

Figure 1.10 (a) The light-driven switching process for **1.22**. (b) X-ray structure of the open-form of the Pt/**1.22** complex, with partial atom numbering. H atoms are omitted for clarity. (c) Uptake of open- and closed-forms of Pt/**1.22** complex by A375 cells, (24 h incubation at 37 °C). The merged confocal images, obtained from z-stacks, of the compounds (green) and the nuclear marker TO-PRO-3 (blue) are shown (right) together with the corresponding differential interference contrast (DIC) images (left).[89]

1.6 Photoinduced cytotoxicity of a diarylethene having the thiazole rings

Conventional cancer treatments such as surgery, radiation therapy, and chemotherapy can cause serious side effects due to the loss of normal organ functions. "Photopharmacology" has been proposed as one approach to solve such problems.[110,111] By introducing molecular switches, light can be used as an external control to regulate drug activity in the living body. There has been a lot of research on the incorporation of molecular switches into existing drugs to control drug activity.[89,110,111] However, It is more desirable to use light-responsive molecules that act as anticancer agents in order to achieve precise control based on molecular-level switch mechanisms.

In 2015, our laboratory reported that Madin-Darby Canine Kidney (MDCK) cells were seeded on a surface coated with **1.16c** having the thiazole rings in the molecule, and blue-visible light (λ = 436 nm) could be irradiated to selectively kill the cells in the light-

irradiated area (Figure 1.11).[84] The photoinduced cell death of **1.16c** was confirmed to be apoptosis by cell staining experiments using the Apoptotic and Necrotic Cell Detection Kit. Whereas, the photoinduced toxicity was not observed in the open-ring isomer of **1.16**. In addition, the photoinduced cytotoxicity of this molecule was not observed when the N atom of the thiazole rings were replaced with CCH_3. For this reason, it is highly likely that the nitrogen-containing heterocycles in the DAE molecule are related to the photoinduced cytotoxicity. However, there are very few reported cases of photoinduced cytotoxicity using DAE with a simple structure. Therefore, there is a lack of information to clarify the relationship between intramolecular nitrogen-containing heterocycles and photoinduced cytotoxicity.
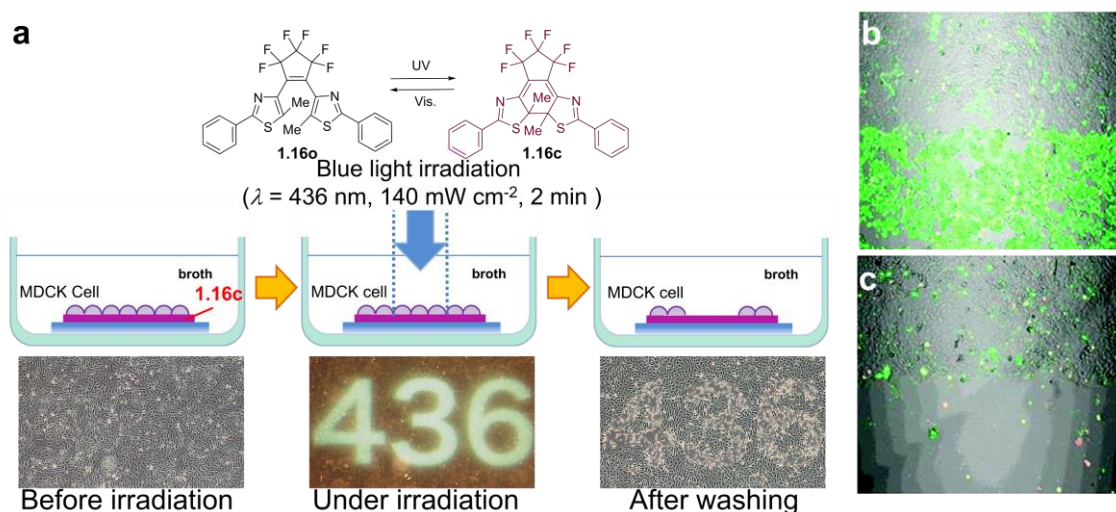
Figure 1.11 (a) Schematic illustration and photograph of MDCK cell damage on a **1.16c**-coated surface. (b, c) Apoptosis assay of the MDCK cells dosed with **1.16c** in the absence (b) or presence (c) of caspase inhibitor Z-VAD-FMK, respectively.[84]

1.7 Scope of this thesis

The synthesis of DAEs was first reported in 1988.[112,113] Since then, many researchers have been conducting basic and applied research for deployment in various fields. In particular, the systems that produce visible macroscopic changes or movements caused by changes at the molecular level, such as photoisomerization of DAE molecules, are very attractive and have the potential to perform new functions. In addition, light is an excellent tool for local and remote manipulation. Therefore, photoresponsive materials have the potential to overcome challenges such as localized or remote manipulation that cannot be achieved with conventional materials. In this doctoral dissertation, we report on our

research results on the control of functions by light, such as selective cell killing, optical manipulation of photomechanical behavior, and photo-tunable luster material using DAE molecules.

In Chapter 2, we evaluated the photoinduced cytotoxicity of DAE from the viewpoint of molecular structure and size. In order to clarify the relationship between intramolecular nitrogen-containing heterocycles and photoinduced cytotoxicity, we investigated the photoinduced cytotoxicity of a series of DAEs containing thiazole or pyridine rings. These results gave some common features of DAEs showing photocytotoxicity. Therefore, it has the potential to provide a molecular design of DAE with a simple structure to achieve precise control based on a switching mechanism at the molecular level. Moreover, we described a photo-tuned cell killing technique using DAE molecules, photo-isomerizing-molecular switches. To send this molecule to DNA in cell nucleus, and to demonstrate cytotoxicity by this molecule in a living cell, for both we controlled by UV and visible blue light irradiation independently. The open-ring isomer does not show the distribution ability, that is, unable to intercalate into DNA of the nucleus, whereas upon UV light irradiation, the generated closed-ring isomer can intercalate. This isomer, thus being ready for the action, exerted photocytotoxicity upon another blue light irradiation. The achieved photocytotoxicity was confirmed, with molecular-biological study, being due to the double strand break of the DNA. Furthermore, the magnitude of photoinduced cytotoxicity was successfully controlled by adjusting the design by increasing the number of thiazole rings.

In Chapter 3, we present the relationship between the photosalient effect and UV light intensity to crystals of DAEs having thiazoyl and thienyl derivatives. The change in the size of the crystal unit cell upon UV light irradiation is larger for asymmetric DAE with thiazole and thiophene rings than those for the corresponding symmetric DAEs. As a result, the crystals of an asymmetric DAE show much more drastic photosalient effects than those of the corresponding symmetric DAE crystals upon UV light irradiation. In the case of asymmetric DAE, the photoresponse of diarylethene crystals is found to depend on the intensity of UV light, that is, photoinduced bending is switched to photosalient phenomena by increasing the light intensity. In addition, an efficient surface peeling of crystals by multi-step light irradiation using asymmetric DAE crystals is reported. Thin crystals fabricated by this approach make up less than half the thickness of the original crystals. This shows the potential for photocontrol of various photomechanical behaviors by the same crystal depending on the irradiation conditions.

In Chapter 4, we present a DAE-based photo-tunable organic gold luster material. Through recrystallization, the compound formed plate-like microcrystals, which were then laminated to form a film. The yellowish gold-colored textured film was achieved by a

13

combination of absorption and specular reflection from the surface of the stacked microcrystals. The produced films showed a change in color to deep gold upon UV light irradiation due to the change in the absorption band caused by the photocyclization of DAE molecule. The film reverted to its original color upon exposure to visible light due to the photocycloreversion of the DAE molecule. We have succeeded in developing a material whose luster color changes reversibly with light.

In Chapter 5, the conclusion of this dissertation is presented. In this doctoral dissertation, we have successfully used photochromism of DAE, to control the function of cell killing, photomechanical behavior, and luster color by light. These showed that microscopic structural changes caused by photocyclization-cycloreversion reactions of DAE by light can act as a control of the function of various systems.

1.8 References

[1] H. Dürr, H. B-Laurent, Photochromism Molecules and Systems, studies in organic chemstry 40, **1990**, p5.

[2] M. Irie, *Chem. Rev.* **2000**, *100*, 1685-1716.

[3] M. Irie, T. Fukaminato, T. Sasaki, N. Tamai, T. Kawai, *Nature* **2002**, *420*, 759–760.

[4] M. Irie, T. Fukaminato, K. Matsuda, S. Kobatake, *Chem. Rev.* **2014**, *114*, 12174–12277.

[5] K. Uchida, M. Irie, *Chem. Lett.* **1995**, *24*, 969–970.

[6] M. Irie, K. Uchida, *Bull. Chem. Soc. Jpn.* **1998**, *71*, 985–996.

[7] M. Morimoto, M. Irie, *Chem. Commun.* **2005**, 3895–3905.

[8] M. Irie, *Proc. Jpn. Acad., Ser. B* **2010**, *86*, 472–483.

[9] K. Amimoto, T. Kawato, *J. Photochem. Photobiol. C* **2005**, *6*, 207–226.

[10] A. Takanabe, M. Tanaka, K. Johmoto, H. Uekusa, T. Mori, H. Koshima, T. Asahi, *J. Am. Chem. Soc.* **2016**, *138*, 15066−15077.

[11] T. Taniguchi, H. Sugiyama, H. Uekusa, M. Shiro, T. Asahi, H. Koshima, *Nat. Commun.* **2018**, *9*, 538.

[12] T. Taniguchi, H. Sato, Y. Hagiwara, T. Asahi, H. Koshima, *Commun. Chem.* **2019**, *2*, 19.

[13] H. Sugiyama, K. Johmoto, A. Sekine, H. Uekusa, *Cryst. Growth Des.* **2019**, *19*, 4324−4331.

[14] H. Sugiyama, H. Uekusa, *Acta Cryst.* **2021**, *C77*, 56–60.

[15] G. M. J. Schmidt, *Pure Appl. Chem.* **1971**, *27*, 647–678.

[16] S. Kobatake, K. Uchida, E. Tsuchida, M. Irie, *Chem. Commun.* **2002**, 2804–2805.

[17]   S. Kobatake, M. Irie, *Bull. Chem. Soc. Jpn.* **2004**, *77*, 195–210.

[18]   J. G. Victor, J.M. Torkelson, *Macromolecules* **1987**, *20*, 2241–2250.

[19]   H. Sugiyama, H. Uekusa, *CrystEngComm* **2018**, *20*, 2144–2151.

[20]   K. Uchida, Y. Nakayama, M. Irie, *Bull. Chem. Soc. Jpn.* **1990**, *63*, 1311–1315.

[21]   S. Kobatake, T. Yamada, K. Uchida, N. Kato, M. Irie, *J. Am. Chem. Soc.* **1999**, *121*, 2380–2386.

[22]   S. Kobatake, M. Irie, *Tetrahedron* **2003**, *59*, 8359–8364.

[23]   M. Irie, O. Miyatake, K. Uchida, *J. Am. Chem. Soc.* **1992**, *114,* 8715–8716.

[24]   S. Kobatake, M. Yamada, T. Yamada, M. Irie, *J. Am. Chem. Soc.* **1999**, *121*, 8450–8456.

[25]   S. Kobatake, S. Takami, H. Muto, T. Ishikawa, M. Irie, *Nature* **2007**, *446*, 778–781.

[26]   S. P. Venkateshan, *Mechanical Measurements*, John Wiley & Sons, New York, **2008**.

[27]   M. Morimoto, M. Irie, *J. Am. Chem. Soc.* **2010**, *132*, 14172–14178.

[28]   S. Kobatake, H. Hasegawa, K. Miyamura, Cryst. Growth Des. **2011**, *11*, 1223–1229.

[29]   D. Kitagawa, S. Kobatake, *J. Phys. Chem. C* **2013**, *117*, 20887−20892.

[30]   D. Kitagawa, C. Iwaihara, H. Nishi, S. Kobatake, *Crystals* **2015**, *5*, 551−561.

[31]   A. Hirano, T. Hashimoto, D. Kitagawa, K. Kono, S. Kobatake, *Cryst. Growth Des.* **2017**, *17*, 4819–4825.

[32]   D. Kitagawa, H. Nishi, S. Kobatake, *Angew. Chem. Int. Ed.* **2013**, *52*, 9320–9322.

[33]   D. Kitagawa, H. Tsujioka, F. Tong, X. Dong, C. J. Bardeen, S. Kobatake, *J. Am. Chem. Soc.* **2018**, *140*, 4208−4212.

[34]   D. Kitagawa, R. Tanaka, S. Kobatake, *CrystEngComm* **2016**, *18*, 7236−7240.

[35]   D. Kitagawa, K. Kawasaki, R. Tanaka, S. Kobatake, *Chem. Mater.* **2017**, *29*, 7524−7532.

[36]   A. Hirano, D. Kitagawa, S. Kobatake, *CrystEngComm* **2019**, *21*, 2495–2501.

[37]   K. Uchida, S. Sukata, Y. Matsuzawa, M. Akazawa, J. J. D. de Jong, N. Katsonis, Y. Kojima, S. Nakamura, J. Areephong, A. Meetsma, B. L. Feringa, *Chem. Commun.* **2008**, 326–328.

[38]   S. Ohshima, M. Morimoto, M. Irie, *Chem. Sci.* **2015**, *6*, 5746–5752.

[39]   F. Terano, M. Morimoto, M. Irie, *Angew. Chem. Int. Ed.* **2012**, *4*, 901–904.

[40]   D. Kitagawa, S. Kobatake, *Chem. Commun.* **2015**, *51*, 4421−4424.

[41]   E. Hatano, M. Morimoto, K. Hyodo, N. Yasuda, S. Yokojima, S. Nakamura, K. Uchida, *Chem. Eur. J.* **2016**, *22*, 12680–12683.

[42] F. Tong, D. Kitagawa, X. Dong, S. Kobatake, C. J. Bardeen, *Nanoscale*, **2018**, *10*, 3393–3398.

[43] R. Kajiya, S. Sakakibara, H. Ikawa, K. Higashiguchi, K. Matsuda, H. Wada, K. Kuroda, A. Shimojima, *Chem. Mater.* **2019**, *31*, 9372–9378.

[44] R. Nishimura, A. Fujimoto, N. Yasuda, M. Morimoto, T. Nagasaka, H. Sotome, S. Ito, H. Miyasaka, S. Yokojima, S. Nakamura, B. L. Feringa, K. Uchida, *Angew. Chem. Int. Ed.* **2019**, *58*, 13308–13312.

[45] A. Fujimoto, N. Fujinaga, R. Nishimura, E. Hatano, L. Kono, A. Nagai, A. Sekine, Y. Hattori, Y. Kojima, N. Yasuda, M. Morimoto, S. Yokojima, S. Nakamura, B. L. Feringa, K. Uchida, *Chem. Sci.* **2020**, *11*, 12307–12315.

[46] S. C. Sahoo, M. K. Panda, N. K. Nath, P. Naumov, *J. Am. Chem. Soc.* **2013**, *135*, 12241–12251.

[47] Y. Hagiwara, T. Taniguchi, T. Asahi, H. Koshima, *J. Mater. Chem. C* **2020**, *8*, 4876–4884.

[48] S. Hasebe, Y. Hagiwara, J. Komiya, M. Ryu, H. Fujisawa, J. Morikawa, T. Katayama, D. Yamanaka, A. Frube, H. Sato, T. Asahi, H. Koshima, *J. Am. Chem. Soc.* **2021**, *143*, 8866–8877.

[49] E. Uchida, R. Azumi, Y. Norikane, Nat. Commun. **2015**, *6*, 7310.

[50] Y. Yue, Y. Norikane, R. Azumi, E. Koyama, *Nat. Commun.* **2018**, *9*, 3234.

[51] L. Dong, Y. Zhao, *Mater. Chem. Front.* **2018**, *2*, 1932–1943.

[52] A. Ryabchun, Q. Li, F. Lancia, I. Aprahaman, N. Katsonis, *J. Am. Chem. Soc.* **2019**, *141*, 1196–1200.

[53] F. Lancia, A. Ryabchun, A. D. Nguindjel, S. Kwangmettatam, N. Katsonis, *Nat. Commun.* **2019**, *10*, 4819.

[54] J. Kim, J. W. Kim, H. C. Kim, L. Zhai, H. U. Ko, R. M. Muthoka, *Int. J. Precis. Eng. Manuf.* **2019**, *20*, 2221–2241.

[55] Y. S. Kim, M. Liu, Y. Ishida, Y. Ebina, M. Osada, T. Sasaki, T. Hikima, M. Takata, T. Aida, *Nat. mater.* **2015**, *14*, 1002–1007.

[56] Z. Sun, Y. Yamauchi, F. Araoka, Y. S. Kim, J. Bergueiro, Y. Ishida, Y. Ebina, T. Sasaki, T. Hikima, T. Aida, *Angew. Chem. Int. Ed.* **2018**, *57*, 15772–15776.

[57] Y. Takashima, S. Hatanaka, M. Otsubo, M. Nakahata, T. Kakuta, A. Hashidzume, H. Yamaguchi, A. Harada, *Nat. Commun.* **2012**, *3*, 1270.

[58] M. Nakahata, Y. Takashima, A. Hashidzume, A. Harada, *Angew. Chem. Int. Ed.* **2013**, *52*, 5731–5735.

[59] K. Iwaso, Y. Takashima, A. Harada, *Nat. Chem.* **2016**, *8*, 625–632.

[60] S. Ikejiri, Y. Takashima, M. Osaki, H. Yamaguchi, A. Harada, *J. Am. Chem. Soc.*

2018, *49*, 17308–17315.

[61] H. Trommsdorf, *Ann. Chem. Pharm.* **1834**, *11*, 190–207.

[62] H. D. Roth, *Angew. Chem., Int. Ed. Engl.* **1989**, *28*, 1193–1207.

[63] M. A. Garcia-Garibay, *Acc. Chem. Res.* **2003**, *36*, 491–498.

[64] P. Naumov, S. C. Sahoo, B. A. Zakharov, E. V. Boldyreva, *Angew. Chem. Int. Ed.* **2013**, *52*, 9990–9995.

[65] R. Medishetty, A. Husain, Z. Bai, T. Runcˇevski, R. E. Dinnebier, P. Naumov, J. J. Vittal, *Angew. Chem. Int. Ed.* **2014**, *53*, 5907–5911.

[66] M. K. Panda, T. Runčevski, A. Husain, R. E. Dinnebier, P. Naumov, *J. Am. Chem. Soc.* **2015**, *137*, 1895–1902.

[67] N. K. Nath, T. Runčevski, C. Lai, M. Chiesa, R. E. Dinnebier, P. Naumov, *J. Am. Chem. Soc.* **2015**, *137*, 13866–13875.

[68] P. Naumov, S. Chizhik, M. K. Panda, N. K. Nath, E. Boldyreva, *Chem. Rev.* **2015**, *115*, 12440–12490.

[69] A. Khalil, E. Ahmed, P. Naumov, *Chem. Commun.* **2017**, *53*, 8470–8473.

[70] I. Colombier, S. Spagnoli, A. Corval, P. L. Baldeck, M. Giraud, A. Leaustic, P. Yu, M. Irie, *J. Chem. Phys.* **2007**, *126*, 011101.

[71] D. Kitagawa, T. Okuyama, R. Tanaka, S. Kobatake, *Chem. Mater.* **2016**, *28*, 4889–4892.

[72] E. Hatano, M. Morimoto, T. Imai, K. Hyodo, A. Fujimoto, R. Nishimura, A. Sekine, N. Yasuda, S. Yokojima, S. Nakamura, K. Uchida, *Angew. Chem. Int. Ed.* **2017**, *56*, 12576–12580.

[73] A. Bianco, S. Perissinotto, M. Garbugli, G. Lanzani, C. Bertarelli, *Laser Photonics Rev.* **2011**, *5*, 711–736.

[74] T. Fukaminato, S. Ishida, R. Métivier, *NPG Asia Materials* **2018**, *10,* 859–881.

[75] M. Sakai, T. Seki, Y. Takeoka, *Small* **2018**, *14*, 1800817.

[76] S. Ishida, D. Kitagawa, S. Kobatake, S. Kim, S. Kurihara, T. Fukaminato, *Chem. Commun.* **2019**, *55*, 5681–5684.

[77] L. Wang, Q. Li, *Chem. Soc. Rev.* **2018**, *47*, 1044–1097.

[78] Y. Wakayama, R. Hayakawa, K. Higashiguchi, K. Matsuda, *J. Mater. Chem. C* **2020**, *8*, 10956–10974.

[79] U. A-Atar, R. Fernandes, B. Johnsen, D. Baillie, N. R. Branda, *J. Am. Chem. Soc.* **2009**, *131*, 15966–15967.

[80] K. Sumaru, K. Kikuchi, T. Takagi, M. Ymaguchi, T. Satoh, K. Morishita, T. Kanamori, *Biotechnol. Bioeng.* **2013**, *110*, 348−352.

[81] J. Zhang, J. Wang, H. Tian, *Mater. Horiz.* **2014**, *1*, 169–184.

[82]   R. Klajn, *Chem. Soc. Rev.* **2014**, *43*, 148–184.

[83]   R. Kodama, K. Sumaru, K. Morishita, T. Kanamori, K. Hyodo, T. Kamitanaka, M. Morimoto, S. Yokojima, S. Nakamura, K. Uchida, *Chem. Commun.* **2015**, *51*, 1736–1738.

[84]   J. Okuda, Y. Tanaka, R. Kodama, K. Sumaru, K. Morishita, T. Kanamori, S. Yamazoe, K. Hyodo, S. Yamazaki, T. Miyatake, S. Yokojima, S. Nakamura, K. Uchida, *Chem. Commun.* **2015**, *51*, 10957–10960.

[85]   T. Tian, Y. Song, J. Wang, B. Fu, Z. He, X. Xu, A. Li, Xin Zhou, S. Wang, X. Zhou, *J. Am. Chem. Soc.* **2016**, *138*, 955−961.

[86]   P. Shi, E. Ju, Z. Yan, N. Gao, J. Wang, J. Hou, Y. Zhang, J. Ren, X. Qu, *Nat. Commun.* **2016**, *7*, 13088−13096.

[87]   V. G. López, F. Chen, L. G. Nilewski, G. Duret, A. Aliyan, A. B. Kolomeisky, J. T. Robinson, G. Wang, R. Pal, J. M. Tour, *Nature* **2017**, *548*, 567−572.

[88]   A. S. Lubbe, Q. Liu, S. J. Smith, J. W. Vries, J. C. M. Kistemaker, A. H. Vries, I. Faustino, Z. Meng, W. Szymanski, A. Herrmann, B. L. Feringa, *J. Am. Chem. Soc.* **2018**, *140*, 5069−5076.

[89]   A. Presa, R. F. Brissos, A. B. Caballero, I. Borilovic, L. Korrodi-Gregório, R. Pérez-Tomás, O. Roubeau, P. Gamez, *Angew. Chem. Int. Ed.* **2015**, *54*, 4561–4565.

[90]   A. Presa, L. Barrios, J. Cirera, L. Korrodi-Gregório, R. Pérez-Tomás, S. J. Teat, P. Gamez, *Inorg. Chem.*, **2016**, *55*, 5356–5364.

[91]   S. Samanta, J. Locklin, *Langmuir* **2008**, *24*, 9558−9565.

[92]   K. Uchida, N. Nishikawa, N. Izumi, S. Yamazoe, H. Mayama, Y. Kojima, S. Yokojima, S. Nakamura, K. Tsujii, M. Irie, *Angew. Chem. Int. Ed.* **2010**, *45*, 5942-5944.

[93]   P. Tannouri, K. M. Arafeh, J. M. Krahn, S. L. Beaupré, C. Menon, N. R. Branda, *Chem. Mater.* **2014**, *26*, 4330−4333.

[94]   K. Takase, K. Hyodo, M. Morimoto, Y. Kojima, H. Mayama, S. Yokojima, S. Nakamura, K. Uchida, *Chem. Commun.* **2016**, *52*, 6885−6887.

[95]   N. H. Xie, Y. Chen, H. Ye, C. Li, M. Q. Zhu, *Front. Optoelectron.* **2018**, *4*, 317–332.

[96]   S. Yagai, K. Iwai, M. Yamauchi, T. Karatsu, A. Kitamura, S. Uemura, M. Morimoto, H. Wang, F. Würthner, *Angew. Chem. Int. Ed.* **2014**, *53*, 2602−2606.

[97]   B. Adhikari, Y. Yamada, M. Yamauchi, K. Wakita, X. Lin, K. Aratsu,T. Ohba, T. Karatsu, M. J. Hollamby, N. Shimizu, H. Takagi, R. Haruki, S. Adachi, S. Yagai, *Nat. Commun.* **2017**, *8*, 15254.

18

[98] B. Adhikari, T. Suzuki, L. Xu, M. Yamauchi, T. Karatsu, S. Yagai, *Polymer* **2017**, *128*, 356e362.

[99] T. Kobayashi, Y. Kitamoto, Y. Hirai, T. Kajitani, T. Seki, S. Yagai, *Commun. Chem.* **2018**, *1*, 58.

[100] B. Adhikari, K. Aratsu, J. Davis, S. Yagai, *Angew. Chem. Int. Ed.* **2019**, *58*, 3764–3768.

[101] T. Fukushima, K. Tamaki, A. Isobe, T. Hirose, N. Shimizu, H. Takagi, R. Haruki, S. Adachi, M. J. Hollamby, S. Yagai, *J. Am. Chem. Soc.* **2021**, *143*, 5845–5854.

[102] K. Higashiguchi, G. Taira, J. Kitai, T. Hirose, K. Matsuda, *J. Am. Chem. Soc.* **2015**, *137*, 2722−2729.

[103] A. Sakaguchi, K. Higashiguchi, H. Yotsuji, K. Matsuda, *J. Phys. Chem. B* **2017**, *121,* 4265−4272.

[104] H. Yotsuji, K. Higashiguchi, R. Sato, Y. Shigeta, K. Matsuda, *Chem. Eur. J.* **2017**, *23*, 15059–15066.

[105] A. Sakaguchi, K. Higashiguchi, K. Matsuda, *Chem. Commun.* **2018**, *54*, 4298–4301.

[106] N. Nishikawa, S. Sakiyama, S. Yamazoe, Y. Kojima, E. Nishihara, T. Tsujioka, H. Mayama, S. Yokojima, S. Nakamura, K. Uchida, *Langmuir* **2013**, *29*, 8164–8169.

[107] R. Nishimura, K. Hyodo, H. Sawaguchi, Y.Yamamoto, Y. Nonomura, H. Mayama, S. Yokojima, S. Nakamura, K. Uchida, *J. Am. Chem. Soc.* **2016**, *138*, 10299–10303.

[108] R. Nishimura, H. Mayama, Y. Nonomura, S Yokojima, S. Nakamura, K. Uchida, *Langmuir* **2019**, *35*, 14124–14132.

[109] R. Nishimura, K. Hyodo, H. Mayama, S. Yokojima, S. Nakamura, K. Uchida, *Commun. Chem.* **2019**, *2*, 90.

[110] T. van Leeuwen, A. S. Lubbe, P. Štacko, S. J. Wezenberg, B. L. Feringa, *Nat. Rev. Chem.* **2017**, *1*, 0096.

[111] K. Hüll, J. Morstein, D. Trauner, *Chem. Rev.* **2018**, *118*, 10710–10747.

[112] M. Irie, M. Mohri, *J. Org. Chem.* **1988**, *53*, 803–808.

[113] S. Nakamura, M. Irie, *J. Org. Chem.* **1988**, *53*, 6136–6138.

Chapter 2

Photoinduced cytotoxicity and cell killing mechanism of photochromic diarylethene

2.1 Introduction

Nitrogen-containing heterocyclic compounds have attracted much attention in the application of organic chemistry, especially in the rapidly expanding field of medicinal chemistry and pharmaceutical industry.[1] The Food and Drug Administration (FDA) database has revealed many of the unique small molecule drugs contain N-based heterocycles, indicating the structural importance of N-based heterocycles in drug design and drug discovery.[1,2] However, one major drawback of general chemotherapy is the development of unpleasant treatment-related side effects due to poor selectivity of therapeutic agents.[3] Photopharmacology has been proposed as one approach to solve such problems.[4] By introducing molecular switches, light can be used as an external stimuli to control drug activity in the living body. There have been reported studies on the incorporation of molecular switches into existing drugs to control drug activity.[5] Ideally, to achieve precise control based on molecular switching mechanisms at the molecular level, it is more desirable to use photoresponsive molecules that act as anticancer drugs. However, the number of expected photo-responsive molecules having the ability to act agents is still small.

Diarylethenes (DAEs) are photoswitchable molecules, and they have been applied to optical memories and phototriggers.[6] Recently, they have also been used in biological applications such as photopharmacology[4.7] and single molecule localization microscopy[8,9], and the use of optical switches in this field has recently attracted increasing interest. DAEs are generally known as thermally stable photochromic molecules, which are converted to closed or open forms when exposed to UV or visible light.[6]

In 2015 our group reported the photoinduced cytotoxicity of a DAE having thiazole rings in the molecule.[10] The photoinduced cytotoxicity of this derivative was observed when it reached some critical sites in the cell (i.e., DNA or mitochondria) in the closed-form, where it exerted a lethal effect in response to blue-visible (λ = 436 nm) light irradiation. Importantly, this DAE showed photoinduced cytotoxicity upon blue-visible light irradiation, even though it did not show the toxic release by photodegradation[11] or the drug structure in the molecule[12]. The photoinduced cytotoxicity of this molecule was not observed when the N atom of the thiazole rings were replaced with CCH_3.[10] For this reason, it was highly likely that the nitrogen-containing heterocycles in the DAE molecule

are related to the photoinduced cytotoxicity. However, there were two problems. One was that very few cases of photoinduced cytotoxicity using simple structured DAE were reported. Therefore, no information concerning the relationship between intramolecular nitrogen-containing heterocycles and photoinduced cytotoxicity was reported. The other was the data collected so far is not sufficient to understand the mechanism of photoinduced cytotoxicity and wavelength dependence on the cytotoxicity.

In this chapter, we describe the two contents. The first is an investigation of the photoinduced cytotoxicity of symmetric DAE to clarify the relationship between the photoinduced cytotoxicity and molecular structure, size, of DAEs with heterocycles. The second is a systematic investigation of light-induced structure-activity relationships to elucidate the cell killing mechanism of DAE.

2.2 Experimental

2.2.1. Materials

All commercial reagents were used as received unless otherwise stated. Diarylethenes (DAEs) **2.1o**,[13] **2.2o**,[14] **2.7o**,[15] **2.8o**,[16] **2.9o**,[17] **2.10o**,[18] **2.11o**,[19] **2.13o**,[20] **2.14o**,[21] **2.15o**,[13] and **2.17o**[22] were synthesized according to the procedure described in the literature. The DNA used was sodium salts of DNA from Salmon testes (average M_w: 1.3×10^6, ca. 2000 bp); SIGMA-ALDRICH D1626[23]. A_{260}/A_{280} is a measure of nucleic acid purity. DNA is known to absorb light at 260 nm, and an $A_{260/280}$ ratio of 1.8-2.0 indicates that the sample is of good purity with little or no contamination.[24] The A_{260}/A_{280} ratio in Dulbecco's phosphate-buffered saline (D-PBS; pH 7.1-7.7, Wako, Osaka, Japan): DMSO = 95: 5 (v/v) of the DNA used in this study ranged from 1.8 to 2.0.

2.2.2 General information

^{1}H (400 MHz), ^{13}C (100 MHz), and ^{19}F NMR (376 MHz) spectra were recorded on JEOL JNM-400 spectrometer. Chemical shifts are reported in ppm from the signals of tetramethylsilane (TMS) for ^{1}H NMR (TMS: 0.00 ppm, s)[25], solvent peak for ^{13}C NMR (CHCl$_3$: 77.16 ppm)[22], and hexafluorobenzene (C$_6$F$_6$) for ^{19}F NMR (C$_6$F$_6$: -164.9 ppm) in CDCl$_3$. In the case of molecules with perfluorocyclopentene rings, the ^{13}C NMR measurement by the ^{1}H decoupling method lacks signals from the fluorine-bonded carbon atoms. To measure these lacking signals, we performed ^{13}C NMR measurements using the ^{19}F decoupling method. However, the ^{13}C NMR using the ^{19}F decoupling method gave no clear data because the peaks were split by ^{1}H coupling. Note, therefore, that the ^{13}C NMR data in this paper were measured using the standard ^{1}H decoupling method. High

resolution mass spectrometry (HRMS) was recorded on JEOL JMS-S3000 SpiralTOF. Melting points were observed on Yanaco MP-500D. Absorption spectra of the solutions were monitored on a Hitachi UH-4150 spectrophotometer. Fluorescence spectra of the solutions were monitored on a Hitachi F-7100 Fluorescence spectrophotometer. Electron spin resonance (ESR) spectra were monitored on a JEOL JES-FR30EX spectrometer. Circular dichroism (CD) spectra were monitored on a JASCO J-820 Spectropolarimeter. For the UV light irradiation, a UV hand lamps SPECTROLINE Model EB-280C/J (λ = 313 nm) and an AS ONE Handy UV Lamp LUV-6 (dominant wavelength: 365 nm, 810 μW cm^{-2}) and a KEYENCE UV-400 attached with UV-50H (λ = 365 nm, 110 mW cm^{-2}) were used. For visible light irradiation, lumencor SPECTRA III (λ = 438 nm, 120 mW), Asahi spectra CL-1503 attached with CL-H1-430-9-1 and CL-H1LCB01, and a 500W USHIO SX-UI501XQ Xenon lamp with Toshiba color filters (Y-48, Y-44, UV-29: λ > 480 nm) or Asahi spectra optical filters (MZ0430: λ = 436 nm, 18 mW cm^{-2} or MZ0550: λ = 550 nm, 6 mW cm^{-2}) were used. Determination of the quantum yields of the photochromic isomerization reactions were performed in a homemade setup. Irradiation was performed in 1 cm path quartz cuvettes under continuous stirring, using Mercury lamp (500 W USHIO optical module H500) at 365 $\pm$ 4 nm and Xenon lamp (500W USHIO SX-UI501XQ) at 470 $\pm$ 12 nm (Thorlabs) as irradiation sources. The intensities of the irradiation light were estimated comparing the photochromic reactions of DAEs as standards. Agarose gel electrophoresis was performed Takara bio Mupid-exU. All measurements were performed at room temperature unless otherwise specified.

The Gaussian16 program package[26] was used for geometry optimization with density functional theory (DFT)[27,28] for ground states. The B3LYP[29-31] and ωB97X-D[32] functionals were adopted as exchange-correlation terms of DFT. The gaussian 6-31G(d) basis set was adopted for all calculations. As for the solvent effect, a polarizable continuum model (PCM)[33] was employed for water.

The Avogadro ver. 1.2.0 (Hanwell et al., 2012)[34] was used for calculation of geometrical parameters of the DAE molecule obtained by DFT calculation.

HeLa cell line derived from human cervical adenocarcinoma was purchased from Riken Cell Bank (No. RCB0007). Light irradiation of HeLa cells in a medium containing each DAE was carried out by using a PC-controlled micro-projection system (DESM-01, Engineering System Co.) installed in an inverted research microscope (IX70, Olympus Co.).[35-38] Near-UV light with wavelength of 365 nm, blue light with wavelength of 436 nm or green light with wavelength of 546 nm was irradiated onto arbitrary areas of the sample as observed through the same objective lens.

2.2.3 X-ray crystallographic analysis

X-ray crystallographic analysis for bulk crystals of **2.3o**, **2.4o**, and **2.5o** were performed with an X-ray diffractometer (Bruker AXS, D8 QUEST) with Mo Kα radiation (λ = 0.71073 Å). The crystals were cooled using a low temperature controller (Japan Thermal Engineering, JAN 2-12). The diffraction frames were integrated with the Bruker SAINT program. The cell constants were determined by the global refinement. The data were corrected for absorption effects using the multi-scan method (SADABS). The structure was solved by the direct method and refined by the full-matrix least-squares method using the SHELX-2014 program. The positions of all hydrogen atoms were calculated geometrically and refined by the riding model. The crystallographic data can be obtained free of charge from the Cambridge Crystallographic Data Center via www.ccdc.cam.ac.uk/data_request/cif. (CCDC 2095136-2095138: Figures 2.1-2.3 and Tables 2.1-2.3).
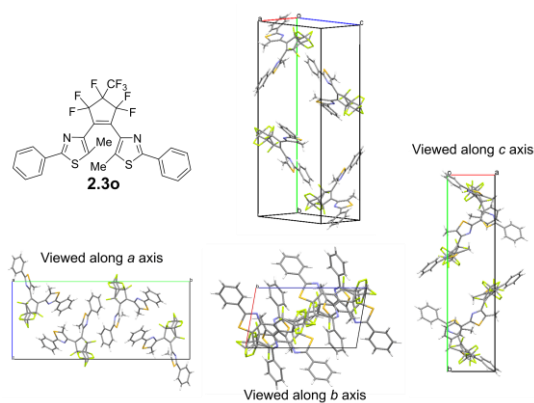

Figure 2.1 Molecular packing of **2.3o** in the crystal.

Table 2.1 Crystal data of **2.3o** crystal.

	2.3o
formula	$C_{26}H_{16}F_8N_2S_2$
formula weight	572.53
T / K	128(2)
crystal system	monoclinic
space group	P 1 2$_1$/c 1
a / Å	6.9257(3)
b / Å	28.2706(15)
c / Å	12.4537(6)
α / °	90
β / °	99.8416(17)
γ / °	90
V / Å³	2402.5(2)
Z	4
R_1 (I > 2σ(I))	0.0398
wR_2 (I > 2σ(I))	0.0979
R_1 (all data)	0.0594
wR_2 (all data)	0.1150
CCDC No.	2095136
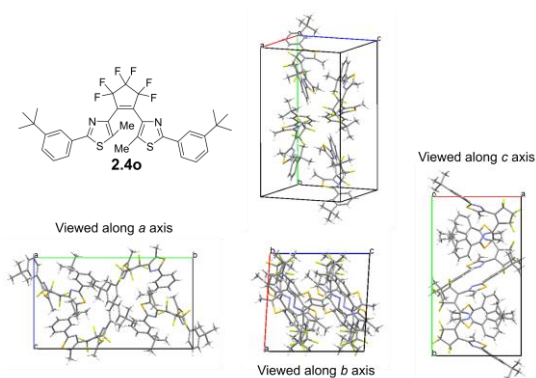
Figure 2.2 Molecular packing of **2.4o** in the crystal.

Table 2.2 Crystal data of **2.4o** crystal.

	2.4o
formula	$C_{33}H_{32}F_6N_2S_2$
formula weight	634.72
T / K	173(2)
crystal system	monoclinic
space group	P 1 2₁/c 1
a / Å	11.9900(5)
b / Å	21.3155(10)
c / Å	12.2134(5)
α / °	90
β / °	93.3338(17)
γ / °	90
V / Å³	3116.1(2)
Z	4
R_1 (I > 2σ(I))	0.0554
wR_2 (I > 2σ(I))	0.1504
R_1 (all data)	0.0637
wR_2 (all data)	0.1576
CCDC No.	2095138
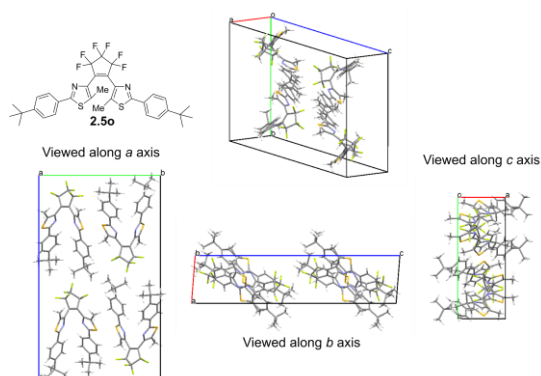
Figure 2.3 Molecular packing of **2.5o** in the crystal.

Viewed along *a* axis

Viewed along *c* axis

Viewed along *b* axis

2.5o

Table 2.3 Crystal data of **2.5o** crystal.

	2.5o
formula	$C_{33}H_{32}F_6N_2S_2$
formula weight	634.72
T / K	173(2)
crystal system	monoclinic
space group	P 1 2$_1$/$_C$ 1
a / Å	6.57040(10)
b / Å	16.6413(3)
c / Å	28.0569(5)
α / °	90
β / °	94.4663(6)
γ / °	90
V / Å³	3058.43(9)
Z	4
R_1 (I > 2σ(I))	0.0325
wR_2 (I > 2σ(I))	0.0848
R_1 (all data)	0.0329
wR_2 (all data)	0.0854
CCDC No.	2095137

2.2.4 Photoinduced cytotoxicity experiments

Since clear microscopic image was difficult to obtained for the cells in a well of 96 well plates, we used cell culture dish for the microscopic observation. Typical experimental conditions are as follows.

1. The HeLa cells (8×10^5) were seeded in a 35-mϕ dish together with 2 mL of a medium (Minimum Essential Media: MEM) containing a predetermined concentration of DAE.

2. After incubation for 18 h, the culture medium was replaced with a fresh one. Then, local light irradiation was carried out in order to achieve better distinction.

3. Changes in the appearance were observed 2 hours after irradiation.

The DAEs were added in the culture medium as ethanol solution due to their poor water solubility. The maximum amount of ethanol added to the medium was 0.5% and we had confirmed that the ethanol with those concentrations had no influence on the viability or

growth of HeLa cells in advance.

As a guidance in the comparing investigation to know the tendency of the structure dependent cytotoxicity of DAEs, we determined the lower limit concentration (LLC) of DAEs at which the photocytotoxicity started to appear clearly as follows.

1. The HeLa cells (5×10^5) were seeded in each well of 96 well plates together with 0.1 mL of a culture medium (MEM) containing a predetermined concentration of DAE (0.02, 0.05, 0.1, 0.2, 0.5, 1, and 2 ppm or 0.02, 0.05, 0.1, 0.2, 0.5, 1, 2, and 5 ppm).

2. After incubation for 18 h, the dark cytotoxicity was evaluated from the number of live cells.

3. Culture medium was replaced with a fresh one, and then blue light (λ = 436 nm, 180 mW cm^{-2}) was irradiated for 2 min.

4. The cells were observed 2 hours after irradiation, and the lower limit concentration expressing photoinduced cytotoxicity was determined with the criterion that more than 80% exhibited a change in appearance.

2.2.5 Estimation of DNA intercalation of DAE using ethidium bromide

We estimated the intercalation of DAE into DNA using ethidium bromide (EB), a known intercalator of DNA. In aqueous solution of DNA, EB emits strong fluorescence in the intercalating state. Accordingly, the number of available binding sites of DNA can be estimated directly from the fluorescence intensity (I) under the binding equilibrium at a certain concentration of free EB. When much stronger intercalators (closed ring DAEs) are added, they occupy the binding sites of DNA preferentially. Accompanied by the decrease in the number of binding sites available for EB, I decrease proportionally. Consequently, (number of binding sites unoccupied by DAE)/(number of binding sites occupied by DAE) corresponds to the experimental value of (I_0-I)/I.

2.2.6 DNA intercalation experiments[12,39]
Preparation of sample

To a 100 mL sample tube, 57 mL of D-PBS solution, 1.5 mL of DMSO, 1.77×10^{-3} g (4.49×10^{-6} mol) of ethidium bromide (EB), and 3.0×10^{-4} g (4.63×10^{-7} mol bp^{-1}, ca. 2000 bp) of DNA (sodium salts of DNA from salmon testes; SIGMA-ALDRICH D1626)[20] were added and stirred for 24 h at room temperature to form the DNA solution.

To a 10 mL sample tube, 1.5×10^{-6} mol of open- or closed-ring isomers of DAE derivatives dissolved in 1.5 mL of DMSO were added. These solutions and DMSO were

mixed while changing the composition ratio and adjusting it to become 100 μL in total, and 3.9 mL of DNA solutions were added. The concentrations in the mixed solution were D-PBS/DMSO = 95: 5 (v/v), DNA: 3.9 nM bp^{-1} and EB: 75 μM. The concentration of open- or closed-ring isomers of DAEs in the final mixed solutions were 0, 5, 10, 15, 20, and 25 μM (Table 2.4).

Measurement

Fluorescence spectra of solutions of DNA with EB were measured just after the addition and 24 hours after the addition of open-/closed-ring isomers of DAEs. These measurements were performed three times for each condition. The fluorescence intensity of EB was recorded at the emission wavelength of 610 nm.

Fluorescence spectra were monitored at constant concentrations of DNA and EB (3.9 nM bp^{-1} and 75 μM, respectively), while adding increasing amounts of DAEs (in the range of 0-25 μM) (Table 2.4).

Table 2.4 Mixed Ratio of DAE solutions and DMSO.

	DAE concentrations in final mixture					
	0 μM	5 μM	10 μM	15 μM	20 μM	25 μM
DAE solution / μL	0	20	40	60	80	100
DMSO / μL	100	80	60	40	20	0

2.2.7 Optimized structure by DFT calculation

To investigate the relationship between molecular bulkiness and DNA intercalation of the open- and closed-ring isomers of DAE derivatives, the optimized geometry of the open- and closed-ring isomers of each molecule were determined using DFT calculations. The procedure consists of two steps:

1. Full optimization of ground state energies on the B3LYP/6-31G(d) or ωB97XD/6-31G(d) level of theory. The effect of water as solvent was included using the polarizable continuum model (PCM).

2. Calculation of vibrational frequencies to prove that the optimized structure corresponds to a global minimum on the potential energy surface.

2.2.8 Western blot assay

Whole-cell lysates were prepared as described elsewhere.[40] The lysate proteins were

fractionated by size by sodium dodecyl sulfate-polyacrylamide gel electrophoresis (SDS-PAGE) and then electroblotted onto polyvinylidene difluoride (PVDF) membranes. The blots were probed with the indicated antibodies, which are listed in Table 2.5. The blots were visualized using a chemiluminescence detection kit (Cell Signaling Technology, Danvers, MA) according to the manufacturer's instructions.

Table 2.5 Details of antibodies used.

name of antibody	name of provider	dilution
Phospho-ATM (Ser1981)	Cell Signaling Technology	1:1000
Phospho-ATR (Ser428)	Cell Signaling Technology	1:1000
Phospho-Histone H2A.X (Ser139)	Cell Signaling Technology	1:1000
Phospho-Chk1 (Ser345)	Cell Signaling Technology	1:1000
Phospho-Chk2 (Thr68)	Cell Signaling Technology	1:1000
BAX	Cell Signaling Technology	1:1000
BAK	Cell Signaling Technology	1:1000
CleavedCaspase-3	Cell Signaling Technology	1:1000

2.2.9 Existence of the generation of singlet oxygen by blue light irradiation in the presence of DNA

To investigate whether the cytotoxicity by blue light irradiation to the closed-ring isomers of DAEs is due to the generation of reactive oxygen species (ROS), ROS were detected by fluorescence spectroscopy using the non-fluorescent probe $DCFH_2$ (2',7'-dichlorofluorescein). The production of ROS was monitored by increases in the fluorescence intensity of the emission of DCF (2',7'-dichlorofluorescein). The preparation and measurement of the samples were carried out as follows.

Preparation of sample

To a 100 mL sample tube, 57 mL of D-PBS solution, 1.5 mL of DMSO, 3.6×10^{-4} g (8.97×10^{-7} mol) of $DCFH_2$, and 3.0×10^{-3} g (4.63×10^{-6} mol bp^{-1}, ca. 2000 bp) of DNA (sodium salts of DNA from salmon testes; SIGMA-ALDRICH D1626)[23] were added and stirred for 24 h at room temperature to form the DNA-$DCFH_2$ solution.

To a 10 mL sample tube, 1.5×10^{-6} mol of closed-ring isomers of DAEs or RB dissolved in 1.5 mL of DMSO were added. These solutions (60 μL) and DMSO (40 μL) were added to 3.9 mL of DNA-$DCFH_2$ solutions. The solutions were stirred for 24 h. The

28

concentrations in the mixed solution were D-PBS/DMSO = 95:5 (v/v), DNA: 38.5 nM bp[-1], DCFH$_2$: 15 μM, and DAEs: 15 μM.

Measurement

Fluorescence spectra were measured three times after irradiating the solutions by blue light (0-60 min), and the fluorescence intensity at 525 nm of DCF was recorded.

2.2.10 Synthesis

·Synthesis of 1,2-bis(5-methyl-2-phenylthiazol-4-yl)-3-trifluoromethylpentafluorocyclopentene (2.3o)

The derivative **2.3o** was obtained in 2% yield as a byproduct during the synthesis of 1,2-bis(5-methyl-2-phenylthiazol-4-yl)perfluorocyclohexene (**2.11o**).[19]

2.3o: m.p. 171.0-172.0°C

^{1}H NMR (400 MHz, CDCl$_3$, ppm) δ 7.90-7.87 (m, 4H), 7.43-7.42 (m, 6H), 2.09 (s, 6H).

^{13}C NMR (100 MHz, CDCl$_3$, ppm) δ 166.0, 140.2, 137.5, 133.1, 130.5, 129.1, 126.6, 12.3.

^{19}F NMR (376 MHz, CDCl$_3$, ppm) δ -76.2 (quin, J = 17 Hz, 3F), -105.5 (conformer A: q, J = 17 Hz) and -106.2 (conformer B: q, J = 17 Hz) (conformer A: conformer B = 2: 3 (ratio of the peak areas), 2F), -109.7 (conformer B: s) and -110.5 (conformer A: s) (conformer A: conformer B = 2: 3 (ratio of the peak areas), 2F), -184.8 (s, 1F). HRMS (MALDI, positive): m/z calcd. for C$_{26}$H$_{16}$F$_8$N$_2$NaS$_2$ [M+Na]$^+$: 595.05194, found: 595.05182.

·Synthesis of 1,2-bis(5-methyl-2-(3-*tert*-butyl)phenylthiazol-4-yl)perfluorocyclopentene (2.4o)

The total synthetic route of **2.4o** is shown in Scheme 2.1.
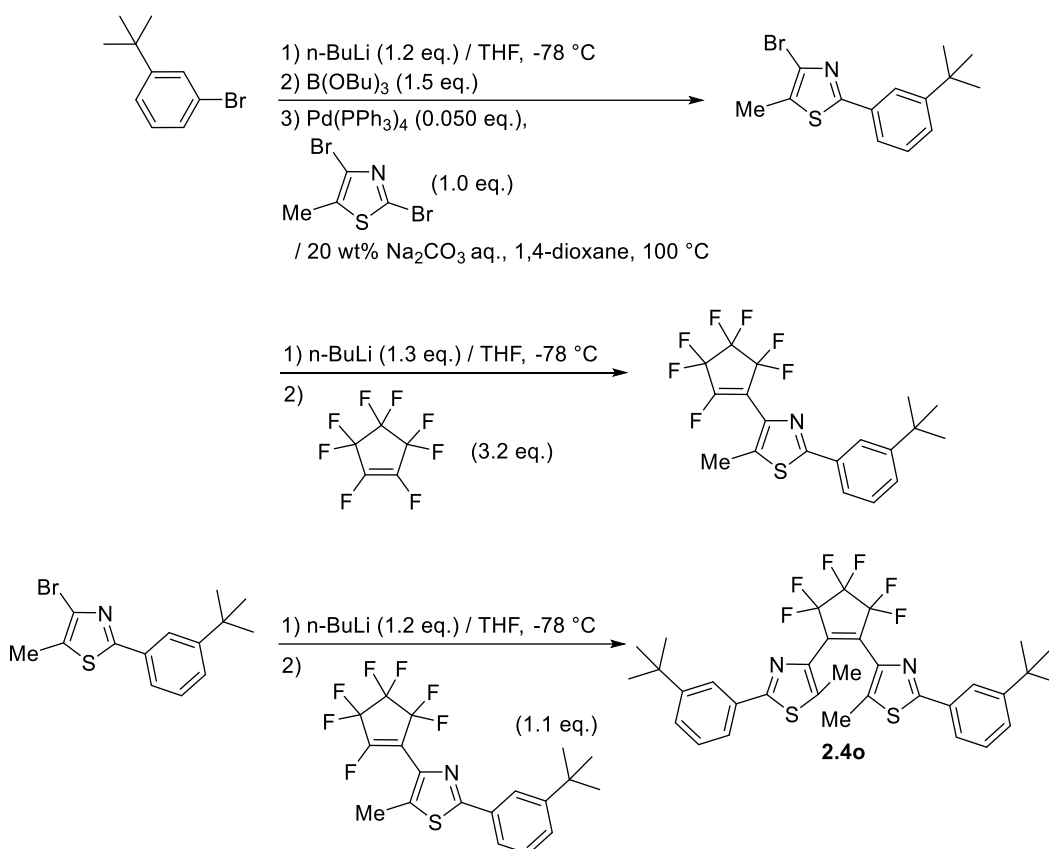
Scheme 2.1 Synthetic route of **2.4o**.

4-Bromo-5-methyl-2-(3-*tert*-butyl)phenylthiazole

To a 200 mL three neck flask containing 1.66 g (7.79 mmol) of 1-bromo-3-*tert*-butylbenzene in 45 mL of THF anhydrous on the dry ice- methanol bath at -78°C in an argon gas atmosphere. To the solution, 6.0 mL (9.60 mmol, 1.2 eq.) of 1.6 N *n*-BuLi hexane solution was gradually added in keeping the temperature and stirred for 1 h at the temperature. Then the 3.2 mL (11.96 mmol, 1.5 eq.) of tributyl borate was added, followed by stirring another 10 min, then the temperature of the reaction mixture was allowed warm to room temperature. Then the mixture was stirred for 1 h at the temperature. After reaction was over, 2 mL of water was added, and the solvents were evaporated in vacuo. The reaction mixture was added the 2,4-dibromo-5-methylthiazole[41] (2.00 g, 7.75 mmol, 1.0 eq.), tetrakis(triphenylphosphine)palladium(0) (0.45 g, 0.39 mmol, 0.050 eq.), a 20 wt% Na$_2$CO$_3$ aq. (15 mL), and 1,4-dioxane (30 mL), and the mixture was refluxed for 17 h. After reaction was over, the reaction mixture was allowed to cool to room temperature. The mixture was extracted with 50 mL of diethyl ether with four times. The organic layer was washed with 200 mL of brine and dried over sodium sulfate anhydrous. After removal of sodium sulfate by filtration, the solvents were removed in vacuo. The resulting crude

30

product was purified by column chromatography on silica gel using hexane as eluent, to obtain 1.77 g (5.71 mmol) of the 4-bromo-5-methyl-2-(3-*tert*-butyl)phenylthiazole as white solid in 73% yield.

m.p. 91.6-92.4°C. ^{1}H NMR (400 MHz, CDCl$_3$, ppm) δ 7.90 (dd, J = 1.8, 1.8 Hz, 1H), 7.66 (ddd, J = 7.7, 1.8, 1.1 Hz, 1H), 7.46 (ddd, J = 7.7, 1.8, 1.1 Hz, 1H), 7.35 (dd, J = 7.7, 7.7 Hz, 1H), 2.44 (s, 3H), 1.36 (s, 9H). ^{13}C NMR (100 MHz, CDCl$_3$, ppm) δ 166.2, 152.2, 132.7, 128.8, 128.6, 127.6, 125.3, 123.5, 123.0, 34.9, 31.4, 13.1. HRMS (MALDI, positive): *m/z* calcd. for C$_{14}$H$_{17}$NSBr [M+H]$^+$: 310.02596, found: 310.02563.

4-(2,3,3,4,4,5,5-Heptafluorocyclopentenyl)-5-methyl-2-(3-*tert*-buthylphenyl)thiazole

To a 200 mL three neck flask containing 1.50 g (4.83 mmol) of 4-bromo-5-methyl-2-(3-*tert*-butyl)phenylthiazole in 30 mL of THF anhydrous on the dry ice- methanol bath at -78°C in an argon gas atmosphere. To the solution, 3.8 mL (6.08 mmol, 1.3 eq.) of 1.6 N *n*-BuLi hexane solution was gradually added in keeping the temperature and stirred for 1 h at the temperature. To the mixture, the 1.3 mL (15.33 mmol, 3.2 eq.) of perfluorocyclopentene was gradually added, followed by stirring another 10 min. The temperature of the reaction mixture was allowed to warm to -40°C, then the solution was stirred another 4 h at the temperature. After reaction was over, 15 mL of water was added, and the mixture was allowed to warm to room temperature. Solvent of THF was evaporated in vacuo, then 300 mL of water was added. The mixture was extracted with 50 mL of diethyl ether with four times. The organic layer was washed with 100 mL of brine and dried over sodium sulfate anhydrous. After removal of sodium sulfate by filtration, the solvents were removed in vacuo. The resulting crude product was purified by column chromatography on silica gel using hexane as eluent, to obtain 1.78 g (4.20 mmol) of the 4-(2,3,3,4,4,5,5-heptafluorocyclopentenyl)-5-methyl-2-(3-*tert*-buthylphenyl)thiazole as pale-yellow solid in 87% yield.

m.p. 61.7-62.5°C. ^{1}H NMR (400 MHz, CDCl$_3$, ppm) δ 7.93 (dd, J = 1.8, 1.8 Hz, 1H), 7.70 (ddd, J = 7.7, 1.8, 1.2 Hz, 1H), 7.49 (ddd, J = 7.7, 1.8, 1.2 Hz, 1H), 7.38 (dd, J = 7.7, 7.7 Hz, 1H), 2.54 (d, J = 2.7 Hz, 3H), 1.37 (s, 9H). ^{13}C NMR (100 MHz, CDCl$_3$, ppm) δ 148.4, 137.2, 121.6, 118.5, 118.3, 117.5, 115.7, 114.3, 113.8, 13.4, 40.6, 26.0. ^{19}F NMR (376 MHz, CDCl$_3$, ppm) δ -111.3 (d, J = 11.6 Hz, 2F), -121.6 (d, J = 15.9 Hz, 2F), -128.2 (br s, 1F), -133.4 (s, 2F). HRMS (MALDI, positive): *m/z* calcd. for C$_{19}$H$_{17}$F$_7$NS [M+H]$^+$: 424.09644, found: 424.09668.

1,2-Bis(5-methyl-2-(3-*tert*-butylphenyl)thiazole-4-yl)perfluorocyclopentene (2.4o)

   To a 100 mL three neck flask containing 0.83 g (2.68 mmol) of 4-bromo-5-methyl-2-(3-*tert*-butyl)phenylthiazole in 30 mL of THF anhydrous on the dry ice- methanol bath at -78°C in an argon gas atmosphere. To the solution, 2.1 mL (3.36 mmol, 1.2 eq.) of 1.6 N *n*-BuLi hexane solution was gradually added in keeping the temperature and stirred for 1 h at the temperature. To the mixture, THF anhydrous solution containing 1.30 g (3.07 mmol, 1.1 eq.) of 4-(2,3,3,4,4,5,5-heptafluorocyclopentenyl)-5-methyl-2-(3-*tert*-buthylphenyl)thiazole was added, followed by stirring another 10 min. The temperature of the reaction mixture was allowed to warm to -40°C, then the solution was stirred another 5 h at the temperature. After reaction was over, 10 mL of water was added, and the mixture was allowed to warm to room temperature. Solvent of THF was evaporated in vacuo, then 300 mL of water was added. The mixture was extracted with 40 mL of diethyl ether with four times. The organic layer was washed with 100 mL of brine and dried over sodium sulfate anhydrous. After removal of sodium sulfate by filtration, the solvents were removed in vacuo. The resulting crude product was purified by column chromatography on silica gel using a mixture of hexane and dichloromethane (3: 1 (v/v)) as eluent, to obtain 1.12 g of crude product. Recrystallization from methanol, 0.87 g (1.37 mmol) of **2.4o** was obtained as colorless needle crystals in 51% yield.

m.p. 157.8-158.5°C. ^{1}H NMR (400 MHz, CDCl$_3$, ppm) δ 7.86 (dd, J = 1.6, 1.6 Hz, 2H), 7.68 (ddd, J = 7.8, 1.6, 1.1 Hz, 2H), 7.46 (ddd, J = 7.8, 1.6, 1.1 Hz, 2H), 7.35 (dd, J = 7.7, 7.7 Hz, 2H), 2.12 (s, 6H), 1.33 (s, 18H). ^{13}C NMR (100 MHz, CDCl$_3$, ppm) δ 166.3, 152.2, 140.4, 137.0, 132.9, 128.8, 127.7, 124.0, 123.5, 34.9, 31.4, 12.3. ^{19}F NMR (376 MHz, CDCl$_3$, ppm) δ -113.5 (s, 4F), -135.2 (s, 2F). HRMS (MALDI, positive): *m/z* calcd. for C$_{33}$H$_{32}$F$_6$N$_2$NaS$_2$ [M+Na]$^+$: 657.18033, found: 657.18024.

   ·Synthesis of 1,2-bis(5-methyl-2-(4-*tert*-butyl)phenylthiazol-4-yl)perfluorocyclopentene (2.5o)

   The total synthetic route of **2.5o** is shown in Scheme 2.2.

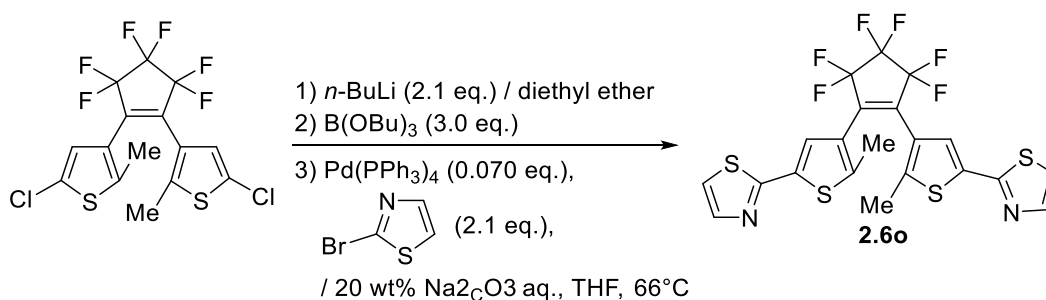**Scheme 2.2** Synthetic route of **2.5o**.

4-Bromo-5-methyl-2-(4-*tert*-butyl)phenylthiazole

To a 300 mL three neck flask containing 1.66 g (7.79 mmol) of 1-bromo-4-*tert*-butylbenzene in 30 mL of THF anhydrous on the dry ice- methanol bath at -78°C in an argon gas atmosphere. To the solution, 6.0 mL (9.60 mmol, 1.2 eq.) of 1.6 N *n*-BuLi hexane solution was gradually added in keeping the temperature and stirred for 1 h at the temperature. Then the 3.2 mL (11.96 mmol, 1.5 eq.) of tributyl borate was added, followed by stirring another 10 min, then the temperature of the reaction mixture was allowed warm to room temperature. Then the mixture was stirred for 1 h at the temperature. After reaction was over, 10 mL of water was added, and the solvents were evaporated in vacuo. The reaction mixture was added the 2,4-dibromo-5-methylthiazole[41] (2.00 g, 7.75 mmol, 1.0 eq.), tetrakis(triphenylphosphine)palladium(0) (0.45 g, 0.39 mmol, 0.050 eq.), a 20 wt% Na_2CO_3 aq. (16 mL), and 1,4-dioxane (30 mL), and the mixture was refluxed for 16 h. After reaction was over, the reaction mixture was allowed to cool to room temperature. The mixture was extracted with 30 mL of ethyl acetate with four times. The organic layer was washed with 200 mL of brine and dried over sodium sulfate anhydrous. After removal of sodium sulfate by filtration, the solvents were removed in vacuo. The resulting crude product was purified by column chromatography on silica gel using a mixture of hexane

33

and dichloromethane (3: 1 (v/v)) as eluent, to obtain 1.72 g (5.54 mmol) of the 4-bromo-5-methyl-2-(4-*tert*-butyl)phenylthiazole as white solid in 71% yield.

m.p. 72.3-73.2°C. ^{1}H NMR (400 MHz, CDCl$_3$, ppm) δ 7.80 (d, J = 8.4 Hz, 2H), 7.43 (d, J = 8.4 Hz, 2H), 2.43 (s, 3H), 1.34 (s, 9H). ^{13}C NMR (100 MHz, CDCl$_3$, ppm) δ 165.7, 153.9, 130.3, 128.8, 126.0, 125.9, 125.2, 35.0, 31.3, 13.2. HRMS (MALDI, positive): *m/z* calcd. for C$_{14}$H$_{17}$NSBr [M+H]$^+$: 310.02596, found: 31.02566.

4-(2,3,3,4,4,5,5-Heptafluorocyclopentenyl)-5-methyl-2-(4-*tert*-buthylphenyl)thiazole

To a 200 mL three neck flask containing 2.00 g (6.45 mmol) of 4-bromo-5-methyl-2-(4-*tert*-butyl)phenylthiazole in 45 mL of THF anhydrous on the dry ice- methanol bath at -78°C in an argon gas atmosphere. To the solution, 5.0 mL (8.00 mmol, 1.2 eq.) of 1.6 N *n*-BuLi hexane solution was gradually added in keeping the temperature and stirred for 1 h at the temperature. To the mixture, the 1.64 mL (19.34 mmol, 3.0 eq.) of perfluorocyclopentene was gradually added, followed by stirring another 10 min. The temperature of the reaction mixture was allowed to warm to -40°C, then the solution was stirred another 4 h at the temperature. After reaction was over, 15 mL of water was added, and the mixture was allowed to warm to room temperature. Solvent of THF was evaporated in vacuo, then 300 mL of water was added. The mixture was extracted with 50 mL of diethyl ether with four times. The organic layer was washed with 100 mL of brine and dried over sodium sulfate anhydrous. After removal of sodium sulfate by filtration, the solvents were removed in vacuo. The resulting crude product was purified by column chromatography on silica gel using hexane as eluent, to obtain 2.25 g (5.31 mmol) of the 4-(2,3,3,4,4,5,5-heptafluorocyclopentenyl)-5-methyl-2-(4-*tert*-buthylphenyl)thiazole as pale-yellow solid in 82% yield.

m.p. 88.3-88.7°C. ^{1}H NMR (400 MHz, CDCl$_3$, ppm) δ 7.83 (d, J = 8.4 Hz, 2H), 7.46 (d, J = 8.4 Hz, 2H), 2.53 (d, J = 2.9 Hz, 3H), 1.35 (s, 9H). ^{13}C NMR (100 MHz, CDCl$_3$, ppm) δ 166.4, 154.2, 138.5, 135.7, 130.2, 126.4, 126.1, 35.1. 31.3, 12.5. ^{19}F NMR (376 MHz, CDCl$_3$, ppm) δ -111.4 (d, J = 11.8 Hz, 2F), -121.6 (d, J = 15.9 Hz, 2F), -128.2 (br s, 1F), -133.4 (s, 2F). HRMS (MALDI, positive): *m/z* calcd. for C$_{19}$H$_{17}$F$_7$NS [M+H]$^+$: 424.09644, found: 424.09591.

1,2-Bis(5-methyl-2-(4-*tert*-butylphenyl)thiazole-4-yl)perfluorocyclopentene (2.5o)

To a 100 mL three neck flask containing 1.20 g (3.87 mmol) of 4-bromo-5-methyl-2-(4-*tert*-butyl)phenylthiazole in 30 mL of THF anhydrous on the dry ice- methanol bath at -78°C in an argon gas atmosphere. To the solution, 2.9 mL (4.64 mmol, 1.2 eq.) of 1.6 N *n*-BuLi hexane solution was gradually added in keeping the temperature and stirred for 1 h

at the temperature. To the mixture, THF anhydrous solution containing 1.64 g (3.87 mmol, 1.0 eq.) of 4-(2,3,3,4,4,5,5-heptafluorocyclopentenyl)-5-methyl-2-(4-*tert*-buthylphenyl)thiazole was added, followed by stirring another 30 min. The temperature of the reaction mixture was allowed to warm to -40°C, then the solution was stirred another 5 h at the temperature. After reaction was over, 10 mL of water was added, and the mixture was allowed to warm to room temperature. Solvent of THF was evaporated in vacuo, then 300 mL of water was added. The mixture was extracted with 40 mL of diethyl ether with four times. The organic layer was washed with 100 mL of brine and dried over sodium sulfate anhydrous. After removal of sodium sulfate by filtration, the solvents were removed in vacuo. The resulting crude product was purified by column chromatography on silica gel using a mixture of hexane and dichloromethane (3: 1 (v/v)) as eluent, to obtain 1.55 g of crude product. Recrystallization from ethyl acetate, 1.47 g (2.32 mmol) of **2.5o** was obtained as colorless needle crystals in 60% yield.

m.p. 189.3-189.7°C. ^{1}H NMR (400 MHz, CDCl$_3$, ppm) δ 7.81 (dd, J = 8.5, 2.1 Hz, 4H), 7.44 (dd, J = 8.5, 2.1 Hz, 4H), 2.05 (s, 6H), 1.34 (s, 18H). ^{13}C NMR (100 MHz, CDCl$_3$, ppm) δ 166.0, 136.8, 130.5, 126.4, 126.1, 121.3, 59.0, 35.0, 31.3, 12.3. ^{19}F NMR (376 MHz, CDCl$_3$, ppm) δ -113.8 (s, 4F), -135.2 (s, 2F). HRMS (MALDI, positive): *m/z* calcd. for C$_{33}$H$_{32}$F$_6$N$_2$S$_2$ [M]$^+$: 634.19056, found: 634.19030.

·**Synthesis of 1,2-bis(2-methyl-5-(2-thiaozoyl)lthiophen-3-yl)perfluorocyclopentene (2.6o)**

The total synthetic route of **2.6o** is shown in Scheme 2.3.

Scheme 2.3 Synthetic route of **2.6o**.

**1,2-Bis(2-methyl-5-(2-thiazolyl)thiophen-3-yl)perfluorocyclopenthene (2.6o)**

To a 200 mL four neck flask containing 1.00 g (2.29 mmol) of 1,2-bis(5-chloro-2-methylthiophen-3-yl)perfluorocyclopenthene[42] in 50 mL of dry diethyl ether on the dry

ice- methanol bath at -20°C in an argon gas atmosphere. To the solution, 3.15 mL (5.04 mmol, 2.1 eq.) of 1.6 N *n*-BuLi hexane solution was gradually added in keeping the temperature and stirred for 1 h on the ice- salt bath at -4°C. After that, the mixture was cooled on a dry ice- methanol bath at -20°C. Then the 1.84 mL (6.87 mmol, 3.0 eq.) of tributyl borate was added, followed by stirring another 10 min, then the temperature of the reaction mixture was allowed warm to room temperature. Then the mixture was stirred for 1 h at the temperature. After reaction was over, 10 mL of water was added, and the solvents were evaporated in vacuo. The reaction mixture was added the 2-bromothiazole (0.789 g, 4.81 mmol, 2.1 eq.), tetrakis(triphenylphosphine)palladium(0) (0.185 g, 0.16 mmol, 0.070 eq.), a 20 wt% Na_2CO_3 aq. (20 mL), and THF (20 mL), and the mixture was refluxed for 18 h. After reaction was over, the reaction mixture was allowed to cool to room temperature, and the solvent of THF was evaporated in vacuo. The mixture was extracted with 30 mL of diethyl ether with three times. The organic layer was dried over sodium sulfate anhydrous. After removal of sodium sulfate by filtration, the solvents were removed in vacuo. The resulting crude product was purified by column chromatography on silica gel using a mixture of hexane and chloroform (1: 1 (v/v)) as eluent, to obtain 1.22 g of crude product. Recrystallization from hexane and dichloromethane (3.3: 1 (v/v)), 0.819 g (1.53 mmol) of **2.6o** was obtained as pale-yellow solid in 67% yield.

m.p. 166.8-167.8°C. ^{1}H NMR (400 MHz, CDCl$_3$, ppm) δ 7.77 (d, J = 3.3 Hz, 2H), 7.48 (s, 2H), 7.29 (d, J = 3.3 Hz, 2H), 2.00 (s, 6H). ^{13}C NMR (100 MHz, CDCl$_3$, ppm) δ 160.8, 144.3, 143.5, 135.8, 125.6, 118.8, 14.9. ^{19}F NMR (376 MHz, CDCl$_3$, ppm) δ -113.3 (s, 4F), -135.0 (s, 2F). Anal. Calcd for $C_{21}H_{12}F_6S_4$: C, 47.18; H, 2.26; N, 5.24; Found: C, 46.94; H, 2.31; N, 5.17.

·**Synthesis of 1,2-bis(2-methyl-5-(pyrid-4-yl)thien-3-yl)perfluorocyclohexene (2.12o)**

The total synthetic route of **2.12o** is shown in Scheme 2.4.
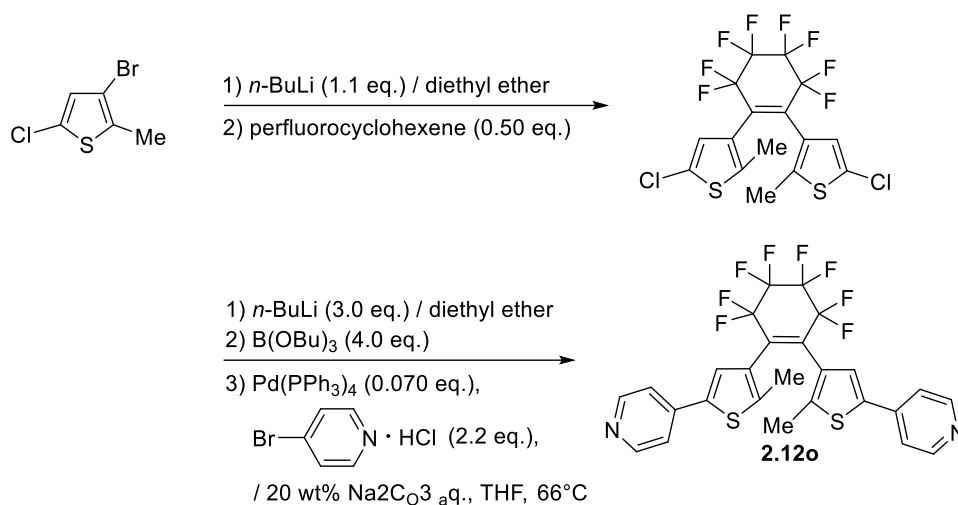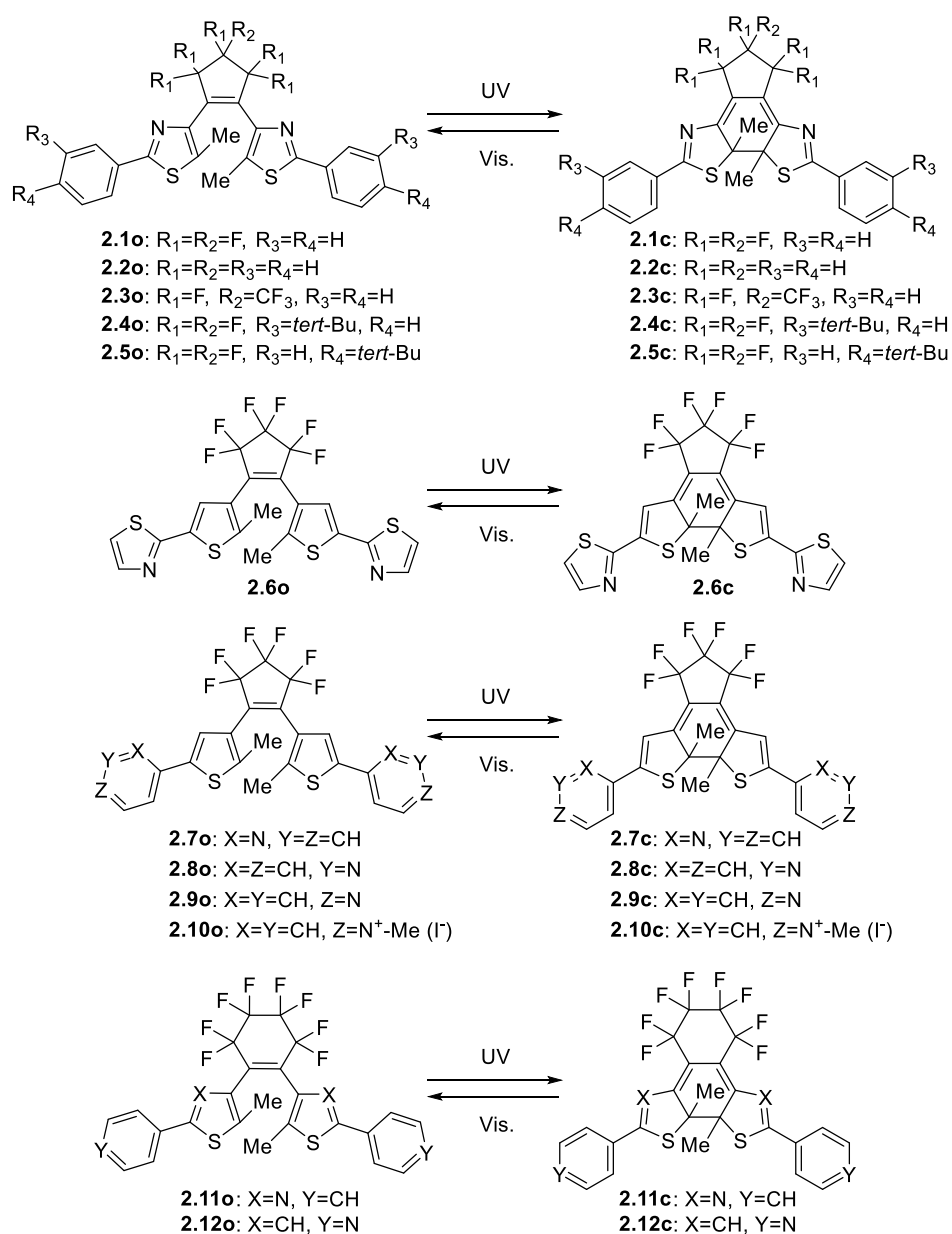
Scheme 2.4 Synthetic route of **2.12o**.

1,2-Bis(5-chloro-2-methylthien-3-yl)perfluorocyclohexene

To a 100 mL three neck flask containing 2.00 g (9.46 mmol) of 3-bromo-5-chloro-2-methylthiophene[42] in 30 mL of dry diethyl ether on the dry ice- methanol bath at -78°C in an argon gas atmosphere. To the solution, 6.5 mL (10.41 mmol, 1.1 eq.) of 1.6 N *n*-BuLi hexane solution was gradually added in keeping the temperature and stirred for 1 h at the temperature. To the mixture, the 1.24 g (4.73 mmol, 0.50 eq.) of perfluorocyclohexene in 10 mL of dry diethyl ether was gradually added, followed by stirring another 3 h at the temperature. After reaction was over, 30 mL of water was added, and the mixture was allowed to warm to room temperature. The mixture was extracted with 30 mL of diethyl ether with five times. The organic layer was washed with 100 mL of brine and dried over sodium sulfate anhydrous. After removal of sodium sulfate by filtration, the solvents were removed in vacuo. The resulting crude product was purified by column chromatography on silica gel using hexane as eluent, to obtain 1.58 g of yellow oily crude product. Since further purification was difficult, it was used as is for the next reaction.

^{1}H NMR (400 MHz, CDCl$_{3,}$ppm) δ 6.71 (s, 2H), 2.08 (s, 6H). ^{13}C NMR (100 MHz, CDCl$_3$, ppm) δ 139.3, 127.7, 126.2, 125.4, 13.9.

1,2-Bis(2-methyl-5-(pyrid-4-yl)thien-3-yl)perfluorocyclohexene (2.12o)

To a 100 mL four neck flask containing 1.31 g (2.69 mmol) of 1,2-bis(5-chloro-2-methylthiophen-3-yl)perfluorocyclohexene in 50 mL of dry diethyl ether on the ice- salt bath at -10°C in an argon gas atmosphere. To the solution, 5.1 mL (8.16 mmol, 3.0 eq.) of 1.6 N *n*-BuLi hexane solution was gradually added in keeping the temperature and stirred

for 1 h at the temperature. Then the 2.9 mL (10.84 mmol, 4.0 eq.) of tributyl borate was added, followed by stirring another 10 min, then the temperature of the reaction mixture was allowed warm to room temperature. Then the mixture was stirred for 1 h at the temperature. After reaction was over, 10 mL of water was added, and the solvents were evaporated in vacuo. The reaction mixture was added the 4-bromopyridine hydrochloride (1.15 g, 5.92 mmol, 2.2 eq.), tetrakis(triphenylphosphine)palladium(0) (0.22 g, 0.19 mmol, 0.070 eq.), a 20 wt% Na_2CO_3 aq. (20 mL), and THF (20 mL), and the mixture was refluxed for 16 h. After reaction was over, the reaction mixture was allowed to cool to room temperature, and the solvent of THF was evaporated in vacuo. The mixture was extracted with 30 mL of diethyl ether with five times. The organic layer was washed with 100 mL of brine and dried over sodium sulfate anhydrous. After removal of sodium sulfate by filtration, the solvents were removed in vacuo. The resulting crude product was purified by column chromatography on silica gel using a mixture of hexane and ethyl acetate (3: 7 (v/v)) as eluent, to obtain 0.88 g (1.52 mmol) of **2.12o** as pale-yellow oil in 57% yield.

^{1}H NMR (400 MHz, CDCl$_3$, ppm) δ 8.58 (dd, J = 4.6, 1.6 Hz, 4H), 7.48 (dd, J = 4.6, 1.6 Hz, 4H), 7.31 (s, 2H), 2.21 (s, 6H). ^{13}C NMR (100 MHz, CDCl$_3$, ppm) δ 150.6, 142.4, 140.4, 138.6, 127.2, 125.3, 119.6, 14.7. ^{19}F NMR (376 MHz, CDCl$_3$, ppm) δ -109.3 (conformer A: s) and -113.8 (conformer B: s) (conformer A: conformer B = 2: 3 (ratio of the peak areas), 4F), -135.1 (conformer A: s) and -138.1 (conformer B: s) (conformer A: conformer B = 2: 3 (ratio of the peak areas), 4F). Anal. Calcd for $C_{26}H_{16}F_8N_2S_2$: C, 54.54; H, 2.82; N, 4.89; Found: C, 54.37; H, 2.82; N, 4.84.

· **1-(3-Methyl-5-phenylthiophen-2-yl)-2-(4-methyl-2-phenylthiazol-5-yl)perfluorocyclopentene (2.16o)**

The synthetic route of **2.16o** is shown in Scheme 2.5.
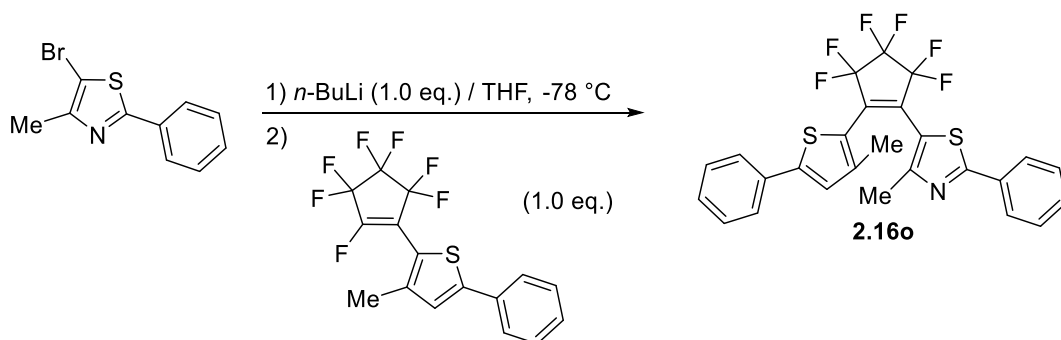
Scheme 2.5 Synthetic route of **2.16o**.

To a 100 mL four neck flask containing 1.75 g (6.89 mmol) of 5-bromo-4-methyl-2phenylthiazole[13] in 25 mL of THF anhydrous on the dry ice- methanol bath at -78°C in an argon gas atmosphere. To the solution, 4.3 mL (6.88 mmol, 1.0 eq.) of 1.6 N n-BuLi hexane solution was gradually added in keeping the temperature and stirred for 1 h at the temperature. To the mixture, THF anhydrous solution containing 2.52 g (6.88 mmol, 1.0 eq.) of 2-(2,3,3,4,4,5,5-heptafluorocyclopenten-1-yl)-3-methyl-5-phenylthiophene[43] was added, followed by stirring another 2 h. After reaction was over, 10 mL of water was added, and the mixture was allowed to warm to room temperature. Solvent of THF was evaporated in vacuo, then 100 mL of water was added. The mixture was extracted with 50 mL of diethyl ether with four times. The organic layer was washed with 150 mL of brine and dried over sodium sulfate anhydrous. After removal of sodium sulfate by filtration, the solvents were removed in vacuo. The resulting crude product was purified by column chromatography on silica gel using a mixture of hexane and dichloromethane (8:2 to 7:3 (v/v)) as eluent, to obtain 2.72 g (5.22 mmol) of **2.16o** was obtained as pure yellow powder in 76% yield.

m.p. 93.0-93.8°C. ^{1}H NMR (400 MHz, CDCl$_3$, ppm) δ = 7.95-7.93 (m, 2H), 7.58 (d, J = 7.9 Hz, 2H), 7.46-7.43 (m, 2H), 7.39 (tt, 7.9, 7.2 Hz, 2H), 7.33 (t, J = 7.2 Hz, 1H), 7.10 (s, 1H), 2.10 (s, 3H), 1.86 (s, 3H). ^{13}C NMR (100 MHz, CDCl$_3$, ppm) δ 170.4, 156.4, 148.7, 142.6, 133.1, 132.8, 131.1, 129.2, 129.2, 128.1, 126.8, 126.8, 126.0, 122.0, 117.8, 17.0, 16.0. ^{19}F NMR (376 MHz, CDCl$_3$, ppm) δ = -134.3 (s, 2F), -112.4 (s, 2F), -112.3 (s, 2F). HRMS (MALDI, positive): m/z calcd. for C$_{26}$H$_{17}$F$_6$NS$_2^+$ [M]$^+$: 521.07011, found: 521.07007.

2.3 Results and Discussions

2.3.1 Photoinduced cytotoxicity of photochromic symmetric diarylethene derivatives: The relation of the structure and the cytotoxicity

The derivatives **2.1-2.12** (Scheme 2.6) used in this study were synthesized by applying the general procedure. The synthesis of these compounds excluding the known compounds is supported by NMR, HRMS, elemental analysis, and X-ray crystallographic analysis (see Experimental for details, Figures 2.1-2.3, and Tables 2.1-2.3).

2.1o: R$_1$=R$_2$=F, R$_3$=R$_4$=H
2.2o: R$_1$=R$_2$=R$_3$=R$_4$=H
2.3o: R$_1$=F, R$_2$=CF$_3$, R$_3$=R$_4$=H
2.4o: R$_1$=R$_2$=F, R$_3$=*tert*-Bu, R$_4$=H
2.5o: R$_1$=R$_2$=F, R$_3$=H, R$_4$=*tert*-Bu

2.1c: R$_1$=R$_2$=F, R$_3$=R$_4$=H
2.2c: R$_1$=R$_2$=R$_3$=R$_4$=H
2.3c: R$_1$=F, R$_2$=CF$_3$, R$_3$=R$_4$=H
2.4c: R$_1$=R$_2$=F, R$_3$=*tert*-Bu, R$_4$=H
2.5c: R$_1$=R$_2$=F, R$_3$=H, R$_4$=*tert*-Bu

2.6o

2.6c

2.7o: X=N, Y=Z=CH
2.8o: X=Z=CH, Y=N
2.9o: X=Y=CH, Z=N
2.10o: X=Y=CH, Z=N$^+$-Me (I$^-$)

2.7c: X=N, Y=Z=CH
2.8c: X=Z=CH, Y=N
2.9c: X=Y=CH, Z=N
2.10c: X=Y=CH, Z=N$^+$-Me (I$^-$)

2.11o: X=N, Y=CH
2.12o: X=CH, Y=N

2.11c: X=N, Y=CH
2.12c: X=CH, Y=N

Scheme 2.6 Molecular structures of the DAEs.

We investigated the photochemical properties of twelve DAEs of thiazoyl or pyridyl derivatives at first. The absorption maxima of open- and closed-ring isomers, the photostationary state (PSS) and the quantum yields of photochromic reactions (cyclization ($\Phi_{o \to c}$) and cycloreversion ($\Phi_{c \to o}$)) are summarized in Table 2.6. The corresponding spectra are shown in Figures 2.4 and 2.5. Before UV light irradiation, strong absorption bands are observed below $\lambda = 400$ nm, which are due to the π-π* transitions of the open-ring isomer. When irradiated with UV light, these open-ring isomers undergo a photocyclization reaction to produce closed-ring isomers, and new absorptions due to π-π* transitions of the closed-ring isomers are observed. For DAEs with an aryl moiety of the thiophene rings, the absorption bands in the visible region derived from the closed ring isomers are often observed at longer wavelengths than those of DAEs with an aryl moiety of the thiazole rings.[6] In fact, the absorption bands in the visible region of **2.6c**-**2.10c** and **2.12c** are observed at longer wavelengths than those of **2.1c**-**2.5c** and **2.11c**.

The thiazoyl and pyridyl derivative groups (referred to below as "thiazole group" and "pyridine group") show photo-cyclization quantum yields in the range of about 0.2-0.5 and 0.5-0.7, respectively. Whereas, these photocycloreversion quantum yields due to visible light irradiation are generally more than one order of magnitude smaller than the photocyclization quantum yields. Therefore, both of these isomers absorb UV light, but exhibit a PSS with a closed-ring isomer formation fraction of more than 80% upon UV light irradiation. In the thiazole group, the open- and closed-ring isomers of **2.1**, **2.3**-**2.5**, and **2.11**, which have very similar molecular skeletons, have nearly same absorption bands and maximum wavelengths. Similarly, the open- and closed-ring isomers of **2.7**-**2.9** and **2.12** of the pyridine group, which have very similar basic skeletons, show similar absorption bands.
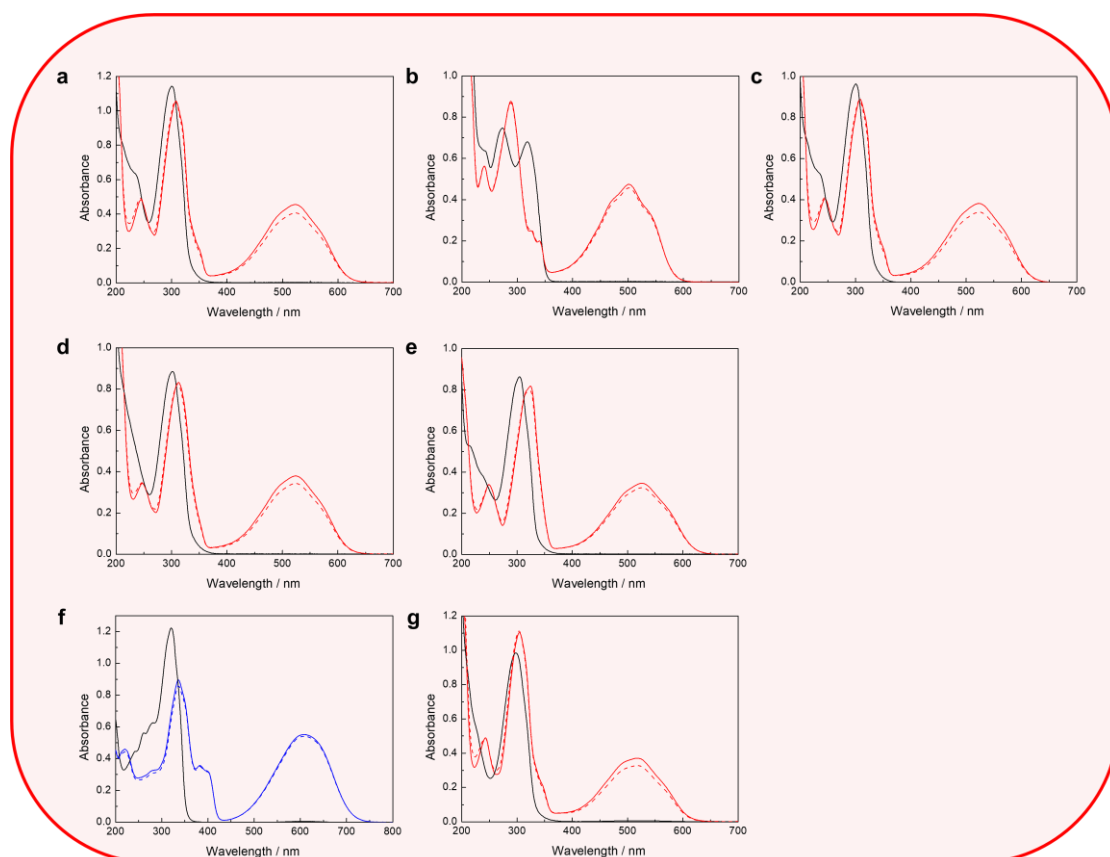
Figure 2.4 Absorption spectral changes of derivatives having thiazole group (**2.1** (a), **2.2** (b), **2.3** (c), **2.4** (d), **2.5** (e), **2.6** (f), and **2.7** (g)) in hexane. Absorption spectra of open-ring isomers: black solid line, closed-ring isomers: red or blue solid line, photostationary state (PSS) upon UV light (λ = 313 nm) irradiation: red or blue broken line. See Table 2.6 for detailed values of PSS.
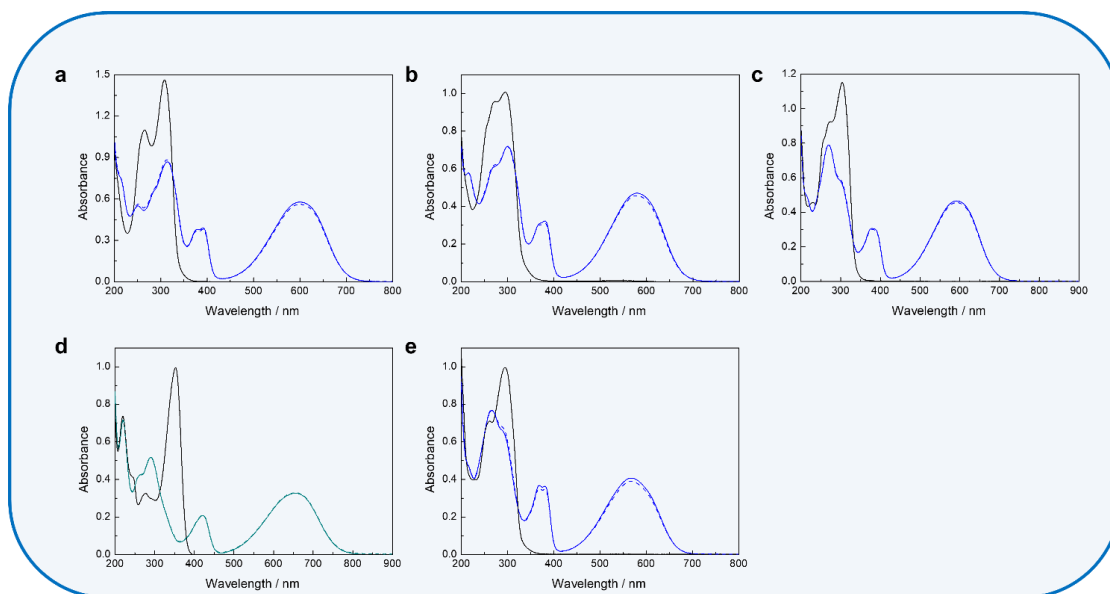
Figure 2.5 Absorption spectral changes of derivatives having pyridine group (**2.7** (a), **2.8** (b), **2.9** (c), **2.10** (d), and **2.12** (e)) in methanol. Absorption spectra of open-ring isomers: black solid line, closed-ring isomers: blue or emerald green solid line, photostationary state (PSS) upon UV light (λ = 313 or 365 nm) irradiation: blue or emerald green broken line. See Table 2.6 for detailed values of PSS.

Table. 2.6 Photochemical properties of DAEs having thiazole or pyridine rings in organic solvents.

	Solvent	λ_{max} [nm] (ε [10^4 M^{-1} cm^{-1}])		PSS [%] (λ_{irr} [nm])	$\Phi_{o \to c}$ (λ_{irr} [nm])	$\Phi_{c \to o}$ (λ_{irr} [nm])
		Open-ring	Closed-ring			
2.1		300 (3.4)[13]	525 (1.0)[13]	89 (313)	0.32 (313)[13]	0.02 (492)[13]
2.2		318 (2.3)	502 (1.6)	96 (313)	0.32 (313)	0.0062 (492)
2.3	hexane	301 (3.7)	524 (1.5)	89 (313)	0.23 (313)	0.012 (492)
2.4		302 (3.7)	525 (1.6)	91 (313)	0.19 (313)	0.011 (492)
2.5		304 (4.3)	525 (1.7)	94 (313)	0.24 (313)	0.011 (492)
2.6		320 (3.7)	610 (1.7)	98 (313)	0.47 (313)	0.0031 (546)
2.7		307 (3.7)	601 (1.5)	97 (313)	0.53 (280)	0.0080 (580)
2.8	methanol	296 (2.9)	582 (1.4)	97 (313)	0.60 (280)	0.010 (580)
2.9		305 (3.6)	592 (1.5)	98 (313)	0.57 (280)[18]	0.0086 (580)
2.10[18]		353 (5.05)	655 (1.62)	100 (365)	0.71 (280)	/
2.11[19]	hexane	298 (3.1)	518 (1.1)	88 (313)	0.29 (313)	0.015 (492)
2.12	methanol	302 (2.9)	578 (1.1)	97 (313)	0.56 (280)	0.0089 (580)

As reported in derivative **2.1**, the photoinduced cytotoxicity of DAE is likely to be caused by closed-ring isomer. Then, we investigated the photoresponsivity, reversibility, and thermal stability of these derivatives in polar solvents including water in consideration of their use in cells (Figure 2.6 and Table 2.7).

The absorption maxima of the open- and closed-ring isomers of the twelve derivatives in polar solvents containing water were observed at almost the same wavelength as in water-free solvents (Figure 2.6 (left)). The values of these derivatives for PSS by UV light irradiation under these conditions were almost the same as those in water-free solvent. When the derivatives in the PSS state were irradiated with visible light ($\lambda > 480$ nm) containing absorption in the visible region of the closed-ring form, complete decolorization was observed, indicating more than 90% isomerization to the open-ring isomer. These compounds can be switched back and forth by alternating UV and visible light irradiation over several cycles, reaching essentially the same absorption maxima and minima after each cycle (Figure 2.6 (top right)). This behavior indicating that there are no significant irreversible side reactions. Note, however, that for derivative **2.10**, it shows irreversibility and fatigue, albeit slightly.

DAEs are known to undergo not only photochemical reactions, but also thermal reactions. In particular, the closed-ring form may revert to the open-ring isomer via a thermal pathway. This may be beneficial for other applications, but undesirable for our application. Therefore, we investigated the thermal stability of the twelve derivatives by monitoring the absorbance of the ring-closed isomers at their maximum values at 37°C, a common temperature of cell culture (Figure 2.6 (bottom right)). The closed-ring isomers except **2.10** showed almost same absorbance after keeping at 37°C for 24 h. A decrease in absorbance was observed for **2.10**, but it still retained about 80% of the closed-ring isomers.
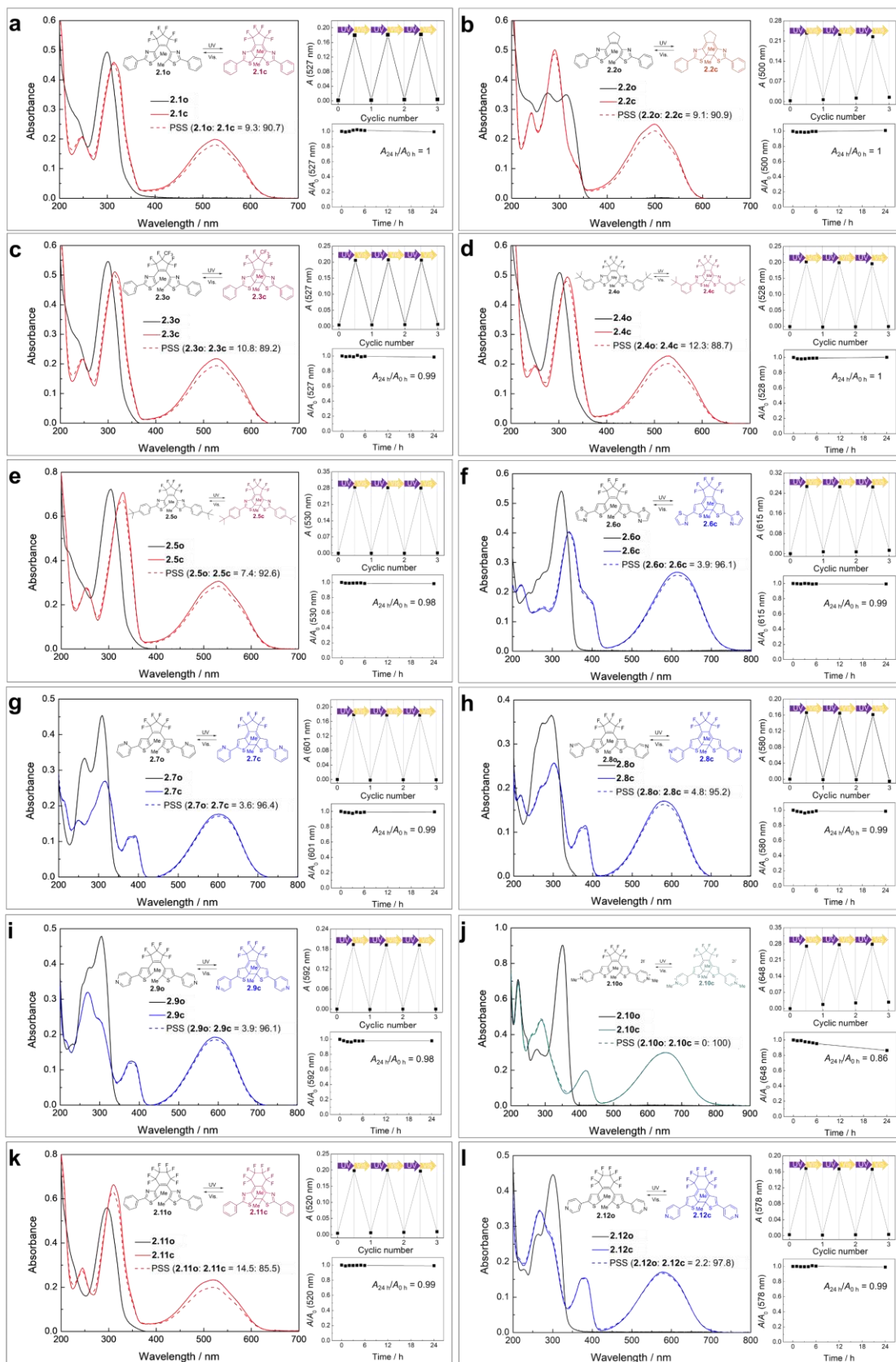
Figure 2.6 Absorption spectra, reversibility, and thermal stability of DAEs having thiazole (a-f and k) or pyridine rings (g-j and l) in water/ethanol = 3:7 (v/v). The absorption spectra of the open- (black solid line) and closed-ring isomers (colored solid lines other than black) and the PSS^{UV} (broken line) are shown. In each panel the reversibility (top right) and the thermal stability (low right) are shown. For obtaining the PSS^{UV} absorption spectra, the samples were irradiated with their optimal wavelength (see footnotes of Table 2.6). For the reversibility, the samples were alternately irradiated with UV (a-i, k, and l: $\lambda = 313$ nm, j: $\lambda = 365$ nm) and visible light ($\lambda > 480$ nm). For the thermal stability, the samples of each closed-ring isomer were kept at 37 °C (Figure 2.7).
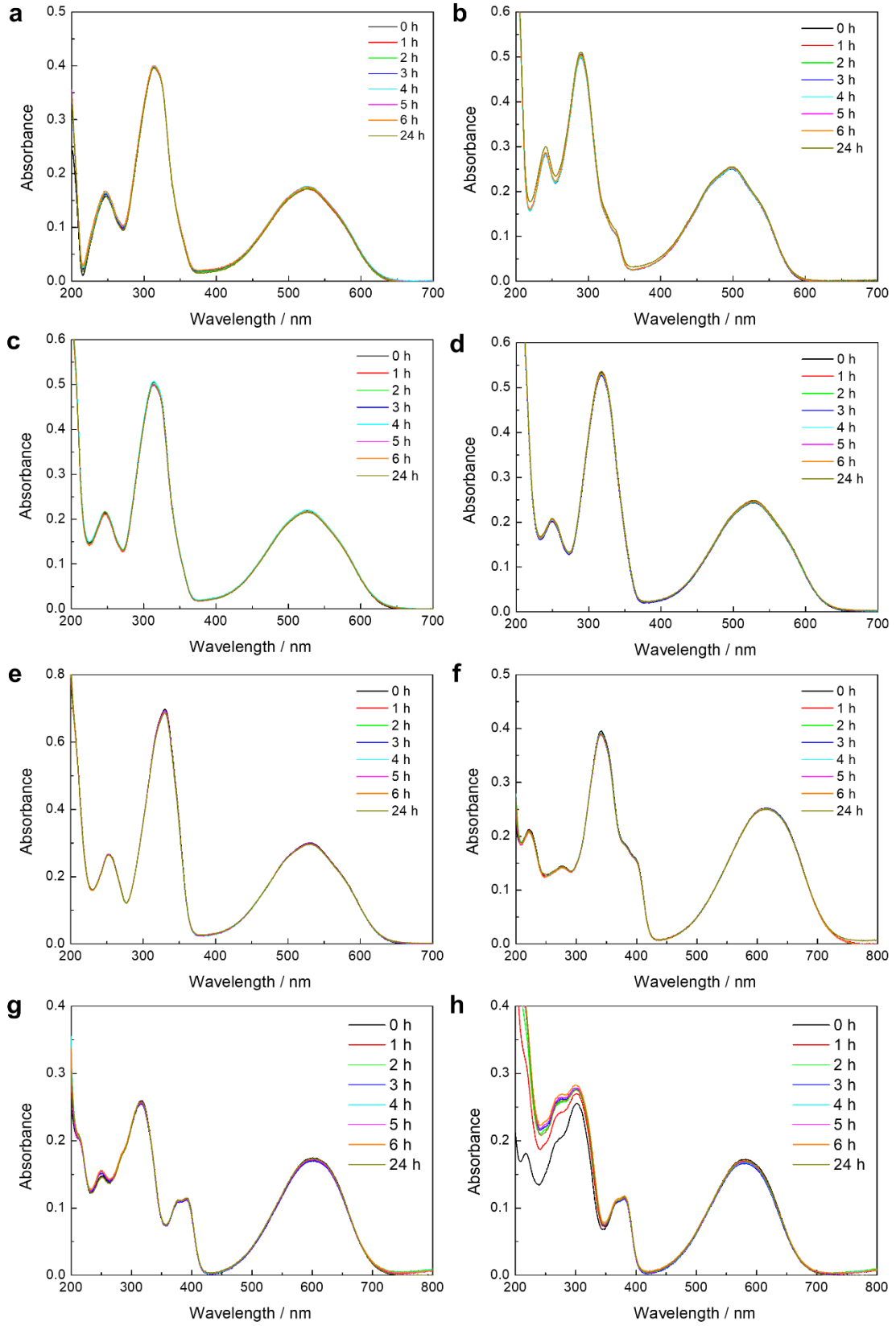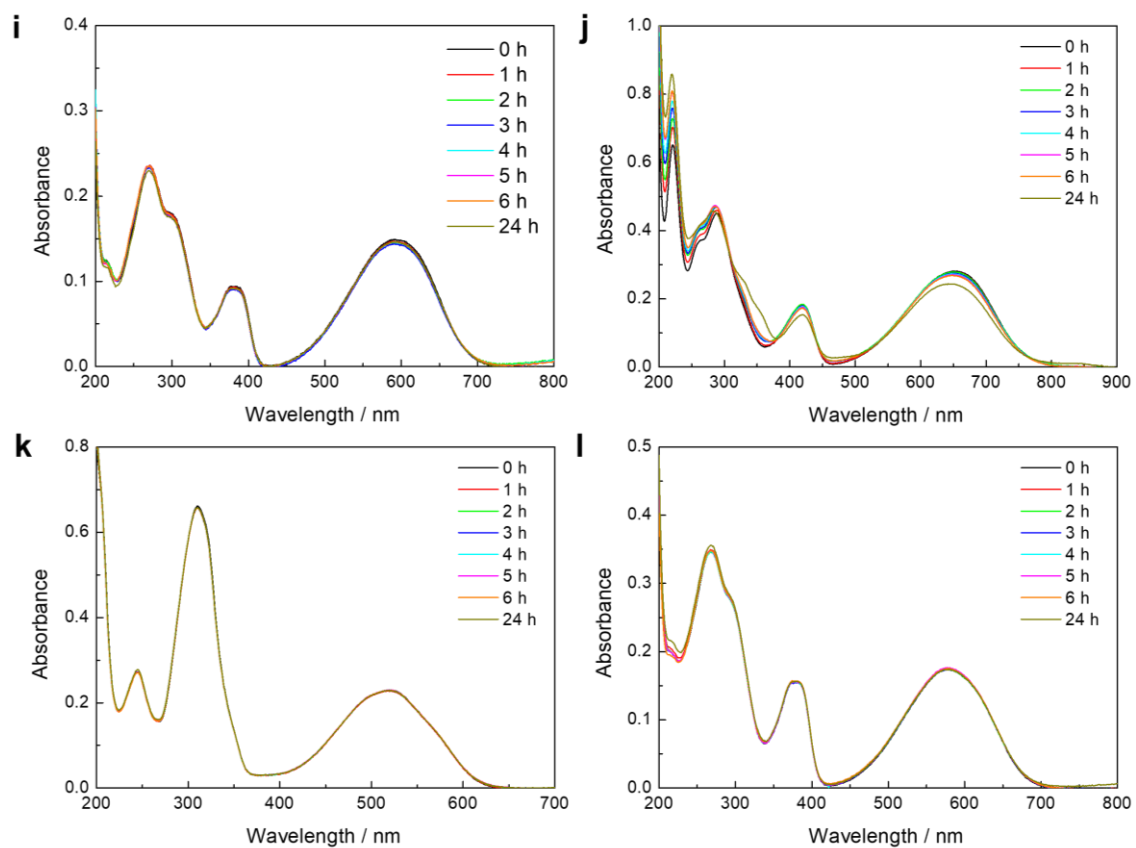
Figure 2.7 Time-dependent Absorption spectral changes of **2.1**-**2.12** in water/ethanol = 3: 7 (v/v) at 37°C. **2.1c** (a), **2.2c** (b), **2.3c** (c), **2.4c** (d), **2.5c** (e), **2.6c** (f), **2.7c** (g), **2.8c** (h), **2.9c** (i), **2.10c** (j), **2.11c** (k), and **2.12c** (l).

Table 2.7 Maximum absorption wavelength, photostationary state, reversibility, and thermal stability of DAEs having thiazole or pyridine rings in water/ethanol = 3:7 (v/v).

	λ_{max} [nm]		PSS [%]	Reversibility	Thermal stability [%][e]
	Open-ring	Closed-ring	(λ_{irr} [nm])	[%][a]	
2.1	300	527	91 (313)	100[b]	100
2.2	314	500	91 (313)	95[b]	100
2.3	299	527	89 (313)	100[b]	99
2.4	302	528	89 (313)	97[b]	100
2.5	305	530	93 (313)	99[b]	98
2.6	323	615	96 (313)	99[b]	99
2.7	309	601	96 (313)	99[b]	99
2.8	295	580	95 (313)	97[b]	99
2.9	305	592	96 (313)	99[b]	98
2.10	350	648	100 (365)	/[c, d]	86
2.11	296	520	86 (313)	99[b]	99
2.12	300	578	98 (313)	99[b]	99

[a] Reversibility: A/A_0 at the absorption maximum in the visible range after 2 cycles.
[b] Reversibilities were measured by alternating UV light (λ = 313 nm) and visible light (λ > 480 nm).
[c] Reversibilities were measured by alternating UV light (λ = 365 nm) and visible light (λ > 480 nm).
[d] Not measured due to the partial decomposition.
[e] Thermal stability: A/A_0 at the absorption maximum in the visible range after 24 h at 37 °C.

We investigated the photoinduced cytotoxicity of these derivatives. Comparative evaluation of cytotoxicity was performed with the lower limit concentration (ppm) of DAEs when cell swelling characteristic of cell death was remarkably observed upon irradiated with 436 nm light. The photocytotoxicity was observed only for the closed-ring isomers, and cell death was selectively observed only in the portion irradiated with 436 nm light (ex. photoinduced cytotoxicity of **2.1c**: Figure 2.8). In contrast, no toxicity was observed for open-ring isomers. The closed-ring isomers which showed the toxicity with lower limit concentrations less than 2 ppm were **2.1c**, **2.3c**, **2.6c-2.9c**, **2.11c**, and **2.12c**. Comparing the LLCs of these eight closed-ring isomers, the thiazole group showed higher photocytotoxicity than the pyridine group (Figure 2.9).

In the case of the thiazole group, **2.1c** and **2.6c**, which differ in the position of the thiazole ring, and the branched structure of **2.3c**, which has a trifluoromethyl group at 4-position of perfluorocyclopentene ring moiety, had almost the same level of photocytotoxicity. Photoinduced cytotoxicity was not observed at concentrations up to 2

ppm for **2.2c**, in which the perfluorocyclopentene ring of the basic structure **2.1** was changed to a cyclopentene ring. In addition, photoinduced cytotoxicity was not observed for **2.4c** and **2.5c**, in which bulky tertiary butyl groups were introduced at both ends of the molecule **1c**. In the case of the pyridine group, **2.7c-2.9c**, which have different bond positions in the pyridine rings, photoinduced cytotoxicity was higher in the order **2.7c** < **2.8c** < **2.9c**. Whereas, no photoinduced cytotoxicity was observed for **10c**, which has an ionic structure. Comparing the molecular structures of **2.1c** and **2.11c**, they differed only at the ethene moiety. A derivative **2.1c** having perfluorocyclopentene ring showed four times higher toxicity compared **2.11c** having perfluorocyclohexene ring. The similar tendency was observed for **2.9c** and **2.12c**. The **2.9c** showed five times higher toxicity compared to **2.12c**.

Photoinduced cytotoxicity was observed only when the closed-ring isomers were dosed in cell cultures as in derivative **2.1**.[10] Thus, we examined the intercalation of DAEs into DNA with respect to the influence of their isomerization states.
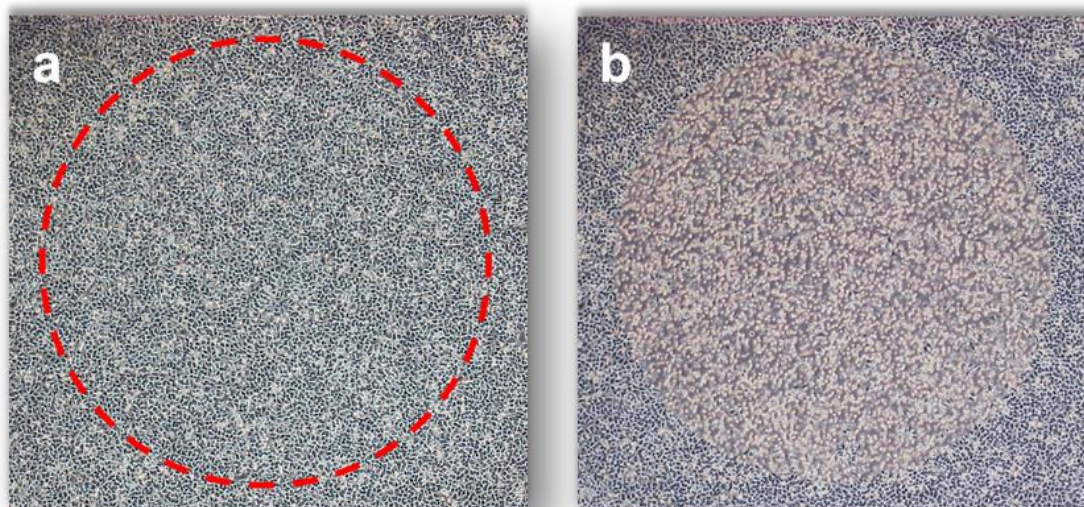
Figure 2.8 Photoinduced cytotoxicity of **2.1c**. HeLa cells were disseminated and cultured in media containing **2.1c** (0.2 ppm) for 1 day until they grew confluent. Then, blue light of 436 nm wavelength was irradiated for 4 min along the circular pattern (red broken line). Two hours later, the cells in the irradiated area were observed. Before blue light irradiation: (a) and after blue light irradiation: (b). Only the cells in the irradiated part selectively died.

Compound		2.1	2.2	2.3	2.4	2.5	2.6	2.7	2.8	2.9	2.10	2.11	2.12
LLC / ppm	Open-ring						> 2						
	Closed-ring	0.05	>2	0.05	>2	>2	0.05	1.0	0.5	0.2	>2	0.2	1.0
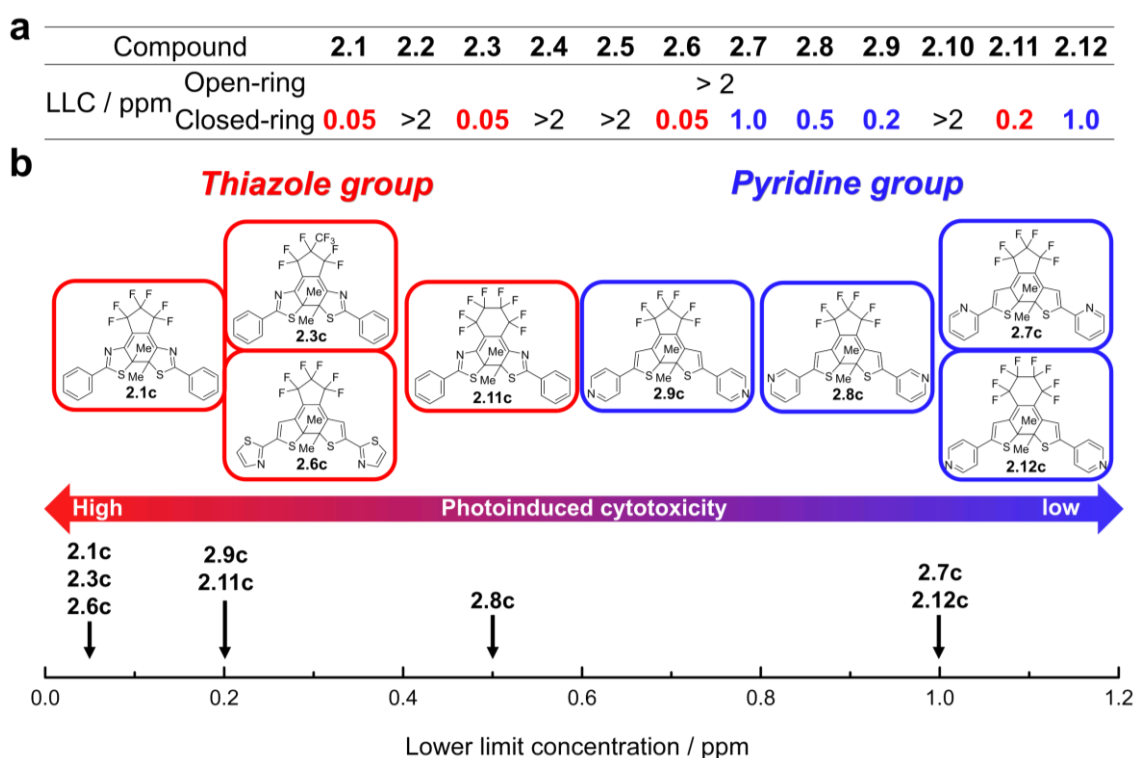
Figure 2.9 Photoinduced cytotoxicity of DAEs depending on the molecular structures. (a) Lower limit concentration (LLC) of open- and closed-ring isomers of **2.1-2.12** for photoinduced cytotoxicity. The lower limit concentration here is defined as the lowest concentration of the investigated compound that exhibited >90% cytotoxicity (cell death/cell shrinkage and rounding) in the irradiated area upon irradiation with blue light (λ = 436 nm, 4 min). Experiments to evaluate the lower limit concentration were performed up to 2 ppm. (b) Relationship between the molecular structure of DAE and the LLC of photoinduced cytotoxicity. In the DAEs that showed photoinduced cytotoxicity, DAEs having thiazole ring showed higher photoinduced cytotoxicity than those having pyridine rings.

The difference in DNA intercalation ability between the open- and closed-ring isomers of DAE is likely due to their structural differences. As an example, the X-ray structures of open- and closed-ring isomers of **2.1** are shown in Figure 2.10a. The molecule **2.1o** is free to rotate along the two single bonds from ethene moiety to the aryl groups in solution. Therefore, this is a bulky structure and less likely to be inserted into DNA base pairs. In contrast, the **2.1c** has a six-membered cyclohexadiene ring at the center of the molecule and are very planar in structure. In order to investigate this in more detail, the structural optimization of the open- and closed-ring isomers of the derivatives was carried out using DFT calculations (Figures 2.11, 2.12, and Table 2.8). The calculated results showed that

51

the dihedral angle (φ) of the aryl group attached to the ethene moiety is 44 ° < φ < 59 ° for the open-ring isomers, whereas it is 10 ° > φ for the closed-ring isomers and thus very small. Therefore, the structures of the closed-ring isomers are planer than those of open-ring isomers. Therefore, the intercalation ability of the closed-ring isomers is expected to be better than that of the open-ring isomers.

Then, we observed the potential interactions between DNA and the open- and closed-ring isomers of DAEs by a fluorescence reduction experiment based on the competitive binding of ethidium bromide (EB) and each DAE to the DNA. We prepared a solution containing sodium salts of DNA from Salmon testes.[23] Displacement of EB from the fluorescent EB‑DNA adduct by a DNA-interacting molecule will induce fluorescence quenching.[12,39] Fluorescence spectra were monitored at constant concentrations of DNA and EB (3.9 nM bp^{-1} and 75 μM, respectively), while adding increasing amounts of DAEs (in the range of 0-25 μM) (see Experimental for details). From the data obtained, it is observed that the closed-ring isomers show a large decrease in emission intensity compared to the open-ring isomers. ese results show that DAEs interact with DNA, and that their open-/closed- ring isomers behave very differently. The affinity of the open- and closed-ring isomers for DNA was evaluated and compared using the Stern-Volmer quenching constant, K_{SV}.

$$I_0/I = 1 + K_{SV}\,[\text{DAE}] \qquad (2.1)$$

Herein, I_0 and I are the emission intensities of initial complex (DNA-EB) and after addition of DAEs, respectively. A plot of I_0/I vs. concentration of DAE [DAE] will give a straight line whose slope is equal to K_{SV}. The larger values of K_{SV} indicate the larger decrease of fluorescent intensity by addition of the derivatives, suggesting the high intercalation ability.

Among the twelve derivatives studied, the K_{SV} values of the closed-ring isomers except for **2.10c** were in the range of 18-34 × 10^{-3} M^{-1}, indicating that the K_{SV} values were one order of magnitude higher than the open-ring isomers (K_{SV} < 6 × 10^{-3} M^{-1}), and indicating a higher affinity for DNA (Figure 2.10b-d). The difference in DNA intercalation ability between the open- and closed-ring isomers of DAE is attributed to the difference in structures.
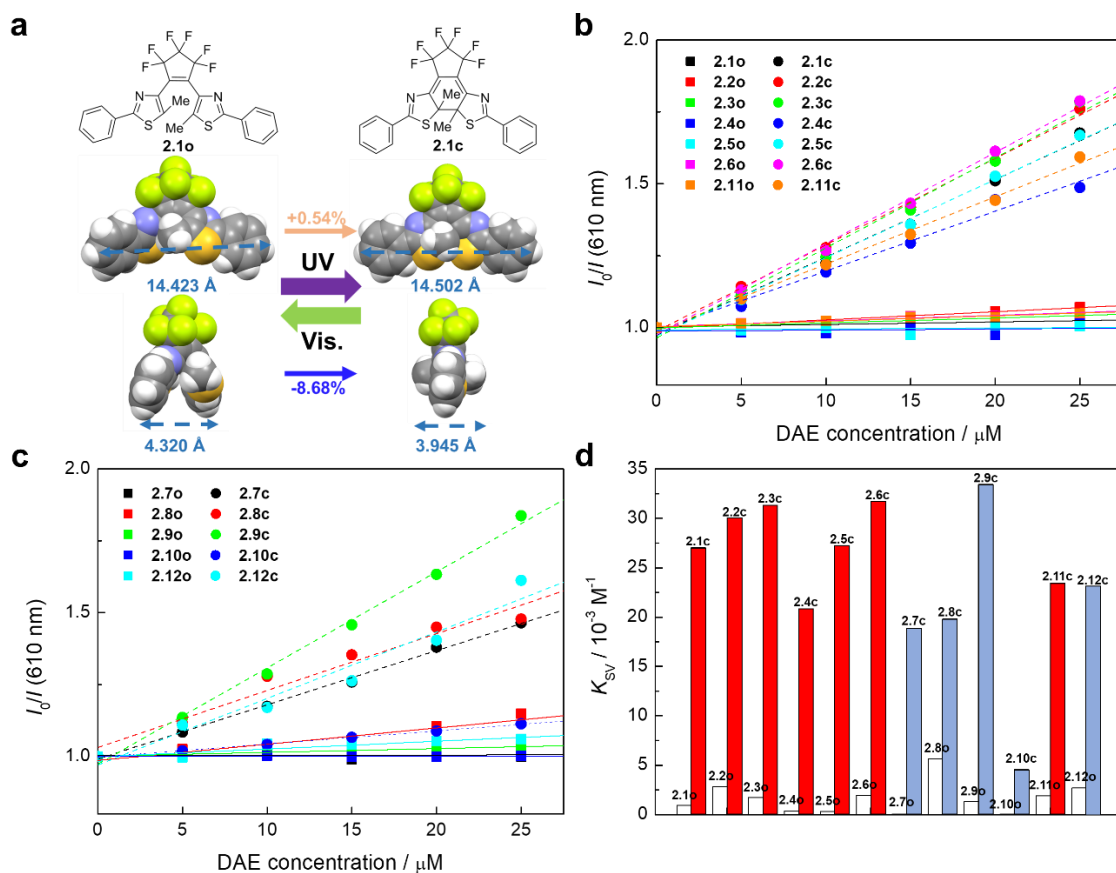
Figure 2.10 Molecular Planarity and DNA Intercalation. (a) Representation of the X-ray structures of the open- and closed-ring isomers of **2.1** illustrating their structural variations. (b, c) Plots of I_0/I vs. [DAE] for the titration of DNA-EB with open- (square) and closed-ring (circle) isomers of twelve DAEs (thiazole group: (b) and pyridine group: (c)) at λ_{ex} = 486 nm and λ_{em} = 610 nm: experimental data points and linear fitting of the data. Concentration of [DAE]: 0-25 μM; [DNA]: 3.9 nM bp^{-1}; [EB]: 75 μM. (d) The K_{SV} values for the twelve DAEs determined from the slope of the linear fitting of the data.
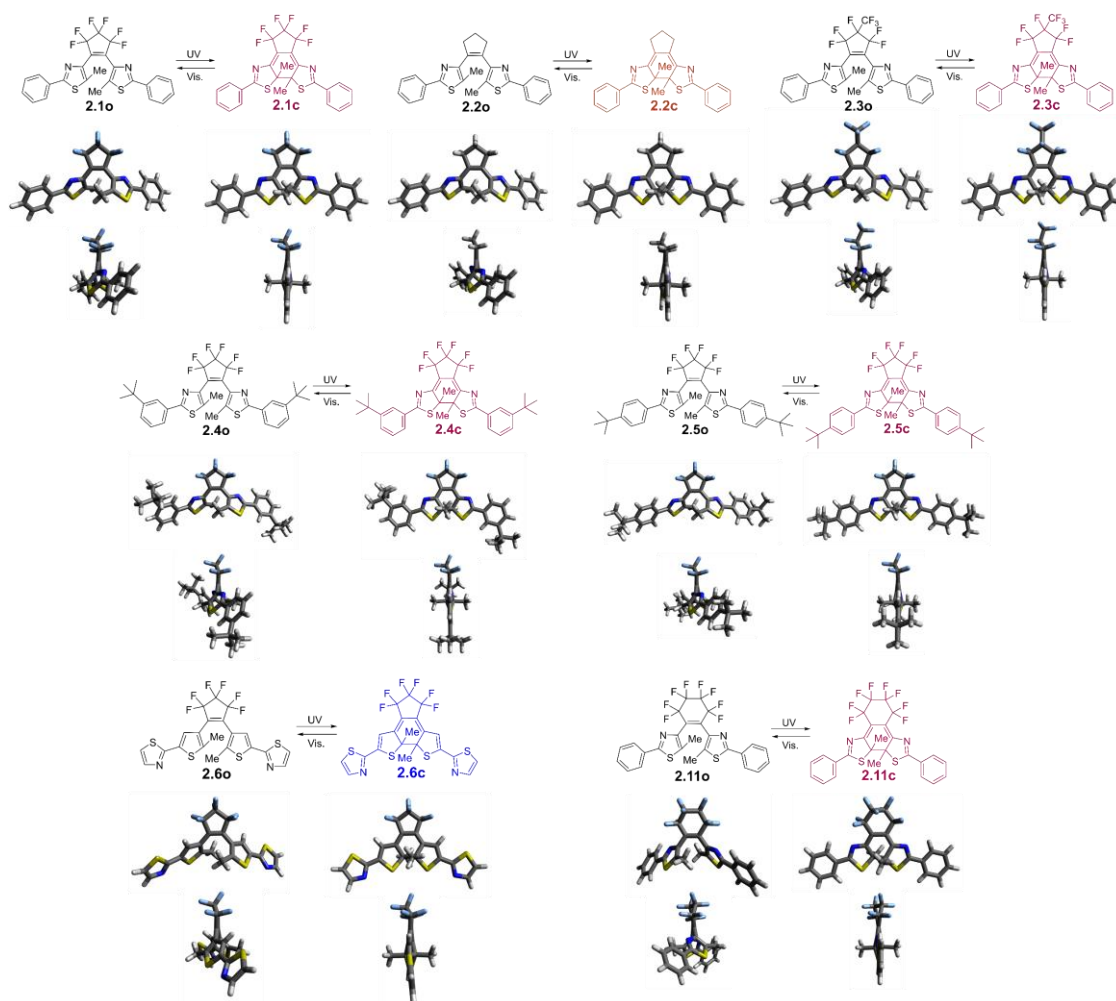
Figure 2.11 Structures of open- and closed-ring isomers of derivatives having thiazole group optimized on the B3LYP/PCM(water)//6-31G(d) level of theory.
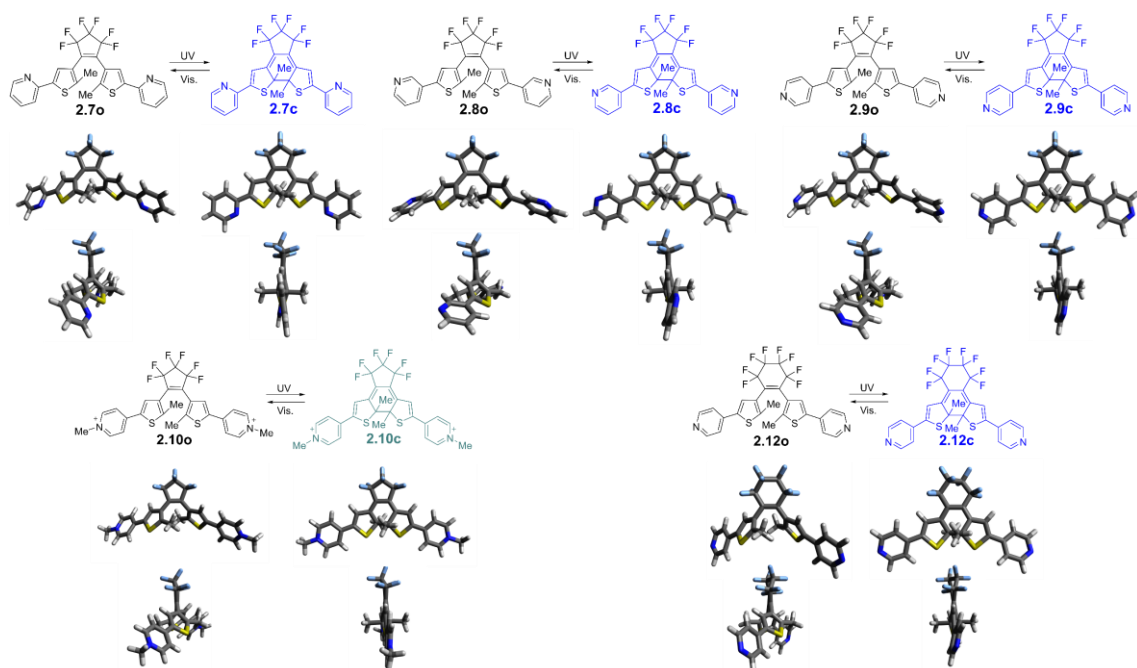
Figure 2.12 Structures of open- and closed-ring isomers of derivatives having pyridine group optimized on the B3LYP/PCM(water)//6-31G(d) level of theory.

Table 2.8 Geometric parameters of optimized structures of open- and closed-ring isomers of **2.1**-**2.12** on the B3LYP/PCM(water)/6-31G(d) level of theory.

2.1o: R$_1$=R$_2$=F, R$_3$=R$_4$=H
2.2o: R$_1$=R$_2$=R$_3$=R$_4$=H
2.3o: R$_1$=F, R$_2$=CF$_3$, R$_3$=R$_4$=H
2.4o: R$_1$=R$_2$=F, R$_3$=*tert*-Bu, R$_4$=H
2.5o: R$_1$=R$_2$=F, R$_3$=H, R$_4$=*tert*-Bu

2.1c: R$_1$=R$_2$=F, R$_3$=R$_4$=H
2.2c: R$_1$=R$_2$=R$_3$=R$_4$=H
2.3c: R$_1$=F, R$_2$=CF$_3$, R$_3$=R$_4$=H
2.4c: R$_1$=R$_2$=F, R$_3$=*tert*-Bu, R$_4$=H
2.5c: R$_1$=R$_2$=F, R$_3$=H, R$_4$=*tert*-Bu

2.6o

2.6c

2.7o: X=N, Y=Z=CH
2.8o: X=Z=CH, Y=N
2.9o: X=Y=CH, Z=N
2.10o: X=Y=CH, Z=N$^+$-Me (I$^-$)

2.7c: X=N, Y=Z=CH
2.8c: X=Z=CH, Y=N
2.9c: X=Y=CH, Z=N
2.10c: X=Y=CH, Z=N$^+$-Me (I$^-$)

2.11o: X=N, Y=CH
2.12o: X=CH, Y=N

2.11c: X=N, Y=CH
2.12c: X=CH, Y=N
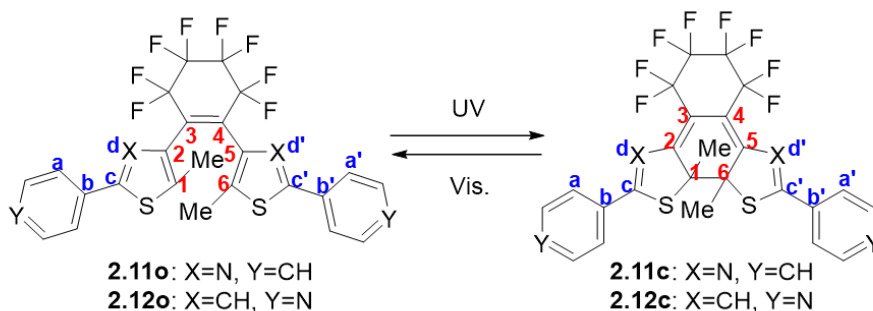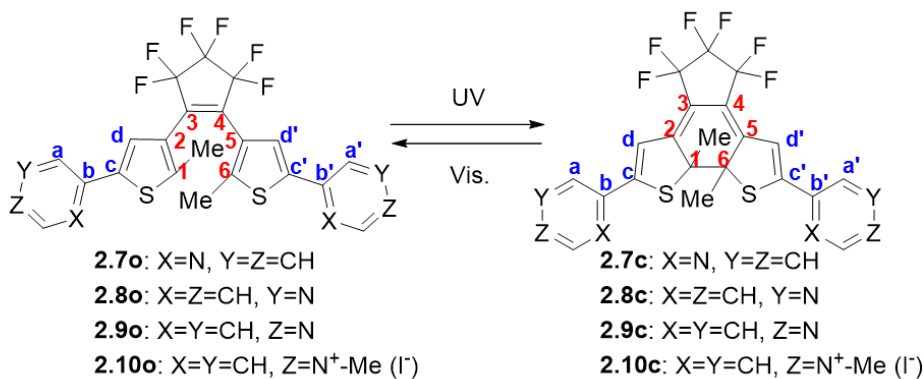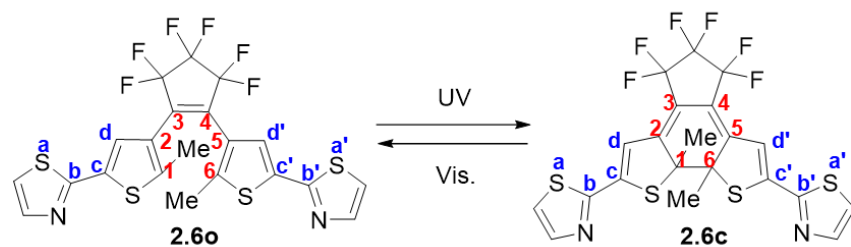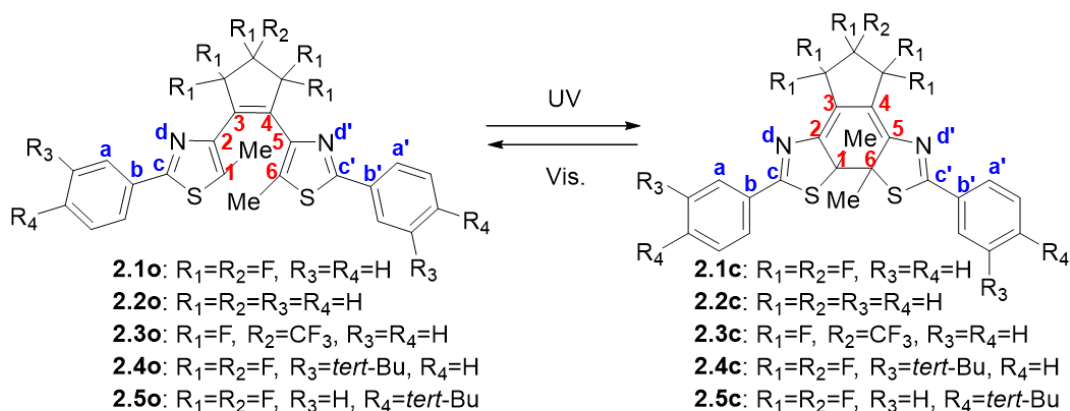
$$\varphi_1 = \sphericalangle (C_1, C_2, C_3, C_4)$$
$$\varphi_2 = \sphericalangle (C_3, C_4, C_5, C_6)$$

$$\varphi_1 = \sphericalangle (C_1, C_2, C_3, C_4)$$
$$\varphi_2 = \sphericalangle (C_3, C_4, C_5, C_6)$$

$$\theta_1 = \sphericalangle (C_a, C_b, C_c, C_d), \theta_2 = \sphericalangle (C_{a'}, C_{b'}, C_{c'}, C_{d'})$$

		ΔE [kJ/mol]	$r_{C1\text{-}C6}$ [Å]	φ_1 / φ_2 [°]	θ_1 / θ_2 [°]
2.1	Open-ring	47.667	3.675	-47.4 / -44.2	5.5 / 3.5
	Closed-ring		1.548	7.8 / 7.3	2.5 / 3.4
2.2	Open-ring	36.219	3.646	-48.3 / -47.9	2.7 / 2.4
	Closed-ring		1.542	6.3 / 6.8	6.4 / 7.3
2.3	Open-ring	48.782	3.681	-44.0 / -47.0	3.5 / 4.4
	Closed-ring		1.549	7.7 / 7.5	2.6 / 3.3
2.4	Open-ring	46.742	3.677	-47.4 / -44.3	5.5 / 2.5
	Closed-ring		1.548	7.7 / 7.3	3.1 / 3.6
2.5	Open-ring	44.796	3.674	-47.3 / -44.0	3.0 / 1.9
	Closed-ring		1.549	7.9 / 7.3	2.7 / 2.9
2.6	Open-ring	57.858	3.705	-49.3 / -46.5	-0.3 / -0.2
	Closed-ring		1.549	-8.8 / -7.6	3.2 / 3.1
2.7	Open-ring	59.234	3.700	46.0 / 48.8	0 / -0.1
	Closed-ring		1.549	-8.4 / -7.3	6.2 / 6.1
2.8	Open-ring	56.650	3.702	46.5 / 49.3	26.4 / 26.4
	Closed-ring		1.549	-8.8 / -7.7	-20.1 / -20.5
2.9	Open-ring	62.781	3.708	46.8 / 49.6	16.3 / 16.3
	Closed-ring		1.549	-8.9 / -7.6	-16.1 / -15.5
2.10	Open-ring	82.288	3.745	51.2 / 48.1	-1.6 / 2.7
	Closed-ring		1.549	-9.3 / -7.8	-6.1 / -8.0
2.11	Open-ring	34.930	3.702	57.4 / 57.4	-2.7 / -2.7
	Closed-ring		1.543	-5.4 / -5.4	-3.6 / -3.6
2.12	Open-ring	48.097	3.713	59.0 / 59.0	-17.6 / -17.6
	Closed-ring		1.542	-6.1 / -6.1	-17.4 / -17.4

[a] Energy of the closed-ring isomers compared to the open-ring isomers

The poor intercalation ability of **2.10c** is most likely due to its hydrophilic nature caused by its ionic structure. It has been reported that small molecules with high hydrophobicity have a good affinity for DNA.[44] In fact, the closed-ring isomers except for **2.10c** were almost insoluble in water and showed relatively high affinity for DNA. These results agree with that the ladder structure of DNA base pairs is stabilized by hydrophobic interaction, hence the hydrophobic DAE derivatives intercalate between DNA base pairs that can exist more stable than aqueous solvent, while the hydrophilic DAE derivative is stabled in the

aqueous media outside of DNA.

The closed-ring isomer of **2.2** showed good affinity for DNA from DNA intercalation experiments, but photoinduced cytotoxicity was not observed. The difference between the F and H atoms in the ethene moiety of derivatives **2.1** and **2.2** may cause them to behave differently in cells, which may affect their cytotoxicity. The introduction of fluorine atoms into small drug molecules has the potential to enhance a number of pharmacokinetic and physicochemical properties, such as an enhance cell membrane permeability.[45,46] P. Gamez et al. have reported that platinum complexes consisting of DAE and cisplatin behave differently in cells depending on the F and H atoms in the ethene moiety, which is related to their cytotoxicity.[12] Unlike those platinum complexes, derivatives **2.1** and **2.2** were unfortunately non-fluorescent, so their subcellular localization could not be observed, but since they showed similar toxicity correlations, their subcellular behavior may be similar.

The relationship between molecular size and photoinduced cytotoxicity was discussed. The distance between the base pair along the DNA helix axis is 3.4 Å and the helix diameter is 20 Å.[23,47] In addition, the presence of an intercalating agent between DNA base pairs can locally extend the distance between the base pairs by up to 6.8 Å.[48,49] Accordingly, the entire molecule must fall within this size in order to fit between the base pairs of DNA. Therefore, DFT calculations were used to calculate the optimized structures of the closed-ring isomers and to evaluate their molecular sizes. From the structures of the optimized closed-ring isomers, thickness (distance between methyl groups of central reactive carbons), width (molecular width of terminal aromatic ring substituents), and length (distance between terminal aromatic ring substituents) were calculated to evaluate the molecular size (Figure 2.13 and Table 2.9). In the case of **2.4c**, its width was expected to be longer than the distance between base pairs in DNA. In addition, the length of **2.5c** was expected to be longer than the diameter of the DNA helix. Therefore, it is highly likely that **2.4c** and **2.5c**, which have a terminal tert-butyl group, cannot intercalate the entire molecules between DNA base pairs. In the closed-ring isomers that showed photoinduced cytotoxicity, the thickness and width were within 6.8 Å and the length was within 20 Å, respectively. Thus, it is possible that the molecular size affects the photoinduced cytotoxicity.
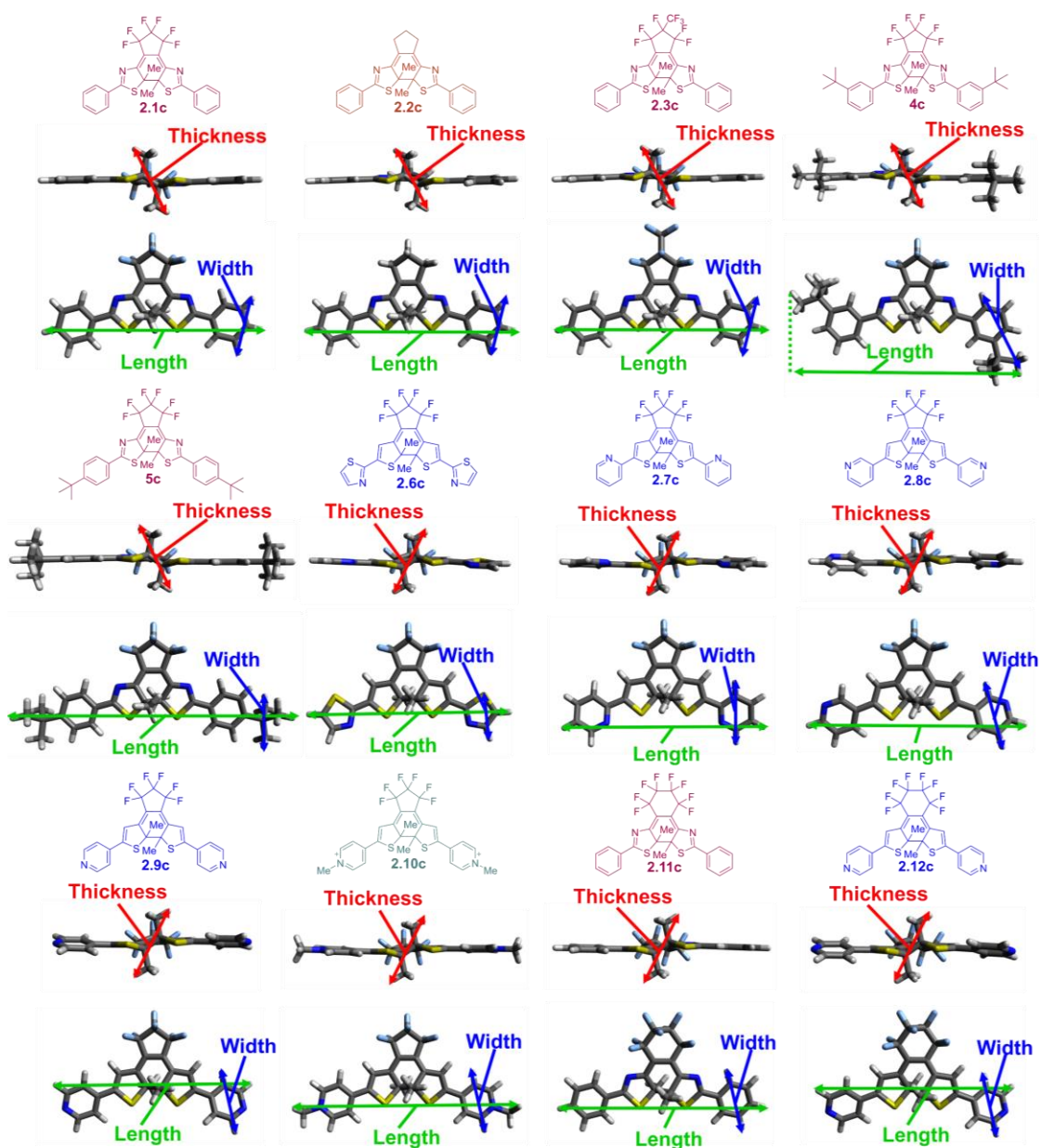
Figure 2.13 Structures of closed ring isomers of **2.1**-**2.12** optimized on the B3LYP/PCM(water)/6-31G(d) level of theory used to calculate molecular sizes. Molecular thickness (red line), width (blue line), and length (green line).

Table 2.9 Molecular size parameters of optimized structures of closed-ring isomers of **2.1-2.12** on the B3LYP/PCM(water)/6-31G(d) level of theory.

	Thickness [Å]	Width [Å]	Length [Å]
2.1c	5.646	4.306	16.739
2.2c	5.622	4.297	16.686
2.3c	5.642	4.306	16.739
2.4c	5.646	**7.291**	18.553
2.5c	5.646	4.356	**21.145**
2.6c	5.646	3.603	16.043
2.7c	5.644	4.903	15.954
2.8c	5.644	4.896	16.497
2.9c	5.645	4.892	15.648
2.10c	5.650	4.907	18.256
2.11c	5.644	4.967	16.705
2.12c	5.643	4.892	15.595

2.3.2 Phototunable cell killing by photochromic diarylethene of thiazoyl and thienyl derivatives

To clarify the mechanism of the closed-ring isomers involved in photoinduced cell death, photoinduced cytotoxicities were investigated by derivative **2.1**[13] having two thiazole rings in the molecule (Figure 2.14), which has the highest photoinduced cytotoxicity in our previous works.[50] The cytotoxicity depends not only on the DAE concentration in the culture medium, but also on the initial amount of seeded cells; cytotoxicity appears more in the case of smaller amount of seeded cells even at the constant DAE concentration in the culture medium. This observation suggests that the DAE becomes partitioned into the cells much more than in the culture medium. Further, especially in case that the inherent toxicity in the dark (dark toxicity) of DAE is strong, the amount of the cells after overnight incubation could be decreased due to the slow growth. From these circumstances, it was difficult to estimate IC_{50} with a certain reliability. Therefore, among the concentration series from 0.02 ppm to 5 ppm, we determined the lower limit concentration (LLC) of DAEs at which the photocytotoxicity started to appear clearly in a prescribed condition described in the Supporting Information for photoinduced cytotoxicity experiments. Photoinduced HeLa cell death was not observed for **2.1o**, while **2.1c** showed photoinduced cytotoxicity when irradiated with blue light ($\lambda = 436$ nm), even though **2.1c** had absorption

at both 436 and 546 nm. Cell death was observed only in the exposed region with blue light. The mechanism of photoinduced cell killing by blue light irradiation is described later.
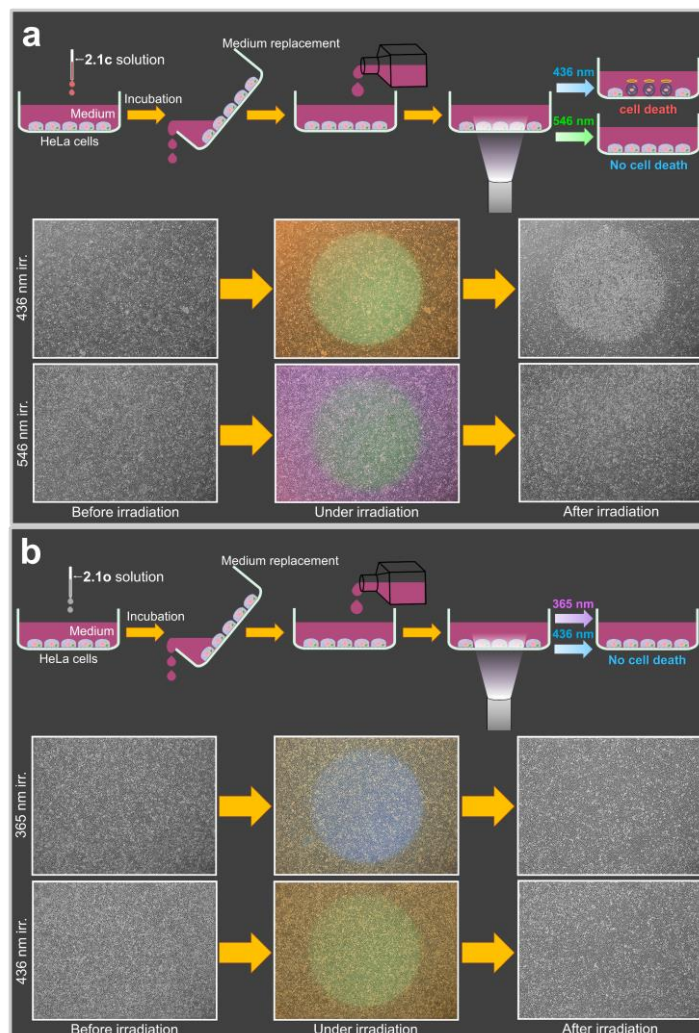
Figure 2.14 (a, b) Schematic illustration (top) and photograph (bottom) of fates of **2.1** incorporated HeLa cells after photoirradiation. The photoinduced cell death of HeLa cells were observed when exposed to light at 436 nm in the presence of **2.1c**. (a) HeLa cells were disseminated and cultured in media containing **2.1c** (0.2 ppm) for 1 day until they grew confluent. After replacing the medium with a fresh one to remove the excess amount of **2.1c** remaining in the medium, the cells were exposed to blue light ($\lambda = 436$ nm, 180 mW cm^{-2}, 2 min) or green light ($\lambda = 546$ nm, 30 mW cm^{-2}, 4 min). (b) The same preparation of HeLa cells as (a), for the media containing **2.1o** (0.2 ppm). After replacement with a fresh medium, the cells were exposed to UV light ($\lambda = 365$ nm, 90 mW cm^{-2}, 2 min) or blue light ($\lambda = 436$ nm, 180 mW cm^{-2}, 2 min).

The compound **2.1c** having two thiazole rings showed photoinduced cytotoxicity, and thus we prepared an asymmetric **2.13o**[20] having one thiazole ring, and a symmetric **2.14o**[21] with no thiazole ring to examine the effect of the number of thiazole rings on cytotoxicity (Scheme 2.7). The absorption maxima of open- and closed-ring isomers of **2.13** closely approximate the values averaged between the corresponding symmetric derivatives **2.1** and **2.14** (Table 2.10).[20] As a result, photoinduced HeLa cell death by **2.13** was also observed only for the closed-ring isomer **2.13c** when blue light ($\lambda = 436$ nm) was irradiated (Figure 2.15). However, **2.14** showed no photoinduced cytotoxicity in either open- or closed-ring isomers. Moreover, an increase in the numbers of thiazole rings in the molecule lowered the LLC for photoinduced cytotoxicity (Figure 2.16). In the case of **2.1c**, shrinkage and rounding of HeLa cells in the area irradiated by blue light ($\lambda = 436$ nm) were observed at LLC of 0.05 ppm (equivalent to 50 µg/L and 1 nM).[50] Cell shrinkage and cell rounding are known as one of the characteristics of apoptotic cells,[51] and we have reported that **2.1c**-induced cell death is caused by apoptosis.[10,50] These photoinduced cytotoxicities were caused at lower concentrations than the toxicity without light irradiation (Table 2.11). In particular, the photoinduced cytotoxicity of **2.1c** with very low doses presents a very attractive possibility for its application in cancer therapy.
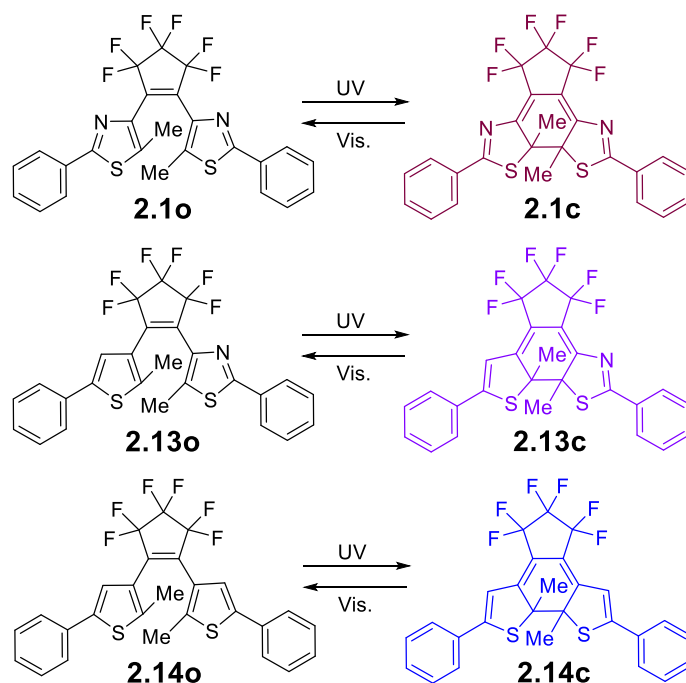
Scheme 2.7 Molecular structure of diarylethene derivatives **2.1**, **2.13**, and **2.14**.

Table 2.10 Photochromic properties of DAEs **2.1**, **2.13**, and **2.14** in hexane.[13,20,21]

	λ_{max} [nm] (ε [10^4 M^{-1} cm^{-1}])		$\Phi_{o \to c}$	$\Phi_{c \to o}$
	Open-ring	Closed-ring	Open-ring	Closed-ring
2.1[13]	300 (3.4)	525 (1.0)	0.32 (313 nm)	0.020 (492 nm)
2.13[20]	295 (3.5)	550 (1.5)	0.25 (313 nm)	0.013 (492 nm)
2.14[21]	280 (3.6)	575 (1.6)	0.59 (313 nm)	0.013 (492 nm)
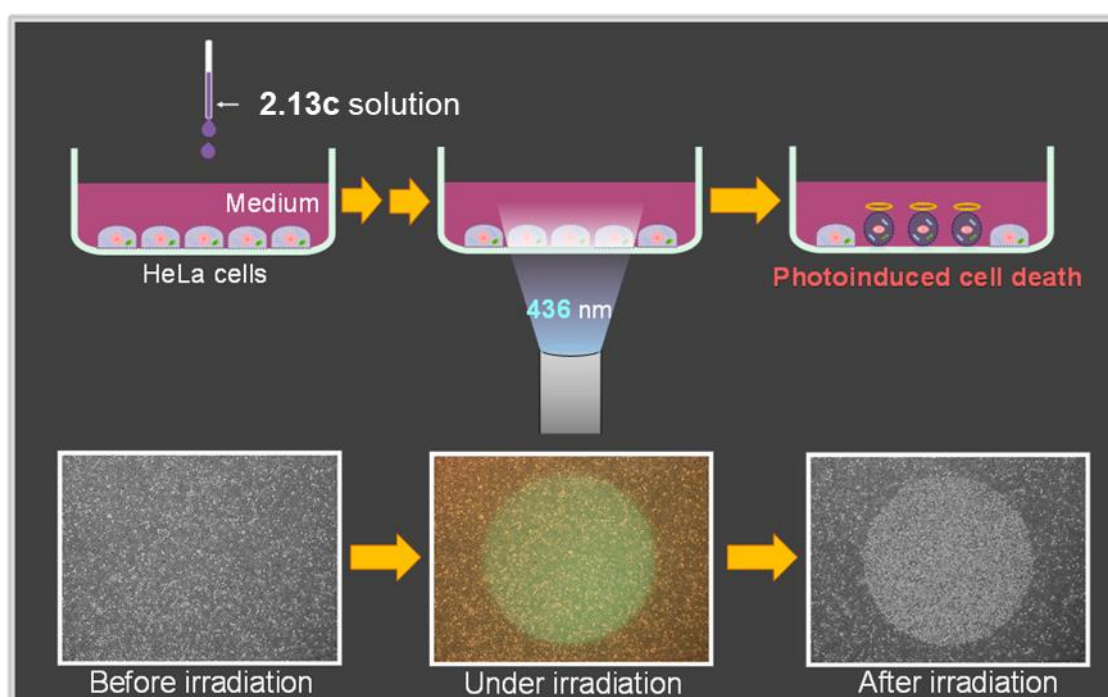
Figure 2.15 Schematic illustration and photos of photoinduced HeLa cell death of **2.13c**. HeLa cells were disseminated and cultured in media containing **2.13c** (0.2 ppm) for 1 day until they grew confluent. After changing the medium, the cells were exposed to blue light (λ = 436 nm, 180 mW cm^{-2}, 2 min). Photoinduced cell death of **2.13c** was observed in the irradiated area.

Table2.11 Concentration at which cytotoxicity is observed without light irradiation (dark toxicity) for the closed-ring isomers of **2.1**, **2.13**, and **2.14**.

	Cytotoxicity in the dark / ppm
2.1c	0.2
2.13c	1
2.14c	0.2

	Lower limit concentration (LLC) / ppm	
	Open-ring	Closed-ring
2.1[50]	>5	0.05
2.13	>5	0.2
2.14	>5	>5
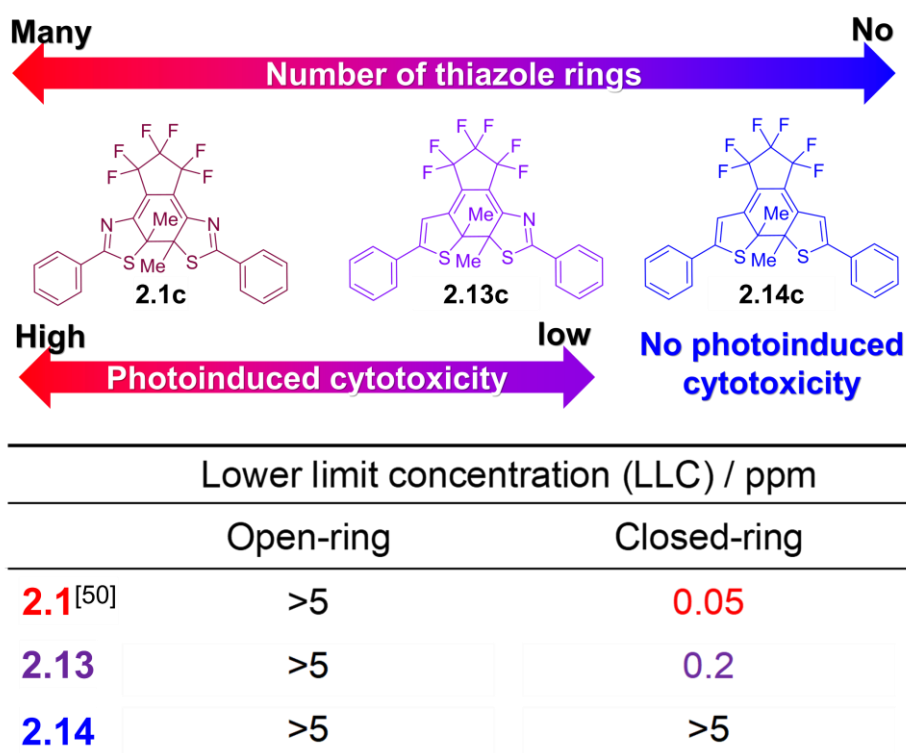
Figure 2.16 Lower limit concentration (LLC) of open- and closed-ring isomers of **2.1**, **2.13**, and **2.14** for photoinduced cytotoxicity. The lower limit concentration here is defined as the lowest concentration of the investigated compound that exhibited >80% cytotoxicity (cell death/cell shrinkage and rounding) in the irradiated area upon irradiation with blue light (λ = 436 nm, 4 min). Experiments to evaluate the lower limit concentration were performed up to 5 ppm.

The first evaluation was to investigate the photoresponsivity, reversibility, and thermal stability of the derivatives in polar solvents, including water, for use in cells. For the molecule, we chose derivative **2.1** having two thiazole rings in the molecule, which has the highest photoinduced cytotoxicity in our previous works.[10,50] The absorption maxima of the open- (**2.1o**) and closed-ring (**2.1c**) isomers of **2.1** in polar solvents containing water

were observed at almost the same wavelengths as in water-free organic solvent, which have been previously reported (Figure 2.17). The photostationary state (PSS) by UV light ($\lambda = 365$ nm) irradiation under these conditions is more than 70% for the generation of the closed-ring form. When the derivative **2.1** in the PSS state was irradiated with visible light ($\lambda > 480$ nm) containing absorption in the visible region of the closed-ring form, complete decolorization was observed, indicating about 100% isomerization to the open-ring form. This molecule can be switched back and forth between UV and visible light irradiation over several cycles, reaching essentially the same absorption maxima and minima after each cycle. The two derivatives **2.13** and **2.14** showed photoresponsivity, reversibility, and thermal stability in polar solvent mixtures of water and organic solvents, similar to **2.1** (Figure 2.17). This behavior indicating that there are no significant irreversible side reactions.
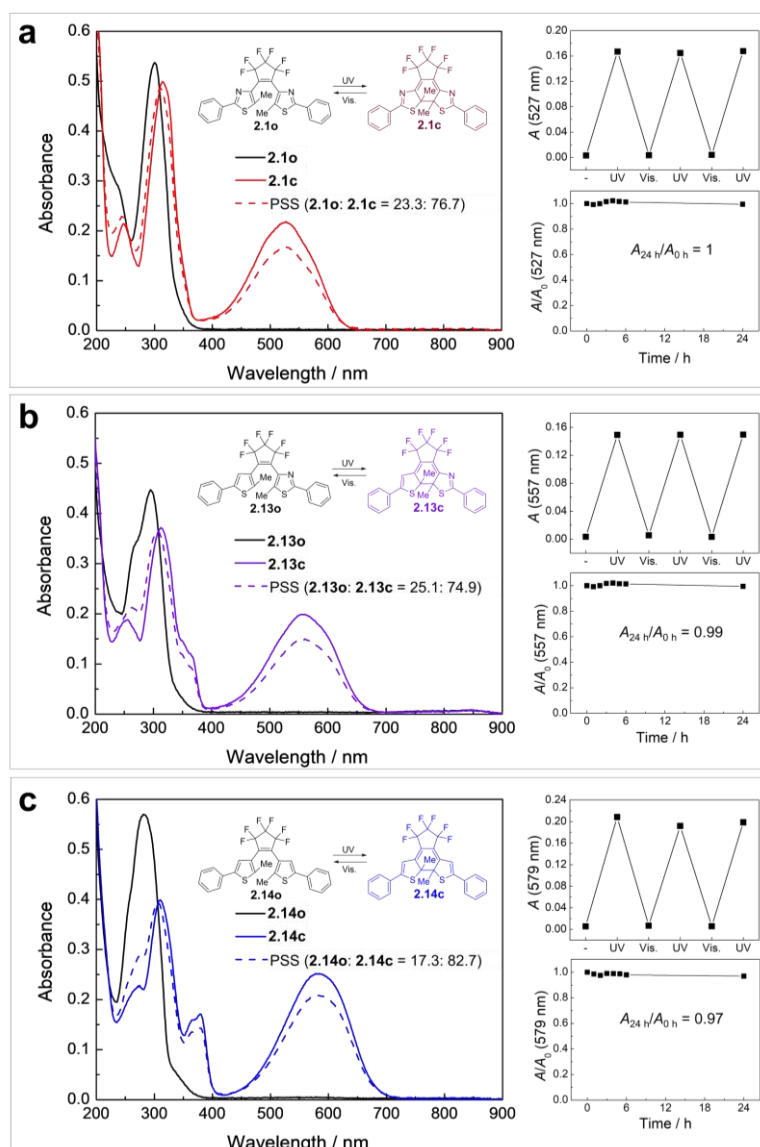
Figure 2.17 Absorption spectra, reversibility, and thermal stability of DAEs **2.1** (a), **2.13** (b), and **2.14** (c) in water/ethanol = 3:7 (v/v). The absorption spectra of the open- (solid black line) and closed-ring isomers (solid-colored lines other than black) and the PSS[UV] (broken line) are shown. In each panel the reversibility (top right) and the thermal stability (low right) are shown. For the reversibility, a sample was alternately irradiated with UV (λ = 365 nm) and visible light (λ > 480 nm). For the thermal stability, a sample of the closed-ring isomer was kept at 37 °C.

Photoinduced cytotoxicity was observed only in cases where cell cultures were dosed with closed-ring isomers. Apoptosis is known to be one of several integrated responses to DNA damage.[52] Thus, we examined whether there is a difference in the ratio of intercalation for two isomers of DAE into DNA. We observed the interactions between

DNA and each isomer of the DAEs by using ethidium bromide (EB). We prepared a solution containing sodium salts of DNA from Salmon testes[23] and EB. In an aqueous solution, EB is fluorescent only when it is intercalated in DNA. It has been confirmed that the pH is kept constant and that the fluorescence enhancement by intercalation of EB is hardly affected by ionic components in solution. Displacement of EB from the fluorescent EB‑DNA adduct by a DNA-interacting molecule can induce fluorescence quenching.[12,39,50,53] Fluorescence spectra were monitored at constant concentrations of DNA and EB (3.9 nM bp^{-1} and 75 μM, respectively) while increasing the amounts of DAEs (in the range of 0−25 μM) (Table 2.4). It has been observed that closed-ring isomers show a large decrease in emission intensity compared to open-ring isomers (Figure 2.18b and c). These results show that DAEs interact with DNA, and that open- or closed-ring isomers behave very differently. The affinity of the open- and closed-ring isomers for DNA was evaluated and compared using the Stern‑Volmer quenching constant, K_{SV}.

$$I_0/I = 1 + K_{SV}[DAE] \qquad (2.1)$$

Here, I_0 and I are the fluorescence emission intensities before and after the addition of DAEs. A plot of I_0/I vs. concentration of DAE ([DAE]) will give a straight line whose slope is equal to K_{SV}. The larger values of K_{SV} indicate the larger decrease of fluorescent intensity, suggesting a high intercalation ability. Among the derivatives studied, the K_{SV} values of the closed-ring isomers were in the range of 27−40 × 10^3 M^{-1}, indicating that the K_{SV} values were one order of magnitude higher than that of the open-ring isomers (K_{SV} < 1.6 × 10^3 M^{-1}). The results also indicate a high affinity with DNA (Figures 2.18d, 2.19, and Table 2.12).
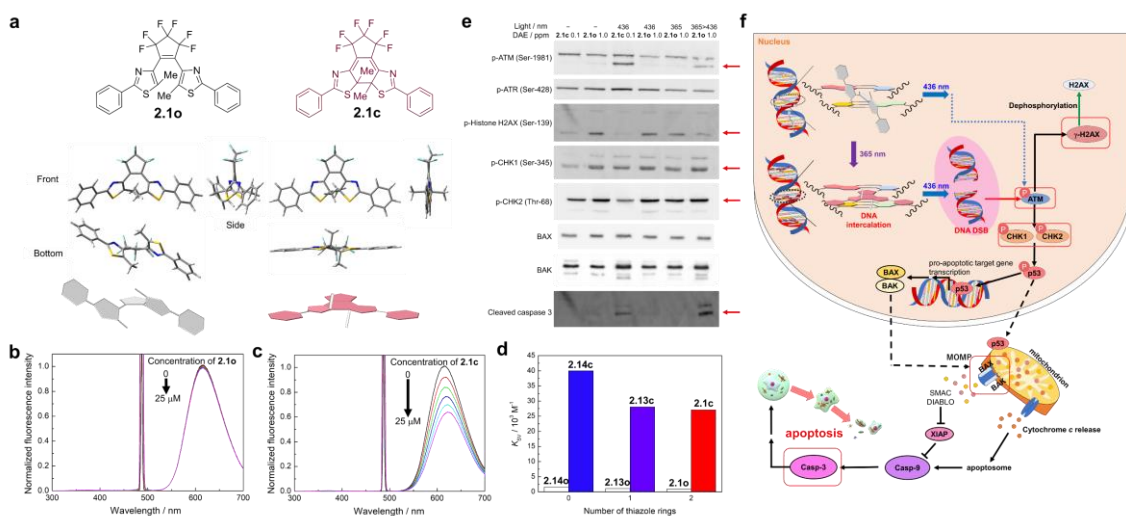
Figure 2.18 (a) Optimized structures at the B3LYP/PCM(water)/6-31G(d) level of theory for open- and closed-ring isomers of **2.1**. (b, c) Normalized fluorescence spectral changes of EB-DNA while adding **2.1o** (b) and **2.1c** (c) in buffer solution (D-PBS/DMSO = 95:5 (v/v), DNA: 3.9 nM bp^{-1}, EB: 75 μM, λ_{ex} = 486 nm). Results just after addition (within 1 min). Concentration of **2.1o** or **2.1c**: 0 (solid black line), 5 (solid red line), 10 (solid green line), 15 (solid blue line), 20 (solid light-blue line), and 25 μM (solid magenta line). (d) The K_{SV} values were calculated corresponding to Eq. (1) for open- and closed-ring isomers of **2.1**, **2.13**, and **2.14**. (e) Western blot analysis of phosphorylated ATM (Ser-1981), phosphorylated ATR (Ser-428), phosphorylated Histone H2AX (Ser-139), phosphorylated CHK1 (Ser-345), phosphorylated CHK2 (Thr-68), BAX, BAK, and cleaved caspase-3 using HeLa cell in the presence of **2.1**. Note that the concentration of **2.1c** was 0.1 ppm and the concentration of **2.1o** was 1.0 ppm. (f) Schematic illustration of the DNA damage-induced apoptotic signaling pathway by photoinduced DNA double-strand break by **2.1**. Solid arrows indicate stimulation, broken arrows indicate movement, T-shaped lines indicate inhibition, dotted line means very weak activity, and circled P (Ⓟ) indicate phosphorylation. The red frames were actually detected by western blot. Western blot analysis shows that ATM activity by **2.1c** is very strong, while the activity by **2.1o** is very weak. The principal kinases relaying the ATM/ATR-initiated checkpoint signaling is thought to be preferentially CHK2 for ATM and CHK1 for ATR, but ATM maybe act through the activation of CHK1 as well as CHK2.[54,55] The DNA damage-induced apoptosis signaling pathway was simplified based on a reference.[56]

68
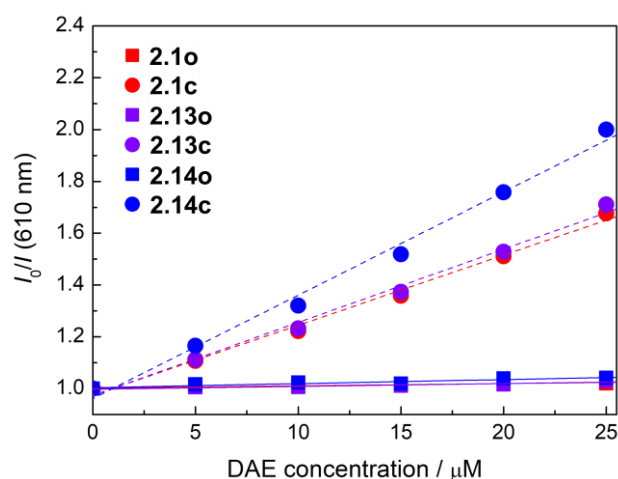
Figure 2.19 Plots of I_0/I vs. [DAE] for the titration of EB-DNA with open- (square point and solid line)/closed- (circle point and broken line) ring isomers of **2.1** (red), **2.13** (blue), and **2.14** (violet) in buffer solution (D-PBS/DMSO = 95:5 (v/v)) at λ_{ex} = 486 nm and λ_{em} = 610 nm: experimental data points and linear fitting of the data. Concentration of DAE: 0-25 μM, DNA: 3.9 nM bp^{-1}, EB: 75 μM.

Table 2.12 Stern-Volmer constants (K_{SV}) for EB-DNA of open- and closed-ring isomers of **2.1**, **2.13**, and **2.14**.

Compound	K_{SV} / M^{-1}	r
2.1o	$9.1{\times}10^2$	0.9530
2.1c	$2.7{\times}10^4$	0.9964
2.13o	$1.1{\times}10^3$	0.9430
2.13c	$2.8{\times}10^4$	0.9959
2.14o	$1.6{\times}10^3$	0.9402
2.14c	$4.0{\times}10^4$	0.9954

r: Regression coefficient.

A static binding reaction between DNA and a drug occurs when there are similar independent binding sites in the DNA: that is, the binding capacity of DNA at each binding site in DNA is equal. When the binding constant of a DAE isomer (K_b) is larger than that of EB (K_{b_EB} = $6.58{\times}10^4$ M^{-1}), the DAE removes the EB from the DNA. The intensity of the fluorescence clearly decreased with the addition of closed-ring DAEs, indicating the replacement of intercalating EB by the closed-ring forms. By contrast, there was no significant decrease by the open-ring structures. Based on the following equation (2.2)[57], apparent K_b (K_{b_app}) was estimated by the linear fitting of a double logarithmic plot of the data obtained by the addition of DAEs.

$$\log K_{b\_app} = \log\{(I_0\text{-}I)/I\}\text{-}n\log[DAE] \quad (2.2)$$

Here, I_0 and I are the fluorescence emission intensities before and after the addition of DAEs, and n is the reaction order of DAE. Since the calculated values of K_{b_app} were larger than K_{b_EB} (Figure 2.20 and Table 2.13) in practice, K_b was estimated directly from the values of K_{b_EB}. On the other hand, in the case of DAEs in open-ring structures, the calculated values of K_{b_app} were much smaller than those of K_{b_EB}.
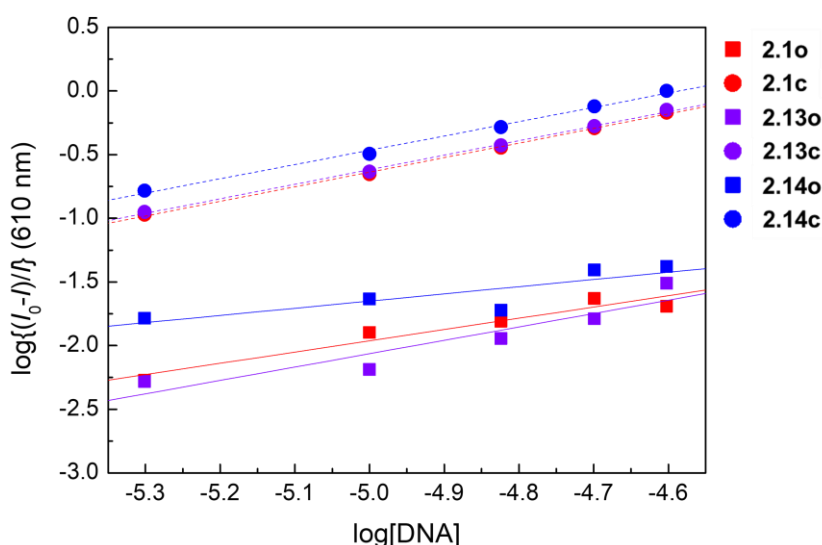
Figure 2.20 Plots of $\log(I_0\text{-}I)/I$ vs. log[DAE] for the titration of EB-DNA with open-(square point and solid line)/closed- (circle point and broken line) ring isomers of **2.1** (red), **2.13** (blue), and **2.14** (violet) in buffer solution (D-PBS/DMSO = 95:5 (v/v)) at λ_{ex} = 486 nm and λ_{em} = 610 nm: experimental data points and linear fitting of the data. Concentration of DAE: 0-25 μM, DNA: 3.9 nM bp^{-1}, EB: 75 μM.

Table 2.13 Apparent binding constants (K_{b_app}) and binding sites (n) of **2.1c**, **2.13c**, and **2.14c** to DNA.

Compound	K_{b_app} / M^{-1}	n	r
2.1o	2.91×10^2	0.88	0.9658
2.1c	1.24×10^5	1.15	0.9993
2.13o	1.55×10^3	1.05	0.9338
2.13c	1.23×10^5	1.14	0.9991
2.14o	1.49×10^1	0.56	0.8445
2.14c	1.41×10^5	1.12	0.9975

r: Regression coefficient.

70

The difference in DNA intercalation ability between the open- and closed-ring isomers of DAE is attributed to the difference in structures. The open-ring isomers of DAE have bulky and flexible structures due to the free rotation along two single bonds attached to the allyl group. In contrast, the closed-ring isomers are planar rigid structures with a six-membered cyclohexadiene ring in the center of the molecule. Therefore, the intercalation ability of the closed-ring isomers is superior to that of the open-ring isomers (Figures 2.18a, 2.21, 2.22, and Tables 2.14 and 2.15). The structural difference was confirmed by DFT[27,28] calculations using different functionals of B3LYP[29-31] and ωB97X-D[32] with a solvent water model PCM[33]. These results indicate that the DNA intercalating ability of DAEs is likely switched through the photoisomerization. In other words, we can trigger the DNA intercalation of DAE by the UV light irradiation. The diamond part of Figure 2.23 clearly shows this possibility. We added the **2.1o** to the HeLa cell culture medium, and then we carried out two steps of irradiation: the first with UV light ($\lambda = 365$ nm) and the second with blue light ($\lambda = 436$ nm). As shown in Figure 2.23, only in the diamond domain, where the two irradiated areas overlapped, we observed the photoinduced cytotoxicity. For this case, no cell death was observed after only the first UV light irradiation. This experiment revealed the detailed mechanism by which UV irradiation changes **2.1o** to a closed-ring isomer (**2.1c**) then the photogenerated **2.1c** causes photoinduced cytotoxicity.
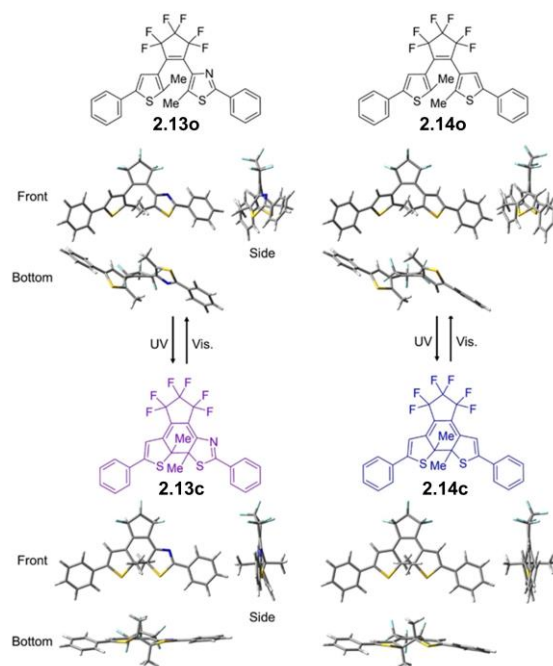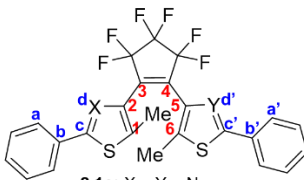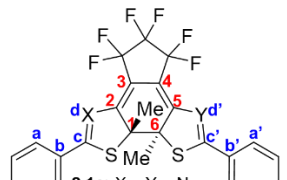
Figure 2.21 Structure of open- and closed-ring isomers of **2.13** and **2.14** optimized on the B3LYP/PCM(water)/6-31G(d) level of theory.

Table 2.14 Geometric parameters of optimized structures of open- and closed-ring isomers of **2.1**, **2.13**, and **2.14** on the B3LYP/PCM(water)/6-31G(d) level of theory.

2.1o: X = Y = N
2.13o: X= CH, Y = N
2.14o: X = Y = CH

2.1c: X = Y = N
2.13c: X= CH, Y = N
2.14c: X = Y = CH

$\varphi_1 = ∢(C_1, C_2, C_3, C_4)$
$\varphi_2 = ∢(C_3, C_4, C_5, C_6)$

$\theta_1 = ∢(C_a, C_b, C_c, C_d)$, $\theta_2 = ∢(C_{a'}, C_{b'}, C_{c'}, C_{d'})$

	2.1o	2.1c	2.13o	2.13c	2.14o	2.14c
E [kJ/mol][a]	0	47.667	0	49.823	0	52.286
r_{C1-C6} [Å]	3.675	1.548	3.678	1.549	3.686	1.549
φ_1/φ_2 [°]	-47.4 / -44.2	7.8 / 7.3	-47.7 / -44.6	7.2 / 7.4	-48.5 / -45.6	-8.7 / -7.7
θ_1/θ_2 [°]	5.5 / 3.5	2.5 / 3.4	25.1 / 2.7	-18.9 / 3.6	25.0 / 24.9	-16.6 / -16.6

a: Energy relative to open-ring isomer.

Figure 2.22 Structures of open- and closed-ring isomers of **2.1**, **2.13**, and **2.14** optimized on the ωB97X-D/PCM(water)/6-31G(d) level of theory.

72

Table 2.15 Geometric parameters of optimized structures of open- and closed-ring isomers of **2.1**, **2.13**, and **2.14** on the ωB97X-D/PCM(water)/6-31G(d) level of theory.

2.1o: X = Y = N
2.13o: X= CH, Y = N
2.14o: X = Y = CH

2.1c: X = Y = N
2.13c: X= CH, Y = N
2.14c: X = Y = CH

$\varphi_1 = \sphericalangle (C_1, C_2, C_3, C_4)$
$\varphi_2 = \sphericalangle (C_3, C_4, C_5, C_6)$

$\theta_1 = \sphericalangle (C_a, C_b, C_c, C_d)$, $\theta_2 = \sphericalangle (C_{a'}, C_{b'}, C_{c'}, C_{d'})$

	2.1o	2.1c	2.13o	2.13c	2.14o	2.14c
E [kJ/mol][a]	0	39.891	0	44.208	0	47.823
$r_{C1\text{-}C6}$ [Å]	3.506	1.543	3.513	1.543	3.523	1.543
φ_1/φ_2 [°]	-46.5 / -43.6	7.0 / 6.6	-47.3 / -44.4	6.5 / 6.6	-48.0 / -45.6	-7.6 / -6.9
θ_1/θ_2 [°]	10.7 / 7.8	4.8 / 6.6	30.5 / 8.9	2.7 / 7.0	30.1 / 30.4	-27.8 / -27.4

a: Energy relative to open-ring isomer.
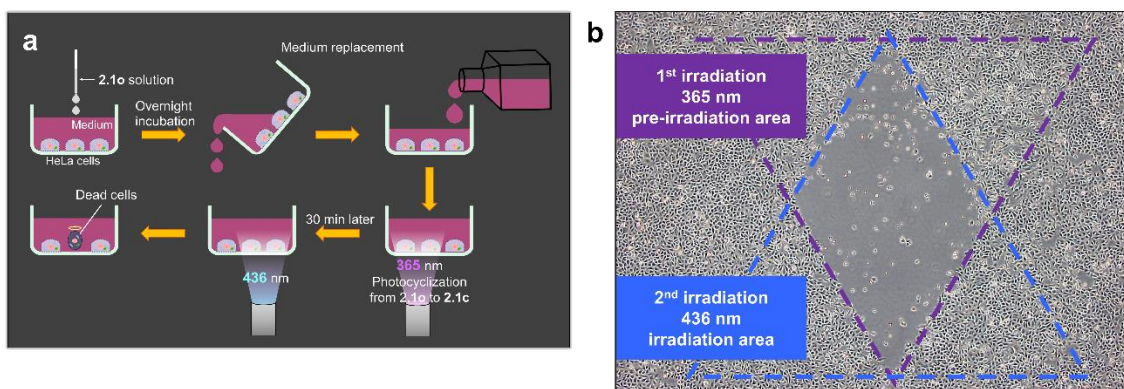
Figure 2.23 Schematic illustration (a) and photograph (b) of the domain of photoinduced HeLa cell death by **2.1**. HeLa cells were disseminated and cultured in media containing **2.1o** (0.5 ppm) for 1 day until they grew confluent. After replacing the medium with a new one to remove excess **2.1**, UV light (λ = 365 nm, 100 mW cm^{-2}) was irradiated for 20 s along the inverted triangle pattern (purple broken line). Immediately after irradiation, the medium was replaced, and 30 min after irradiation, blue light (λ = 436 nm, 180 mW cm^{-2}) was irradiated for 4 min along the triangle pattern (broken blue line).

Irradiation or drugs used for cancer chemotherapy results in DNA damage in some cells, which can lead to apoptotic death.[58] In particular, DNA double-strand breaks (DSBs) are

particularly cytotoxic because even a single DSB can trigger chromosomal aberrations and cell death.[59,60] In such cases, the frequency of cleavage in a DNA molecule is overwhelmingly small, so it is highly likely that fragmented and intact DNA cannot be distinguished in electrophoresis. In fact, we couldn't confirm it in our system (Figure 2.24). Therefore, to clarify the mechanism of cell death of HeLa cells, a molecular biological study on the mechanism of photoinduced cytotoxicity was carried out. Western blot analysis (Table 2.5) indicated that the light irradiation at 436 nm to the HeLa cells, dosed with **2.1c** activated ATM kinase and DNA replication stress (γ-H2AX)[56,61] (Figure 2.18e and f), strongly suggested DNA DSBs.[62] In addition, CHK1, CHK2, BAX, BAK, caspase-3 and BAX multiplication were also activated,[54,56,63,64] suggesting that the photoinduced cell death was apoptosis by caspase cascade activity due to nuclear DNA damage[62,63] (Figures 2.18e and 2.25). On the other hand, in the presence of **2.1o**, γ-H2AX was detected, but the activity of ATM kinase was weak, and the elevations of BAX, BAK, and cleaved caspase-3 were not detected, even when irradiated with light at 365 or 436 nm. Therefore, DNA damage occurs even by **2.1o**, but induction of apoptosis and its related cell death does not occur.
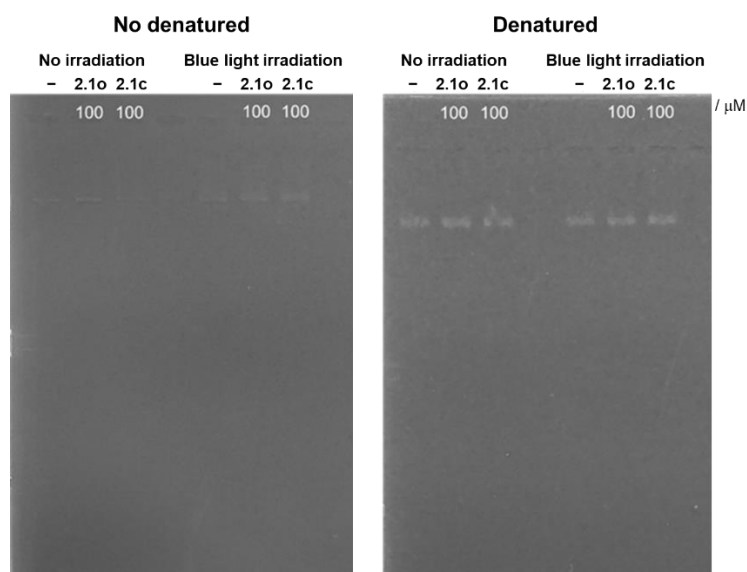
Figure 2.24 Agarose gel electrophoresis of **2.1** incubated with plasmid DNA without/with blue light (λ = 430 nm, 20 mW cm^{-2}, 1 h) irradiation. There was not observed fragmentation of DNA in either condition.
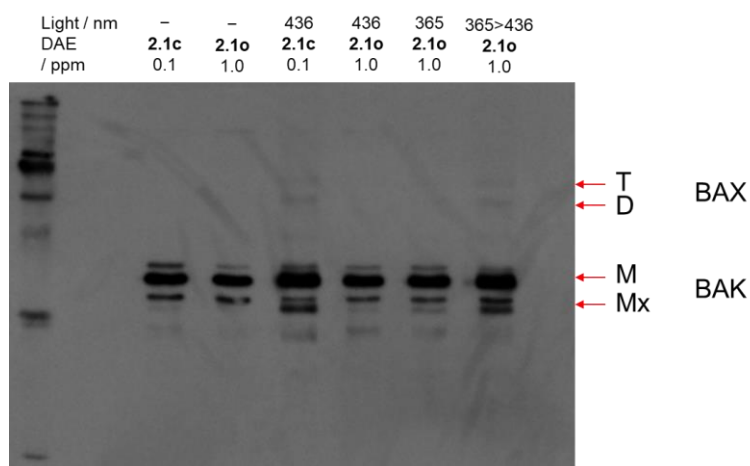
Figure 2.25 Western blot analysis of BAX multimer following DNA damage using HeLa cell in the presence of **2.1**. BAX multimerization was shown when irradiated at 436 nm in the presence of **2.1c**, and continuously irradiated at 365 nm and 436 nm in the presence of **2.1o**. Note that the concentrations of **2.1o** and **2.1c** were 1.0 and 0.1ppm, respectively. Overexpressed BAX accelerates apoptotic death.[63,64]

The open-ring isomers of derivatives **2.1**, **2.13**, and **2.14** do not normally have absorption longer than 400 nm (Figure 2.17). Therefore, irradiating these closed-ring isomers with visible light at 436 or 546 nm causes ring opening. However, photoinduced cytotoxicity was induced upon blue light irradiation at 436 nm, but cell death was not induced by green light irradiation at 546 nm. Thus, in order to investigate the mechanism by which this photoinduced cell death is triggered by blue light irradiation, the interaction between the derivatives and DNA was investigated. The interaction between DNA and DAEs **2.1** and **2.13** can be traced by hypochromic and bathochromic shifts in the absorption spectra in the presence of DNA (Figure 2.26). The shifts are characteristic of the association of a ligand with DNA,[65] indicating interaction between DNA and DAEs with a thiazole ring. Large red-shifts in the absorption maxima were observed for both open- and closed-ring isomers of **2.1**. Similar red-shifts were observed for both **2.13o** and **2.13c**. The red-shift for **2.1c** was larger than that for **2.13c**. The absorbance of the red-shifted band increased with increasing concentration of DNA, without any shift of the absorption maxima (Figures 2.27 and 2.28).

Figure 2.26 Absorption spectral changes of **2.1**, **2.13**, and **2.14** in buffer solution (D-PBS/DMSO = 95:5 (v/v)) in the presence of DNA. Concentration of open-/closed-ring isomers of DAEs: 15 μM, DNA: 3.9 nM bp^{-1}. (a-f) Time-dependent changes in absorption spectra of **2.1o** (a), **2.1c** (b), **2.13o** (c), **2.13c** (d), **2.14o** (e), and **2.14c** (f).
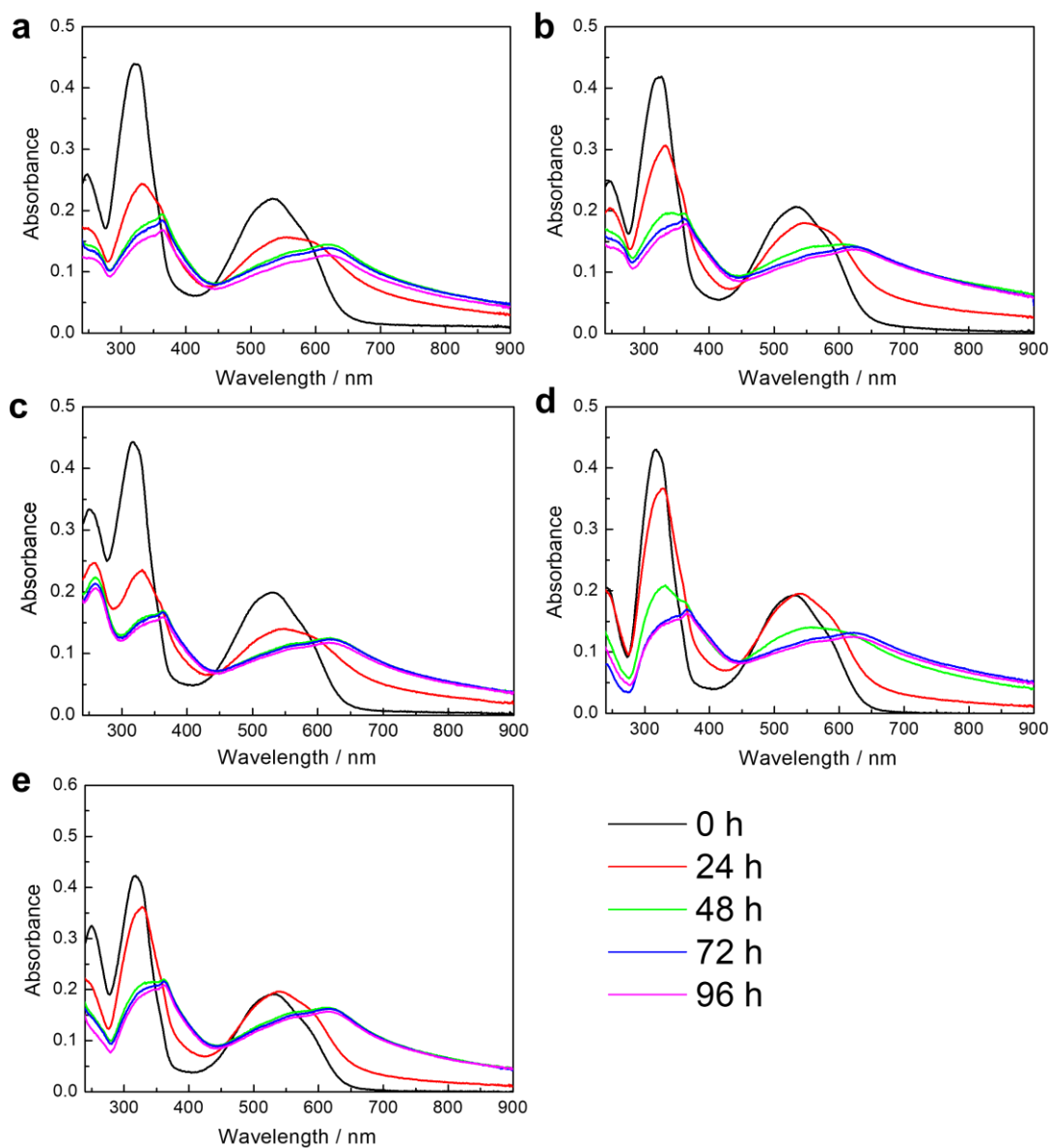
Figure 2.27 Absorption spectral changes of **2.1c** due to time course in the presence of each DNA concentration in the buffer solution (D-PBS/DMSO = 95:5 (v/v), **2.1c**: 15 μM). (a-e) Absorption spectra of **2.1c** at each DNA concentration. DNA concentrations were 3.9 (a), 7.7 (b), 23.1 (c), 30.8 (d), and 38.5 (e) nM bp^{-1}.
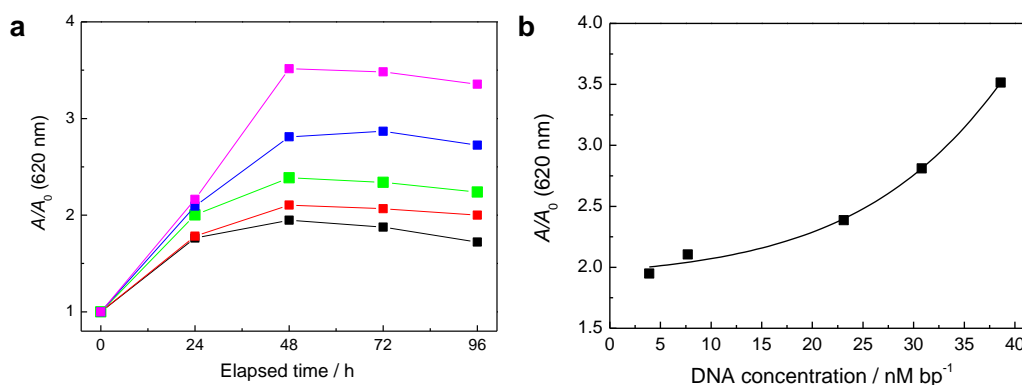
Figure 2.28 Relationship between increase in absorption intensity at 620 nm of **2.1c** and DNA. (a) Plots of A/A_0 vs. time absorbance increase of **2.1c** with each concentration of DNA. DNA concentrations were 3.9 (black square), 7.7 (red square), 23.1 (green square), 30.8 (blue square), and 38.5 (magenta square) nM bp^{-1}. From the absorption spectrum of **2.1c** at each DNA concentration (Figure 2.27), the absorption intensity at 620 nm immediately after addition of **2.1c**: A_0 and the absorption intensity at 620 nm for each elapsed time of addition of **2.1c**: A were determined. The absorption intensity at 620 nm of **2.1c** at each DNA concentration showed a maximum value after 48 hours. (b) Plot of A/A_0 vs. each DNA concentration at 48 h after addition of **2.1c**. The higher the DNA concentration, the greater the absorbance of **2.1c** at 620 nm.

In contrast, no spectral shift was observed for **2.14o** and **2.14c** without a thiazole ring. To confirm that the red-shifts of the absorption bands of **2.1** and **2.13** are attributable to the interaction with DNA, the absorption spectra of DAEs without DNA were compared (Figure 2.29). In all isomers of **2.1**, **2.13**, and **2.14**, the absorption bands were not red-shifted, and there was almost no absorbance 24 hours after the start of measurement. Thus, the red-shifts observed for the open- and closed-ring isomers of **2.1** and **2.13** with thiazole rings are due to interaction with DNA. In addition, the decreasing rate of the absorption intensities of both isomers of **2.1**, **2.13**, and **2.14** in aqueous media in the presence of DNA are much slower than those in the absence of DNA (Figures 2.26 and 2.29). The results suggest hydrophobic DAEs in aqueous media are stabilized in the presence of DNA molecules to avoid the precipitation of DAEs. Furthermore, when the **2.1c**-DNA complex formed by these interactions was irradiated with blue light at 436 nm, the **2.1o**-DNA complex was generated by photocyclization (Figure 2.30a and b). The photogenerated **2.1o**-DNA complex from the CD spectrum had a new band at 436 nm, but there was no absorption at >546 nm (Figure 2.30b). Alteration of the CD spectrum by light irradiation was not observed for **2.1o** (Figure 2.31). There are two specific bands in the DNA spectrum, a positive band associated with base stacking and a negative band associated with right-

handed helicity.[66,67] These bands are very sensitive to the interaction between the DNA and the molecule. Simple groove bonding and hydrophobic interactions cause little change in the base stacking and helicity bands.[68] Therefore, the open- and closed-ring isomers are likely to have different interaction positions due to the difference in the bulkiness of their molecules. Then, we examined the effect of the irradiation at 546 nm, which had been confirmed to induce the ring opening of **2.1c**. We observed that there was no cell damage when the light at 546 nm was irradiated to HeLa cells under the coexistence of **2.1c**. On the other hand, the irradiation at 436 nm, after the irradiation at 546 nm (to induce ring opening), resulted in cell death (Figure 2.30c and d). Therefore, this suggests that the photoinduced cell death was caused by the **2.1o**-DNA complex generated by in situ photoinduced ring opening. Note that this **2.1o**-DNA is generated by ring-opening after the interaction between **2.1c** and DNA, which is different from the interaction between **2.1o** and DNA.
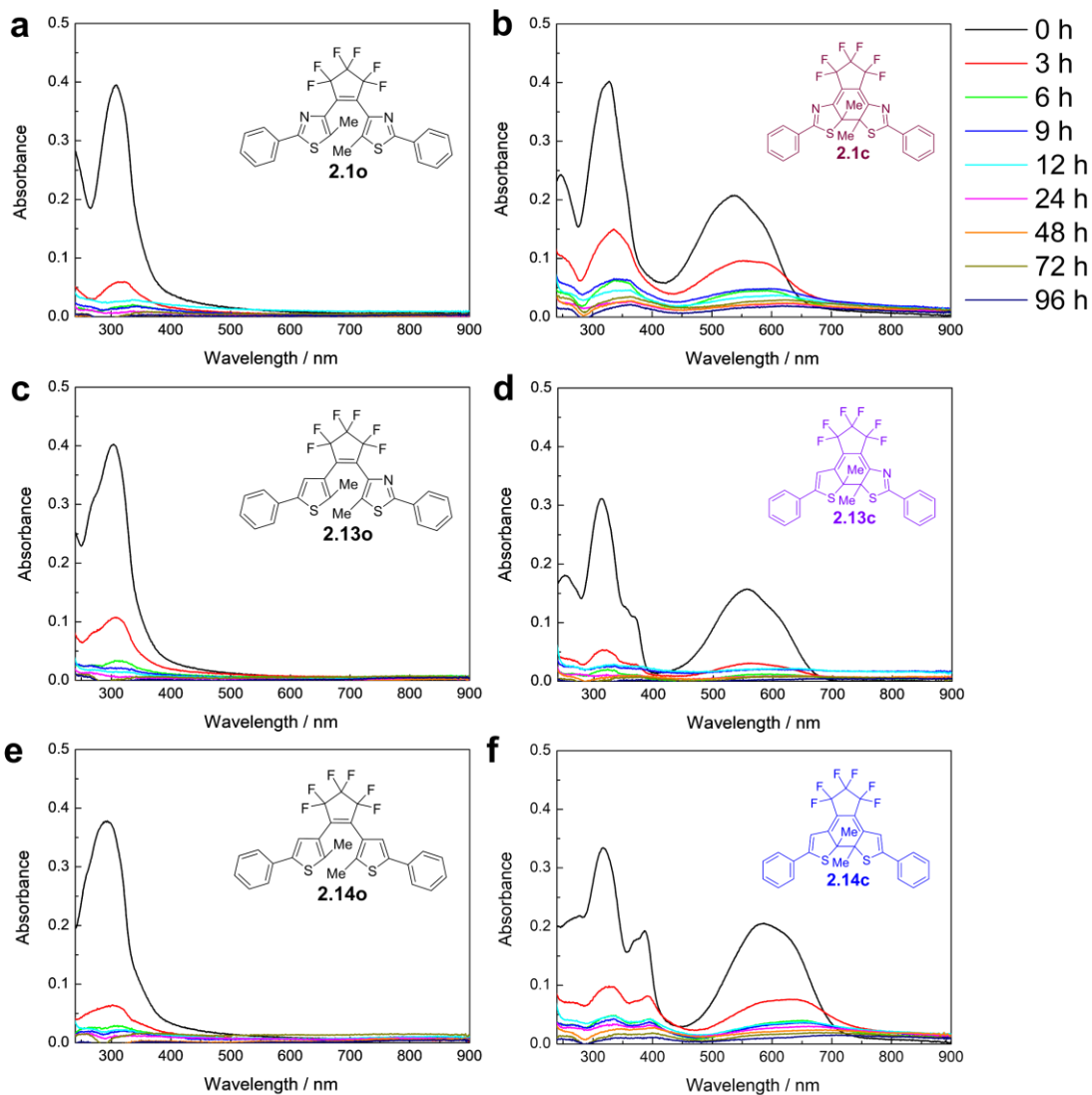
Figure 2.29 Absorption spectral changes of **2.1**, **2.13**, and **2.14** in buffer solution (D-PBS/DMSO = 95:5 (v/v)) in the absence of DNA. (a-f) Time-dependent changes in the absorption spectra of **2.1o** (a), **2.1c** (b), **2.13o** (c)**, 2.13c** (d), **2.14o** (e), and **2.14c** (f) (open-/closed-ring isomers of DAEs: 15 μM). In the absence of DNA, no red-shift of maximum absorption wavelength was observed.
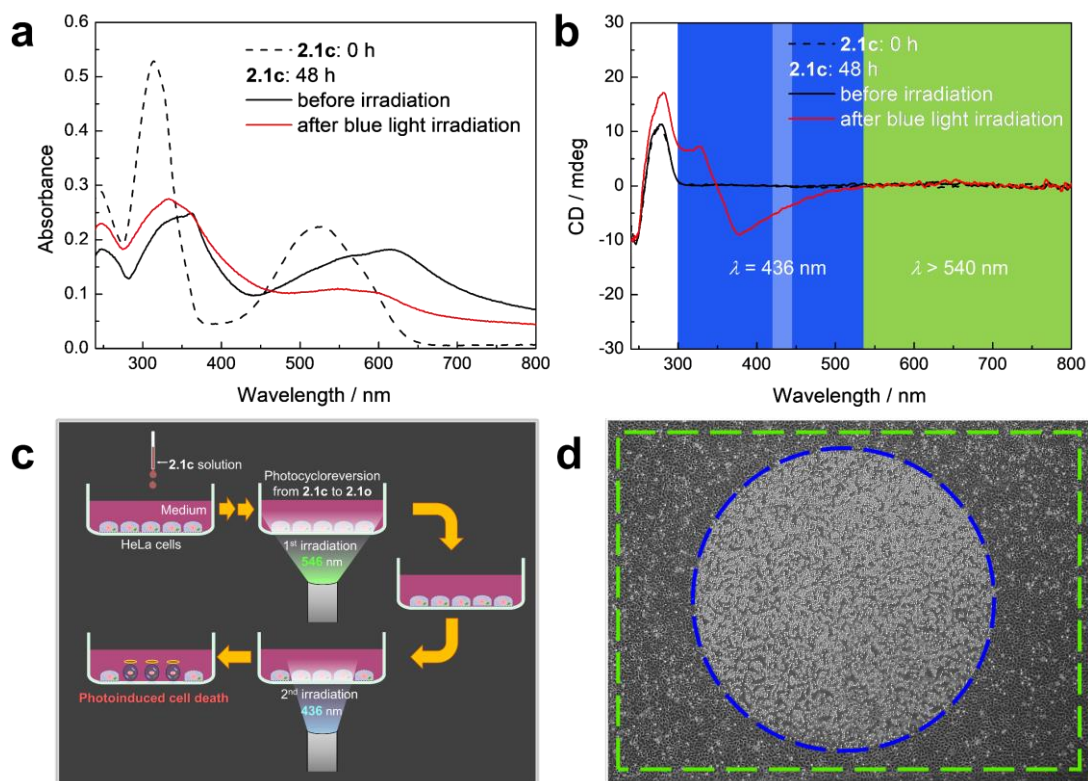
Figure 2.30 (a, b) Absorption spectra (a) and CD spectra (b) before and after blue light ($\lambda = 436$ nm, 18 mW cm^{-2}, 10 min) irradiation for **2.1** with red-shift of absorption (elapsed time since the addition of **2.1c**: 48 h) in the presence of DNA in buffer solution (D-PBS/DMSO = 95:5 (v/v), **2.1c**: 15 μM, DNA: 38.5 nM bp^{-1}). Before blue light irradiation, nothing was observed except the CD spectrum due to DNA[69]. (c, d) Schematic illustration (c) and photograph (d) of the procedure of cytotoxic photoresponse of **2.1**. HeLa cells cultured in the presence of **2.1c** (0.2 ppm) were first irradiated with green light ($\lambda = 546$ nm, 30 mW cm^{-2}, 4 min) inducing photocycloreversion from **2.1c** to **2.1o** in a rectangular area (range including the circular irradiated area: broken green line). No photoinduced cytotoxicity (shrinkage and rounding of HeLa cells) were observed at this stage. Next, the second blue light ($\lambda = 436$ nm, 180 mW cm^{-2}, 2 min) was irradiated in the circular area (broken blue line). Photoinduced cytotoxicity against HeLa cells was observed in the area where 436 nm light was irradiated after irradiation with 546 nm light, whereas cytotoxicity was not observed for the case where only 546 nm light was irradiated even in the presence of **2.1c**.
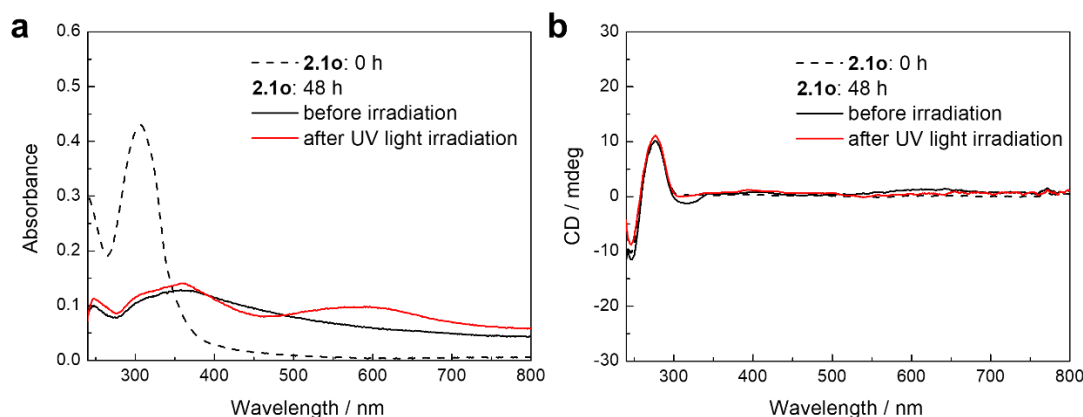
Figure 2.31 Absorption spectra (a) and CD spectra (b) before and after blue light ($\lambda = 436$ nm, 18 mW cm^{-2}, 10 min) irradiation for **2.1** with red-shift of absorption (elapsed time since the addition of **2.1o**: 48 h) in the presence of DNA in buffer solution (D-PBS/DMSO = 95:5 (v/v), **2.1o**: 15 μM, DNA: 38.5 nM bp^{-1}).

The major difference in absorption spectra between **2.1o** and **2.1o**-DNA complex is in the absence or presence of a band at 436 nm. When the open form has no band at 436 nm and the closed form has absorption at 436 nm, irradiation of the closed form with 436 nm blue light induces a photocycloreversion reaction (Figure 2.32a). The presence of the thiazole ring in the molecule induces an interaction between the DAE and DNA, causing the absorption band to be red-shifted, and giving the open form a band at 436 nm, which it does not naturally have. Accordingly, the **2.1**-DNA complex having open and closed forms with absorption at 436 nm can undergo a cyclic photocyclization and photocycloreversion reactions upon blue light irradiation. These cyclic reactions could function like a clipper, damaging DNA and causing cell death (Figure 2.32b). Thus, we prepared derivatives **2.15**,[13] **2.16**, and **2.17**[22] (Figure 2.32c) with inverted structures of **2.1**, **2.13**, and **2.14**, having both open- and closed-ring isomers with absorption at 436 nm (Figure 2.33 and Table 2.16). They showed photosensitivity, reversibility, and thermal stability in polar solvent mixtures of water and organic solvents, as in **2.1**, **2.13**, and **2.14** (Figure 2.34). Then, we investigated their photoinduced cytotoxicity. Dark toxicity of the closed-ring isomers of **2.15**, **2.16**, and **2.17** was observed at 5 ppm (Table 2.17). The photoinduced cytotoxicity of **2.15**, **2.16**, and **2.17** was not observed up to 5 ppm for the open-ring isomers as in **2.1**, **2.13**, and **2.14** (Table 2.18). Interestingly, the closed-ring isomers of **2.15**, **2.16**, and **2.17** induced photoinduced cell death upon blue light irradiation in the presence of concentration of 0.05 ppm. In particular, it is noteworthy that **2.17c**, which does not have a thiazole ring in the molecule, showed photoinduced cytotoxicity.

Additionally, we confirmed that significant ROS was not generated in the blue light irradiation. (Figure 2.35). This was consistent with the observation that the cell death was localized in the light-irradiated area. These results strongly suggest that the photoinduced cytotoxicity of DAE is caused by repeated photocyclization and photocycloreversion reactions.
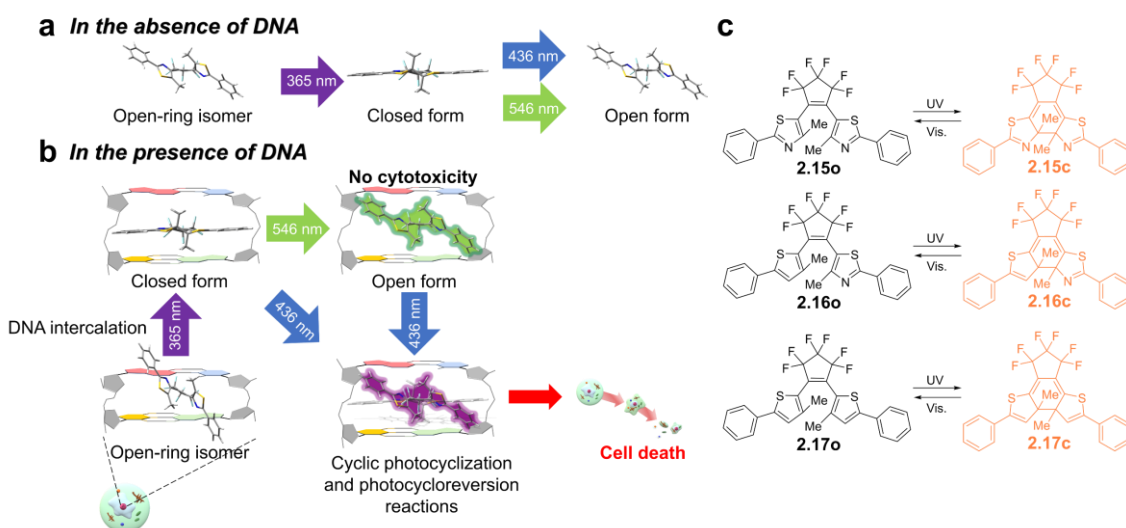
Figure 2.32 (a) Schematic illustration of the structural changes of **2.1** by light irradiation in the absence of DNA. In the absence of DNA, the derivative **2.1** is induced to the closed form by UV light irradiation at 365 nm and to the open form by visible light irradiation at 436 and 546 nm, respectively. (b) Schematic illustration of the photoinduced cytotoxicity of **2.1**. In the presence of DNA, closed form can easily intercalate between DNA base pairs. The interaction of derivative **2.1** with DNA causes a red-shift in absorbance, so that the open form has an absorption at 436 nm. Thus, a DAE having thiazole rings inserted into DNA undergoes repeated photocyclization-cycloreversion reactions upon light irradiation at 436 nm, and induces cell death. (c) Molecular structures of the open- and closed-ring isomers of **2.15**, **2.16**, and **2.17**.
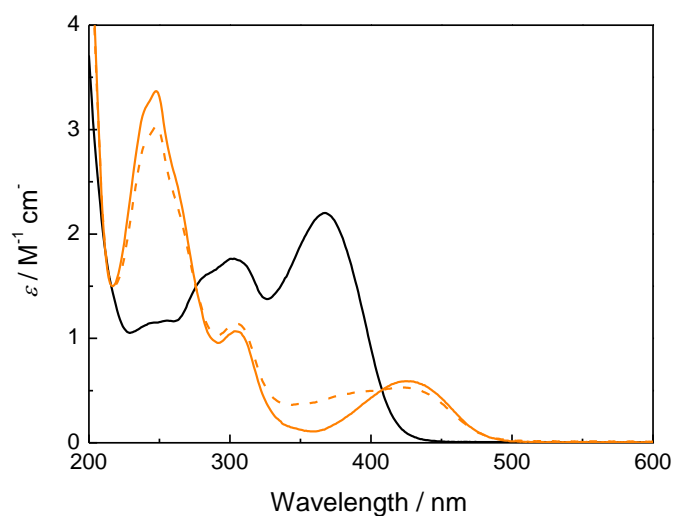
Figure 2.33 Absorption spectral changes of **2.16** in hexane solution. **2.16o**: solid black line, **2.16c**: solid orange line, photostationary state (**2.16o**:**2.16c** = 10.6:89.4) upon 365 nm light irradiation: broken orange line.

Table 2.16 Photochromic properties of DAEs **2.15**, **2.16**, and **2.17** in hexane.[17,20]

	λ_{max} [nm] (ε [10^4 M^{-1} cm^{-1}])		$\Phi_{o \to c}$	$\Phi_{c \to o}$
	Open-ring	Closed-ring	Open-ring	Closed-ring
2.15	363 (2.1)[13]	406 (0.70)[13]	0.22 (366 nm)[13]	0.27 (440 nm)
2.16	367 (2.2)	425 (0.59)	0.20 (366 nm)	0.41 (440 nm)
2.17[45]	370 (2.28)	438 (0.525)	0.17 (366 nm)	0.48 (440 nm)
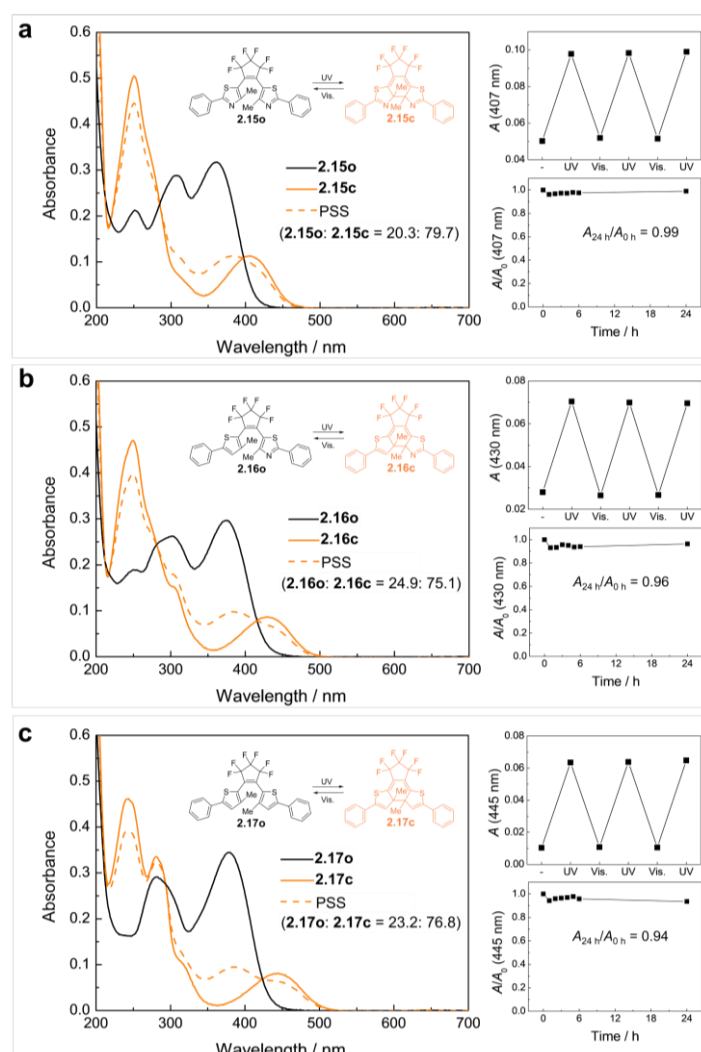
Figure 2.34 Absorption spectra, reversibility and thermal stability of DAEs **2.15** (a), **2.16** (b), and **2.17** (c) in water/ethanol = 3:7 (v/v). The absorption spectra of the open- (solid black line) and closed-ring isomers (solid-colored lines other than black) and the PSS^{UV} (broken line) are shown. In each panel the reversibility (top right) and the thermal stability (low right) are shown. For the reversibility, a sample was alternately irradiated with UV (λ = 365 nm) and visible light ((a): λ > 440 nm, (b) and (c): λ > 480 nm). For the thermal stability, a sample of the closed-ring isomer was kept at 37 °C.

Table 2.17 Concentration at which cytotoxicity is observed without light irradiation (dark toxicity) for the closed-ring isomers of **2.15**, **2.16**, and **2.17**.

	Cytotoxicity in the dark / ppm
2.15c	5
2.16c	5
2.17c	5

Table 2.18 Lower limit concentration (LLC) of open- and closed-ring isomers of **2.15**, **2.16**, and **2.17** for photoinduced cytotoxicity. The lower limit concentration here is defined as the lowest concentration of the investigated compound that exhibited >80% cytotoxicity (cell death/cell shrinkage and rounding) in the irradiated area upon irradiation with blue light ($\lambda = 436$ nm, 4 min). Experiments to evaluate the lower limit concentration were performed up to 5 ppm.

	Lower limit concentration (LLC) / ppm	
	Open-ring	Closed-ring
2.15	> 5	0.05
2.16	> 5	0.05
2.17	> 5	0.05
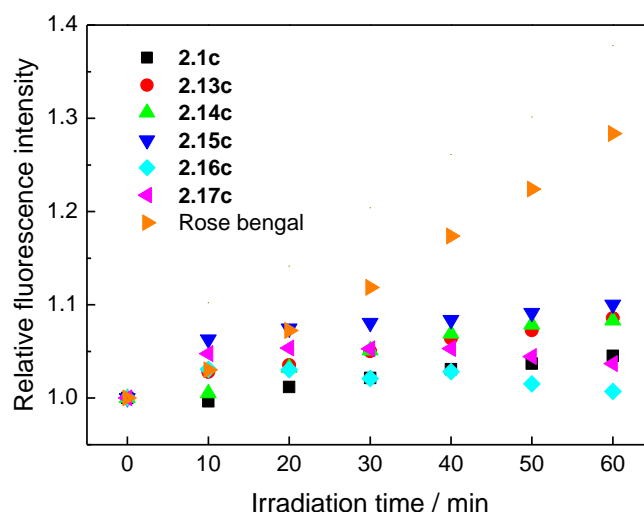
Figure 2.35 Monitoring ROS production by open- and closed-ring isomers of **2.1c**, **2.13**-**2.17** in the presence of DNA in D-PBS/DMSO = 95:5 (v/v) upon blue light ($\lambda = 430$ nm, 20 mW cm^{-2}) irradiation using the ROS sensor, DCFH$_2$ (**2.1c**, **2.13**-**2.17** and RB: 15 μM, DCFH$_2$: 15 μM, DNA: 38.5 nM bp^{-1}, $\lambda_{ex} = 505$ nm, $\lambda_{em} = 525$ nm). The fluorescence intensity increased in proportion to the irradiation time in RB. Note that in the case of DAEs, the fluorescence intensity was comparable to that of **2.14c** which did not show photoinduced cytotoxicity.

2.4 Conclusion

In summary, the photoinduced cytotoxicity of t open- and closed-ring isomers of twelve DAE derivatives with thiazole or pyridine rings in their molecular structures on HeLa cells was investigated. The photocytotoxicity was observed for the relatively planer structured

closed-ring isomers of the DAEs. They are considered to be suitable for the intercalation between base pairs of DNA. Generally, the closed-ring isomers having a thiazole group showed higher photocytotoxicity than the closed ring isomers having a pyridine group. However, the derivative with ionic structure did not have intercalation ability and did not show cytotoxicity, even though it had a nitrogen-containing heterocyclic ring. Furthermore, closed-ring isomers with a molecular size larger than the distance between DNA base pairs or the diameter of the DNA helix did not show photoinduced cytotoxicity. From these results, the common features of the eight DAEs that showed photocytotoxicity are: (1) nitrogen-containing heterocyclic ring (thiazole or pyridine) in the molecular structure, (2) planar structure of DAE, i.e., closed ring isomer, (3) hydrophobicity of the DAE molecule, (4) having fluorinated ring system at the ethene moiety, (5) the molecular size is within the specified range (the thickness and width are each within 6.8 Å and the length is within 20 Å).

By making further efforts to clarify the mechanism of the photoinduced cytotoxicity, we revealed that the overlap of the absorption spectrum of open- and closed-ring isomer for several constructions of DAE in the solution of DNA played an important role for the cell death. HeLa cells administered with open-ring isomer of DAE was killed only when the UV light and the blue light were irradiated in sequence to trigger these two processes. Molecular biological analysis revealed that DNA damage induced in the process was the double-strand break. Also, the complex composed of the DAE having a thiazole ring and DNA showed a red-shift in absorption. In particular, we found that the complex composed of open-ring isomer and DNA, generated by the blue light irradiation to the closed-ring isomer intercalating in the DNA, had an absorbance at 436 nm where open-ring isomer by itself had no absorbance. Therefore, the photocyclization and photocycloreversion reactions of the molecule were considered to be repeated upon irradiation with blue light of 436 nm wavelength as most likely cell-killing mechanism. This unique biological action of light-driven molecular switch in living cell culture suggested novel biological applications such as cell manipulation and photopharmacology.

2.5 References

[1]   N. Kerru, L. Gummidi, S. Maddila, K. K. Gangu, S. B. Jonnakagadda, *Molecules* **2020**, *25*: 1909.

[2]   M. M. Heravi, V. Zadsirjan, *RSC Adv.* **2020**, *10*, 44247–44311.

[3]   C. A. Rabik, M. E. Dolan, *Cancer Treat. Rev.* **2007**, *33*, 9.

[4]   T. van Leeuwen, A. S. Lubbe, P. Štacko, S. J. Wezenberg, B. L. Feringa, *Nat. Rev. Chem.* **2017**, *1*, 0096.

[5]   K. Hüll, J. Morstein, D. Trauner, *Chem. Rev.* **2018**, *118*, 10710–10747.

[6]   M. Irie, T. Fukaminato, K. Matsuda, S. Kobatake, *Chem. Rev.* **2014**, *114*, 12174–12277.

[7]   W. A. Velema, W. Szymanski, B. L. Feringa, *J. Am. Chem. Soc.* **2014**, *136*, 2178–2191.

[8]   B. Roubinet, M. Weber, H. Shojaei, M. Bates, M. L. Bossi, V. N. Belov, M. Irie, S. W. Hell, *J. Am. Chem. Soc.* **2017**, 139, 6611–6620.

[9]   M. Irie, M. Morimoto, *Bull. Chem. Soc. Jpn.* **2018**, *91*, 237–250.

[10]   J. Okuda, Y. Tanaka, R. Kodama, K. Sumaru, K. Morishita, T. Kanamori, S. Yamazoe, K. Hyodo, S. Yamazaki, T. Miyatake, S. Yokojima, S. Nakamura, K. Uchida, *Chem. Commun.* 2015, **51**, 10957–10960.

[11]   R. Kodama, K. Sumaru, K. Morishita, T. Kanamori, K. Hyodo, T. Kamitanaka, M. Morimoto, S. Yokojima, S. Nakamura, K. Uchida, *Chem. Commun.* **2015**, *51*, 1736–1738.

[12]   A. Presa, R. F. Brissos, A. B. Caballero, I. Borilovic, L. Korrodi-Gregório, R. Pérez-Tomás, O. Roubeau, P. Gamez, *Angew. Chem. Int. Ed.* **2015**, *54*, 4561–4565.

[13]   K. Uchida, T. Ishikawa, M. Takeshita, M. Irie, *Tetrahedron* **1998**, *54*, 6627–6638.

[14]   M. Herder, B. M. Schmidt, L. Grubert, M. Pätzel, J. Schwarz, S. Hecht, *J. Am. Chem. Soc.* **2015**, *137*, 2738–2747.

[15]   M. Munakata, J. Han, A. Nabei, T. Kuroda-Sowa, M. Maekawa, Y. Suenaga, N. Gunjima, *Inorg. Chim. Acta* **2006**, *359*, 4281–4288.

[16]   S. C. Wei, M. Pan, Y. Z. Fan, H. Liu, J. Zhang, C. Y. Su, *Chem. Eur. J.* **2015**, *21*, 7418–7427.

[17]   S. L. Gilat, S. H. Kawai, J. M. Lehn, *J. Chem. Soc., Chem. Commun.* **1993**, 1439–1442.

[18]   K. Matsuda, Y. Shinkai, T. Yamaguchi, K. Nomiyama, M. Isayama, M. Irie, *Chem. Lett.* **2003**, *32*, 1178–1179.

[19]   E. Hatano, M. Morimoto, K. Hyodo, N. Yasuda, S. Yokojima, S. Nakamura, K. Uchida, *Chem. Eur. J.* **2016**, *22*, 12680–12683.

[20]   Y. Nakagawa, M. Morimoto, N. Yasuda, K. Hyodo, S. Yokojima, S. Nakamura, K. Uchida, *Chem. Eur. J.* **2019**, *25*, 7874–7880.

[21]   M. Irie, T. Lifka, S. Kobatake, N. Kato, *J. Am. Chem. Soc.* **2000**, *122*, 4871–4876.

[22]   K. Uchida, T. Matsuoka, S. Kobatake, T. Yamaguchi, M. Irie, *Tetrahedron* **2001**, *57*, 4559–4565.

[23] K. Tanaka, Y. Okahata, *J. Am. Chem. Soc.* **1996**, *118*, 10679–10683.

[24] S. Loughrey, B. Matlock, Acclaro protein contaminant ID. Thermo Fisher Scientific Inc. **2017**, DNA.1(2.0)1.8-2, Technical Note.

[25] H. E. Gottlieb, V. Kotlyar, and A. Nudelman, *J. Org. Chem.* **1997**, *62*, 7512–7515.

[26] Gaussian 16, Revision C.01, M. J. Frisch, G. W. Trucks, H. B. Schlegel, G. E. Scuseria, M. A. Robb, J. R. Cheeseman, G. Scalmani, V. Barone, G. A. Petersson, H. Nakatsuji, X. Li, M. Caricato, A. V. Marenich, J. Bloino, B. G. Janesko, R. Gomperts, B. Mennucci, H. P. Hratchian, J. V. Ortiz, A. F. Izmaylov, J. L. Sonnenberg, D. Williams-Young, F. Ding, F. Lipparini, F. Egidi, J. Goings, B. Peng, A. Petrone, T. Henderson, D. Ranasinghe, V. G. Zakrzewski, J. Gao, N. Rega, G. Zheng, W. Liang, M. Hada, M. Ehara, K. Toyota, R. Fukuda, J. Hasegawa, M. Ishida, T. Nakajima, Y. Honda, O. Kitao, H. Nakai, T. Vreven, K. Throssell, J. A. Montgomery, Jr., J. E. Peralta, F. Ogliaro, M. J. Bearpark, J. J. Heyd, E. N. Brothers, K. N. Kudin, V. N. Staroverov, T. A. Keith, R. Kobayashi, J. Normand, K. Raghavachari, A. P. Rendell, J. C. Burant, S. S. Iyengar, J. Tomasi, M. Cossi, J. M. Millam, M. Klene, C. Adamo, R. Cammi, J. W. Ochterski, R. L. Martin, K. Morokuma, O. Farkas, J. B. Foresman, and D. J. Fox, Gaussian, Inc., Wallingford CT, **2016**.

[27] P. Hohenberg, W. Kohn, *Phys. Rev. B* **1964**, *136*, 864–871.

[28] W. Kohn, L. J. Sham, *Phys. Rev.* **1965**, *140*, A1133-A1138.

[29] A. D. Becke, *Phys. Rev. A* **1988**, *38*, 3098–3100.

[30] A.D. Becke, *J. Chem. Phys.* **1993**, *98*, 5648–5652.

[31] C. Lee, W. Yang, R. G. Parr, *Phys. Rev. B* **1988**, *37*, 785–789.

[32] J. D. Chai, M. Head-Gordon, *Phys. Chem. Chem. Phys.* **2008**, *10*, 6615–6620.

[33] J. Tomasi, B. Mennucci, R. Cammi, *Chem. Rev.* **2005**, *105*, 2999–3094.

[34] M. D. Hanwell, D. E. Curtis, D. C. Lonie, T. Vandermeersch, E. Zurek, G. R. Hutchison, *J Cheminform.* **2012**, *4*, 17.

[35] K. Sumaru, K. Kikuchi, T. Takagi, M. Yamaguchi, T. Satoh, K. Morishita, T. Kanamori, *Biotechnol. Bioeng.* **2013**, *110*, 348–352.

[36] K. Sumaru, J. Edahiro, Y. Ooshima, T. Kanamori, T. Shinbo, *Biosens. Bioelectron.* **2007**, *22*, 2356–2359.

[37] K. Sumaru, T. Kanamori, T. *Method in Cell Biology* Vol.120, Micropatterning in Cell Biology, Part B (Matthieu Piel, Manuel The ́ry Ed.), Elsevier, **2014**, pp. 185–197.

[38] K. Kikuchi, K. Sumaru, J. Edahiro, Y. Ooshima, T. Takagi, T. Kanamori, *Biotechnol Bioeng.* **2009**, *103*, 552–561.

[39]   A. Presa, L. Barrios, J. Cirera, L. Korrodi-Gregório, R. Pérez-Tomás, S. J. Teat, P. Gamez, *Inorg. Chem.* **2016**, *55*, 5356-5364.

[40]   K. Kirito, M. Uchida, M. Yamada, Y. Miura, N. Komatsu, *J. Biol. Chem*. **1997**, *272*, 16507–16513.

[41]   H. Nishi, T. Namari, S. Kobatake, *J. Mater. Chem.* **2011**, *21*, 17249–17258.

[42]   L. N. Lucas, J. van Esch, R. M. Kellogg, B. L. Feringa, *Tetrahedron Lett.* **1999**, *40*, 1775–1778.

[43]   F. Sun, F. Zhang, H. Guo, X. Zhou, R. Wang, F. Zhao, *Tetrahedron* **2003**, *59*, 7615–7621.

[44]   S. Takenaka, M. Takagi, J. Tanaka, M. Nishi, H. Kondo, *Nucleic Acids Symp. Ser.* **1997**, *37*, 105-106.

[45]   S. Purser, P. R. Moore, S. Swallow, V. Gouverneur, *Chem. Soc. Rev.* **2008**, *37*, 320–330.

[46]   P. Shah, A. D. Westwell, *J. Enzyme Inhib. Med. Chem.* **2007**, *5*, 527–540.

[47]   V. Korpelainen, V. Linko, J. Seppa, A. Lassila, M. A. Kostiainen, *Meas. Sci. Technol.*, **2017**, *28*, 34001–34006.

[48]   H. M. Berman, P. R. Young, *Annu. Rev. Biophys. Bioeng.* **1981**, 10, 87–114.

[49]   S. Biebricher, I. Heller, R. F. H. Roijmans, T. P. Hoekstra, E. J. G. Peterman, G. J. L. Wuite, *Nat. Commun.* **2015**, *6*: 7304.

[50]   Y. Nakagawa, T. Hishida, E. Hatano, K. Sumaru, K. Morishita, M. Morimoto, S. Yokojima, S. Nakamura, K. Uchida, *Org. Biomol. Chem.* **2022**, *20*, 3211–3217.

[51]   D. J. McConkey, *Toxicol Lett.* **1998**, *99*, 157–168.

[52]   J. H. Zhang, M. Xu, *Cell Res.* **2000**, *10*, 205–211.

[53]   F. J. Meyer-Almes, D. Porschke, *Biochemistry* **1993**, *32*, 4246–4253.

[54]   B. Wang, Z. Li, C. Wang, M. Chen, J. Xiao, X. Wu, W. Xiao, *PLOS ONE* **2013**, *8*, e73987.

[55]   A. Growth, J. Lukas, E. A. Nigg, H. H. E. Silljé, C. Wernstedt, J. Bartek, K. Hansen, *EMBO J.* **2003**, *22*, 1676–1687.

[56]   S. Matt, T. G. Hofmann, *Cell. Mol. Life Sci.* **2016**, *73*, 2829–2850.

[57]   Y. Sun, S. Bi, D. Song, C. Qiao, D. Mu, H. Zhang, *Sens. Actuators B Chem.* **2008**, *129*, 799–810.

[58]   S. Elmore, *Toxicol. Pathol.* **2007**, *35*, 495–516.

[59]   C. B. Bennett, A. L. Lewis, K. K. Baldwin, M. A. Resnick, *Proc. Natl. Acad. Sci. USA* **1993**, *90*, 5613–5617.

[60]   C. B. Bennett, T. J. Westmoreland, J. R. Snipe, M. A. Rednick, *Mol. Cell. Biol.* **1996**, *16*, 4414–4425.

[61] S. H. Moon, T. A. Nguyen, Y. Darlington, X. Lu, L. A. Donehower, *Cell Cycle* **2010**, *9*, 2092–2096.

[62] S. Burma, B. P. Chen, M. Murphy, A. Kurimasa, D. J. Chen, *J. Biol. Chem.* **2001**, *276*, 42462–42467.

[63] Z. N. Oltvai, C. L. Milliman, S. J. Korsmeyer, *Cell* **1993**, *74*, 609–619.

[64] H. Kim, H. C. Tu, D. Ren, O. Takeuchi, J. R. Jeffers, G. P. Zambetti, J. J. D. Hsieh, E. H. Y. Cheng, *Mol. Cell* **2009**, *36*, 487–499.

[65] S. M. V. de Almeida, E. A. Lafayette, L. P. B. G. da Silva, C. A. C. Amorim, T. B. de Oliveira, A. L. T. Gois Ruiz, J. E. de Carvalho, R. O. de Moura, E. I. C. Beltrao, M. C. A. de Lima, L. B. de Carvalho Jr., *Int. J. Mol. Sci.* **2015**, *16*, 13023–13042.

[66] J. Kypr, I. Kejnovská, D. Renčiuk, M. Vorlíčková, *Nucleic Acids Res.* **2009**, *37*, 1713–1725.

[67] A. I. S. Holm, L. M. Nielsen, S. V. Hoffmann, S. B. Nielsen, *Phys. Chem. Chem. Phys.* **2010**, *12*, 9581–9596.

[68] M. Heydari, M. E. Moghadam, A. Tarlani, H. Farhangian, *Appl. Biochem. Biotechnol.* **2017**, *182*, 110–127.

[69] G. R. Bishop, J. B. Chaires, *Curr. Protoc. Nucleic Acid Chem.* **2002**, *11*, 7.11.1–7.11.8.

Chapter 3

Photomechanical behavior of diarylethene crystals and their manipulation by light

3.1 Introduction

Photomechanical materials of molecular crystal can convert light energy directly into mechanical action.[1-3] Photomechanical behavior is attributed to changes in the microscopic size of the molecular structure induced by light irradiation. That is, it is brought about by the internal strain induced by the simultaneous presence of both reactant and product domains. The dynamic processes of molecular crystals are either deformation (e.g., bending,[4-11] curling,[12] and twisting[13,14]) which preserves the integrity of the crystal, or disintegration (e.g., cracks,[15-17] peels,[9,15,18-20] splits,[15,21] and explosions[21-23]). The difference between deformation (which preserves the integrity of the crystal) and disintegration is whether the mechanical energy generated by the change in molecular structure can be consumed as a shape change without damaging the crystal, or whether the crystal breaks because it cannot be consumed. Therefore, photosalient phenomena, including crystal disintegration, are affected by the magnitude of lattice axes changes caused by molecular structural changes and the intensity of incident light.[15] Photoinduced crystal deformation has been reported for use in electrical circuit photoswitches,[24] lifting and lowering of objects,[25] and object transport.[26] Photoinduced crystal disintegration, termed the "photosalient effect," has been applied to release the inclusions in hollow crystals and crystalline capsules.[27,28]

Of these photomechanical behaviors, bending behavior is the most common. Photoinduced bending is often observed in elongated crystals. This behavior is affected by the thickness of the crystal,[8,29-31] aspect ratio,[8,32] and rate of forward and reverse reactions[33] as intrinsic factors. The temperature,[33] exposure time,[4,15,25,31] irradiation wavelength,[34] polarization,[35] and irradiation power[36] are also external factors. Such behavior can be applied to artificial muscles[37] and soft robots.[38] However, the preparation of crystals appropriate for bending behavior is difficult due to the complexity of molecular structure, preparation conditions, and other factors. To solve this problem, the fabrication of thin crystals using the photoinduced peeling phenomenon has been reported.[18-20] There are two approaches to using the photoinduced peeling phenomenon to fabricate thin crystals.[18] One is to find molecular crystals that exhibit peeling behavior. The other is to control the way of crystals crack by external factors such as light irradiation conditions. In particular, the latter approach has potential application to a wide variety of

materials and the ability to control photomechanical behaviors, including peeling behavior.

In this chapter, we describe the two contents. The first one is the photosalient effect of diarylethene crystals using three derivatives having thiazole and/or thiophene rings in the molecule, focusing on the effects of crystal size and UV intensity. In the course of the study, it was found that DAE thin crystals having thiazole and thiophene rings in the molecule can switch between photoinduced bending and photosalient phenomena depending on the irradiation power (810 μw cm^{-2} or 277 mW cm^{-2}) of UV light ($\lambda = 365$ nm). In the second, we report a molecular crystalline material that effectively induces peeling phenomena through multi-step irradiation using two UV light sources with different irradiation powers and visible light. Bending and reverting by alternate irradiation with weak UV and visible light produced a strained layer on the crystal surface, and subsequent strong UV light irradiation from the crystal's backside induced a high probability of surface peeling.

3.2 Experimental

3.2.1 Materials

All commercial reagents were used as received unless otherwise stated. Diarylethenes **3.1o**[39] and **3.2o**[40] were synthesized according to the procedure described in the literature.

3.2.2 General information

^{1}H (400 MHz), ^{13}C (100 MHz), and ^{19}F NMR (376.32 MHz) spectra were recorded at 25 °C on an JEOL JNM-400 spectrometer. Chemical shifts are given in parts per million (ppm) using the residual solvent peak(s) as a reference.[41] Multiplicities of the signals are described as follows: s = singlet, d = doublet, t = triplet, q = quartet, m = multiplet or overlap of nonequivalent resonances. J values are expressed in Hz. The NMR spectra of DAEs and the precursor compounds were recorded in CDCl$_3$. Melting points were measured on Yanaco MP-500D. Absorption spectra of the solutions were monitored on Hitachi U-4150 spectrophotometer. Perkin Elmer DSC8500 was used for DSC measurement with rate of elevating temperate of 10°C / min. For monitoring the surface temperature of the crystals under UV irradiation, thermograph testo 882 was used. KEYENCE VHX-500, VH-S30, VH-Z20, VH-S1, VH-Z450 were used to monitor the photomechanical behavior. For the UV light irradaition, KEYENCE UV-400, UV-50H (λ = 365 nm), AS ONE Handy UV Lamp LUV-6 (λ = 365 nm), and a UV hand lamps SPECTROLINE Model EB-280C/J (λ = 313 nm) were used. For the visible light irradiation, observation light from the digital microscopes of a KEYENCE VH-S30, 500W USHIO SX-UI501XQ Xenon lamp attached with Toshiba color filters (Y-50, Y-48, Y-44,

UV-29 or Y-44, UV-29), and a HAYASHI-REPIC LUMINAR ACE Model LA-HDF108AA attached with NPI PLG-1-500V-6, PCL-21, and PYF-22.5 were used. Determination of the quantum yields of the photochromic isomerization reactions were performed in a homemade setup. Irradiation was performed in 1 cm path quartz cuvettes under continuous stirring, using Mercury lamp (500 W USHIO optical module H500) at 365 ± 4 nm and Xenon lamp (500W USHIO SX-UI501XQ) at 470 ± 12 nm (Thorlabs) as irradiation sources. The intensities of the irradiation light were estimated comparing the photochromic reactions of DAEs as standards. Crystal sizes were calculated from photographs taken using ImageJ software[42].

All chemicals were used without further purification. Kanto Chemical spherical silica gels (63-210 μm and 40-50 μm) were used for column chromatography.

3.2.3 X-ray crystallographic analysis

X-ray crystallographic analysis for bulk crystals of **3.1o**, **3.2o**, and **3.3o**, each crystal irradiated with $\lambda = 400$ nm light for 1 min (EXFO OmniCure LX400) and for visible light (ASASHI SPEXTRA MAX-302 attached with ASAHI Techno House color glass filter Y-46) for 16 h, and **3.3c** were performed with an X-ray diffractometer (Bruker AXS, D8 QUEST) with Mo Kα radiation ($\lambda = 0.71073$ Å). The crystals were cooled using a low temperature controller (Japan Thermal Engineering, JAN 2-12). The diffraction frames were integrated with the Bruker SAINT program. The cell constants were determined by the global refinement. The data were corrected for absorption effects using the multi-scan method (SADABS). The structure was solved by the direct method and refined by the full-matrix least-squares method using the SHELX-2014 program. The positions of all hydrogen atoms were calculated geometrically and refined by the riding model. The crystallographic data can be obtained free of charge from The Cambridge Crystallographic Data Center via www.ccdc.cam.ac.uk/data_request/cif. (CCDC 1870382-1870388, 2205431).

X-ray crystallographic analysis for thin crystal of **3.3o** was carried out at BL40XU beamline of SPring-8. Si(111) channel cut monochromator was used and the wavelength and the size of X-ray beam were 0.81128 Å and 75×75 μm (square), respectively. The diffraction data was collected by oscillation method using EIGER detector at 173 K. The data were corrected for absorption effects by multi-scan method with ABSCOR.[43] The structure was solved by the direct method and refined by the full-matrix least-squares method using the SHELX-2014/7 program. The positions of all hydrogen atoms were calculated geometrically and refined by the riding model. The crystallographic data can be obtained free of charge from The Cambridge Crystallographic Data Center via

3.2.4 Synthesis

A derivative **3.3o** was already prepared by Y. Ushiogi et al. They used a microflow system for the synthesis.[44] We prepared **3.3o** by ordinary synthetic method as described below. Synthetic route of **3.3o** was shown in Scheme 3.1.
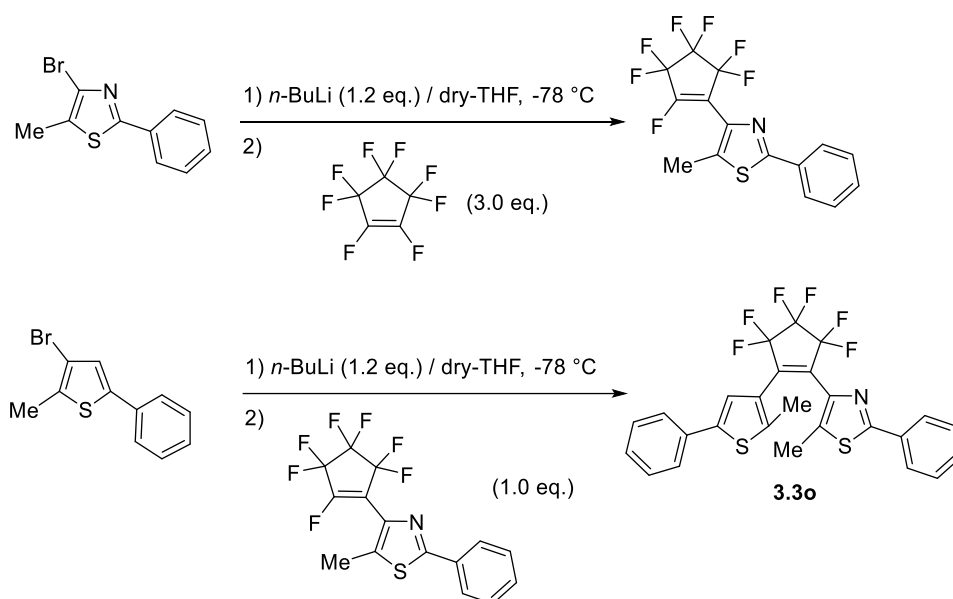
Scheme 3.1 Synthesis of and 1-(2-methyl-5-phenylthien-3-yl)-2-(5-methyl-2-phenylthiazol-4-yl)perfluorocyclopentene (**3.3o**).

4-(2,3,3,4,4,5,5-Heptafluorocyclopentenyl)-5-methyl-2-phenylthiazole[39]

To a 100 mL three necked flask containing 3.46 g (13.61 mmol) of 4-bromo-5-methyl-2-phenylthiazole[39] in 60 mL of THF anhydrous on the dry ice- methanol bath at -78°C in an argon gas atmosphere, 10.21 mL (16.34 mmol, 1.2 eq.) of 1.6 N *n*-BuLi hexane solution was gradually added in keeping the temperature and stirred for 1 h at the temperature. Then the 3.46 mL (40.83 mmol, 3.0 eq.) of perfluorocyclopentene was gradually added, followed by stirring another 30 min, then the temperature of the reaction mixture was allowed to warm to -40°C. Then the mixture was stirred for 4 h at the temperature. After reaction was over, 30 mL of water was added, and the mixture was allowed to warm to room temperature. Solvent of THF was evaporated in vacuo, then 300 mL of water was added. The mixture was extracted with 50 mL of diethyl ether with four times. The combined ether solution was washed with 300 mL of water, followed by washing with 50 mL of brine twice, and dehydrated over sodium sulfate anhydrous. After removal of

sodium sulfate by filtration, the solvents were removed in vacuo. And the obtained residue was purified by silica gel chromatography using a mixture of hexane and chloroform (97/3 v/v) as eluent, to obtain 4.17 g (11.35 mmol) of 4-(2,3,3,4,4,5,5-heptafluorocyclopentenyl)-5-methyl-2-phenylthiazole as pale-yellow crystals in 83% yield.

m.p. 72.8-73.8°C. ^{1}H NMR (400 MHz, CDCl$_3$, ppm) δ 7.93-7.89 (m, 2H), 7.46-7.43 (m, 3H), 2.54 (d, J=2.9 Hz, 3H). ^{13}C NMR (100 MHz, CDCl$_3$, ppm) δ 166.3, 138.9, 135.9, 132.8, 130.7, 129.2, 126.6, 12.4. ^{19}F NMR (376.32 MHz, CDCl$_3$, ppm) δ -111.4 (d, J = 11.5 Hz, 2F), -121.6 (d, J = 15.9 Hz, 2F), -128.1 (br s, 1F), -133.4 (s, 2F).

1-(2-Methyl-5-phenylthien-3-yl)-2-(5-methyl-2-phenylthiazol-4-yl)perfluorocyclopentene (3.3o)

To a 100 mL three necked flask containing 1.38 g (5.45 mmol) of 3-bromo-2-methyl-5-phenylthiophene[40] in 35 mL of THF anhydrous with cooling at -78°C on the dry ice-methanol bath in an argon gas atmosphere, 4.10 mL (6.54 mmol, 1.2 eq.) of 1.6 N n-BuLi hexane solution was gradually added in keeping the temperature and stirred for 1 h at the temperature. To the mixture, THF anhydrous solution containing 2.00 g (5.45 mmol, 1.0 eq.) of 4-(2,3,3,4,4,5,5-heptafluorocyclopentenyl)-5-methyl-2-phenylthiazole was added, and stirred for 30 min at the temperature. Then the mixture was allowed to warm to -40°C, then the solution was stirred another 5 h at the temperature. After reaction was over, 30 mL of water was added, and the mixture was allowed to warm to room temperature. Solvent of THF was evaporated in vacuo, then 100 mL of water was added. The mixture was extracted with 30 mL of diethyl ether with four times. The combined ether solution was washed with 100 mL of water, followed by washing with 50 mL of brine twice, and dehydrated over sodium sulfate anhydrous. After removal of sodium sulfate by filtration, the solvents were removed in vacuo. And the obtained residue was purified by silica gel chromatography using a mixture of hexane and diethyl ether (97/3 v/v) as eluent, to obtain 1.95 g (3.74 mmol) of **3.3o** as white crystals in 54% yield.

m.p. 132.0-132.8°C. ^{1}H NMR (400 MHz, CDCl$_3$, ppm) δ 7.88-7.86 (m, 2H), 7.55 (d, J= 7.8 Hz, 2H), 7.43-7.41 (m, 3H), 7.39 (dd, J= 7.8, 7.4 Hz, 2H) 7.30 (t, J= 7.4 Hz, 2H), 2.04 (s, 3H), 2.00 (s, 3H). ^{13}C NMR (100 MHz, CDCl$_3$, ppm) δ 165.9, 142.4, 141.6, 140.5, 137.0, 133.5, 133.1, 130.5, 129.2, 129.1, 128.1, 126.6, 126.0, 125.7, 122.7, 14.5, 12.4. ^{19}F NMR (376.32 MHz, CDCl$_3$, ppm) δ -135.2 (s, 2F), -113.8 (s, 2F), -113.3 (s, 2F).

3.2.5 Preparation of crystals

The crystals used for the observation of photomechanical behavior were prepared by recrystallization from the hexane solutions or sublimation.

3.2.6 Temperature dependence of photosalient effect

To clarify the relationship between photosalient effect and observed temperatures, the temperature of the crystals was monitored by thermography before and during irradiation with UV light ($\lambda = 365$ nm, 277 mW cm^{-2}) at room temperature and under cooling around 4°C. Monitoring setup under each condition was shown in Figure 3.1. DSC measurement was carried out in order to confirm whether there was a phase transition in that 3-28°C range.
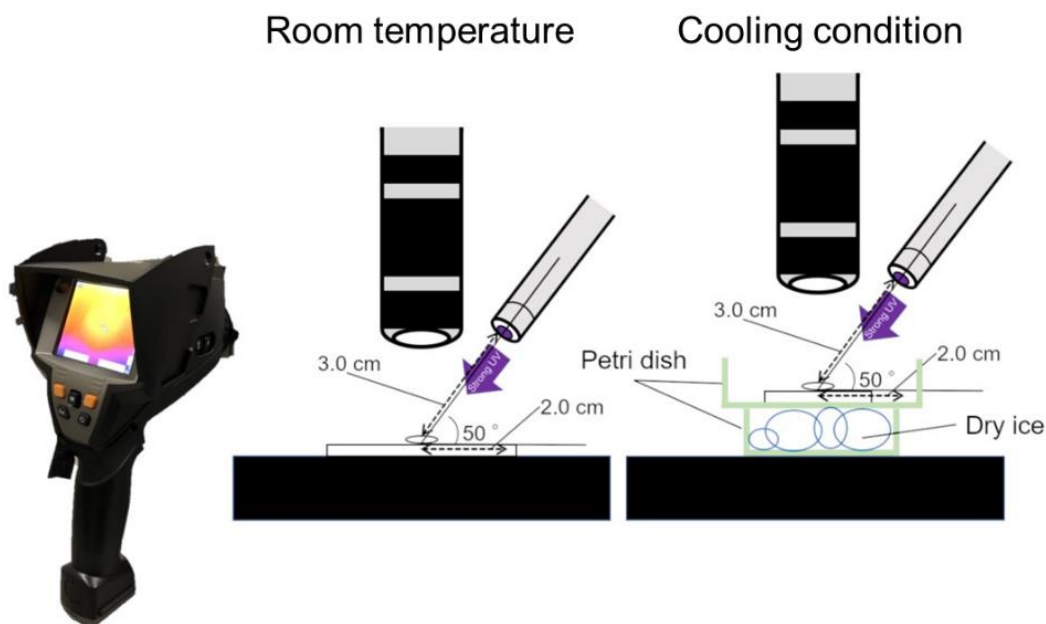
Figure 3.1 Schematic illustration the monitoring by thermography under UV irradiation.

3.3 Results and Discussions

3.3.1 Photosalient effect of diarylethene crystals of thiazoyl and thienyl derivatives

Here, DAEs **3.1**, **3.2**, and **3.3** were used (Scheme 3.2). Although, synthesis of **3.3** was carried out by a microflow system, the photochromic properties were not considered in that earlier work.[44] We first investigated the absorption spectral changes of **3.3** in hexane solution (Figure 3.2). Open-ring isomer **3.3o** has an absorption band at 295 nm in hexane. Upon UV irradiation, the colour of the solution turned purple and a new band appeared at 550 nm, which is attributed to **3.3c**. Upon visible light irradiation, the colour disappeared and the band of **3.3o** was regenerated. Absorption coefficients and quantum yields are summarized in Table 3.1, together with those of **3.1** and **3.2**. The absorption maxima of open- and closed-ring isomers and the quantum yields of photochromic reactions (cyclization ($\Phi_{o \to c}$) and cycloreversion ($\Phi_{c \to o}$)) closely approximate the values averaged between the corresponding symmetric derivatives **3.1** and **3.2**.
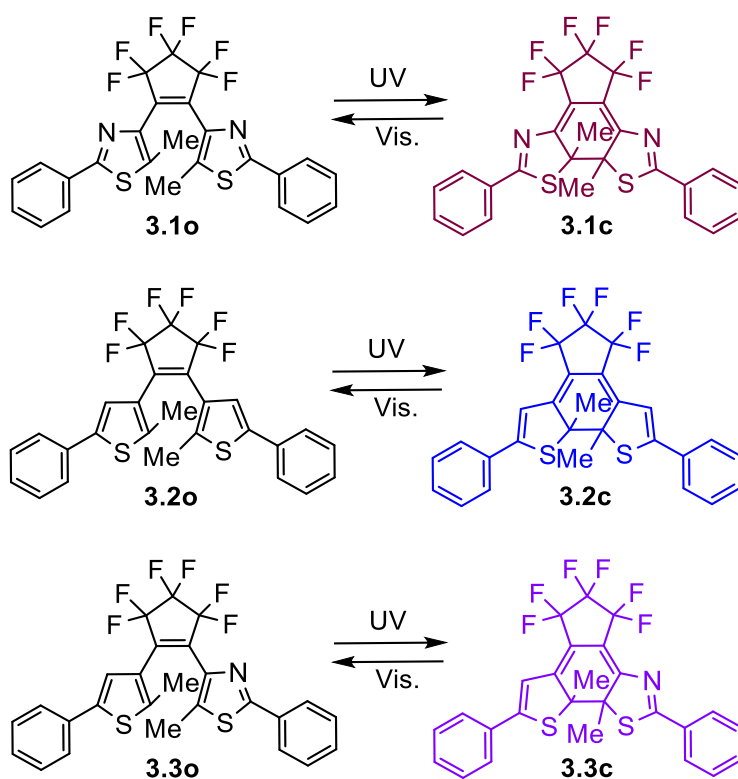
Scheme 3.2 Molecular structures of DAEs **3.1**, **3.2**, and **3.3**.
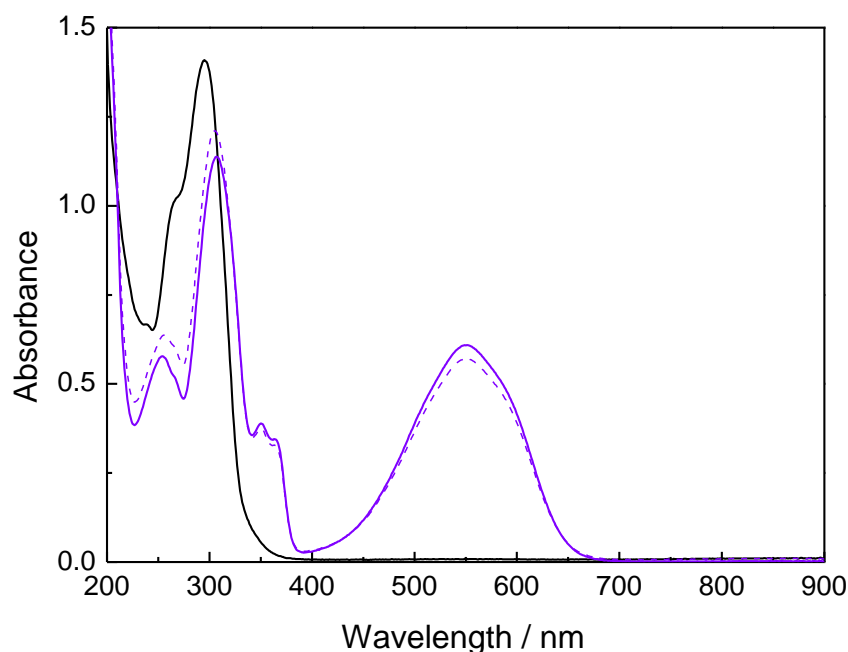
Figure 3.2 Absorption spectral changes of **3.3** in hexane solution. **3.3o**: solid black line, **3.3c**: solid violet line, photostationary state (**3.3o**: **3.3c** = 6.2: 93.8) upon 313 nm light irradiation: broken violet line.

Table 3.1 Photochromic properties of DAEs **3.1**, **3.2**, and **3.3** in hexane solution.

	λ_{max} / nm (ε / 10^4 M^{-1} cm^{-1})		$\Phi_{o \to c}$ (313 nm)	$\Phi_{c \to o}$ (492 nm)
	Open-ring	Closed-ring		
3.1[39]	280 (3.6)	525 (1.0)	0.32	0.020
3.2[40]	280 (3.6)	575 (1.6)	0.59	0.013
3.3	295 (3.5)	550 (1.5)	0.25	0.013

This has often been observed in other asymmetric DAEs.[44,45] The photochromism of **3.1o** and **3.2o** in crystalline states has already been reported. A single crystal of newly prepared **3.3o** also showed photochromism upon alternate irradiation with UV and visible lights. Upon UV irradiation at weak intensity (λ = 365 nm, 810 μW cm^{-2}) for 30 min, crystals of **3.1o** and **3.2o** showed coloration without any photosalient phenomenon (Figure 3.3a-d). These results are consistent with previous reports.[39,40] Upon irradiation by the same weak intensity of UV light (λ = 365 nm, 810 μW cm^{-2}), the crystal **3.3o** displayed both coloration and photosalient phenomena when irradiation was prolonged (80 s) (Figure 3.3e and f).
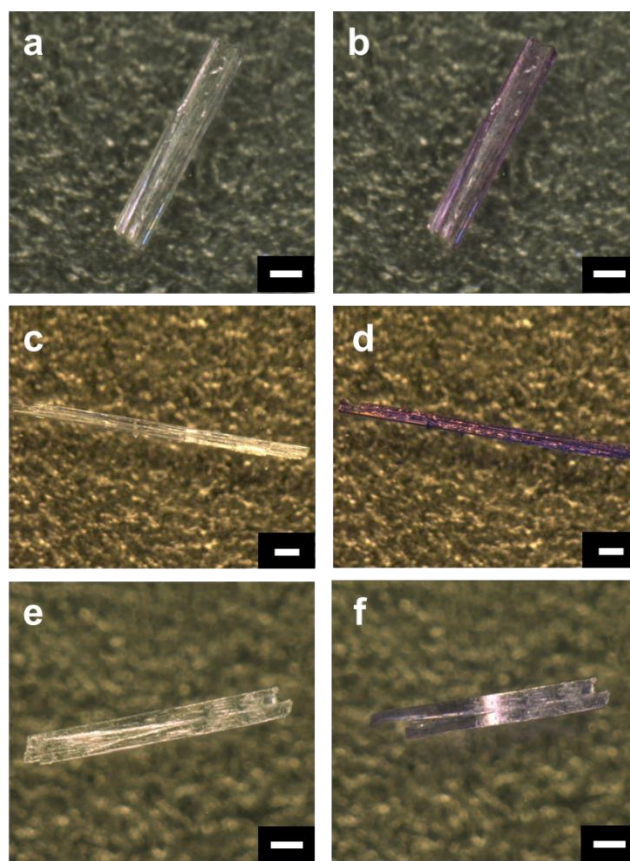
Figure 3.3 Photochromism of single crystals of DAEs **3.1o**: (a) and (b), **3.2o**: (c) and (d), and **3.3o**: (e) and (f). Before UV irradiation: (a, c, e) and after UV irradiation: (b, d, f). Scale bars: 200 μm for (a, b, e, f), and 100 μm for (c, d).

Upon strong UV irradiation ($\lambda = 365$ nm, 277 mW cm^{-2}) to the crystals prepared by recrystallization from hexane solutions, all crystals of **3.1o**, **3.2o**, and **3.3o** showed remarkable photosalient phenomena on their surfaces accompanied with coloration (Figures 3.4-3.7). A schematic illustration showing the differences is also given in Figure 3.7g-i. To compare the crystals' reactivity and deformation, we conducted X-ray analysis of these crystals of open- and closed-ring isomers upon 400-nm light irradiation for 1 min under the same conditions (results summarized in Table 3.2). Graphical images of the deformations for each crystal are depicted in Figure 3.8.
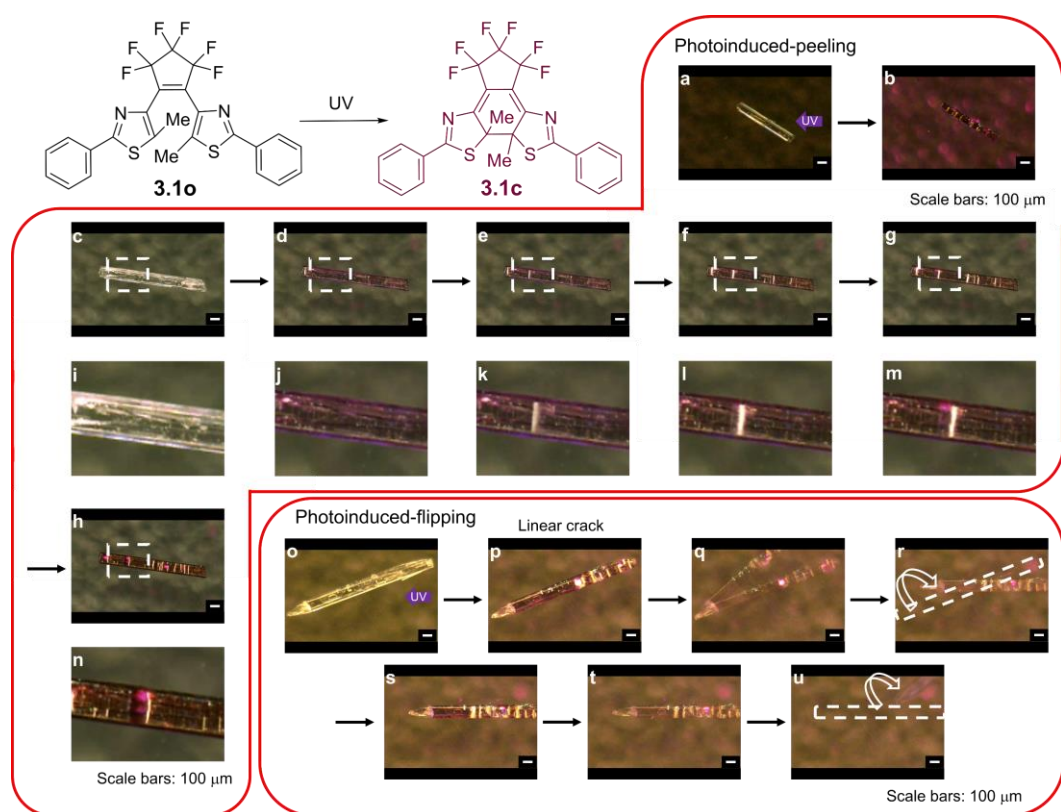
Figure 3.4 Photosalient effect of crystals of **3.1o** (λ = 365 nm, 277 mW cm^{-2}). (a, b) and (c-h): photoinduced-peeling. (o-u): photoinduced-flipping. (i-n) are magnified images of dotted squares in (c-h), respectively.
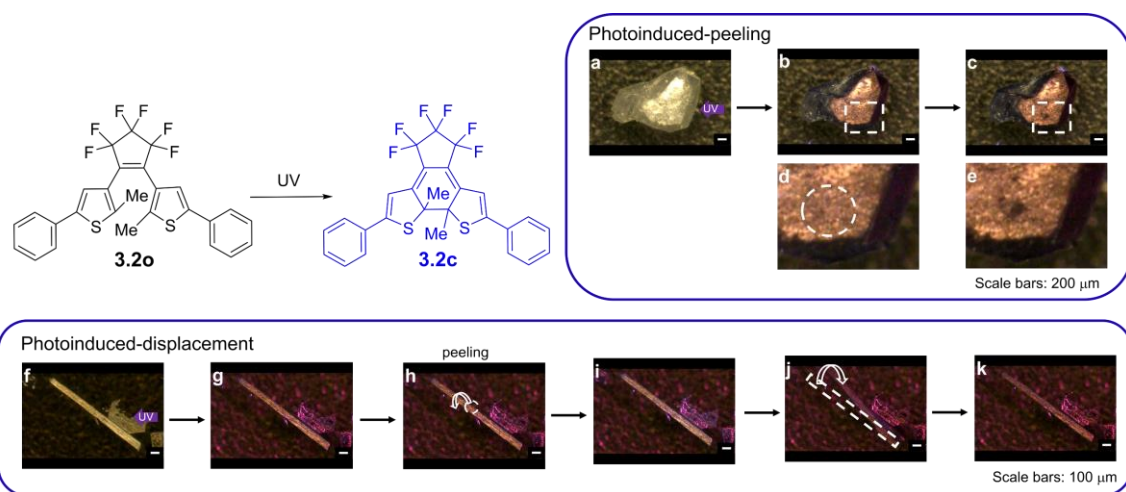
Figure 3.5 Photosalient effect of crystals of **3.2o** (λ = 365 nm, 277 mW cm^{-2}). (a-c): photoinduced-peeling. (f-k): photoinduced-displacement. (d): magnified image of dotted circle part of (b), (e): expanded image of dotted circle part of (c).
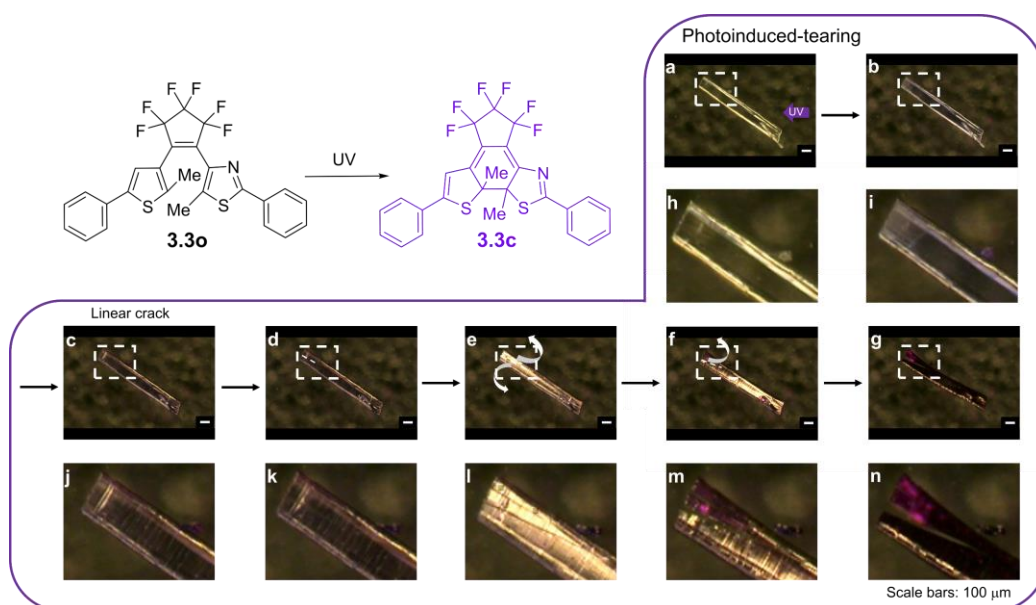
Figure 3.6 Photosalient effect of crystals of **3.3o** ($\lambda = 365$ nm, 277 mW cm^{-2}). (a-g): photoinduced-tearing. (h-n) are magnified images of dotted squares in (a-g), respectively. Progress of tearing was observed during UV irradiation.
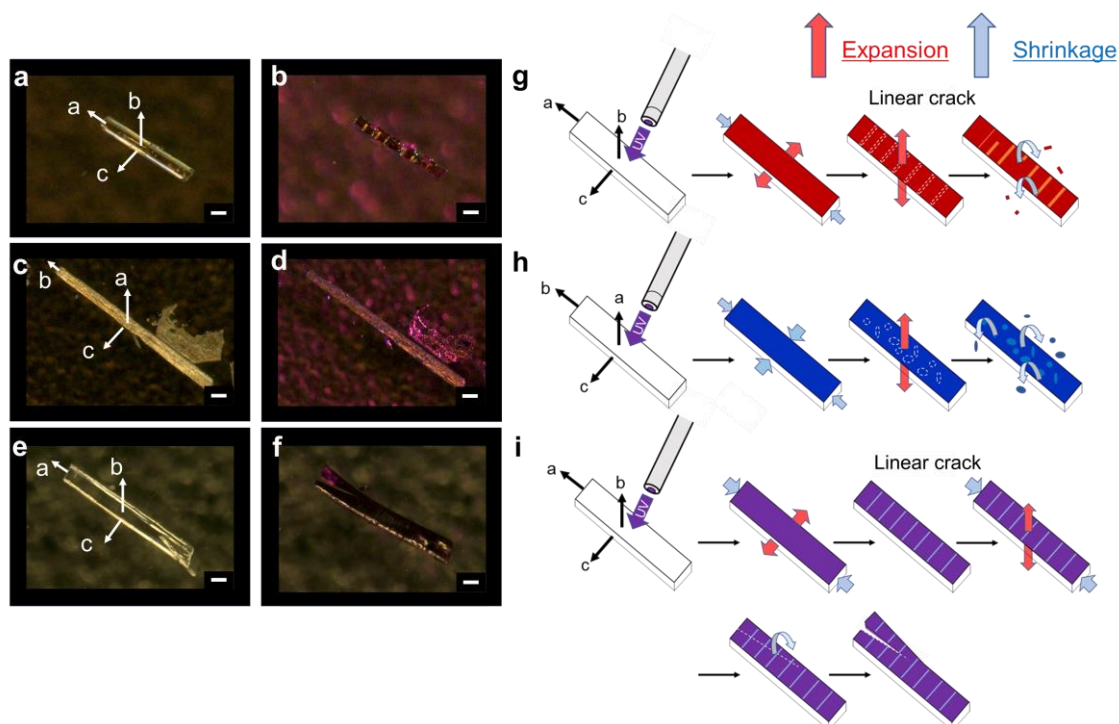
Figure 3.7 Photosalient effect of single crystals of **3.1o**: (a) and (b), **3.2o**: (c) and (d), and **3.3o**: (e) and (f). Before UV irradiation ($\lambda = 365$ nm, 277 mW cm^{-2}): (a), (c) and (e) and after UV irradiation: (b), (d) and (f). Scale bars: 100 μm. Schematic illustration of the differences in photosalient phenomena of **3.1o**: (g), **3.2o**: (h), and **3.3o**: (i).

Table 3.2 Crystal data of open- (**o**) and closed-ring (**c**) isomers of **3.1**, **3.2**, and **3.3**, and crystals upon 400 nm light irradiation with same conditions (light intensity and periods).

	3.1o	**3.1o** after 400 nm light irradiation for 1 min	**3.1c**[4]	**3.2o**	**3.2o** after 400 nm light irradiation for 1 min	**3.2c**[40]	**3.3o**	**3.3o** after 400 nm light irradiation for 1 min	**3.3c**
formula	$C_{25}H_{16}F_6N_2S_2$		$C_{25}H_{16}F_6N_2S_2$	$C_{27}H_{18}F_6S_2$	$C_{27}H_{18}F_6S_2$	$C_{27}H_{18}F_6S_2$	$C_{26}H_{17}F_6NS_2$	$C_{26}H_{17}F_6NS_2$	$C_{26}H_{17}F_6NS_2$
formula weight	522.53	522.53	522.53	520.53	520.53	520.53	521.53	521.53	521.53
T / K	93(2)	93(2)	123(2)	93(2)	93(2)	296(2)	93(2)	93(2)	93(2)
crystal system	monoclinic	monoclinic	monoclinic	monoclinic	monoclinic	triclinic	monoclinic	monoclinic	monoclinic
space group	$P2_1/c$	$P2_1/c$	$P2_1/c$	$P2_1/c$	$P2_1/c$	$P\bar{1}$	$P2_1/c$	$P2_1/c$	$P2_1/n$
a / Å	7.2354(2)	7.1991(2) -0.50%	11.8283(2)	18.6604(6)	18.7362(12) +0.41%	11.770(4)	7.3573(2)	7.3035(5) -0.73%	11.7799(5)
b / Å	25.7171(11)	25.8444(11) +0.50%	18.2383(2)	11.7935(3)	11.7650(8) -0.24%	12.023(5)	25.7066(10)	25.9350(16) +0.89%	18.4174(8)
c / Å	12.6083(5)	12.6318(5) +0.19%	11.8745(2)	21.3133(7)	21.3057(14) -0.04%	9.626(3)	12.5981(5)	12.6145(8) +0.13%	12.0279(5)
α / °	90	90	90	90	90	94.45(3)	90	90	90
β / °	102.3200(13)	102.2601(13) -0.06%	118.5760(1)	95.7023(11)	94.9043(19) -0.83%	95.89(3)	102.4150(12)	102.238(2) -0.17%	118.8479(19)
γ / °	90	90	90	90	90	60.07(3)	90	90	90
V / Å³	2292.04(15)	2296.63(15) +0.20%	2249.61(6)	4667.2(2)	4679.3(5) +0.26%	1173.7(7)	2326.98(14)	2335.1(3) +0.35%	2285.68(17)
Z	4	4	4	8	8	2	4	4	4
(V/Z) / Å³	573.01	574.16	562.40	583.40	584.91	586.85	581.75	583.78	571.42
R_1 ($I > 2\sigma(I)$)	0.0322	0.0393	0.068	0.0377	0.0690	0.0504	0.0482	0.0561	0.0483
wR_2 ($I > 2\sigma(I)$)	0.0713	0.0893	0.207	0.0899	0.1491	0.1263	0.1252	0.1437	0.1409
R_1 (all data)	0.0408	0.0516	0.08	0.0563	0.1356	0.0905	0.054	0.0724	0.0619
wR_2 (all data)	0.0760	0.095	0.219	0.0990	0.1756	0.1538	0.1298	0.1552	0.1643
CCDC No.	1870382	1870383	622801	1870388	1870384	—	1870385	1870387	1870386

103
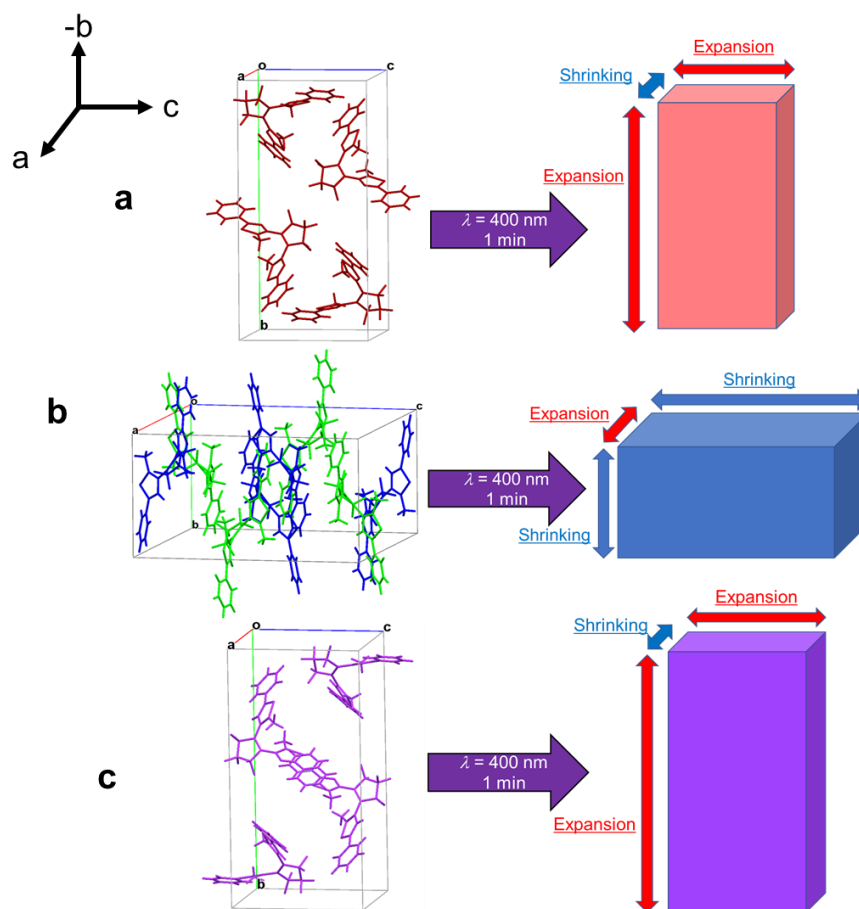
Figure 3.8 Crystal lattice fluctuation of **3.1o** (a), **3.2o** (b), and **3.3o** (c) upon 400-nm light irradiation.

Under UV irradiation (λ = 365 nm, 277 mW cm^{-2}), cracks appeared on the surface of **3.1o** crystals perpendicular to the long axis, followed by the crystal surface being cast off. Moreover, flipping[21] of the peeled[9] crystalline surface was also observed (Figures 3.4, 3.7a and b). This is due to shrinkage of 0.50% along the *a*-axis, which is parallel to the crystal's long axis (Figure 3.8a and Table 3.2). When the crystals are thin, the crystal showed reversible shrinkage and elongation by alternate irradiation with UV and visible light. When the aspect ratio of **3.1o** crystal is high, the crystal showed bending concave to the incidence of UV light.[4] In our case, the crystal is thick enough not to bend, and only the surface was photo-converted to **3.1c** and shrank along the long axis of the crystal (*a*-axis). Then cracks were generated perpendicular to the *a*-axis. Each fragmented crystal showed bending and dispersion on the surface (Figure 3.7g). At the same time, flipping of the crystals was also observed (Figure 3.4).

For the crystals of **3.2o**, cracks in the vertical and horizontal directions appeared on the

surface. Upon UV irradiation ($\lambda = 365$ nm, 277 mW cm^{-2}), the crystalline surface collapsed (Figures 3.5, 3.7c and d). DAE **3.2o** also changed its molecular size in the crystal, and ribbon shaped crystals have been reported to show complicated helical deformation, depending on the direction of the incident light.[13] This is due to the herringbone orientation of **3.2o** molecules in the crystals, where two conformers exist in a unit cell. The size changes of the unit cell of **3.2o** were the smallest among those of the three derivatives, so only a modest photosalient phenomenon was observed for **3.2o**. Nevertheless, it is significant that small-fragment scattering was observed on the surface during UV irradiation (Figure 3.7h). The cracking pattern may be attributed to the release of photo-induced shrinkage of the *a*- and *c*-axes (indicating shrinkage of the crystal's surface area) with the expansion caused by elongation of the *a*-axis (vertical direction of the surface). The direction of photoinduced size changes is different from those found in other crystals (Figure 3.8b and Table 3.2). Therefore, cracking perpendicular to the long axis of the crystal such as **3.1o** was not observed for **3.2o**; instead, irregular breakage of the crystal surface was observed. From the recrystallization of **3.2o** in a hexane solution, not only rod-shaped but also cubic-shaped crystals were obtained. In spite of the difference in the crystal habit, both types of crystals have the same crystal structures. Peeling phenomena were observed for both of them (Figure 3.9).
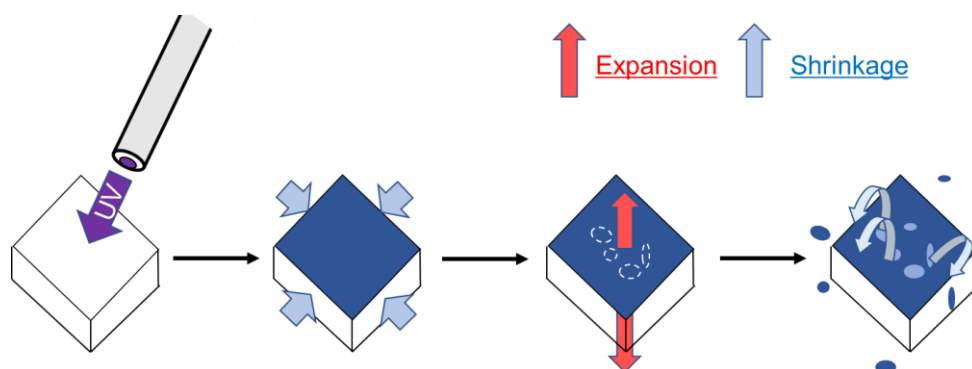
Figure 3.9 Schematic illustration of the photosalient phenomena of cubic shaped **3.2o** crystal.

Upon UV irradiation to the single crystal of **3.3o**, a drastic collapse of the crystal surface was observed. Small cracks were initially generated perpendicular to the long axis on the surface, then drastically larger cracks were generated along the long axis and the whole crystal was scattered (Figure 3.7e, f and i). The initial cracks on the surface are attributed to the shrinkage of the *a*-axis of the unit cell, and as a result only cracks appeared while no breaking of the crystal followed in this direction. On the other hand, the *b*-axis of the

unit cell expanded at the maximum ratio in these crystals (Table 3.2). The direction corresponds to the increase in the widths of **3.3o** crystals. Therefore, this induced tearing along the long axis of the **3.3o** crystals.

In this study, we examined the correlation of area, thickness, and volume of crystals, with respect to the latent periods until the development of the photosalient effect, for three types of DAE bulk crystals. There was no such correlation in the latent periods until the appearance of crystal surface cracks commonly found in the three types of DAE crystals as shown in the supplement (**3.1o**: Figure 3.10, **3.2o**: Figure 3.11, and **3.3o**: Figure 3.12). This is because UV light (λ = 365 nm) is absorbed on the crystal surface and light does not reach the backside of the crystal. That is, in a crystal the dye highly concentrates, and thus the entire molecules in the crystal do not isomerize.[46]
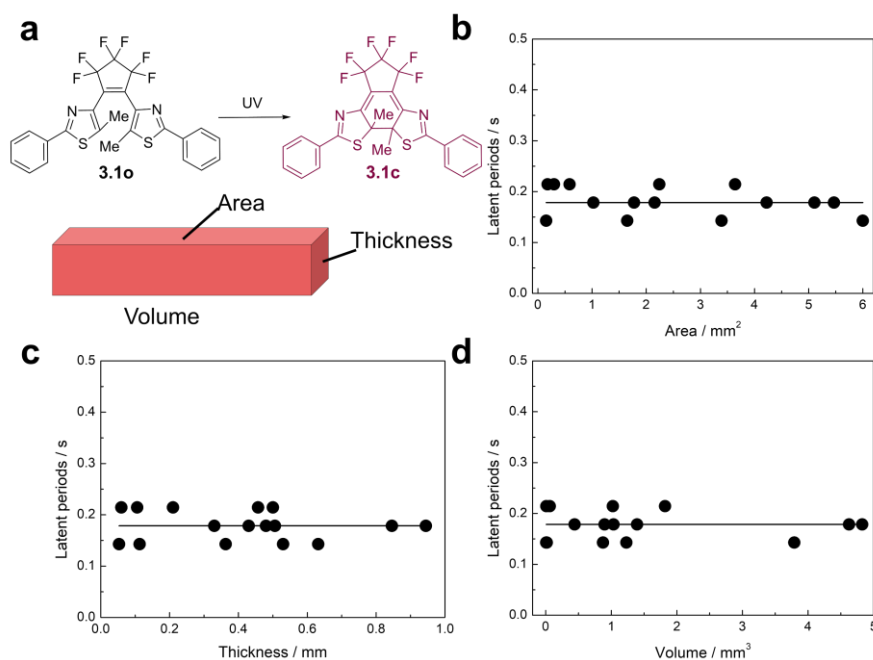
Figure 3.10 Illustration of crystal (a) and the latent periods of photosalient effect (peeling) by area (b), thickness (c), and volume (d) for crystal **3.1o** under UV irradiation (λ = 365 nm, 277 mW cm^{-2}).
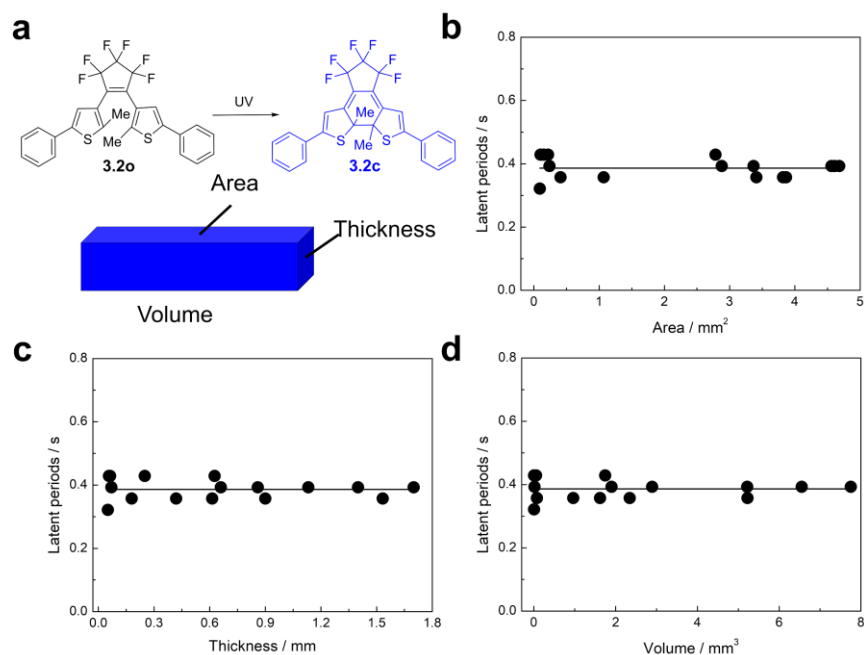
Figure 3.11 Illustration of crystal (a) and the latent periods of photosalient effect (peeling) by area (b), thickness (c), and volume (d) for crystal **3.2o** under UV irradiation (λ = 365 nm, 277 mW cm^{-2})
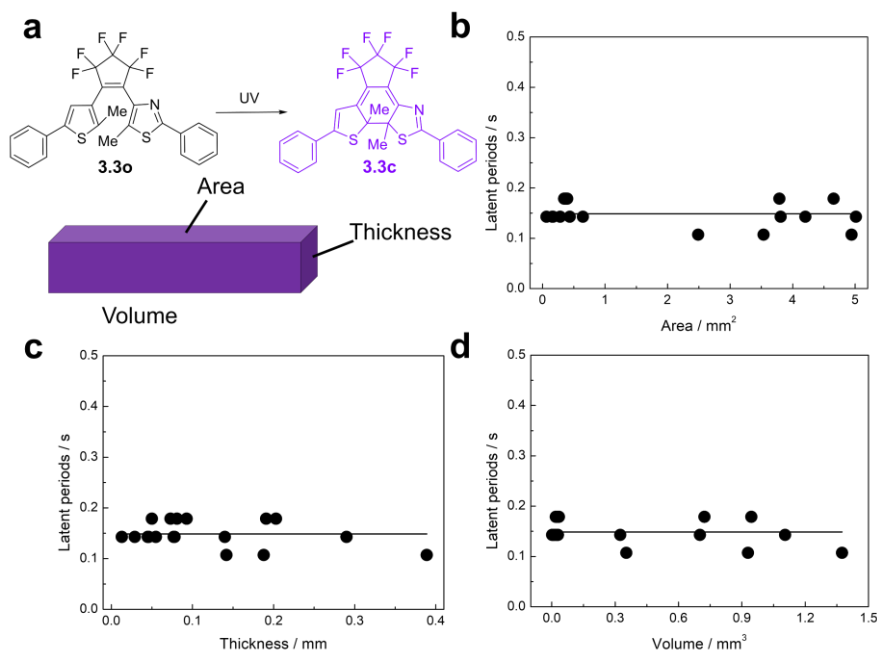
Figure 3.12 Illustration of crystal (a) and the latent periods of photosalient effect (peeling) by area (b), thickness (c), and volume (d) for crystal **3.3o** under UV irradiation (λ = 365 nm, 277 mW cm^{-2}).

The photosalient phenomenon originates in the tension between non-reacted interior and the reacted surface. Therefore, the photosalient phenomenon on the crystal surface has no correlation with the area, thickness and volume of the crystals. In contrast, for the phenomena occurring in the whole crystal, the latent periods for each crystal and the corresponding phenomena are different from each other. Therefore, it is necessary to examine a correlation between crystal area, thickness and volume as mentioned by Naumov.[21] Actually, the tearing of **3.3o** crystals has dependence on the thickness of the crystal, and a thicker crystal takes more time to tear. In fact, in crystals with a certain minimum thickness, cracks were observed only on the surface, but such crystals never split (Figure 3.13).
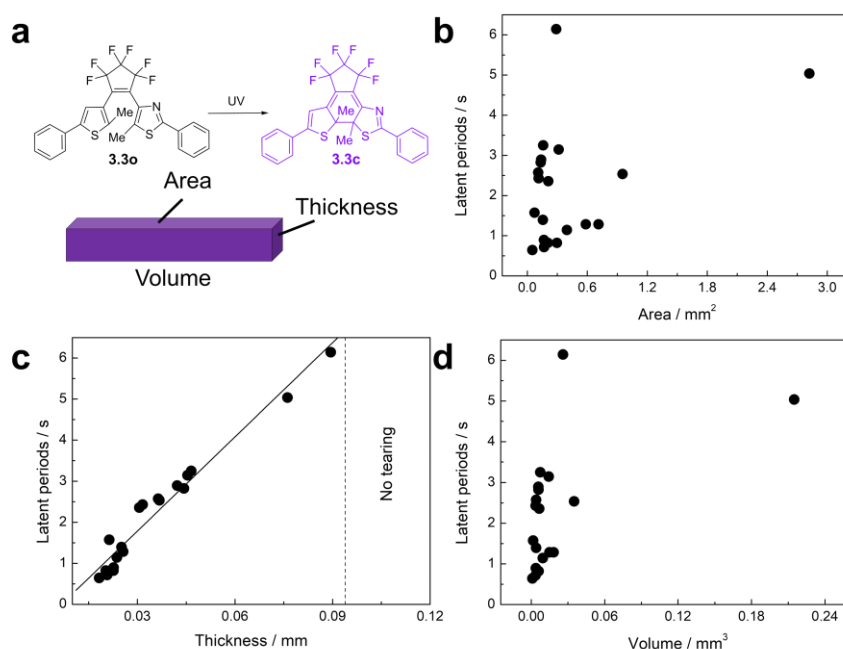
Figure 3.13 Illustration of crystal (a) and the latent periods of photosalient effect (tearing) by area (b), thickness (c), and volume (d) for crystal **3.3o** under UV irradiation ($\lambda = 365$ nm, 277 mW cm^{-2}).

X-ray crystallographic analysis of **3.3o** was carried out, and the results were compared with those of **3.1o** and **3.2o**. The 400-nm light was irradiated for 1 min for all crystals, and the deviation of the crystal axis was monitored. The data are summarized in Table 3.2. Upon 400-nm light irradiation for 1 min to a crystal of **3.1o**, the *a*-axis shrank by 0.50%, while the *b*- and *c*-axes expanded by 0.50, and 0.19%, respectively. As a result of these changes, the volume of a unit cell expanded by 0.20%. For a **3.2o** crystal, the *a*-axis expanded by 0.41%, while the *b*- and *c*-axes shrank by 0.24, and 0.04%, respectively. As

a result of these changes, the volume of a unit cell expanded by 0.26% under the same irradiation. For a **3.3o** crystal, the *a*-axis shrank by 0.73%, while the *b*- and *c*-axes expanded by 0.89, and 0.13%, respectively. The large shrinkage along the *a*-axis induced cracking, and the expansion along the *b*-axis induced tearing. Then the unit cell volume of the **3.3o** crystals expanded by 0.35%, which was the largest change among the three crystals. Furthermore, the largest changes among all axes were observed for the crystal of **3.3o**; such changes in **3.1o** were moderate, and those in **3.2o** were the smallest. As a result of having the largest overall changes, the crystal of **3.3o** has shown the most dramatic photosalient phenomena among the three derivatives. Such dramatic phenomena were observed in Naumov's system.[21,47] Here, each fragmented surface crystal also jumped or scattered, and in fact the most dramatically impressive photosalient phenomena were again observed for **3.3o** crystals.

Next, we attempted to confirm whether the photosalient phenomena observed here were due to strain caused by photoisomerization, i.e., whether thermal effects due to strong UV irradiation had any effect. During the strong UV irradiation, the temperature of each surface was monitored by thermography. Even upon strong UV irradiation, the temperature on the crystals remained nearly unchanged (at room temperature (24-26°C): temperature increase due to UV irradiation; 0.9 ± 0.3°C, under cooling (at 3-5°C): it was 0.6 ± 0.5°C). Accordingly, we conclude that the contribution of temperature rising was negligible (Figures 3.1 and 3.14-3.22).
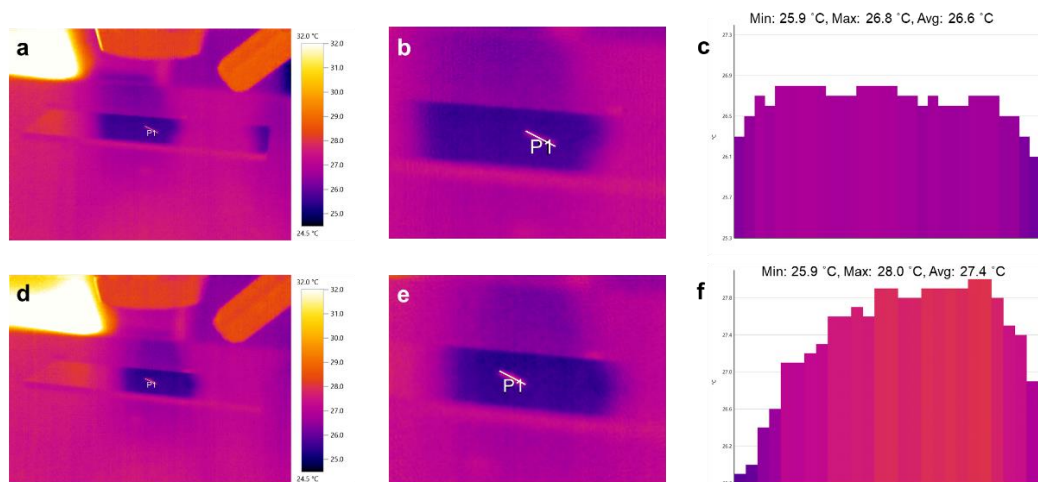
Figure 3.14 Temperature distribution of **3.1o** crystal before (a-c) and during (d-f) (at the time of expression of photosalient effect) UV light ($\lambda = 365$ nm, 277 mW cm^{-2}) irradiation at room temperature (25.4°C). (a) Thermographic image, (b) expanded images of (a), (c) temperature distribution of crystal before UV irradiation. (d) Thermographic image, (e) magnified images of (d), (f) temperature distribution of crystal during UV irradiation. The temperature distributions were measured along the solid line P1 in the crystals, which correspond to the horizontal axis of (c) and (f).
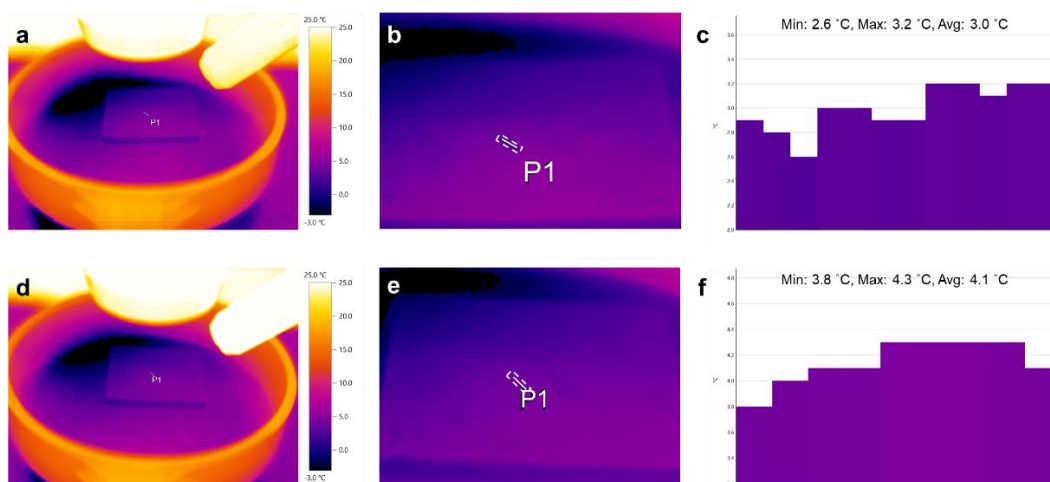
Figure 3.15 Temperature distribution of **3.1o** crystal before (a-c) and during (d-f) (at the time of expression of photosalient effect) UV light ($\lambda = 365$ nm, 277 mW cm^{-2}) irradiation at under cooling. (a) Thermographic image, (b) magnified images of (a), (c) temperature distribution of crystal before UV irradiation. (d) Thermographic image, (e) expanded images of (d), (f) temperature distribution of crystal during UV irradiation. The temperature distributions were measured along the solid line P1 in the crystals, which correspond to the horizontal axis of (c) and (f).
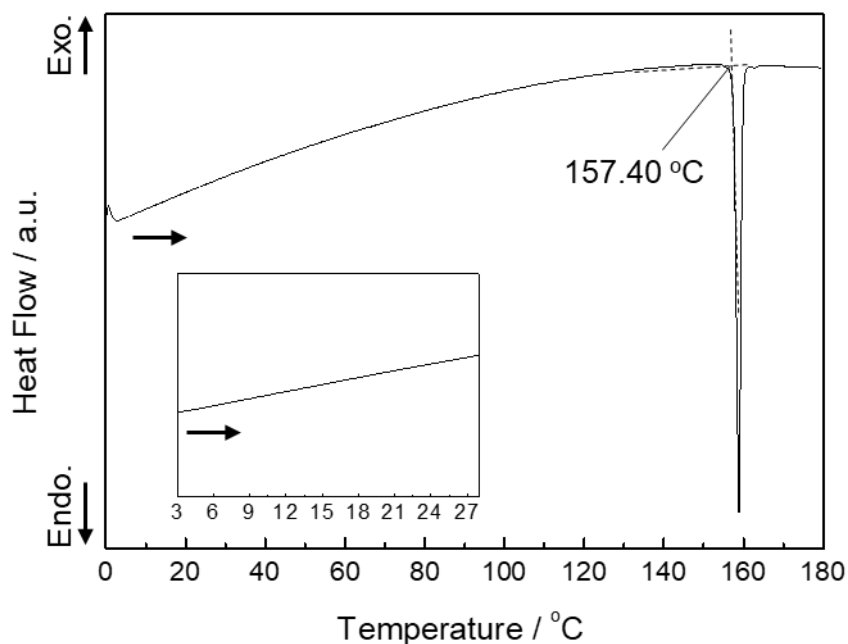
Figure 3.16 DSC curve of **3.1o**: DSC trace at heating rate of 10 °C min^{-1}.
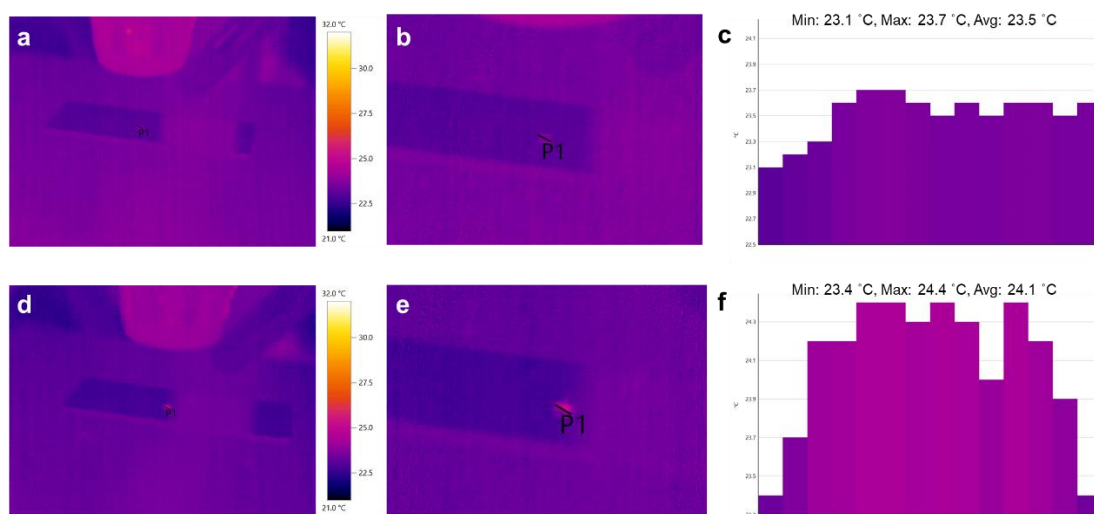
Figure 3.17 Temperature distribution of **3.2o** crystal before (a-c) and during (d-f) (at the time of expression of photosalient effect) UV light (λ = 365 nm, 277 mW cm^{-2}) irradiation at room temperature (24.2˚C). (a) Thermographic image, (b) magnified images of (a), (c) temperature distribution of crystal before UV irradiation. (d) Thermographic image, (e) expanded images of (d), (f) temperature distribution of crystal during UV irradiation. The temperature distributions were measured along the solid line P1 in the crystals, which correspond to the horizontal axis of (c) and (f).
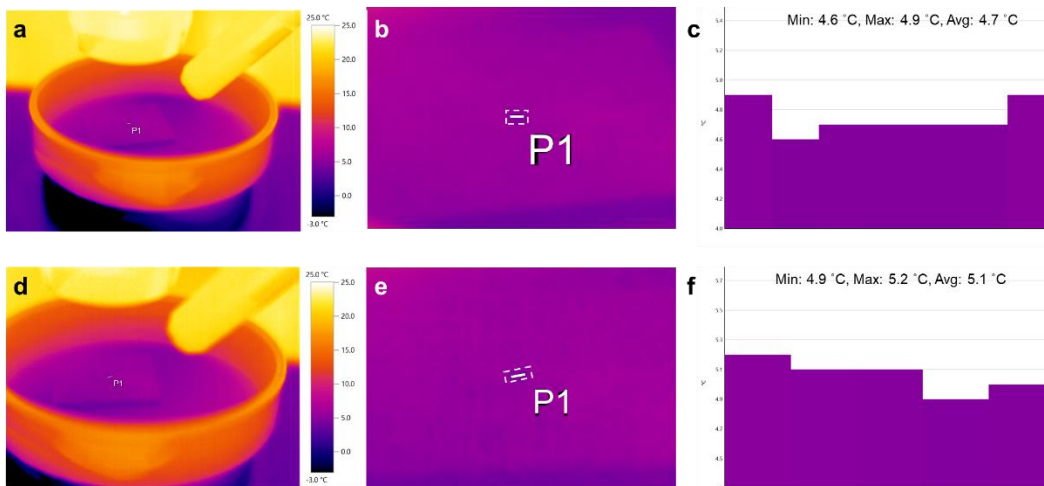
Figure 3.18 Temperature distribution of **3.2o** crystal before (a-c) and during (d-f) (at the time of expression of photosalient effect) UV light ($\lambda = 365$ nm, 277 mW cm^{-2}) irradiation at under cooling. (a) Thermographic image, (b) magnified images of (a), (c) temperature distribution of crystal before UV irradiation. (d) Thermographic image, (e) expanded images of (d), (f) temperature distribution of crystal during UV irradiation. The temperature distributions were measured along the solid line P1 in the crystals, which correspond to the horizontal axis of (c) and (f).
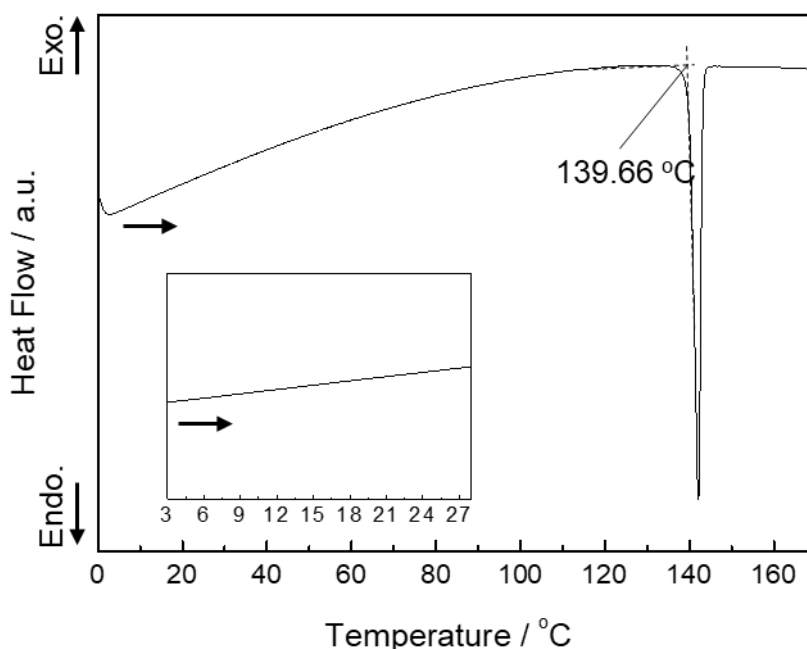
Figure 3.19 DSC curve of **3.2o**: DSC trace at heating rate of 10 °C min^{-1}.
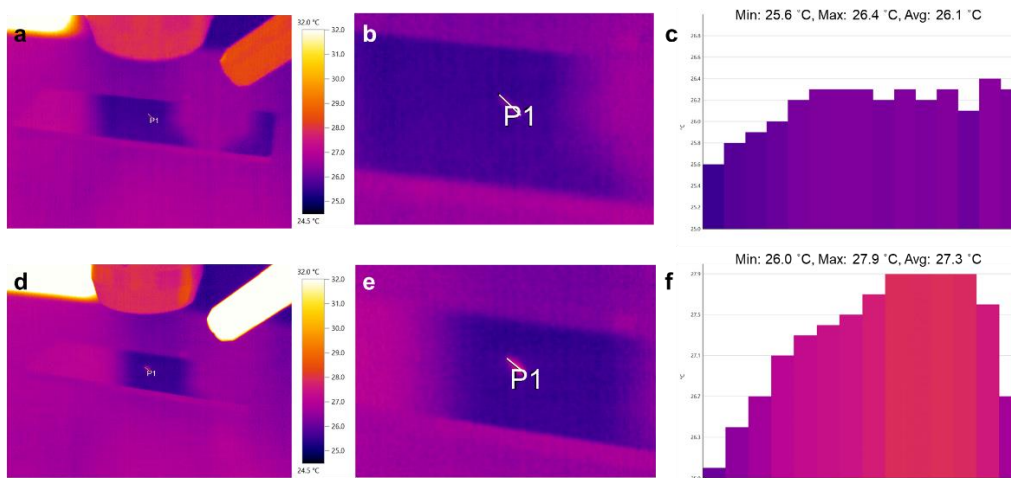
Figure 3.20 Temperature distribution of **3.3o** crystal before (a-c) and during (d-f) (at the time of expression of photosalient effect) UV light (λ = 365 nm, 277 mW cm^{-2}) irradiation at room temperature (25.7˚C). (a) Thermographic image, (b) magnified images of (a), (c) temperature distribution of crystal before UV irradiation. (d) Thermographic image, (e) expanded images of (d), (f) temperature distribution of crystal during UV irradiation. The temperature distributions were measured along the solid line P1 in the crystals, which correspond to the horizontal axis of (c) and (f)
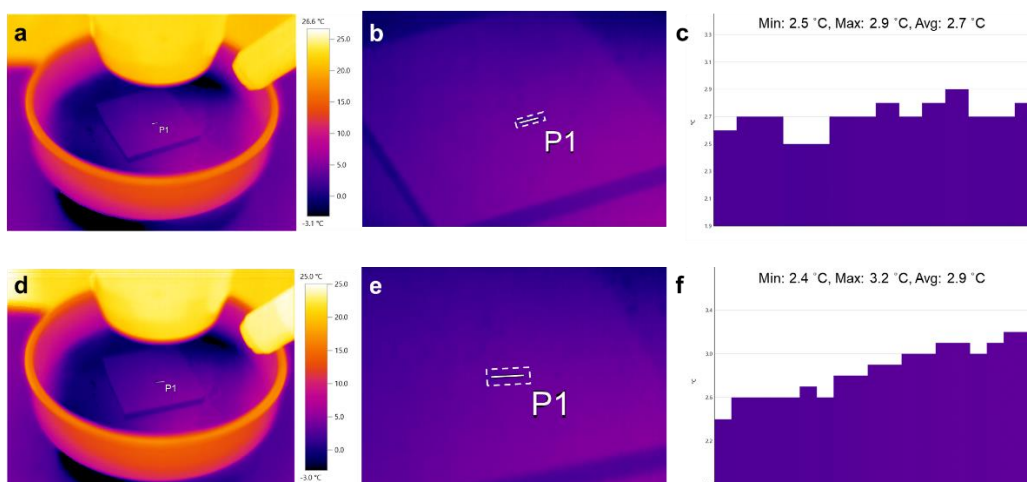
Figure 3.21 Temperature distribution of **3.3o** crystal before (a-c) and during (d-f) (at the time of expression of photosalient effect) UV light (λ = 365 nm, 277 mW cm^{-2}) irradiation at under cooling. (a) Thermographic image, (b) expanded images of (a), (c) temperature distribution of crystal before UV irradiation. (d) Thermographic image, (e) expanded images of (d), (f) temperature distribution of crystal during UV irradiation. The temperature distributions were measured along the solid line P1 in the crystals, which correspond to the horizontal axis of (c) and (f).
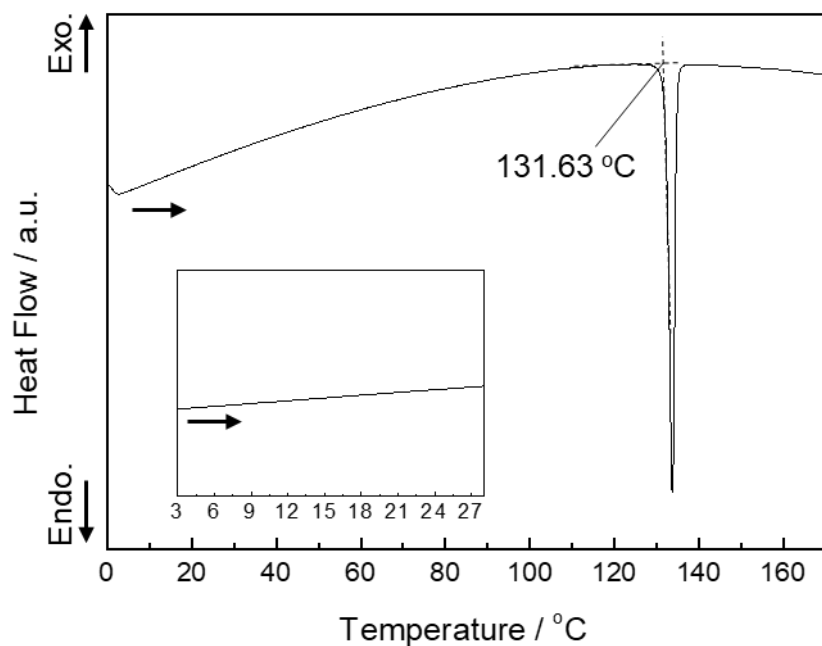
Figure 3.22 DSC curve of **3.3o**: DSC trace at heating rate of 10 °C min^{-1}.

Large changes in the unit cell of the crystals induced rapid responses of the photosalient effect. The relationships of latent periods to light intensities for these crystals are summarized in Figure 3.23. Naturally, irradiation with stronger light shortens the latent periods. With relatively weak intensities of light (below 300 mW cm^{-2}), the responsiveness of the salient phenomena (i.e., shorter latent periods) was **3.3o** > **3.1o** > **3.2o**. This order agrees with the order of relative axis changes of the unit cells.
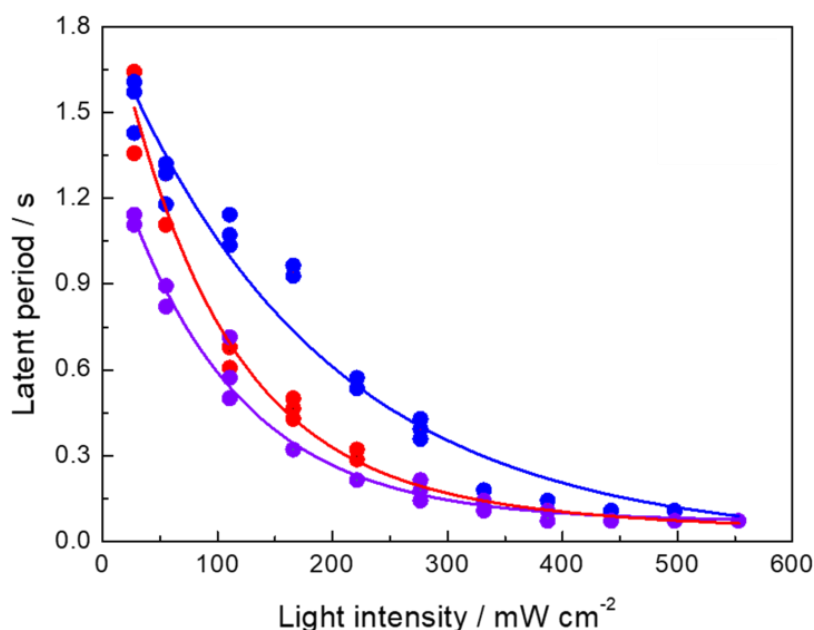
Figure 3.23 Relationship between UV light intensity (λ =365 nm) and latent periods for single crystals of **3.1o** (red), **3.2o** (blue), and **3.3o** (violet). Focusing on the peeling phenomenon, the latent periods were calculated for the photosalient effect.

The results mentioned above indicate that the photosalient phenomena on the crystalline surface of bulk crystals obtained by recrystallization are independent on crystal size. However, the photosalient (tearing) phenomena of the thin crystals prepared by sublimation showed dependence on the thickness of crystals. For the thin crystals of **3.1o** and **3.2o**, photoinduced bending phenomena were already been reported, but there has been no report on photosalient phenomena.[4,13] The crystal structures of thin crystals have been reported to be the same as those of bulk crystals of **3.1o** and **3.2o** prepared by recrystallization.[4,13] Moreover, the structure of the thin crystals of **3.3o** was the same as that of bulk crystals from recrystallization. (Table 3.3). We prepared thin crystals of **3.1o**, **3.2o**, and **3.3o** by sublimation and observed their photoreactive motions upon weak (λ = 365 nm, 810 μW cm^{-2}) and strong (λ = 365 nm, 277 mW cm^{-2}) UV light irradiation. Initially, weak UV light was irradiated to the crystals. Consequently, they showed photoinduced bending as reported,[4,13] where no photosalient phenomena occurred (Figure 3.24).

Table 3.3 Crystal data of thin crystal **3.3o** prepared by sublimation.

	3.3o
formula	$C_{26}H_{17}F_6NS_2$
formula weight	521.53
T / K	173(2)
crystal system	monoclinic
space group	$P2_1/c$
a / Å	7.3873(3)
b / Å	25.9010(8)
c / Å	12.6128(4)
α / °	90
β / °	102.618(2)
γ / °	90
V / Å^3	2355.03(14)
Z	4
(V/Z) / Å^3	588.7575
R_1 (I > 2σ(I))	0.0553
wR_2 (I > 2σ(I))	0.1450
R_1 (all data)	0.0600
wR_2 (all data)	0.1478
CCDC No.	1896376
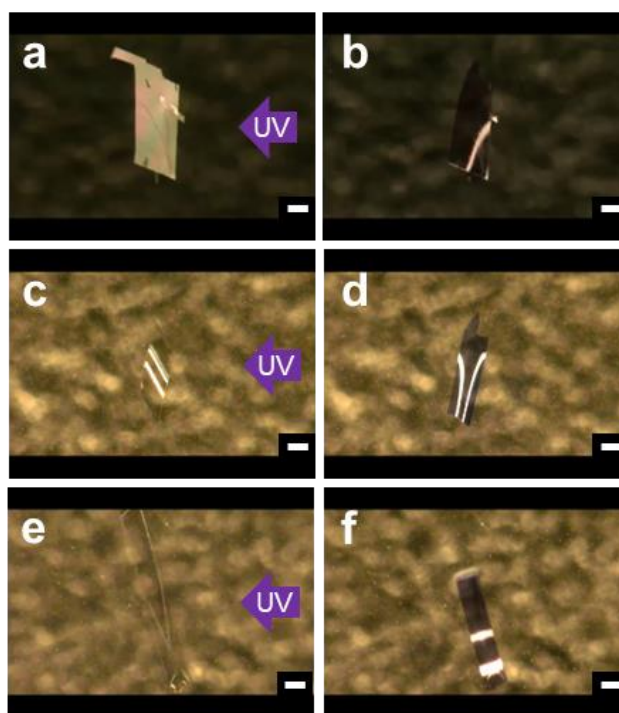
Figure 3.24 Photoinduced bending of thin crystals of DAEs **3.1o**: (a) and (b), **3.2o**: (c) and (d), and **3.3o**: (e) and (f). Before UV irradiation ($\lambda = 365$ nm, 810 μW cm^{-2}): (a, c, e) and after UV irradiation: (b, d, f). Scale bars: 100 μm.

The strong UV light was then irradiated to the same thin crystals (Figure 3.25). Now, instead of bending, the thin crystals of **3.3o**, among the three types, showed distinct photosalient phenomena. The thin crystal of **3.1o** showed bending followed by scattering into small pieces. The thin crystals of **3.2o** also showed bending with strong UV light. Some thin crystals of **3.2o** showed cracking without bending (Figure 3.26). As soon as the UV light was irradiated to the thin crystals of **3.3o**, they immediately and explosively broke down (Figure 3.25e and f); they also showed jumping, which is a much more dramatic photosalient phenomenon compared to the phenomena of **3.1o** and **1.2o** (Figure 3.27). This is attributed to the large size changes from **3.3o** to **3.3c** compared with those of the other crystals (Figure 3.28).
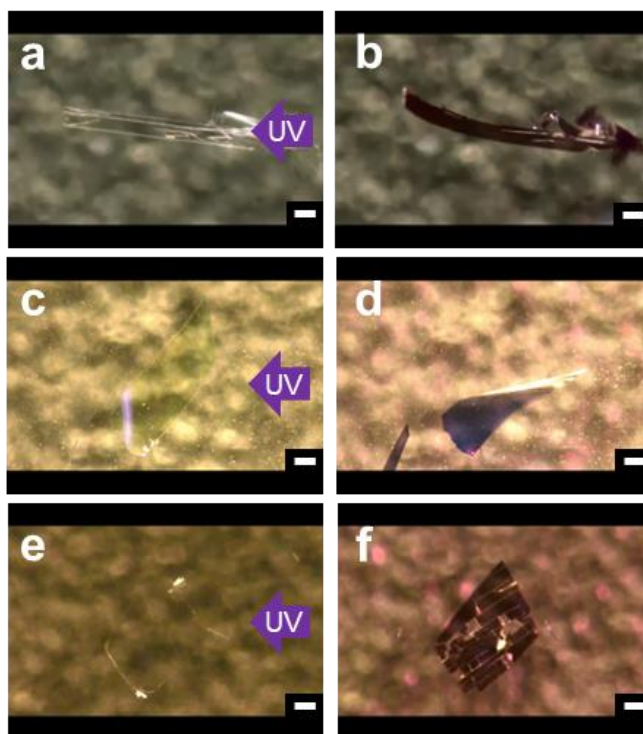
Figure 3.25 Photosalient effect of thin crystals of DAEs **3.1o**: (a) and (b), **3.2o**: (c) and (d), and **3.3o**: (e) and (f). Before UV irradiation ($\lambda = 365$ nm, 277 mW cm^{-2}): (a), (c) and (e), and after UV irradiation: (b), (d) and (f). Scale bars: 100 μm.
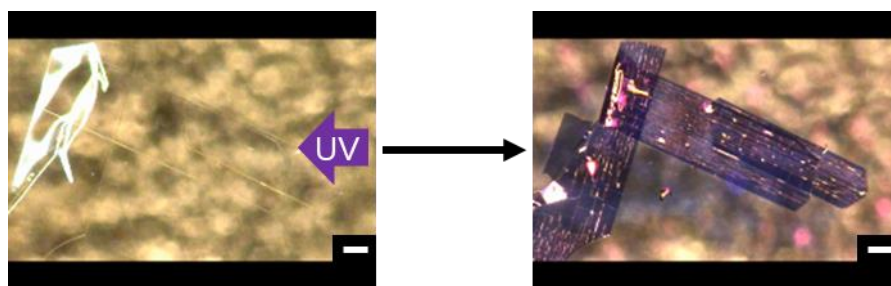
Figure 3.26 Photoinduced-peeling of thin crystals of **3.2o** ($\lambda = 365$ nm, 277 mW cm^{-2}). Scale bars: 100 μm.
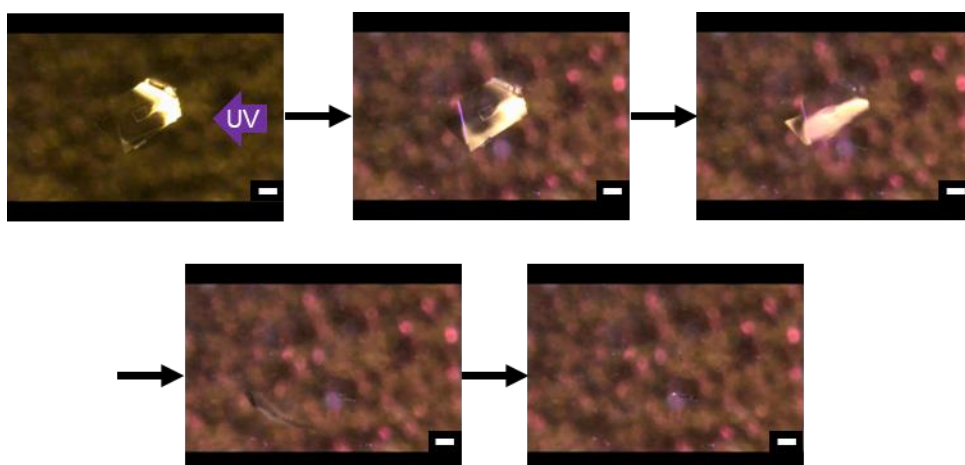
Figure 3.27 Photoinduced jumping of thin crystals of **3.3o** (λ = 365 nm, 277 mW cm^{-2}). Scale bars: 100 µm.
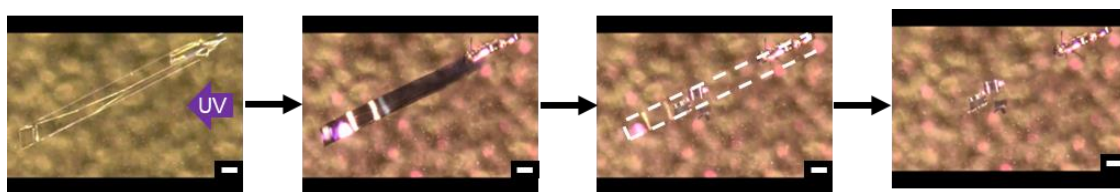
Figure 3.28 Photoinduced explosion of thin crystals of **3.3o** (λ = 365 nm, 277 mW cm^{-2}). Scale bars: 100 µm.

Moreover, when irradiating UV light to **3.3o** rod crystals, photoinduced bending was observed with weak UV light and a photosalient effect was observed with strong UV light, as with the thin crystals (Figure 3.29). Specifically, the **3.3o** rod crystal showed bending when irradiated with weak UV light but reversibly changed back to its original shape with irradiation by visible light (observation of digital microscope: white light). The reversible bending was successfully controlled upon alternate irradiation with the weak UV and visible lights (Figure 3.30). In comparing the curvature on the crystal with weak and strong UV light, the strong UV light produces bending in a short time than does the weak UV light. With strong UV light, the crystal cracked when it bent to about half of the maximum curvature value reached by weak UV light. Therefore, photoinduced bending and photosalient phenomena of the thin crystals of **3.3o** were certainly switched as a function of the intensity of UV light (810 µW cm^{-2} or 277 mW cm^{-2}).

119

Figure 3.29 (a) Molecular packing of **3.3o**. (b) Photoinduced bending of **3.3o** rod crystal due to weak UV light (**3.3o** rod crystal: 2.29 × 0.132 × 0.0325 mm (length × width × thickness), $\lambda = 365$ nm, 810 μW cm^{-2}). (c) Photosalient effect of **3.3o** rod crystal due to strong UV light (**3.3o** rod crystal: 1.01 × 0.154 × 0.0351 mm (length × width × thickness), $\lambda = 365$ nm, 277 mW cm^{-2}). (d) Change in the curvature with irradiation time: photoinduced bending of (b) (black circles) and photosalient effect of (c) (red circles). Scale bars: 0.4 mm for (b), and 100 μm for (c). Both (b) and (c) were irradiated from the *b*-axis direction.

Figure 3.30 Reversible photoinduced bending of **3.3o** rod crystal by UV (λ = 365 nm, 810 μW cm^{-2})-visible (observation of digital microscope: white) light. (a) Photograph of crystals at each irradiation time. (b) Curvature for each irradiation. Scale bars: 0.4 mm. Upon irradiation with UV light, it bent and returned to the state before bending.

3.3.2 Efficient surface peeling, a photoinduced result of photochromic diarylethene crystal by multi-step light irradiation

Here, we used crystals of diarylethene (DAE) **3.3o** (Scheme 3.2). The **3.3o** crystals had an elongated plate-like shape, which is suitable for photoinduced bending behavior. When weak UV light ($\lambda = 365$ nm, 810 μW cm^{-2}) was irradiated on the widest surface of the crystal, the crystal bents to the direction of the light source as its color turned from transparent colorless to violet (Figure 3.31a and b). The coloration of the crystal in violet is due to the generation of **3.3c** by UV light irradiation, which appears in the visible region as an absorption band with a maximal absorption wavelength at 553 nm (Figure 3.32). In the crystal, the dye is so densely packed that UV light is absorbed on the crystalline surface and light does not reach the backside of the crystal.[4] Therefore, not all of the molecules in the crystal are isomerized, and the bending is due to a gradient in the degree of photoisomerization of the DAE molecules in the crystal.[25] Next, the original shape was recovered through visible light irradiation (Figure 3.31c). During these processes, no crack or break was observed in the crystals (Figure 3.31e-h). Subsequently, the widest surface on the backside was irradiated with strong UV light ($\lambda = 365$ nm, 277 mW cm^{-2}). Then, the crystal on the irradiated surface peeled off (Figure 3.31d, i, and j). We later discuss the features of peeling which is different from those of cracking or breaking.
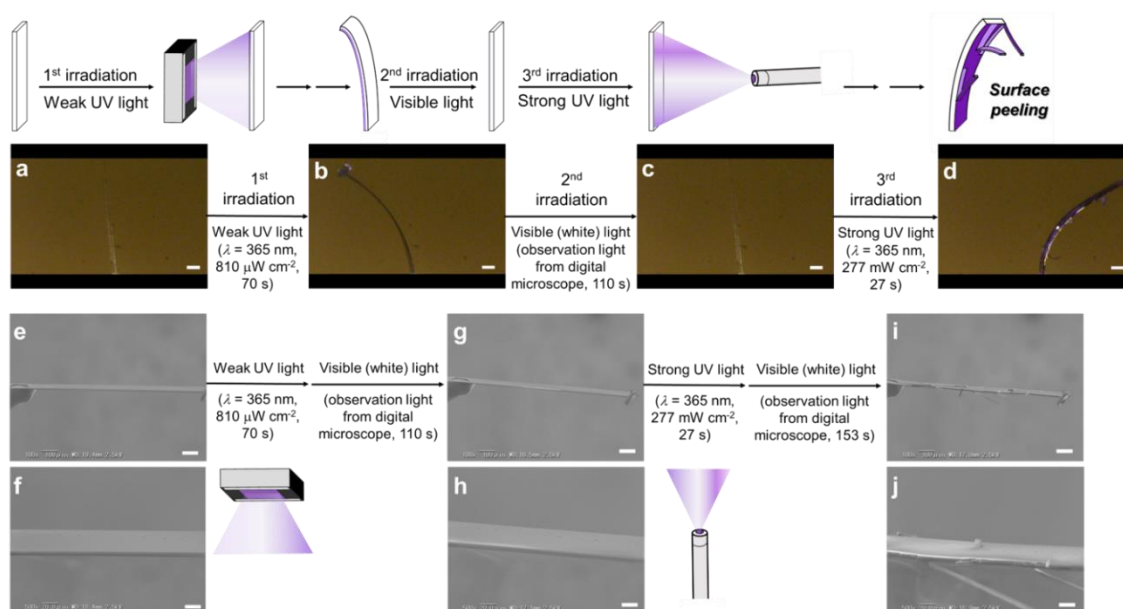
Figure 3.31 Schematic illustration, photographs (a–d), and scanning electron microscope (SEM) images (e–j) of photoinduced surface peeling of thin crystals. Scale bars: 100 μm for (a–d, e, g, and i) and 20 μm for (f, h, and j).
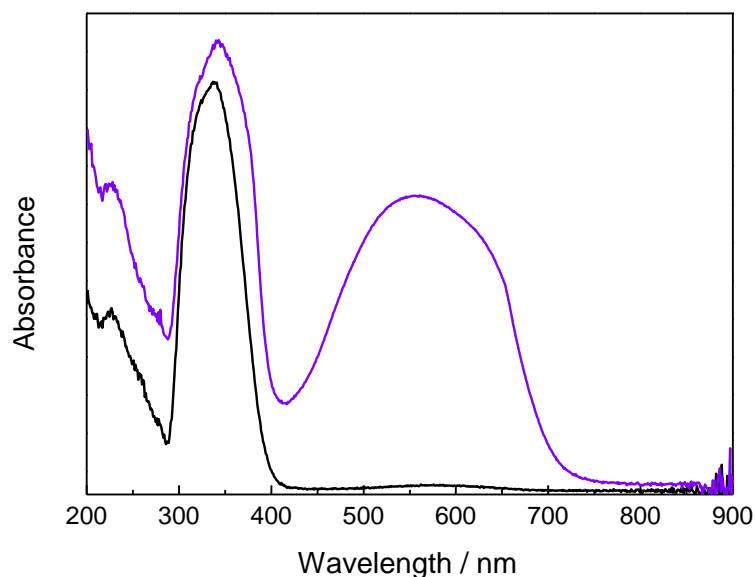
Figure 3.32 Absorption spectral changes of **3.3** in the crystalline state. **3.3o**: black line; photostationary state upon 365-nm light irradiation: violet line.

We investigated the detailed conditions behind the effect of this multi-step light irradiation on the surface peeling of **3.3o** crystals. Surface peeling was observed even when **3.3o** crystals were irradiated with a single step of strong UV light (condition 1: Figures 3.33a and 3.34). In contrast with the results shown in Figure 3.31, more than half of the crystals showed explosion (including separation and splitting) rather than surface peeling (Figure 3.33b). In multi-step irradiation from the same direction, peeling and explosion of crystals were observed at approximately the same ratio (condition 2: Figures 3.33a and 3.35). Under multi-step light irradiation as shown in condition 3, there was some crystal splitting, but the ratio was very small. Many crystals showed preferential surface peeling (Figure 3.33a and d). When we use weak UV light instead of strong one in condition 3, the crystals showed only bending, while surface peeling was not observed (Figure 3.36).　Therefore, the necessary condition for surface peeling of the crystals is most likely related to strong UV light irradiation. The percentages of detached crystals under each irradiation condition in the seventeen crystals were 29% for condition 1, 53% for condition 2, and 88% for condition 3. Among the three irradiation conditions, surface peeling phenomena were dominant only in condition 3. Thus, we focused on multi-step light irradiation of **3.3o** crystals as shown in condition 3, which is likely to efficiently induce surface peeling.

123
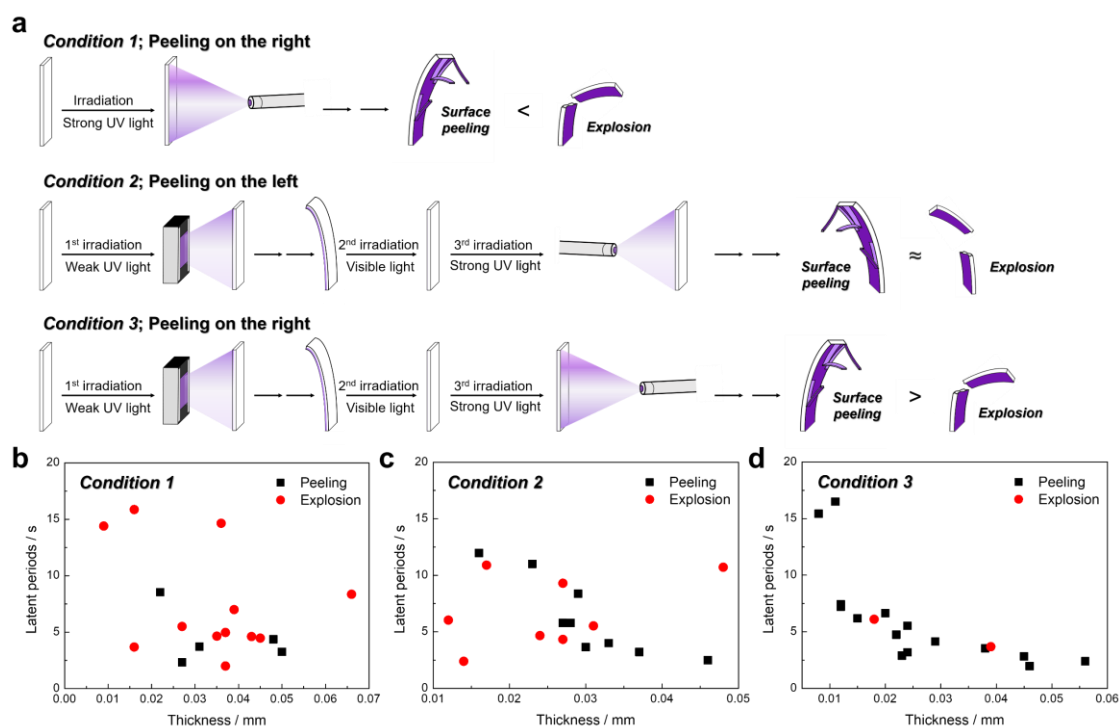
Figure 3.33 (a) Schematic illustration of the light irradiation conditions employed. (b-d) Latent periods of the photoinduced peeling or explosion phenomena by thickness for **3.3o** crystal under each irradiation condition (condition 1: (b), condition 2: (c), and condition 3: (d)). Here, seventeen crystals were used for each irradiation condition. The plots focus on the phenomena (peeling or explosion) that first appeared when irradiated with strong UV light. Weak UV light (λ = 365 nm, 810 μW cm^{-2}) was irradiated for 1 min. For conditions 2 and 3, visible light (observation light from digital microscope: white) was irradiated until the original shape was recovered. Strong UV light (λ = 365 nm, 277 mW cm^{-2}) was irradiated for up to 20 s.
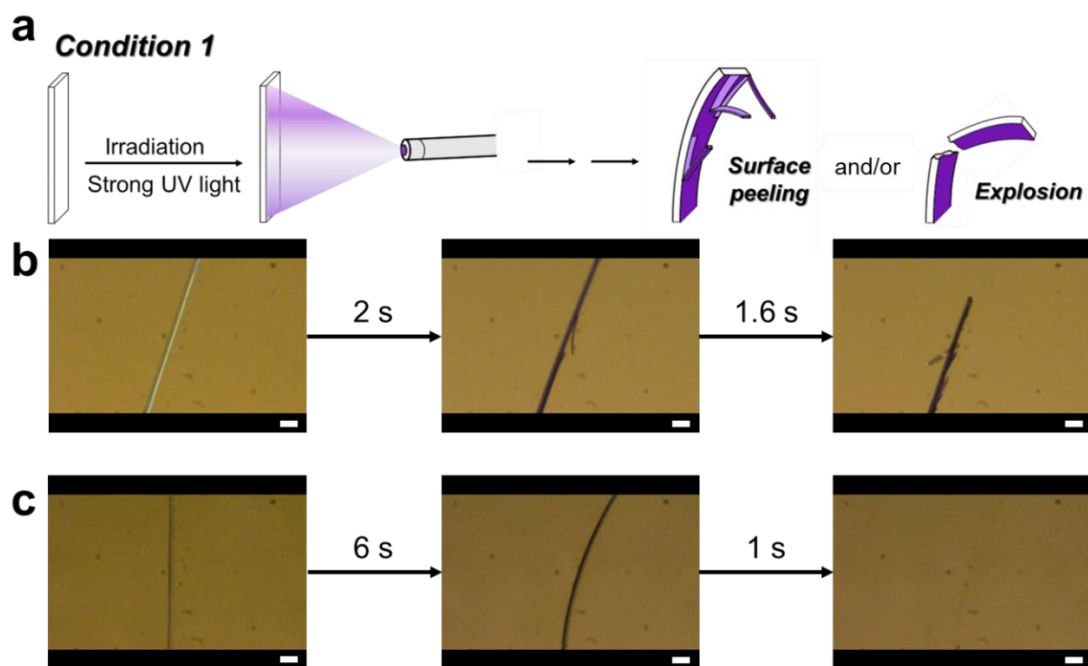
Figure 3.34 Schematic illustration of condition 1 (a) and photographs of the photoinduced peeling and/or explosion for **3.3o** crystal under condition 1 (b and c). Crystal size of (b): 1.055 × 0.085 × 0.016 mm (length × width × thickness). Crystal size of (c): 1.812 × 0.118 × 0.039 mm (length × width × thickness). Scale bars: 100 μm for (b) and 200 μm for (c).
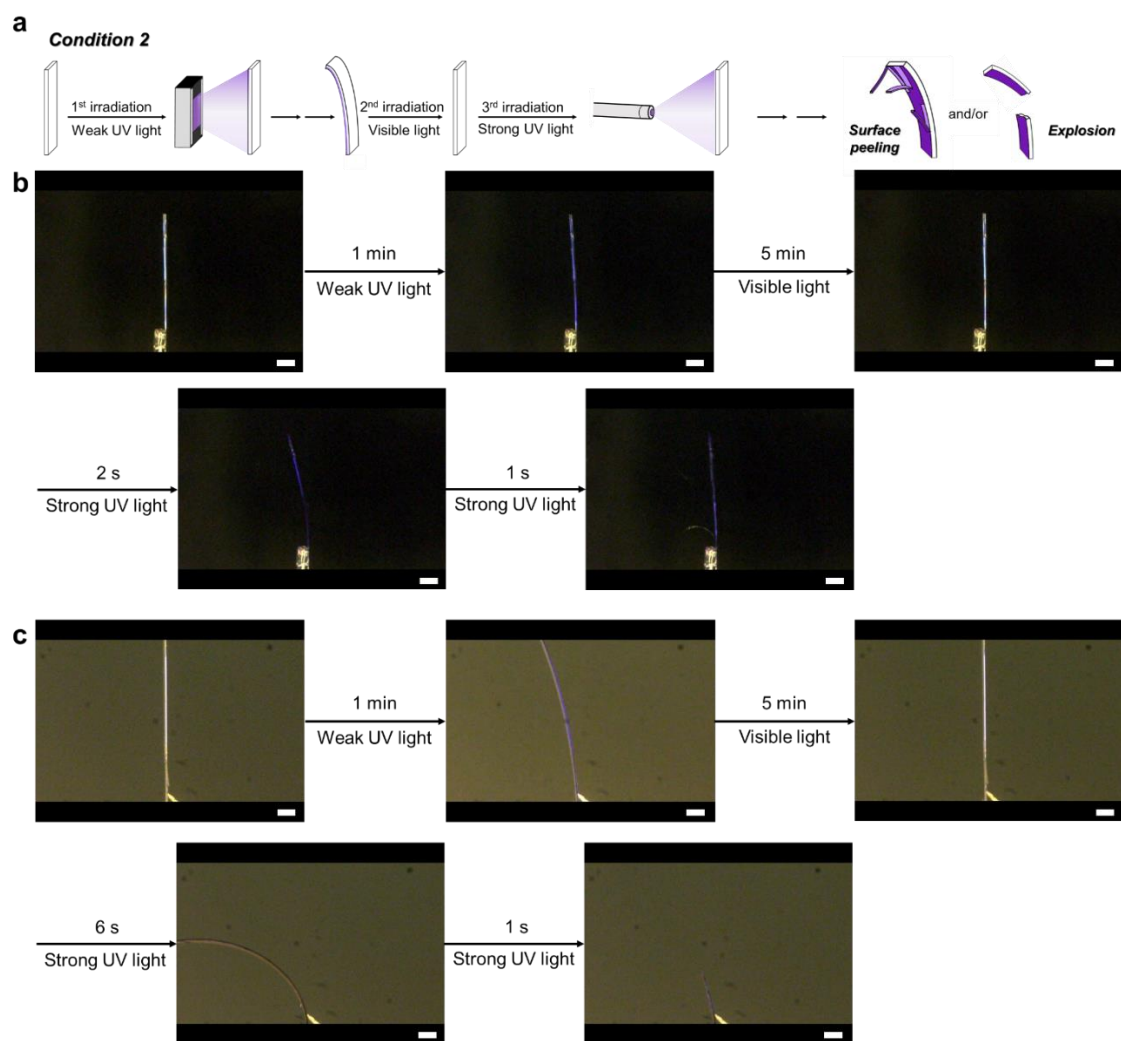
Figure 3.35 Schematic illustration of condition 2 (a) and photographs of the photoinduced peeling or explosion for **3.3o** crystal under condition 2 (b and c). Crystal size of (b): 2.580 × 0.172 × 0.046 mm (length × width × thickness). Crystal size of (c): 2.084 × 0.040 × 0.031 mm (length × width × thickness). Scale bars: 400 μm for (b) and 200 μm for (c).
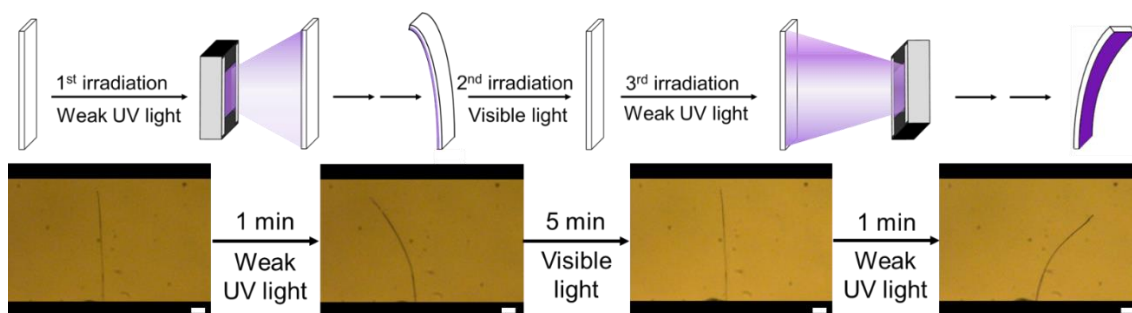
Figure 3.36 Schematic illustration and photographs of photoinduced bending for **3.3o** crystal under multi-step light irradiation. Crystal size: 1.604 × 0.043 × 0.016 mm (length × width × thickness). Scale bars: 200 μm.

X-ray diffraction (XRD) measurements were performed to determine the molecular orientation in the crystals. Here, single crystals obtained by sublimation were used directly for XRD measurements. Figure 3.37a shows the XRD pattern of the **3.3o** crystal prepared by the sublimation used in this study and the pattern calculated from single-crystal X-ray crystallographic data of the bulk crystal of **3.3o** obtained by recrystallization from a hexane solution. As shown in Figure 3.37a, diffraction peaks corresponding to (020), (040), and (060) mirror planes were mainly observed for crystals prepared by the sublimation. This result indicates that the widest surface of the crystal is vertical to the *b*-axis direction. Figure 3.37b shows the molecular packing in the unit cell as viewed from each lattice axis. Such packing gave the widest lattice spacing in the *b*-axis direction and resulted in preferential crystal growth in this plane direction. This result is similar to the crystal growth prediction determined based on the Bravais-Friedel Donnay-Harker (BFDH) method[48,49] (Figure 3.37c).
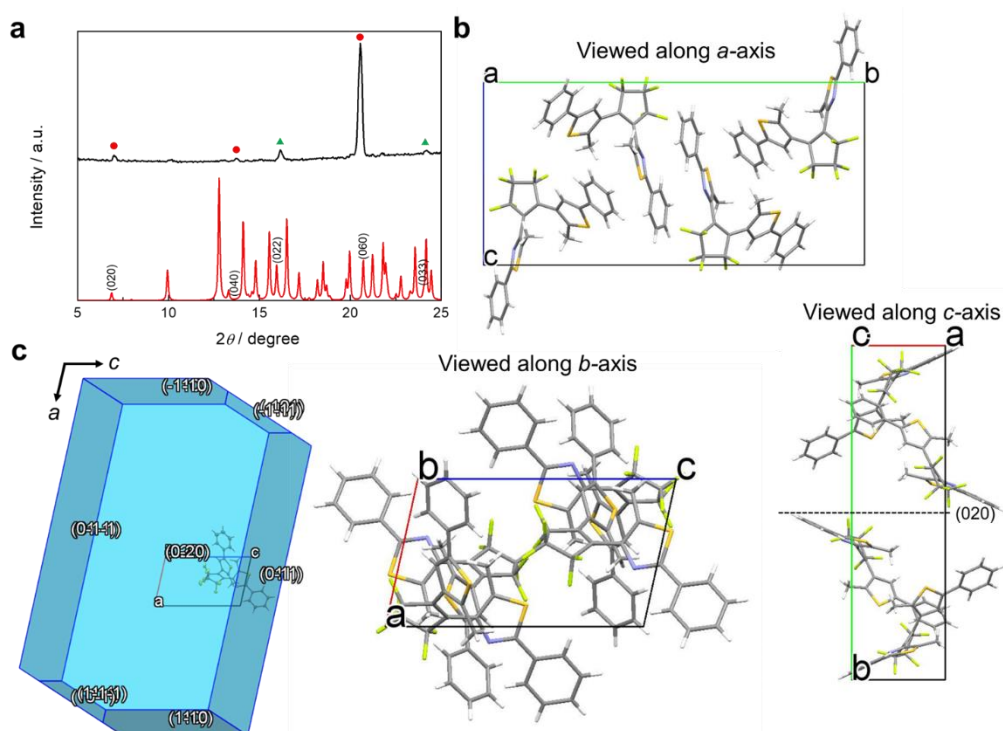
Figure 3.37 (a) XRD pattern of **3.3o** crystals (black) and the pattern calculated from single-crystal X-ray crystallographic data of **3.3o** (red). (b) Molecular packing of **3.3o** in the crystal. (c) Crystal morphology predicted using the Bravais-Friedel-Donnay-Harker (BFDH) method for **3.3o** crystal when viewed along the *b*-axis.

Photocyclization of DAE in the single-crystalline state is a well-known phenomenon.[50] Photochromic reactions of DAEs in the single-crystalline state proceed when the distances between the reactive carbon atoms in the antiparallel conformation are maintained within 4.2-Å.[51] From X-ray crystallographic analysis, the distance of the reactive carbon atoms on thiazole and thiophene rings is found to be 3.543 Å in **3.3o** (Figure 3.38a). This distance is sufficient for the photocyclization of DAE in the crystalline phase. This result supports the idea that the bending behavior of **3.3o** crystals and the photosalient phenomenon are caused by photoisomerization.[15] Figure 3.38d shows the atomic arrangement structure and molecular packing of a **3.3o** crystal after 400-nm light irradiation for 1 min (**3.3o-UV**). In the case of **3.3o-UV**, electron density peaks due to sulfur and carbon atoms of the closed-ring isomer were observed. The sulfur atoms from the closed-ring isomer are closer to the center of gravity of the molecule than those from the open-ring isomer (Figure 3.38a-c). The distance between sulfur atoms of closed-ring isomer extracted from the crystal data of **3.3o-UV** was almost the same as that

128

between sulfur atoms extracted from the crystal data of **3.3c** (Figure 3.38b and c). These electron density peaks disappeared with subsequent visible light irradiation (**3.3o-UV-Vis**.: Figure 3.38d and Table 3.4). Then, the size of the molecular structures extracted from the crystal data of the **3.3o** and **3.3c** was evaluated. By the change from **3.3o** to **3.3c**, the longitudinal axis expanded by about 1.5% and the horizontal axis shrank by about 1.4% (Figure 3.39). These changes in molecular structure and the accompanying changes in atomic arrangement cause changes in the parameters of the unit cell of the crystal, with a shrinkage of the *a*-axis and expansion of the *b*- and *c*-axes (Table 3.4).
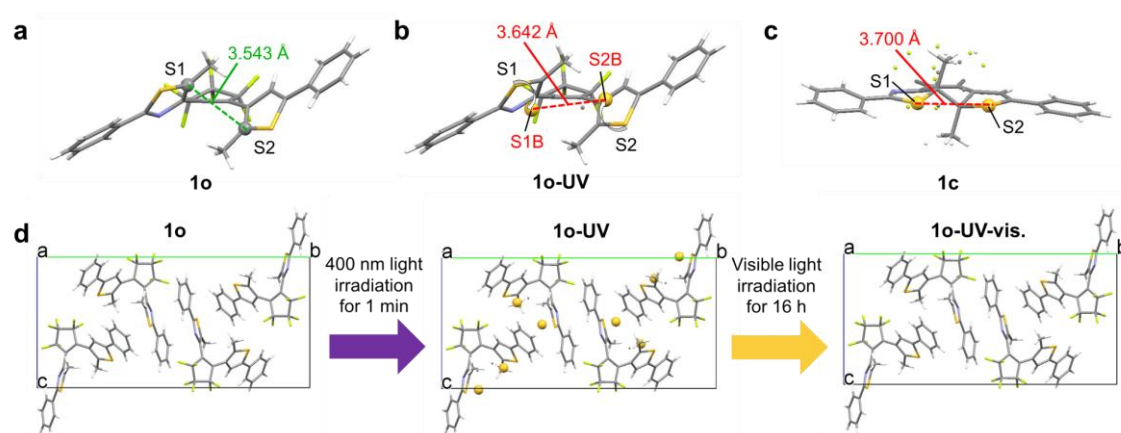
Figure 3.38 Structure and atomic arrangement of **3.3o** (a), **3.3o-UV** (b), and **3.3c** (c) extracted from X-ray structural analysis. In the case of **3.3o-UV**, electron density peaks due to sulfur and carbon atoms of the closed-ring isomer were observed. Note that the distance between sulfur atoms from the closed-ring isomer obtained by **3.3o-UV** is shorter than the distance between sulfur atoms in **3.3c**. (d) Molecular packing of **3.3o**, **3.3o-UV**, and **3.3o-UV-vis.** when viewed along the *a*-axis. Note that the electron density peaks due to sulfur and carbon atoms of the closed-ring isomer, observed in **3.3o-UV**, disappeared in **3.3o-UV-vis.**.

129

Table 3.4 Crystal data of open- (o) and closed-ring (c) isomers of **3.3**, **3.3o-UV**, and **3.3o-UV-vis.**.

	3.3o	**3.3o-UV** (after 400 nm light irradiation for 1 min)	**3.3o-UV-vis.** (after 400 nm light irradiation for 1 min and visible light irradiation for 16 h)	**3.3c**
Formula	$C_{26}H_{17}F_6NS_2$	$C_{26}H_{17}F_6NS_2$	$C_{26}H_{17}F_6NS_2$	$C_{26}H_{17}F_6NS_2$
Formula weight	521.53	521.53	521.53	521.53
T / K	93(2)	93(2)	93(2)	93(2)
Crystal system	monoclinic	monoclinic	monoclinic	monoclinic
Space group	$P2_1/n$	$P2_1/n$	$P2_1/n$	$P2_1/n$
a / Å	7.3573(2)	7.3035(5) -0.73%	7.3563(2) -0.01%	11.7799(5)
b / Å	25.7066(10)	25.9350(16) +0.89%	25.7306(10) +0.09%	18.4174(8)
c / Å	12.5981(5)	12.6145(8) +0.13%	12.5997(5) +0.01%	12.0279(5)
α / °	90	90	90	90
β / °	102.4150(12)	102.238(2) -0.17%	102.4259(12) +0.01%	118.8479(19)
γ / °	90	90	90	90
V / Å³	2326.98(14)	2335.1(3) +0.35%	2329.03(12) +0.09%	2285.68(17)
Z	4	4	4	4
R_1 (I > 2σ(I))	0.0482	0.0561	0.0452	0.0483
wR_2 (I > 2σ(I))	0.1252	0.1437	0.1159	0.1409
R_1 (all data)	0.0540	0.0724	0.0520	0.0619
wR_2 (all data)	0.1298	0.1552	0.1215	0.1643
CCDC No.	1870385	1870387	2205431	1870386
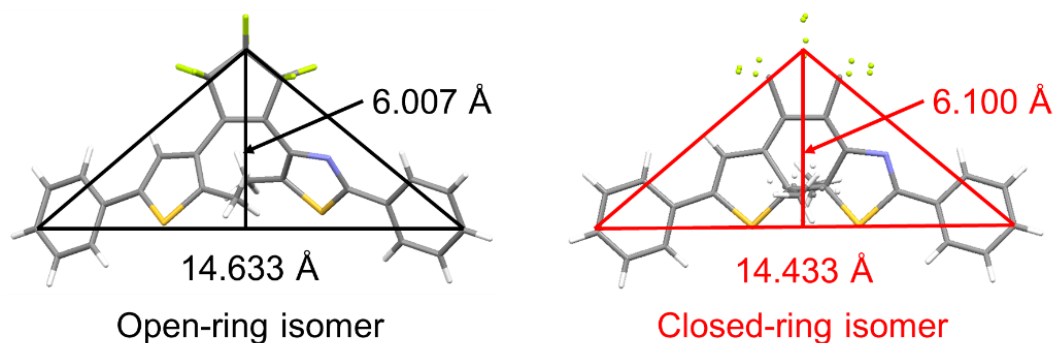
Figure 3.39 Molecular size of open- (**3.3o**) and closed-ring (**3.3c**) isomers in the crystal. Each molecular size was calculated from the crystal data of the open- and closed-ring isomers.

Photochemical reactions in crystals cause changes in molecular structure, which in turn cause changes in the crystal lattice. Such changes in the crystal lattice can induce internal strain and affect the photoresponse of the crystal. However, the difference between **3.3o** and **3.3o-UV-Vis.** by X-ray crystallographic data was very small, less than 0.1%, and not suitable for evaluating the generation of internal strain (Table 3.4). Therefore, we performed XRD measurements after UV-visible light irradiation to gain more detailed insight into the internal strain in the crystal lattice due to UV-visible light irradiation. The photocyclization-cycloreversion reaction cycle under UV-visible light irradiation were repeated four times in the crystals prepared by sublimation. Furthermore, XRD measurements were performed after each cycle (Figure 3.40b-c). Focusing on the diffraction peak on the (060) plane, we found that the peak shifted and the full width at half maximum (FWHM) broadened to the smaller angle as the number of cycles increased. Generally, the shift of the peak toward the small angle is due to the strain of the crystal lattice caused by expansion of the interplanar spacing of a set of diffracting planes.[52] This peak shift seems reasonable because single-crystal X-ray crystallographic analysis shows that the *b*-axis, which is in the same direction as the interplanar spacing, expands in the **3.3o** crystal after UV light irradiation (Figure 3.40b and Table 3.4). However, the FWHM was broadened in the direction of the small angle, but no change was shown along the wide-angle direction. The broadening of the diffraction peaks can be caused by changes in the non-uniform interplanar spacing.[52] If such changes in interplanar spacing are observed, they are likely related to residual strain energy.[52] From these results, we conclude that the strain in the crystal lattice caused by the expansion of the interplanar spacing of the diffraction planes is brought about by the structural changes induced by

the photocyclization-cycloreversion reactions of **3.3** in the crystal. In addition, as mentioned above, UV light is absorbed by the crystal surface of **3.3o** crystals, and light does not reach the backside of the crystal. These results indicate the coexistence of both strained and original layers due to the partial photocyclization-cycloreversion reactions (Figure 3.40a).
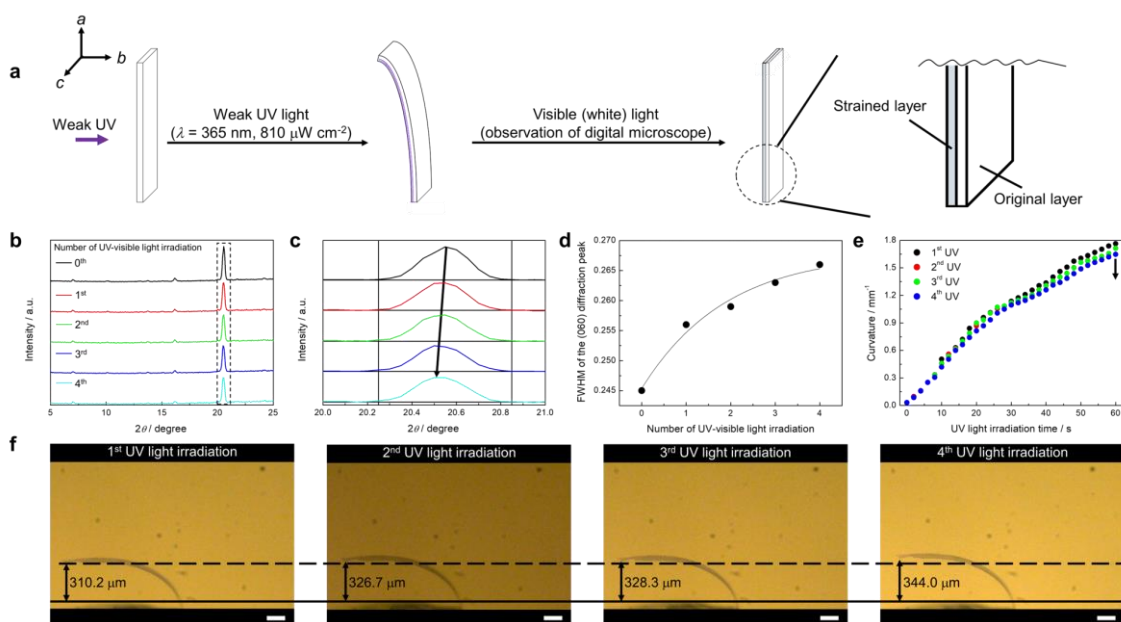
Figure 3.40 (a) Schematic illustration of the formation of strained layer during photoisomerization of **3.3o** crystals upon UV light irradiation. (b, c) XRD spectral changes of **3.3o** crystals before and after UV ($\lambda = 365$ nm, 110 mW cm^{-2}, 1 min)-visible light ($\lambda > 560$ nm, 5 min) irradiation. UV-visible light irradiation was repeated four times. (c) Enlarged view of the (060) diffraction peak in (b), where the peak shifted toward the small angle direction as the number of cycles of UV-visible light irradiation increased. (d) Plots of full width at half maximum (FWHM) for (060) diffraction peak of **3.3o** crystals vs. number of cycles of UV-visible light irradiation. (e, f) Curvature (e) and photoinduced bending (f) of **3.3o** crystal for each weak UV light ($\lambda = 365$ nm, 810 µW cm^{-2}, 1 min) irradiation. Between the weak UV light irradiations, visible light (observation light from digital microscope: white) was irradiated for 5 min. Scale bars: 150 µm.

The photoresponsive properties of the crystals in the presence of a strained layer was investigated. The **3.3o** thin crystal was irradiated with four cycles of weak UV-visible light from the same direction. Each weak UV irradiation induced bending in the **3.3o** thin

132

crystal. As the number of cycles increased, the curvature decreased and the bending became smaller (Figures 3.40e, f, and 3.41). Bending is brought about by internal strain caused by the simultaneous presence of both reactant and product domains. This result indicates that the mechanical behavior resulting from the photoresponsive properties of the strained layer is less remarkable than that of the original layer. In other words, a strained layer is likely to mitigate internal strain generated by the changes in molecular structure brought about by photochemical reaction. Thus, we compared the latent period of photoinduced peeling by thickness of **3.3o** crystals in conditions 2 and 3. The values of latent period until peeling vs. crystal thickness were used to create fitting curves using the following second-order exponential decay function (Eq. 3.1)

$$t(x) = t_0 + \tau_1 e^{-\frac{x}{x_1}} + \tau_2 e^{-\frac{x}{x_2}}, \qquad (3.1)$$

where t_0, τ_n (n = 1, 2), and x_n (n = 1, 2) are fitting parameters (Figure 3.42 and Table 3.5). These results indicate that τ_1 is dominant under condition 2, and latent periods for thin crystals in condition 2 are longer (i.e., it takes longer to peel off) than those in condition 3.
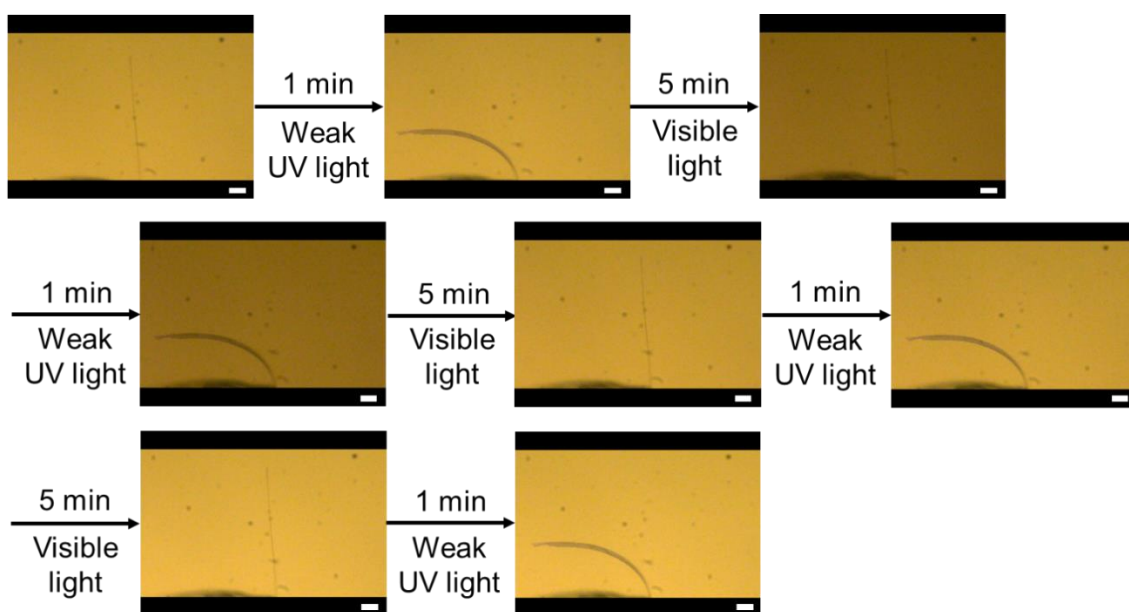
Figure 3.41 Photoinduced bending and return of **3.3o** crystals by weak UV-visible light irradiation. Crystal size: 1.081 × 0.056 × 0.006 mm (length × width × thickness). Scale bars: 150 μm.
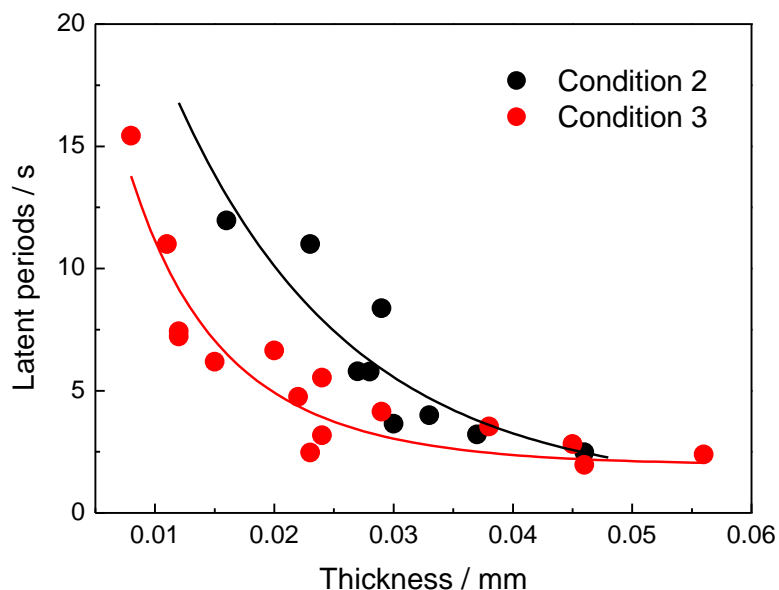
Figure 3.42 Latent periods of the photoinduced peeling by thickness for **3.3o** crystal under conditions 2 and 3. See Figure 3.33a for irradiation condition. Here, the crystals showing peeling in Figure 3.33d were used. The solid lines show fitting curves with second-order exponential decay function.

Table 3.5 Parameters of the fitting curve due to the second-order exponential decay function with respect to the latent period of photoinduced peeling by thickness for **3.3o** crystals in conditions 2 and 3.

	Condition 2	Condition 3
t_0 / s	0.92209	1.96429
τ_1 / s	35.93379	19
τ_2 / s	0.019	18.57126
x_1 / mm	0.01464	0.00447
x_2 / mm	0.01587	0.01334

Now we can understand the reason that condition 3 in Figure 3.33 preferentially induced surface peeling and suppressed crystal explosion compared to the other conditions: The difference in mitigation of internal strain between the original and strained layers causes an instantaneous release of internal strain, avoiding the photosalient effect throughout the crystal. Consequently, the photosalient effect is suppressed in conditions 2 and 3 for a short duration under strong UV light irradiation. In the meantime,

the defects created by the irradiation cycle of weak UV and visible light may spread when strong UV light is irradiated, which results in the peeling phenomena, i.e., much smaller internal strain seems to be required for the progress of peeling. This depends on the concentration and diffusion of defects; there is an appropriate concentration and diffusion of defects for the peeling, since the high concentration and diffusion of defects reduces the internal strain, which provides enough duration time for peeling to occur. Thus, the difference between conditions 2 and 3 is due to the concentration and diffusion of defects near the irradiated surface with strong UV light. For condition 2, the concentration and diffusion of defects has a high value near the irradiated surface with strong UV light. Therefore, it requires much more time for peeling. In other words, the photosalient effect occurs before the peeling. In contrast, for condition 3, the concentration of defects is an appropriate level for the current condition of the strong UV light and the crystal's thicknesses of 0.025–0.06 mm; the peeling occurs within the short period of time before the start of the photosalient phenomena. These results show that surface peeling is efficiently induced when the original layer is irradiated with strong UV light in the presence of original and strained layers with different photoresponses in the crystal.

The mechanism of surface peeling of **3.3o** crystal upon strong UV light irradiation was discussed using crystal data obtained by X-ray crystallographic analysis. In the case of **3.3o** bulk crystal, small cracks were initially generated perpendicular to the long axis on the surface, then drastically larger cracks were generated along the long axis, and the whole crystal was scattered.[15] As mentioned above, photoisomerization of **3.3o** to **3.3c** by UV light irradiation occurs in the surface thin layer of the crystal. Since the ratio of photoisomerization is low in thick crystals such as bulk crystals, shrinkage of the *a*-axis of the unit cell results in the appearance of only cracks along *c*-axis, not crystal explosion. In thin crystals without strain layers, the ratio of photoisomerization is larger than in bulk crystals, resulting in crystal explosion. In thin crystals with strained layers, the difference in internal strain relaxation between the original and strained layers causes cracks without breaking, similar to bulk crystals. In addition, expansion of the *c*-axis of the unit cell can result in cracks along the *a*-axis. However, the change in the *c*-axis is smaller than changes in the *a*- and *b*-axes and sometimes has no effect on surface peeling. Then, the surface peels off due to expansion of the *b*-axis (Figure 3.43). As can be seen from Figure 3.43, the (020) mirror plane is parallel to the two-dimensional plane in the crystal that separates the layers composed of **3.3o** molecules. These layers are likely to provide natural cleavage planes for the separation of the layers.

135
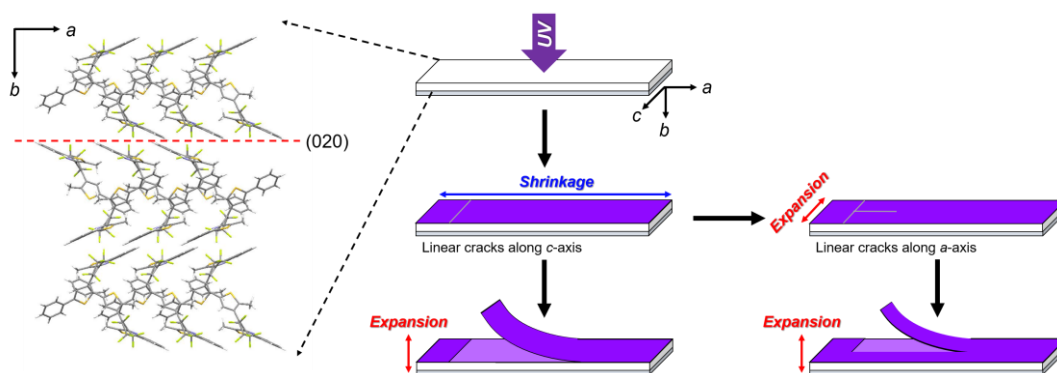
Figure 3.43 Schematic illustration of photoinduced peeling of **3.3o** crystal upon strong UV light irradiation by condition 3.

The latent period of photosalient phenomena is often affected by the crystal size.[15,21] In this work, we examined the correlations between the length, width, thickness, area, and volume of the crystals and the latent periods until the surface peeling occurs for the **3.3o** crystals in condition 3. The surface peeling of crystals was particularly dependent on the thickness of the crystal: The latent periods of peeling were shorter for thicker crystals (Figure 3.44). The bending behavior due to the photochromic reaction depends on the thickness of the crystal: The thinner crystal has a faster bending rate.[29-31] In addition, when **3.3o** crystals were irradiated with strong UV light, bending was observed prior to crystal peeling. Therefore, the mechanical energy generated by the anisotropic change in the lattice axes due to the photochromic reaction is consumed as bending and likely to take longer to peel off as the crystals become thinner. In fact, the inter-dependency among the length, width, and thickness and the curvature (immediately before photoinduced surface peeling) show that the thinner the crystal, the better it bends (Figure 3.45). These results show that the internal strain is consumed by the bending of thinner crystals, and that it takes longer for the crystals to peel off.
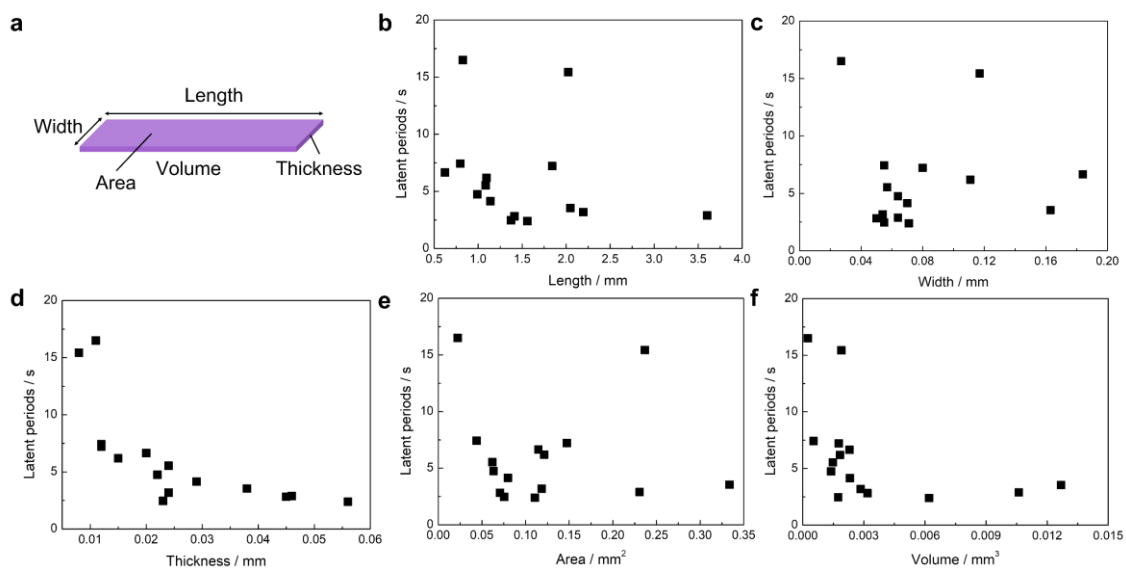
Figure 3.44 Illustration of the crystal (a) and latent periods of the photoinduced peeling by length (b), width (c), thickness (d), area (e), and volume (f) for **3.3o** crystal under condition 3. See Figure 3.33a for irradiation condition. Here, the crystals showing peeling in Figure 3.33d were used.
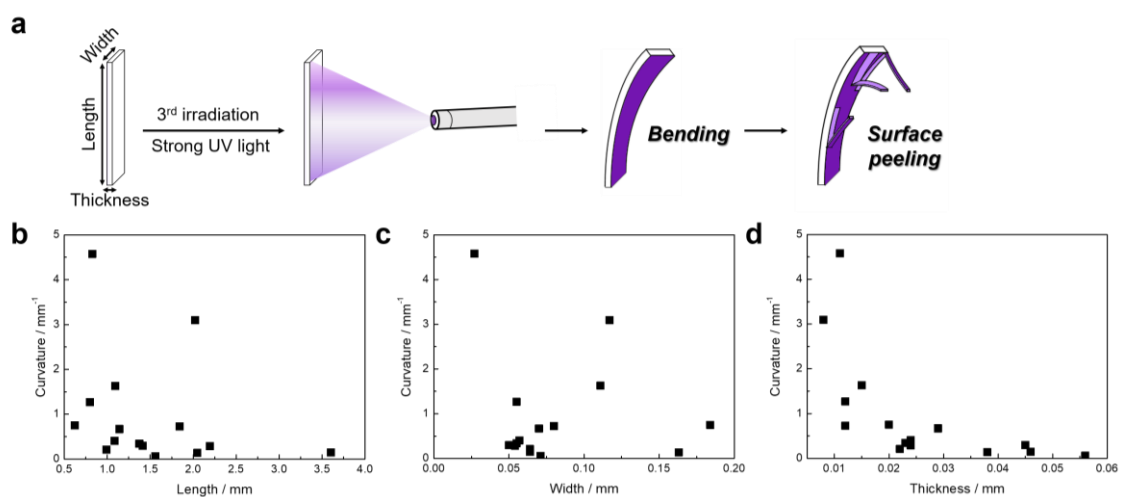
Figure 3.45 (a) Schematic illustration of surface peeling from a bent crystal due to strong UV light irradiation under condition 3. (b-d) Dependence on length (b), width (c), and thickness (d) of curvature of the **3.3o** crystal immediately before showing photoinduced peeling in condition 3. See Figure 3.33a for irradiation condition. Here, the crystals showing peeling in Figure 3.33d were used.

137

The correlation between the thickness of the crystals used and the thickness of the exfoliated crystals at each irradiation condition was examined. The thickness of the peeled crystals ranged from about 2 to 15 μm, less than half the thickness of the original crystals (Figure 3.46a and b). This peeling side were uneven compared to the surface, but it was very minute (Figure 3.47). Therefore, the digital microscope used in this study could not observe the effect of thickness due to unevenness when viewed from the side (Figure 3.48). In addition, when multiple peels were shown at the same time, the thickness of the peeled crystals was nearly the same (Figure 3.48).
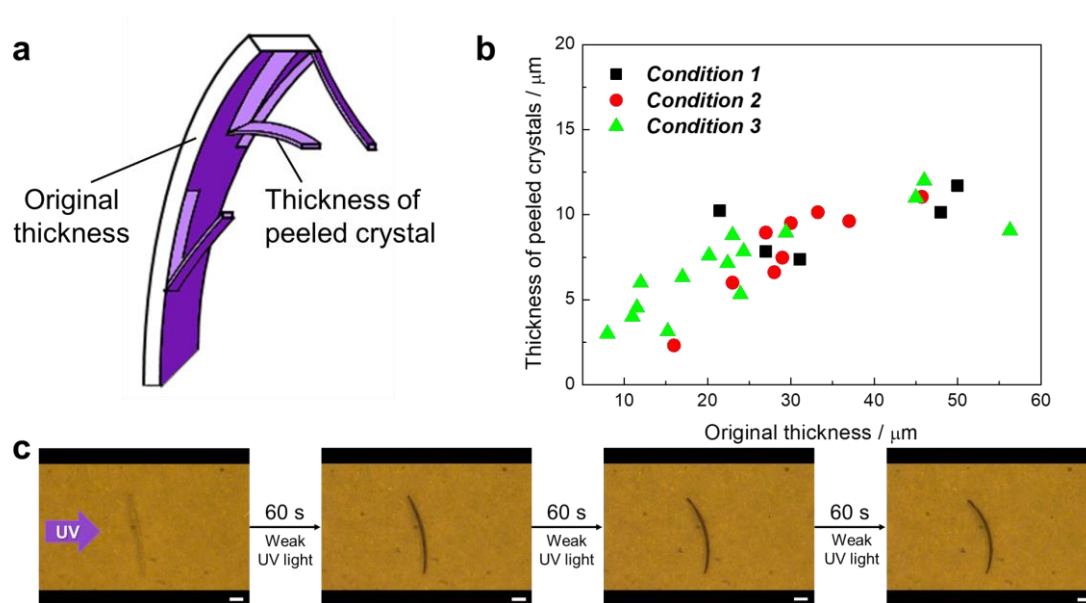
Figure 3.46 Illustration of the peeled crystal (a) and thickness dependence of the peeled crystals under each irradiation condition (b). See Figure 3.33a for irradiation conditions. (c) Photoinduced bending of peeled crystal under weak UV light (λ = 365 nm, 810 μW cm^{-2}) irradiation. Before UV light irradiation, visible light (observation light from digital microscope: white) was irradiated for 5 min to decolorize the peeled crystal. Scale bars: 100 μm.
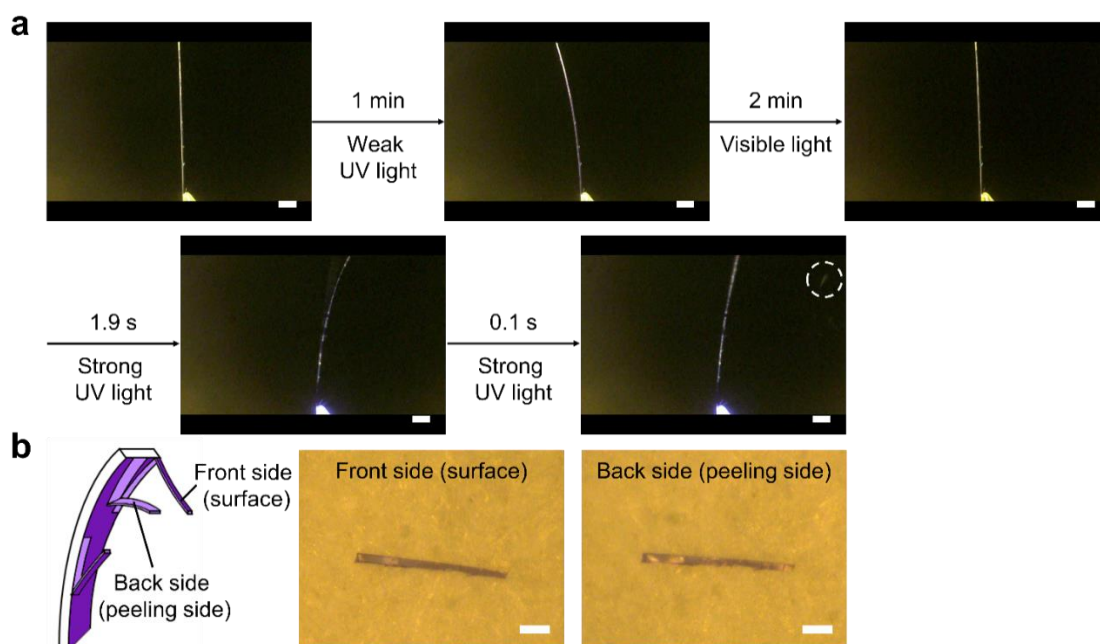
Figure 3.47 (a) Photographs of the photoinduced peeling for **3.3o** crystal under condition 3. Crystal size: 3.603 × 0.064 × 0.046 mm (length × width × thickness). Scale bars: 100 μm. (b) Schematic illustration and photographs of the front and back sides of the peeled crystals. Scale bars: 100 μm.
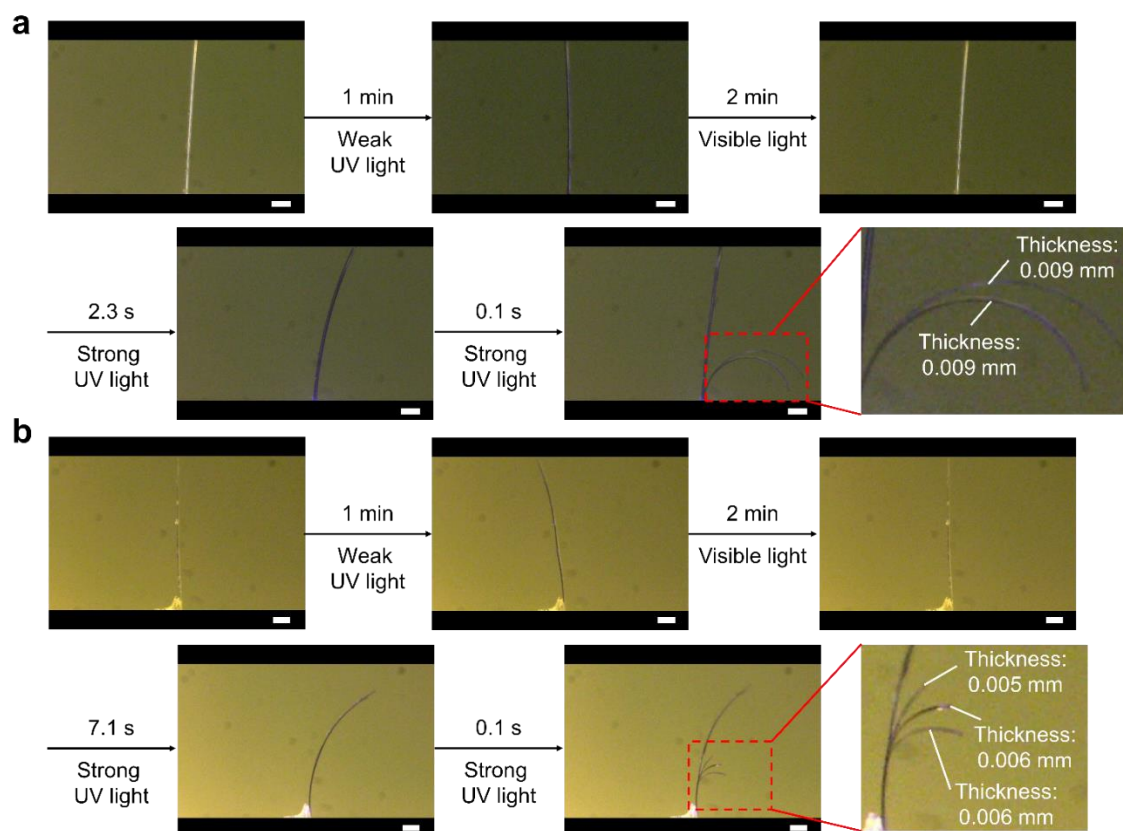
Figure 3.48 (a, b) Photographs of the photoinduced peeling for **3.3o** crystals under condition 3. Crystal size: 1.374 × 0.055 × 0.023 mm (length × width × thickness) for (a) and 1.842 × 0.080 × 0.012 mm (length × width × thickness) for (b). Scale bars: 150 μm for (a) and 200 μm for (b).

The **3.3o** crystals have a high absorbance for the 365 nm of UV light that was used, so the UV light is absorbed by the thin layer of the crystal and does not reach the backside of the crystal. Thus, the strained layer is generated in the region where UV light reaches, so it is likely to be present at a certain thickness. Therefore, Surface peeling does not usually occur at the boundary between the layer and the strained layer but is caused by strain due to changes in the unit lattice resulting from isomerization of the DAE molecule caused by strong UV irradiation, and the strained layer is used to prevent cracking of the entire crystal. In other words, the thickness of the peeled crystal is caused by the reachable region of a strong UV light, so that for crystals above a certain thickness, the thickness of the peeled crystals will be somewhat the same.

Finally, the photoresponsive properties of the peeled crystals were investigated. The peeled crystals showed bending when irradiated with UV light (Figure 3.46c). Therefore,

3.3o thin crystals with less than half of the original thickness are efficiently produced by multi-step light irradiation under condition 3, and the peeled crystals can be used as a photomechanical material.

3.4 Conclusion

In summary, the photosalient phenomena of crystals found in three DAEs were examined while focusing on the effect of crystal size and UV intensity. Although the DAEs of **3.1o** and **3.2o** have been previously investigated in detail, no photosalient effect of their crystals heve been reported.[4,40] This is due to the fact that the photosalient effect was observed only when strong UV light was irradiated. Consequently, it is likely that a much wider class of crystals of DAEs may show the photosalient effect upon irradiation with strong UV light. This possibility should be carefully investigated not only for application of the photosalient effect but also for our understanding of the limitations of using the intensity of UV/visible light in applying the bending phenomena. For the bulk crystals prepared by recrystallization, UV-induced peeling of the surfaces was observed. The peeling phenomena appeared on the crystalline surfaces, so they were independent of crystal sizes. On the other hand, the photosalient phenomena of thin crystals prepared by sublimation did show the size dependency. In particular, the photosalient phenomena of the crystal of **3.3o** showed dependence on thickness, i.e., thinner crystals of **3.3o** showed more remarkable photosalient phenomena. As soon as UV light was irradiated, breaking and jumping phenomena occurred. This finding is in contrast to the observation that the thin crystal of **3.3o** only showed bending with coloration upon weak UV light irradiation. For a bulk crystal of **3.3o**, the crystal showed coloration upon weak UV irradiation, while breaking occurred throughout the entire crystal. The crystal of **3.3o** showed the most remarkable photosalient phenomena in its ability to switch the photoresponse depending on the UV light intensity.

Finally, efficient surface peeling by light irradiation conditions using **3.3o** crystals was reported. Here, weak and strong UV light was used for the generation of a strained layer in the crystal and for surface peeling and explosion of crystals, respectively. When a **3.3o** crystal was irradiated with weak UV and visible light, a strained layer was generated on the irradiated surface of the crystal. Then, strong UV light irradiation from the backside of the initial irradiation direction efficiently induced surface peeling due to the difference in photoresponses between the non-strained and strained parts. The thickness of peeled crystals was less than half of the original crystals and showed bending upon UV light

irradiation. Therefore, multi-step light irradiation can efficiently produce **3.3o** thin crystals, and the peeled crystals have the potential to be used as a photomechanical material. In addition, surface peeling of crystals was observed mainly in multi-step irradiation from different directions, compared to single-step irradiation of strong UV light and multi-step irradiation from the same direction. These results suggest the potential for photocontrol of the photomechanical behaviors observed in the same crystal based on the irradiation conditions.

3.5 References

[1]   P. Naumov, S. Chizhik, M. K. Panda, N. K. Nath, E. Boldyreva, *Chem. Rev.* **2015**, *115*, 12440−12490.

[2]   J. M. Abendroth, O. S. Bushuyev, P. S. Weiss, C. J. Barrett, *ACS nano* **2015**, *9*, 7746−7768.

[3]   T. Kim, L. Zhu, R. O. Al-Kaysi, C. J. Bardeen, *ChemPhysChem* **2014**, *15*, 400−414.

[4]   S. Kobatake, S. Takami, H. Muto, T. Ishikawa, M. Irie, *Nature* **2007**, *446*, 778−781.

[5]   K. Uchida, S. Sukata, Y. Matsuzawa, M. Akazawa, J. J. D. de Jong, N. Katsonis, Y. Kojima, S. Nakamura, A. Meetsma, B. L. Feringa, *Chem. Commun.* **2008**, 326-328.

[6]   D. Kitagawa, R. Tanaka, S. Kobatake, *CrystEngComm* **2016**, *18*, 7236−7240.

[7]   F. Tong, D. Kitagawa, X. Dong, S. Kobatake, C. J. Bardeen, *Nanoscale* **2018**, *10*, 3393−3398.

[8]   N. K. Nath, L. Pejov, S. M. Nichols, C. Hu, N. Sleh, B. Kahr, P. Naumov, *J. Am. Chem. Soc.* **2014**, *136*, 2757−2766.

[9]   F. Terao, M. Morimoto, M. Irie, *Angew. Chem. Int. Ed.* **2012**, *51*, 901−904.

[10]   H. Koshima, H. Nakaya, H. Uchimoto, N. Ojima, *Chem. Lett.* **2012**, *41*, 107−109.

[11]   H. Koshima, K. Takechi, H. Uchimoto, M. Shiro, D. Hashizume, *Chem. Commun.* **2011**, *47*, 11423 −11425.

[12]   T. Kim, M. K. Al-Muhanna, S. D. Al-Suwaidan, R. O. Al-Kaysi, C. J. Bardeen, *Angew. Chem. Int. Ed.* **2013**, *52*, 6889−6893.

[13]   D. Kitagawa, H. Tsujioka, F. Tong, X. Dong, C. J. Bardeen, S. Kobatake, *J. Am. Chem. Soc.* **2018**, *140*, 4208−4212.

[14]   D. Kitagawa, H. Nishi, S. Kobatake, *Angew. Chem. Int. Ed.* **2013**, *52*, 9320−9322.

[15]   Y. Nakagawa, M. Morimoto, N. Yasuda, K. Hyodo, S. Yokojima, S. Nakamura, K. Uchida, *Chem. Eur. J.* **2019**, *25*, 7874−7880.

[16] A. Fujimoto, N. Fujinaga, R. Nishimura, E. Hatano, L. Kono, A. Nagai, A. Sekine, Y. Hattori, Y. Kojima, N. Yasuda, M. Morimoto, S. Yokojima, S. Nakamura, B. L. Feringa, K. Uchida, *Chem. Sci.* **2020**, *11*, 12307−12315.

[17] D. J. Shields, D. P. Karothu, K. Sambath, R. A. A. U. Ranaweera, S. Schramm, A. Duncan, B. Duncan, J. A. Krause, A. D. Gundmundsdottir, P. Naumov, *J. Am. Chem. Soc.* **2020**, *142*, 18565−18575.

[18] M. Tamaoki, D. Kitagawa, S. Kobatake, S. *Cryst. Growth Des.* **2021**, *5*, 3093−3099.

[19] F. Tong, M. Al-Haidar, L. Zhu, R. O. Al-Kaysi, C. J. Bardeen, *Chem. Commun.* **2019**, *55*, 3709−3712.

[20] J. M. Cole, J. d. J. Velazquez-Garcia, D. J. Gosztola, S. G. Wang, Y. Chen, Y. *Chem. Mater.* **2019**, *31*, 4927−4935.

[21] P. Naumov, S. C. Sahoo, B. A. Zakharov, E. V. Boldyreva, *Angew. Chem. Int. Ed.* **2013**, *52*, 9990−9995.

[22] E. Hatano, M. Morimoto, K. Hyodo, N. Yasuda, S. Yokojima, S. Nakamura, K. Uchida, *Chem. Eur. J.* **2016**, *22*, 12680−12683.

[23] D. Kitagawa, T. Okuyama, R. Tanaka, S. Kobatake, *Chem. Mater.* **2016**, *28*, 4889−4892.

[24] D. Kitagawa, S. Kobatake, *Chem. Commun.* **2015**, *51*, 4421−4424.

[25] M. Morimoto, M. Irie, *J. Am. Chem. Soc.* **2010**, *132*, 14172−14178.

[26] R. Nishimura, A. Fujimoto, N. Yasuda, M. Morimoto, T. Nagasaka, H. Satome, S. Ito, H. Miyasaka, S. Yokojima, S. Nakamura, B. L. Feringa, K. Uchida, *Angew. Chem. Int. Ed.* **2019**, *58*, 13308−13312.

[27] E. Hatano, M. Morimoto, T. Imai, K. Hyodo, A. Fujimoto, R. Nishimura, A. Sekine, N. Yasuda, S. Yokojima, S. Nakamura, K. Uchida, *Angew. Chem. Int. Ed.* **2017**, *56*, 12576−12580.

[28] A. Nagai, R. Nishimura, Y. Hattori, E. Hatano, A. Fujimoto, M. Morimoto, N. Yasuda, K. Kamada, H. Sotome, H. Miyasaka, S. Yokojima, S. Nakamura, K. Uchida, *Chem. Sci.* **2021**, *12*, 11585−11592.

[29] D. Kitagawa, C. Iwaihara, H. Nishi, S. Kobatake, *Crystals* **2015**, *5*, 551−561.

[30] D. Kitagawa, S. Kobatake, *Photochem. Photobiol. Sci.* **2014**, *13*, 764−769.

[31] D. Kitagawa, S. Kobatake, *J. Phys. Chem. C* **2013**, *117*, 20887−20892.

[32] H. Wang, J. Liu, K. Ye, Q. Li, J. Zhang, H. Xing, P. Wei, J. Sun, F. Ciucci, J. W. Y. Lam, R. Lu, B. Z. Tang, *CCS Chemistry* **2021**, *3*, 1491–1500.

[33] S. Chizhik, A. Sidelnikov, B. Zakharov, P. Naumov, E. Boldyreva, *Chem. Sci.* **2018**, *9*, 2319–2335.

[34] D. Kitagawa, R. Tanaka, S. Kobatake, *Phys. Chem. Chem. Phys.* **2015**, *17*, 27300−27305.

[35] A. Hirano, D. Kitagawa, S. Kobatake, *CrystEngComm* **2019**, *21*, 2495−2501.

[36] A. Hirano, T. Hashimoto, D. Kitagawa, K. Kono, S. Kobatake, *Cryst. Growth Des.* **2017**, *17*, 4819−4825.

[37] Q. Yu, X. Yang, Y. Chen, K. Yu, J. Gao, Z. Liu, P. Cheng, Z. Zhang, B. Aguila, S. Ma, *Angew. Chem. Int. Ed.* **2018**, *57*, 10192−10196.

[38] X. Lu, H. Zhang, G. Fei, B. Yu, X. Tong, H. Xia, Y. Zhao, *Adv. Mater.* **2018**, *30*, 1706597.

[39] K. Uchida, T. Ishikawa, M. Takeshita, M. Irie, *Tetrahedron* **1998**, *54*, 6627−6638.

[40] M. Irie, T. Lifka, S. Kobatake, N. Kato, *J. Am. Chem. Soc.* **2000**, *122*, 4871−4876.

[41] H. E. Gottlieb, V. Kotlyar, A. Nudelman, *J. Org. Chem.* **1997**, *62*, 7512−7515.

[42] C. A. Schneider, W. S. Rasband, K. W. Eliceiri, *Nat. Methods* **2012**, *9*, 671−675.

[43] T. Higashi, ABSCOR Rigaku Corporation, Tokyo, Japan, **1995**.

[44] Y. Ushiogi, T. Hase, Y. Iinuma, A. Takata, J. Yoshida, *Chem. Commun.* **2007**, 2947−2949.

[45] K. Uchida, M. Irie, *Chem. Lett.* **1995**, 969−970.

[46] P. Commins, A. Natarajan, C. K. Tsai, S. I. Khan, N. K. Nath, P. Naumov, M. A. Garcia-Garibay, *Cryst. Growth Des.* **2015**, *15*, 1983−1990.

[47] R. Medishetty, S. C. Sahoo, C. E. Mulijanto, P. Naumov, J. J. Vittal, *Chem. Mater.* **2015**, *27*, 1821−1829.

[48] A. Bravais, *Études Cristallographiques*, Academie des Sciences, Paris, France **1913**.

[49] J. D. H. Donnay, *Am. Min.* **1937**, *22*, 446–467.

[50] M. Irie, Diarylethene molecular photoswitches: concepts and functionalities. Wiley-VCH, Weinheim, **2021**.

[51] S. Kobatake, K. Uchida, E. Tsuchida, M. Irie, *Chem. Commun.* **2002**, 2804–2805.

[52] R. Bandyopadhyay, J. Selbo, G. E. Amidon, M. Hawley, *J. Pharm. Sci.* **2005**, *94*, 2520–2530.

Chapter 4

Phototunable golden luster microcrystalline film of photochromic diarylethene

4.1 Introduction

A color with metallic luster gives a sense of luxury and has long been used for the exteriors of automobiles, building materials, home appliances, and so on. However, conventional paints designed to express metallic luster have been produced using the addition of metal powders, which can cause environmental pollution.[1-3] Furthermore, paints and coatings with added metal powder have high specific gravity. Therefore, when they are used in large quantities in automobiles and aircraft, the fuel efficiency of such vehicles is adversely affected, increasing emissions of carbon dioxide and other greenhouse gases. In order to solve these problems, a metallic-looking luster material is being developed using an organic compound that does not contain metal. Such materials derived from various organic compounds, including thiophene,[4-9] pyrrole,[10-15] aniline,[16] porphyrin,[17] thiadiazol,[18] stilbene,[19] and azobenzene derivatives,[20-23] have been reported. Many of these promising materials leverage a photonic structure,[24] giving them highly ordered periodic structures that can induce strong Bragg reflections and thus exhibit iridescent structural coloration. In addition, some metallic-looking lustrous materials are formed by stacking with plate-like structures.[19-23] Organic metallic-looking films consisting of several stacked plate-like crystals have been reported, and these were prepared by suction filtration of a recrystallized solution.[19-22] The mechanism of the metallic-looking luster exhibited by these systems is not fully understood, nevertheless some studies have reported that it is due to strong absorption and refractive properties of the material due to the presence of crystalline solids with smooth surfaces.[17,23] The preparation of luster films by suction filtration is very attractive due to the ease of creating materials with luster color. However, the luster color of these films depends on the molecular absorption. For example, lustrous films that show a golden color are popular, but it is very difficult to adjust them to the desired color tone because the color changes slightly depending on the absorption bands of the molecules used. Therefore, the development of color-tunable organic lustrous materials could be one approach to solving this problem.

In developing materials with adjustable luster color, we focused on photochromic molecules. Photochromic compounds can be reversibly transformed between two isomers

with different absorption spectra upon light irradiation.[25,26] In particular, the diarylethene family has thermal stability of both isomers, fatigue-resistant properties, high sensitivity, rapid photoresponse, and reactivity in the solid state.[25,26] In addition, the control of functions by light is an excellent tool that can be expected to work both locally and remotely. Therefore, we considered this type of molecule suitable for our approach and adopted it.

In this chapter, we report a phototunable gold-luster film made of layered microcrystals of a diarylethene molecule. We adopted diarylethene **4.1o** (Scheme 4.1), which has been reported to yield yellow plate-like crystals by recrystallization.[27] The diarylethene undergoes cyclization and cycloreversion reactions upon alternately irradiated with UV and visible light.[25,26] These reactions have enabled the first successful conditioning of phototunable metallic-looking lustrous materials.
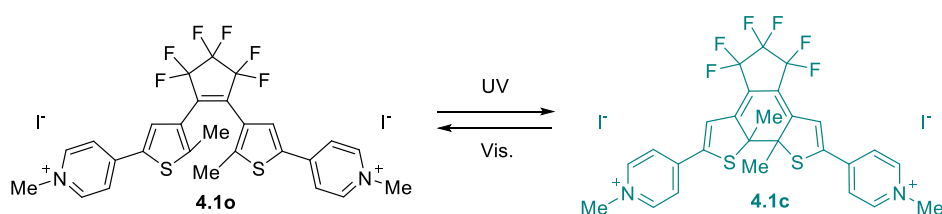
Scheme 4.1 Molecular structure of open- and closed-ring isomers of **4.1**.

4.2 Experimental

4.2.1 Material

All commercial reagents were used as received unless otherwise stated. Diarylethene **4.1o** was synthesized according to the procedure described in the literature.[27] The brass plates used were C2680 and C2801 (Iwasaki Store, Osaka, Japan).

4.2.2 General information

The absorption and reflection spectra were measured with a Hitachi U-4150 spectrophotometer. Specular reflection spectra were measured with a Shimadzu UV-3100 spectrophotometer with an attached 5-degree relative specular reflectance accessory. XRD spectra were measured with the Rigaku RINT2500 (CuKα: 1.5418 Å). SEM images were recorded using the KEYENCE VE-8800. Optical microscopic images were recorded with the Nikon OPTIPHOT2-POL and KEYENCE VHX-500, VH-S30, and VH-Z20. For UV light irradiation, the As ONE Handy UV Lamp LUV-6 (λ = 365 nm, 12 min) was

used. For visible light irradiation, the 500W USHIO SX-UI501 XQ Xenon lamp attached with Toshiba color filters (UV-29, Y-48, and O-56: $\lambda > 560$ nm, 10 min) was used. The diagram of CIELAB color coordinates and CIE1931 coordinates were created using ColorAC.[28] The Gaussian16 program package[29] was used for geometry optimization with density functional theory (DFT)[30,31] for ground states. The B3LYP[32-34] functionals were adopted as exchange-correlation terms of DFT. The gaussian 6-31G(d,p) basis set was adopted for all calculations. Avogadro ver. 1.2.0[35] was used to calculate the geometric parameters obtained from the DFT calculation and crystal structure of **4.1o**.

4.2.3 X-ray crystallographic analysis

X-ray crystallographic analysis for the **4.1o** crystal was carried out at the SPring-8 BL02B1 beamlines. A beamline BL02B1: Si(311) double-crystal monochromator was used, and its wavelength was 0.4137 Å. The size of the X-ray beam was 0.2 (H) × 0.2 (V) mm. The diffractometer was equipped with a PILATUS3 X CdTe 1M detector (DECTRIS Ltd., Baden, Switzerland). The diffraction data was taken at 173 K. The structures were determined by the direct method and refined by the full-matrix least-squares method using the SHELX-2014/7 program. The positions of all hydrogen atoms were calculated geometrically and refined by the riding model. The crystals contained two iodides and one water molecule for each of the **4.1o** molecules. The crystallographic data can be obtained free of charge from the Cambridge Crystallographic Data Centre via www.ccdc.cam.ac.uk/data_request/cif. (CCDC 2122774 and 2122775).

4.2.4 Calculation of color coordinates for optical color change characteristics

To calculate the CIELAB color coordinates of **4.1o-film** before and after light irradiation, the L^* (lightness), a^* (red-green), and b^* (yellow-blue) values of the measured reflection spectrum were calculated using the Hitachi color calculation program. The color change values were calculated from the photometric values in the wavelength range (380–780 nm) as tristimulus values (X, Y, Z) using the following equations:

$$X = \frac{\int_{380}^{780} S(\lambda) \cdot R(\lambda) \cdot x(\lambda) d\lambda}{\int_{380}^{780} S(\lambda) \cdot y(\lambda) d\lambda} , \qquad (4.1)$$

$$Y = \frac{\int_{380}^{780} S(\lambda) \cdot R(\lambda) \cdot y(\lambda) d\lambda}{\int_{380}^{780} S(\lambda) \cdot y(\lambda) d\lambda} , \qquad (4.2)$$

$$Z = \frac{\int_{380}^{780} S(\lambda) \cdot R(\lambda) \cdot z(\lambda) d\lambda}{\int_{380}^{780} S(\lambda) \cdot y(\lambda) d\lambda}, \qquad (4.3)$$

where $S(\lambda)$ is the spectral distribution of the standard illuminant as defined by the International Commission on Illumination (D65)[36], $R(\lambda)$ is the spectral reflectance, and $x(\lambda)$, $y(\lambda)$, and $z(\lambda)$ are isochromatic functions in a 10° field of view[37,38]. Using these obtained values, the lightness (L^*) and color coordinates (a^*, b^*) were calculated from the equations below:

$$L^* = 116 \left(\frac{Y}{Yn}\right)^{\frac{1}{3}} - 16, \qquad (4.4)$$

$$a^* = 500 \left[\left(\frac{X}{Xn}\right)^{\frac{1}{3}} - \left(\frac{Y}{Yn}\right)^{\frac{1}{3}}\right], \qquad (4.5)$$

$$b^* = 200 \left[\left(\frac{Y}{Yn}\right)^{\frac{1}{3}} - \left(\frac{Z}{Zn}\right)^{\frac{1}{3}}\right], \qquad (4.6)$$

where Xn, Yn, and Zn are the tristimulus values ($Xn = 94.810$, $Yn = 100$, $Zn = 107.322$) for a perfectly diffuse reflective surface for a 10° field view under D65 illumination.

Then, using X, Y, and Z values, the chromaticity coordinates (x, y) of CIE 1931 were calculated from the equation shown below

$$x = \frac{X}{X + Y + Z}, \qquad (4.7)$$

$$y = \frac{Y}{X + Y + Z}. \qquad (4.8)$$

4.2.5 Theoretical calculation

The geometry of **4.1o** was optimized by DFT calculations. The initial structure of **4.1o** for the geometry optimization was taken from the X-ray crystallographic data. The iodine ion was omitted from the X-ray crystallographic data, and thus the charge of **4.1o** was set to +2. The procedure consists of two steps:

1. Full optimization of ground state energies by the B3LYP/6-31G(d,p) level of theory.

2. Calculation of vibrational frequencies to confirm that the optimized structure corresponds to a global minimum of the potential energy surface.

When viewed from the (100) plane in the crystal, the molecules were tilted by 54° and the molecular length was 1.87 nm. In contrast, the molecular length obtained by DFT

calculation was 1.93 nm. In this DFT calculation, the effects of iodide and crystal packing are excluded. The difference in molecular length between the crystal and DFT calculations is due to the excess charge repulsion without the effect of crystal packing which result in the increase of the average value of the dihedral angle calculated for the thiophene ring attached to the ethylene moiety by 3% in comparison with that for the crystal without the effects of iodide and crystal packing, and consequently the increase of the molecular length. Except for that, the computational structure agrees with the experimental one.

4.2.6 Preparation of microcrystalline film

In a 50-mL erlenmeyer flask, 85 mg of **4.1o** was added to a mixed solvent of acetone (8 mL) and water (2 mL). The mixture was heated to 80°C to dissolve the **4.1o**. Then, the solution was allowed to stand at room temperature for 48 h to allow the crystals to precipitate. The precipitated crystals were collected by suction filtration using a Kiriyama filter paper ($\varphi = 21$ mm, No. 5A). The sample obtained after filtration was dried under reduced pressure for 24 h, forming **4.1o-film**.

4.2.7 Preparation of crystal film

The 15 mg of **4.1o** was added to a mixture of acetone (0.19 mL) and water (0.05 mL). Then the suspension was heated to dissolve **4.1o**. Next, it was cast onto a glass plate (2.5 × 2.5 cm), stored at room temperature for 24 h, and then dried under reduced pressure for 24 h, forming crystal film.

4.2.8 Preparation of amorphous film

The 15 mg of **4.1o** was added to 0.23 mL of acetonitrile, and the mixture was heated to dissolve **4.1o**. Next, it was cast onto a glass plate (2.5 × 2.5 cm), stored at room temperature for 24 h, and then dried under reduced pressure for 24 h, forming **4.1o-cast film**.

4.3 Results and Discussion

Film of **4.1o** (**4.1o-film**) having gold-luster was prepared using suction filtration of a recrystallized solution (see Experimental section for details). The adjusted **4.1o-film** shows a yellowish gold-colored textured surface (Figure 4.1a). This film could be peeled from the filter paper to form a free-standing film (Figure 4.2). The **4.1o-film** has high absorbance in the violet (380–450 nm) and blue (450–495 nm) regions, and it shows a reflectance of more than 50% for visible light with wavelengths longer than 500 nm (Figures 4.1b and 4.3). The specular reflection spectrum, which is an indicator of metallically lustrous color, was almost the same as that of gold leaf or yellow brass that appears to be gold-colored, although the reflection intensity was lower (Figures 4.4 and 4.5).

When the microcrystalline film was irradiated with UV light ($\lambda = 365$ nm), the reflectance of visible light ($\lambda > 450$ nm) was remarkably reduced due to the formation of the closed ring isomer (**4.1c**), and the color changed to deep gold, which appears to be ordinary metal (Figure 4.1a and b). This is due to the appearance of an absorption band of **4.1c** with a maximum absorption at 700 nm in the wavelength range longer than 500 nm (Figure 4.3), which results in the reduction of the b^* coordinates of the Commission Internationale de l'Éclairage 1976 $L^*a^*b^*$ (CIELAB) color coordinates (Figure 4.1c and Table 4.1). As a similar change in color, brass, which is a mixture of copper and zinc, changes in color from brass-yellow to gold when the percentage of zinc increases from 35% to 40% (Figure 4.5 and Table 4.1). As with the changes in luster color for brass, **4.1o-film** can produce changes upon UV light irradiation (Figure 4.1a and c). In addition, since the luster color change of **4.1o**-film is due to the formation of **4.1c** produced by UV light irradiation, the abundance rate of **1c** in film and the consequent luster color in the yellow region can be adjusted using the UV irradiation time (Figure 4.6).

This change in luster color occurred only on the irradiated front side, with no color change observed on the back side (Figure 4.2). This is because UV light is absorbed on the front surface, so the light does not reach the back side. That is, in a crystal, the dye is highly concentrated, and thus not all of the molecules in the crystal isomerize.[39] Then the film was irradiated with red visible light ($\lambda > 560$ nm), and it returned to its original reflection spectrum and color owing to the photocycloreversion from **4.1c** to **4.1o** (Figures 4.1a-c and 4.4). This reversibility was maintained even after three repetition cycles (Figure 4.1d).

150
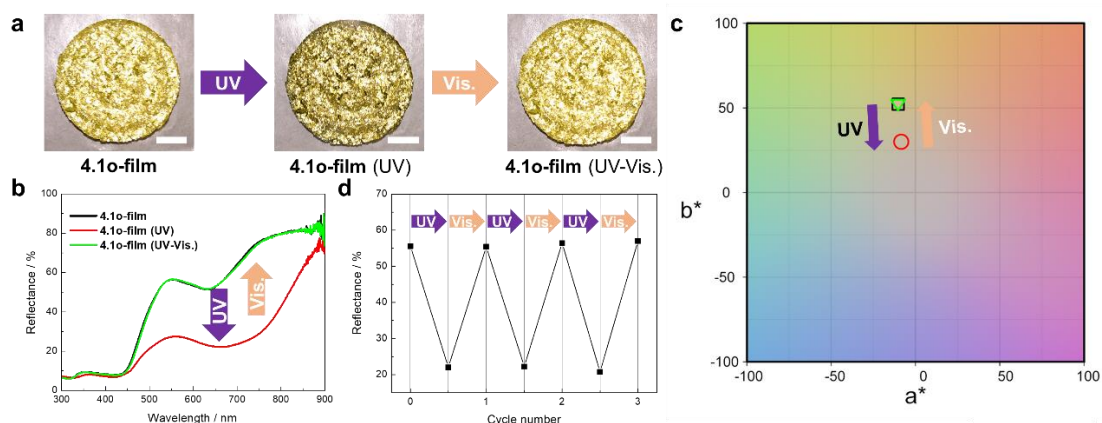
Figure 4.1 (a) Photographs of the metallic-looking luster of **4.1o-film**, and the change in the luster color due to photoisomerization upon UV ($\lambda = 365$ nm)-visible light ($\lambda > 560$ nm) irradiation. Scale bars: 0.5 cm. (b) Reflection spectral changes of **4.1o-film** by UV-visible light irradiation. Reflectance spectra of **4.1o-film** were measured on filter paper. (c) Change of the CIELAB color coordinates for the luster color of **4.1o-film** by UV-visible light irradiation. **4.1o-film** (black square), **4.1o-film (UV)**: photostationary state (red circle), and **4.1o-film (UV-Vis.)** (green triangle). Here $a*$ and $b*$ express the four unique colors of human vision (red, green, blue, and yellow). (d) Reproducibility of reflectance observed at 568 nm by UV-visible light irradiation of **4.1o-film**.
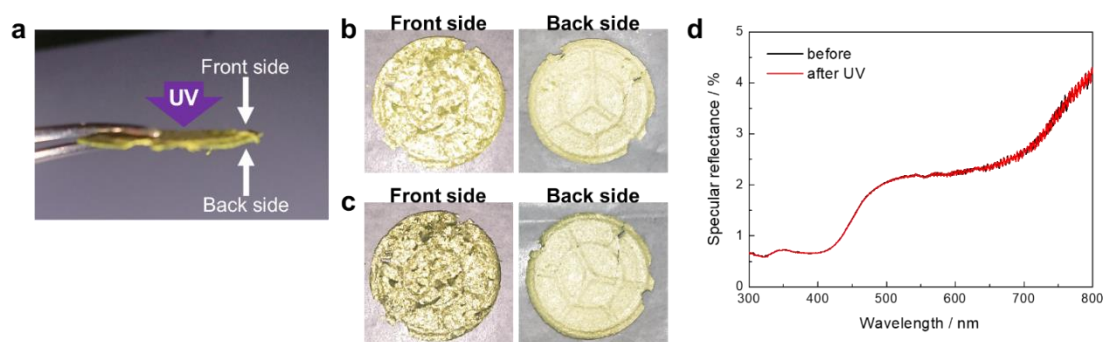
Figure 4.2 (a) Photograph of a **4.1o-film** separated from the filter paper. (b, c) Photographs of the front and back sides of **4.1o-film** before (b) and after UV light irradiation (c). (d) Specular reflectance spectra of back side of **4.1o-film** before and after UV light irradiation from the front side.
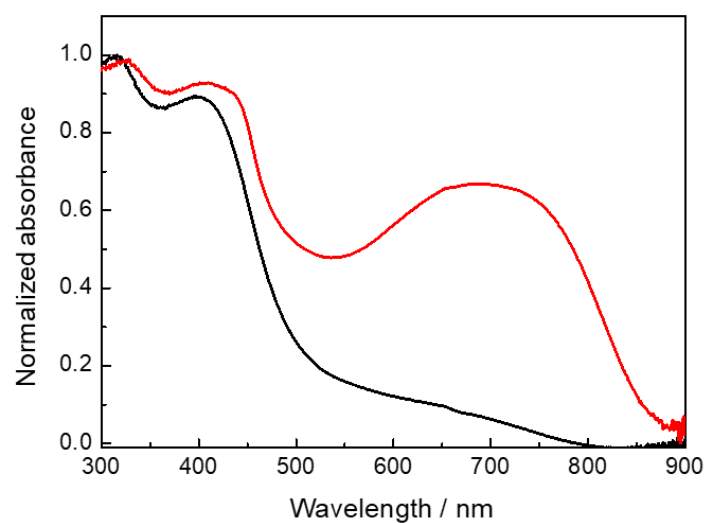
Figure 4.3 Absorption spectral changes of **4.1** in the solid state. **4.1o**: black line; photostationary state upon 365-nm light irradiation: red line.
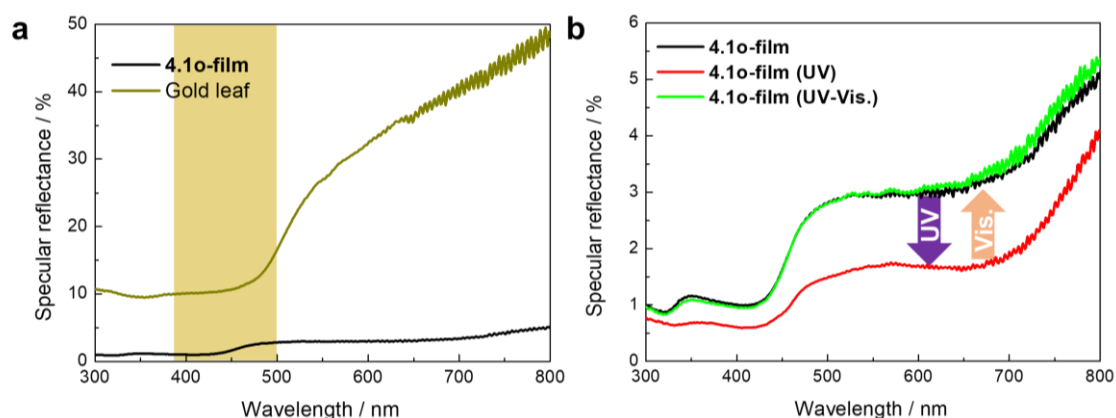
Figure 4.4 (a) Specular reflectance spectra of **4.1o-film** and gold leaf. Similar to gold leaf, the **4.1o-film** is characterized by absorption in the violet (380-450 nm) and blue (450-495 nm) regions. (b) Specular reflectance spectral changes of **4.1o-film** by UV-visible light irradiation.
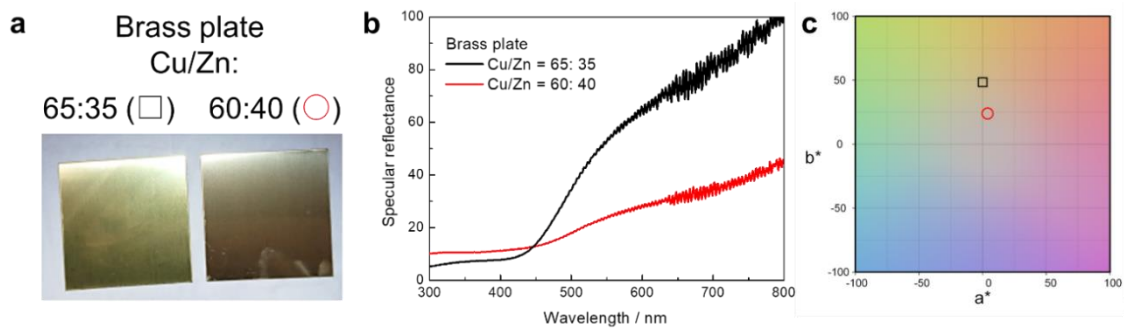
Figure 4.5 (a) Photographs of brass plates at different mixing ratios. (b) Specular reflectance spectra of brass plates with different mixing ratios. (c) CIELAB color coordinates of luster colors of brass plates with Cu:Zn = 65:35 (black square) and 60:40 (red circle).

Table 4.1 CIELAB color coordinates for **4.1o-film** and brass plate.

	L*	a*	b*
4.1o-film	75.6424	-10.3143	52.1532
4.1o-film (UV)	56.4935	-8.4857	30.0073
4.1o-film (UV-Vis.)	76.0966	-10.3385	52.7146
brass plate (Cu:Zn = 65: 35)	84.8640	-0.0168	48.4568
brass plate (Cu:Zn = 60: 40)	77.5731	3.8315	23.9766
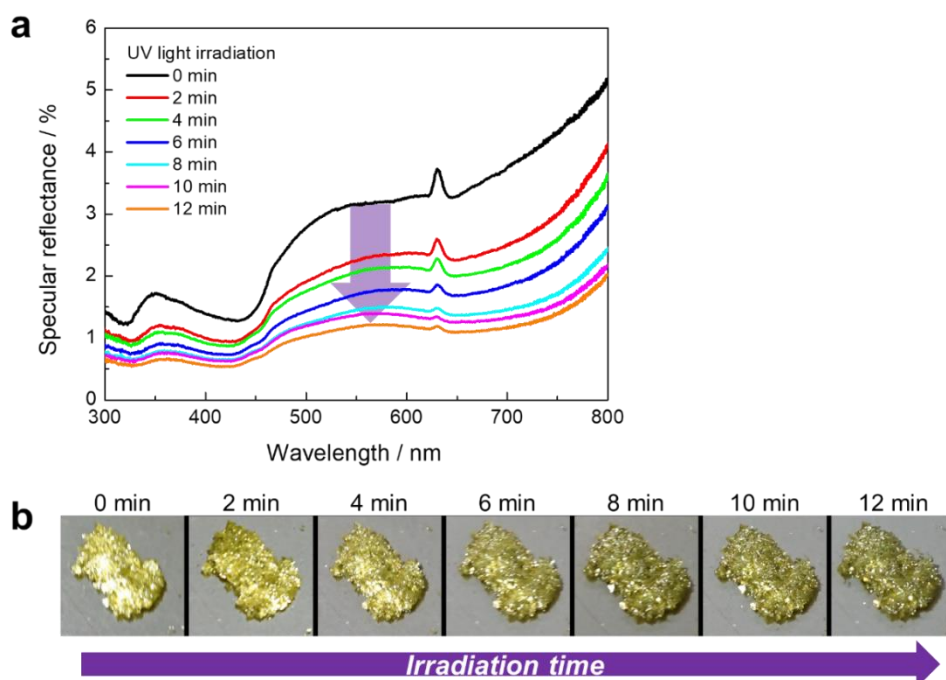
Figure 4.6 (a) Specular reflectance spectral changes of **4.1o-film** by UV light irradiation. (b) Photograph of luster color change of **4.1o-film** due to UV light irradiation.

The structure of the prepared **4.1o-film** was studied. From SEM images, plate-like crystals with a major axis exceeding 50 μm were mainly observed on the surface of the **4.1o-film** (Figure 4.7a (left)). The cross-sectional SEM image shows that the film is formed by a multilayered structure of vertically stacked plate-like crystals (Figure 4.7a (right)). This structure is similar to that of luster films in other organic compounds reported so far.[19-23] The plate-like crystals forming this film were easily obtained by recrystallization from a mixture of water and acetone (see Experimental section for details). The structural details of the plate-like crystal of **4.1o** obtained from single-crystal X-ray analysis are shown in Figure 4.8 and Table 4.2. The structure of the plate-like crystal of **4.1o** showed a monoclinic system and a C2/c space group (Table 4.2). When viewed from the (100) plane, the widest plane of the crystal, the molecules were tilted at 54° and the molecular length was 1.87 nm. The difference in molecular length between the crystal and DFT calculations is due to the fact that the average value of the dihedral angle calculated for the thiophene ring attached to the ethylene moiety is about 1.03 times larger than that for the crystal without the crystal packing effect (Figure 4.9 and Table 4.3). These molecules were layered in a brick-like arrangement tilted along the c-axis and stacked layers with a lamella thickness (d_{cryst}) of 1.52 nm along the a-axis. These stacks

154

gave the widest lattice spacing along the (100) direction, and preferential crystal growth in the direction of this face resulted in the plate-like crystal morphology determined on the basis of the Bravais-Friedel Donnay-Harker (BFDH) method[40,41] (Figure 4.10).
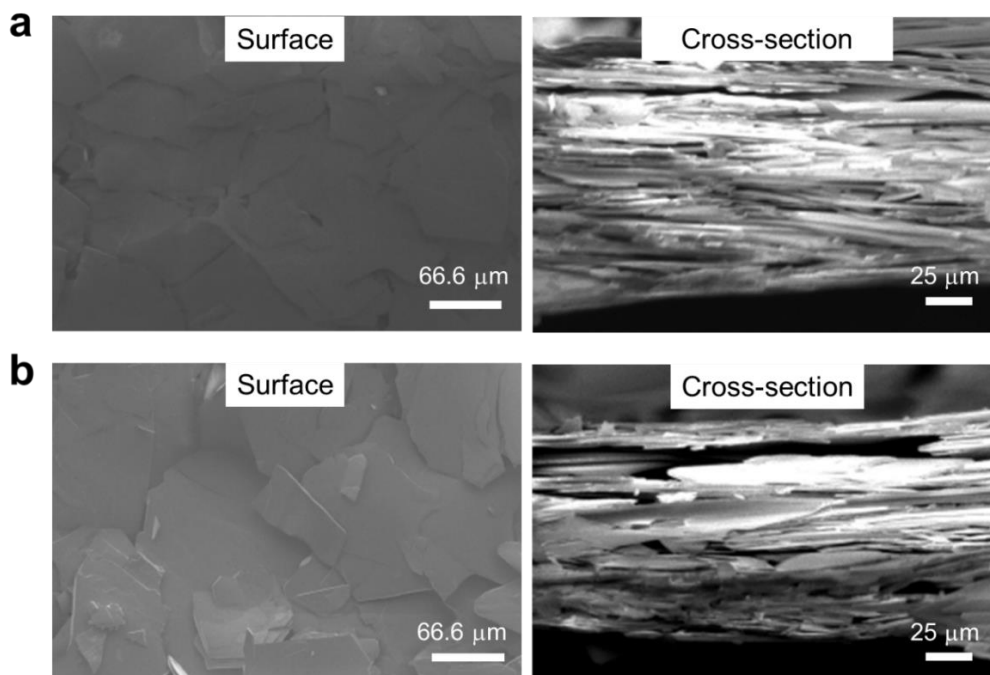
Figure 4.7 SEM images of the surface and cross section of **4.1o-film** (a) before and (b) after UV light irradiation.
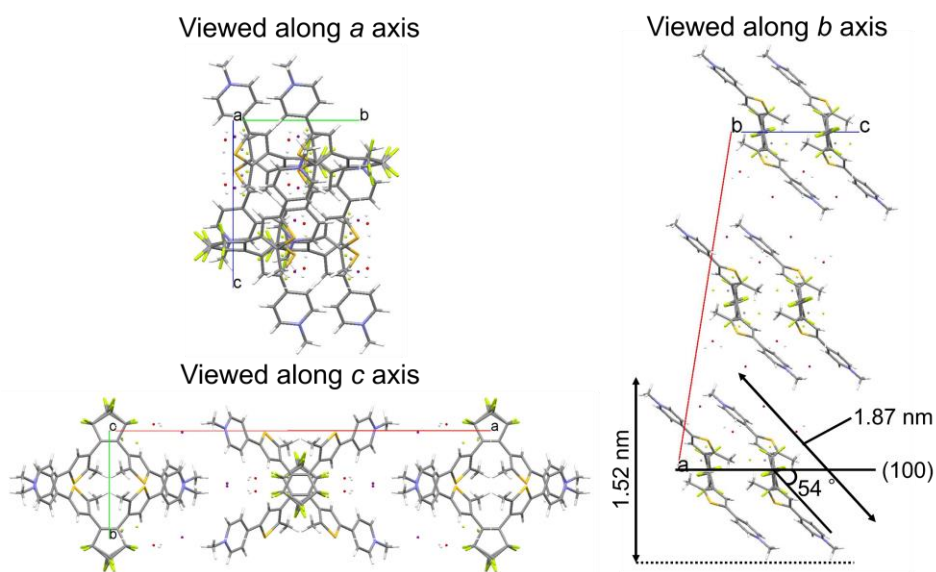
Figure 4.8 Molecular packing of **4.1o** in the crystal.

Table 4.2 Crystal data of **4.1o** and **4.1o-UV** upon 365-nm light irradiation.

	4.1o	**4.1o-UV** (after 365-nm light irradiation for 4 min)
Formula	$C_{27}H_{24}F_6I_2N_2OS_2$	$C_{27}H_{24}F_6I_2N_2OS_2$
Formula weight	824.40	824.40
T / K	173(2)	173(2)
Crystal system	monoclinic	monoclinic
Space group	C2/c	C2/c
a / Å	30.7862(3)	30.7756(3) -0.03%
b / Å	8.5970(1)	8.6120(10) +0.17%
c / Å	11.4838(1)	11.4903(10) +0.06%
α / °	90	90
β / °	99.038(1)	99.045(1) +0.007%
γ / °	90	90
V / Å^3	3001.67(5)	3007.51(5) +0.19%
Z	4	4
R_1 (I > 2σ(I))	0.0404	0.0478
wR_2 (I > 2σ(I))	0.1072	0.1458
R_1 (all data)	0.0406	0.0521
wR_2 (all data)	0.1074	0.1502
CCDC No.	2122774	2122775
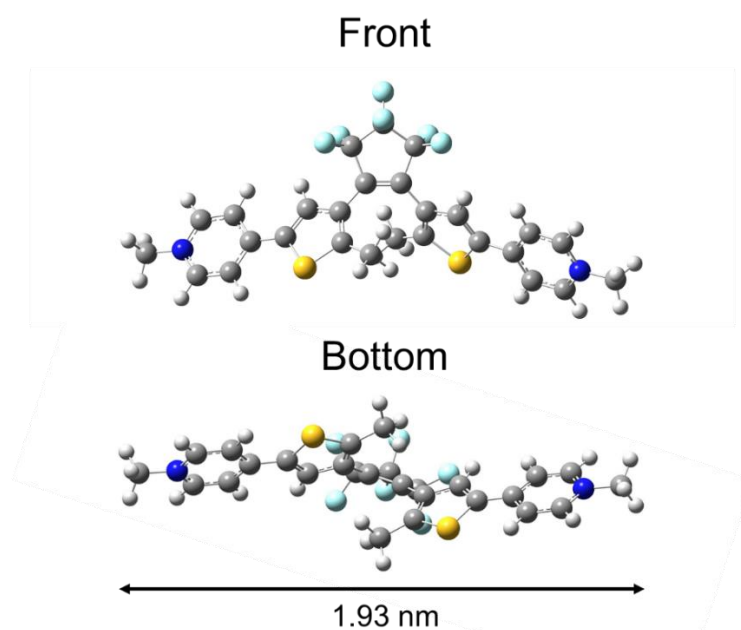
Figure 4.9 Molecular model of **4.1o**. Molecular length was determined from the end-to-end distance of the optimized molecular models calculated by DFT method based on the B3LYP/6-31G(d,p) level of theory.

Table 4.3 Geometric parameters of crystal and optimized structures of **4.1o**.

$\varphi_1 = \sphericalangle(C_1, C_2, C_3, C_4)$, $\varphi_2 = \sphericalangle(C_3, C_4, C_5, C_6)$
$\theta_1 = \sphericalangle(C_a, C_b, C_c, C_d)$, $\theta_2 = \sphericalangle(C_{a'}, C_{b'}, C_{c'}, C_{d'})$

	Crystal[a]	Optimized[b]
$r_{C_1\text{-}C_6}$ [Å]	3.506	3.781
φ_1 [degree]	-45.0	-44.3
φ_2 [degree]	-45.0	-48.2
θ_1 [degree]	15.0	2.0
θ_2 [degree]	15.0	2.9

[a] Geometric parameters of the crystal structure obtained from X-ray crystallographic analysis.
[b] Geometric parameters of optimized structure on the B3LYP/6-31G(d,p) level of theory.
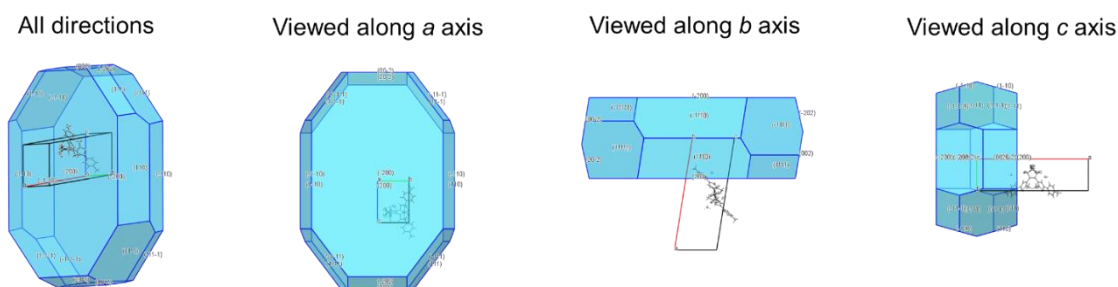
Figure 4.10 Crystal morphology predicted using the Bravais-Friedel-Donnay-Harker (BFDH) method of **4.1o** crystal.

Photocyclization of diarylethene in the single-crystalline state is a well-known phenomenon.[26] Photochromic reactions of diarylethenes in the single-crystalline state proceed when the distances between the reactive carbon atoms in the antiparallel conformation are shorter than within a 4.2-Å distance.[42] From X-ray crystallographic analysis, the distance of the thiophene rings in **4.1o** (3.51 Å) was sufficient for the photocyclization of diarylethene in the crystalline phase. Therefore, UV light irradiation to **4.1o-film** induces a change in the reflection spectrum and a corresponding change in the luster color.

From the XRD measurements, the Bragg diffraction peaks can be observed at regular intervals in the **4.1o-film**, indicating that each plate-like crystal composing the film forms a lamellar structure (Figure 4.11). Continuous periodic diffraction up to the 5th order suggests the formation of an organized stacked layered structure. The XRD pattern of the **4.1o-film** was compared to the pattern calculated from the X-ray crystallographic data of the **4.1o** crystal. As shown in Figure 4.11, only the diffraction peaks corresponding to the (200), (400), (600), (800), and (1000) mirror planes were observed for **4.1o-film**. This result indicates that a flat surface of **4.1o** crystal is a (100) plane, which is consistent with the BFDH calculation. The lamellar thickness (d_{XRD}) of the **4.1o-film** was determined to be 1.53 nm using a Bragg equation (4.9):

$$d_{XRD} = \frac{m\lambda}{2\sin\theta} \ , \qquad (4.9)$$

where m is the order of diffraction, λ is the wavelength of light, and θ is the angle between the incident light and the diffracting crystal planes. From these XRD data, the calculated d_{XRD} was found to be in good agreement with the value of d_{cryst}.
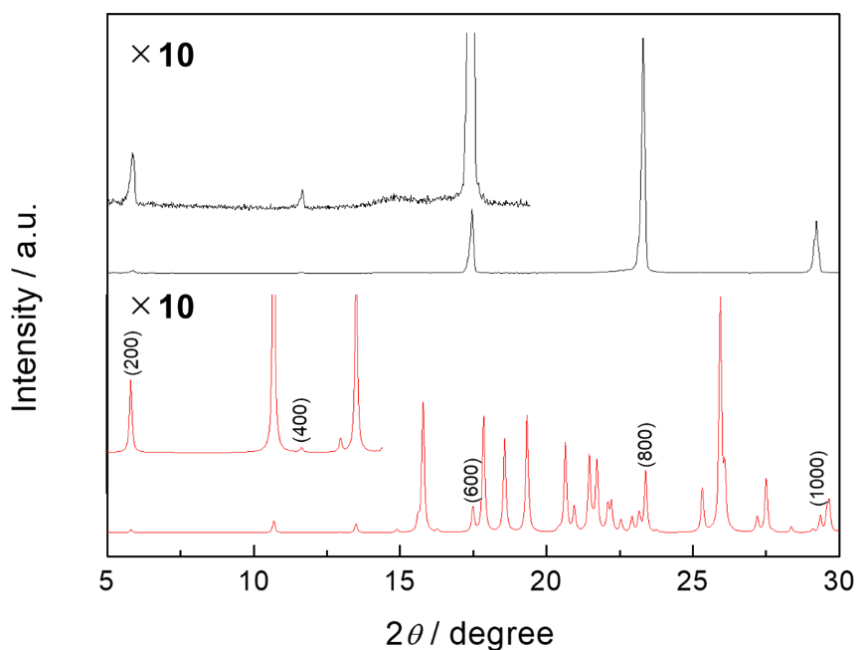
Figure 4.11 XRD pattern of **4.1o-film** (black) and the pattern calculated from single-crystal X-ray crystallographic data of **4.1o** (red).

Next, the effects of UV light irradiation on the planar stacking structure of the films were investigated. It is known that many diarylethene crystals bend upon UV light irradiation. This is due to the gradient distribution of photogenerated closed-ring isomers of the diarylethene molecules from the crystalline surface, since photoirradiation causes photoisomerization only in a thin layer on the surface.[43] Therefore, it is highly likely that UV light irradiation of **4.1o-film** does not significantly affect the planar stacking structure of the film, since the UV light is absorbed by the thin layer on the surface and does not reach the interior. In fact, a stacked structure was also observed in the film after UV light irradiation (Figure 4.7). In addition, photoinduced bending behavior is dependent on the thickness[44,45] and aspect ratio[46] on length and thickness of the crystal. Typical **4.1o** crystals had a very small aspect ratio and very little bending when irradiated with UV light (Figure 4.12). In the XRD pattern, the periodic diffraction was maintained even after UV light irradiation of the **4.1o-film** (Figure 4.13). Therefore, the planar stacking structure of the **4.1o-film** was retained even after UV light irradiation.
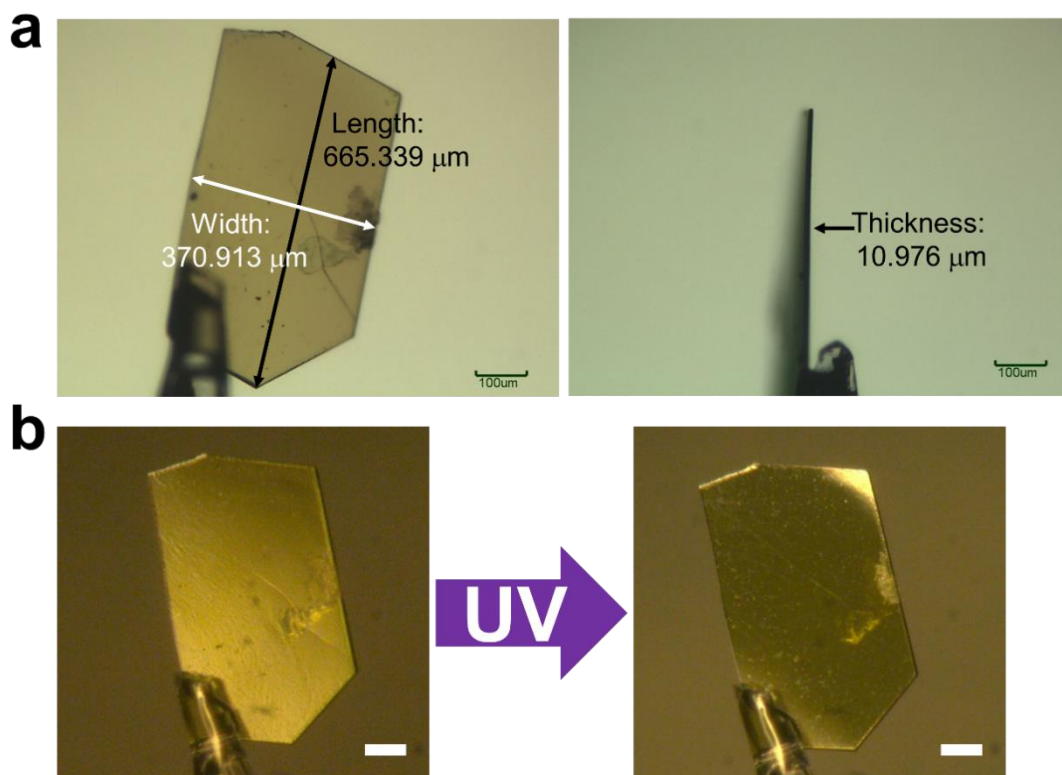
Figure 4.12 (a) Optical microscopy images of front (left) and side view (right) of **4.1o** crystal. (b) Photographs of changes in **4.1o** crystals due to UV light irradiation taken by digital microscopy. When irradiated with UV light, it showed very small bending. Scale bars: 100 μm.
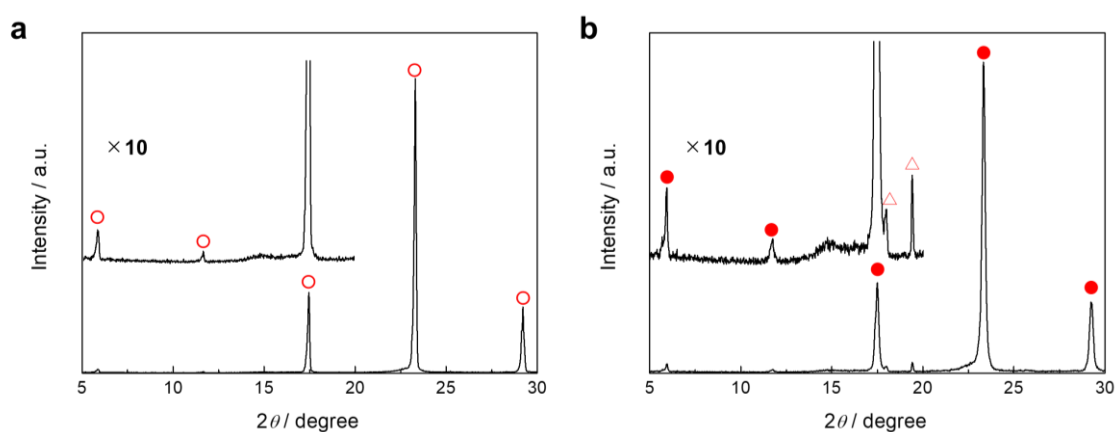
Figure 4.13 XRD pattern of **4.1o-film** before (a) and after UV light irradiation (b). The red circles indicate the peak of the lamellar spacing peak. The continuous periodic diffraction up to the 5th order was maintained even after UV light irradiation. The red triangle shows the peak that is not due to the lamellar structure.

Furthermore, the origin of luster color on the **4.1o-film** was examined. Reflectance spectra of **4.1o-film** were measured on filter paper. Therefore, it was difficult to measure transmission spectra. Instead, we measured absorption, reflection, and transmission spectra of a crystal film showing a golden luster, which was prepared by a casting method on a glass plate (Figures 4.14-4.16). The absorption and reflection spectra show that the reflection at wavelengths shorter than 500 nm is reduced due to the strong absorption of the **4.1o** crystals, while the reflection at wavelengths longer than 500 nm is larger due to the weak absorption of the **4.1o** crystals. These results show that the absorption of the **4.1o** crystal produces a reflection spectrum with a shape similar to that of gold leaf and yellow brass, which appears to be gold. Also, the transmission spectrum shows a decrease in transmittance at wavelengths shorter than 500 nm, where the absorption of the **4.1o** crystal is observed, while an almost constant transmittance is observed at wavelengths longer than 500 nm. In addition, we compared optical photographs of single crystals and multiple overlapping crystals. Consequently, the luster was more strongly apparent in the multiple overlapping crystals than in the single crystal (Figures 4.17 and 4.18). Saito and co-workers suggested that stacking planes may increase specular reflectance due to the absorption of incident light and multiple reflections at each plane, resulting in the appearance of luster.[23] Our results are consistent with theirs.
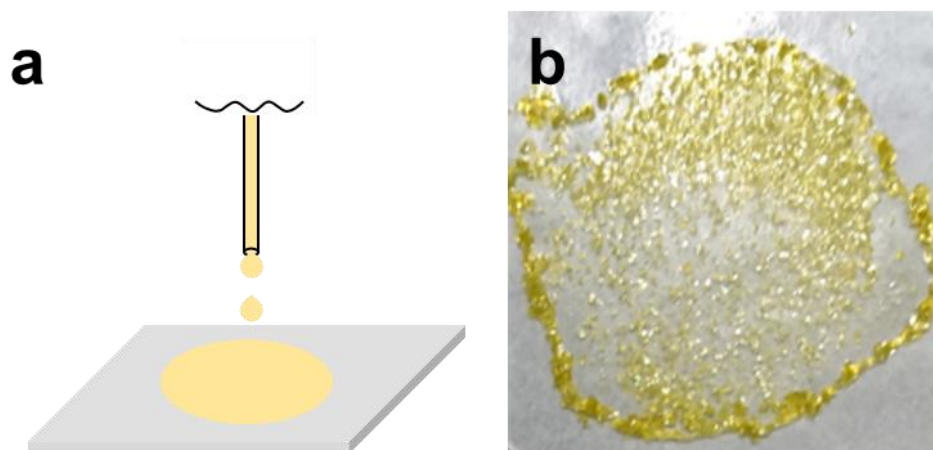
Figure 4.14 Schematic illustration (a) and photograph (b) of the crystal film prepared by the casting method. See the Experimental section for details on the preparation of crystal film.
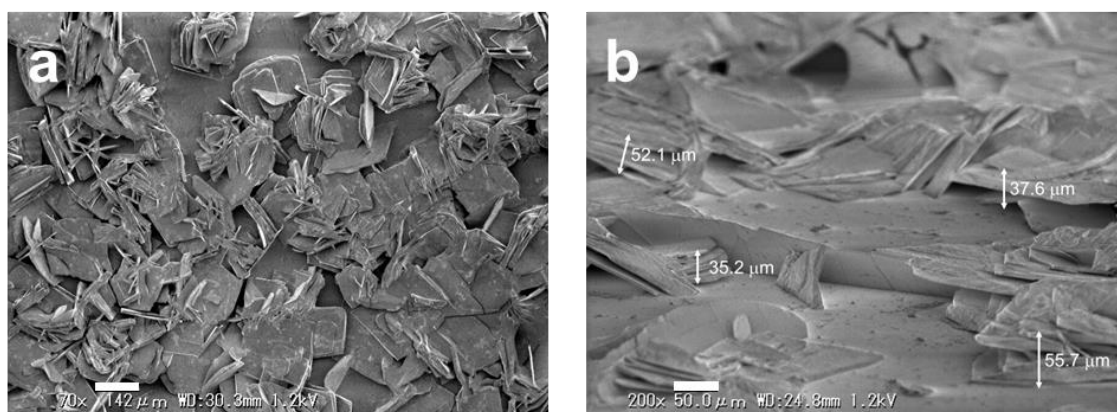
Figure 4.15 SEM images of the surface (a) and cross section (b) of crystal film.
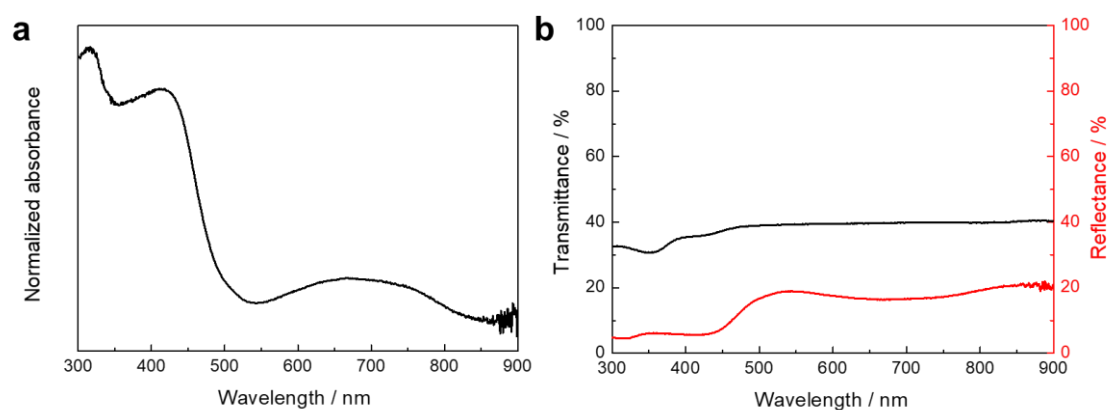
Figure 4.16 Absorption (a), reflection (b: red line), and transmission (b: black line) spectra of crystal film.
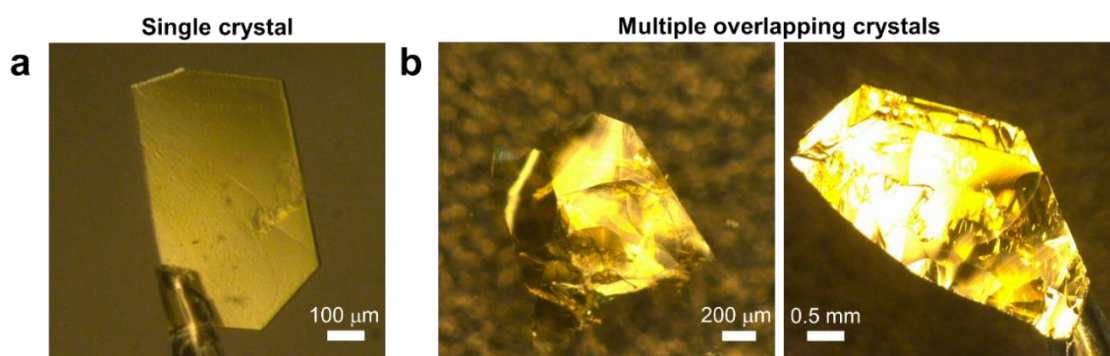
Figure 4.17 Photographs of golden luster of single crystal (a) and multiple overlapping crystals (b) of **4.1o**.
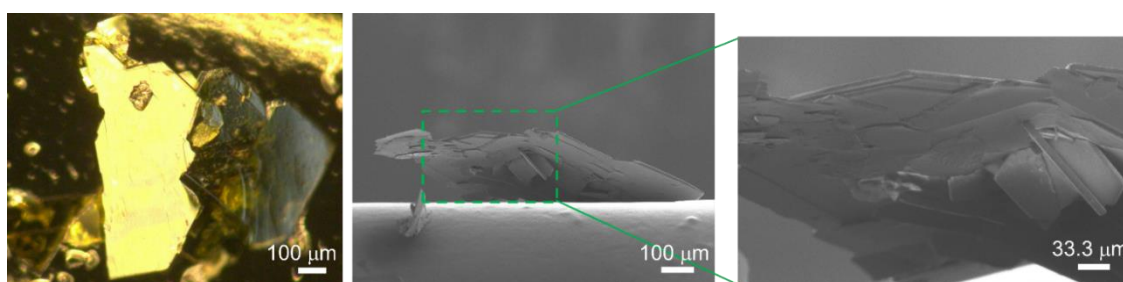
Figure 4.18 Photograph and SEM images of golden luster of multiple overlapping crystals of **4.1o**.

To evaluate the effect of crystal stacking on luster, we evaluated the thickness of the plate-like crystals and the distance between the crystals forming the **4.1o-film** (Figure 4.19). The average of crystal thickness of the **4.1o-film** was 4-5 μm, with a distribution in the 0.5-10 μm range. In addition, the distance between crystals was widely distributed in the 0-10 μm range. Figures 4.7 and 4.15 show that the **4.1o** crystals showing golden luster were overlapped by multiple plates, and the distance between crystals was very disorganized. Therefore, it was very difficult to evaluate from the thickness of the plate-like crystals and the distance between the crystals.
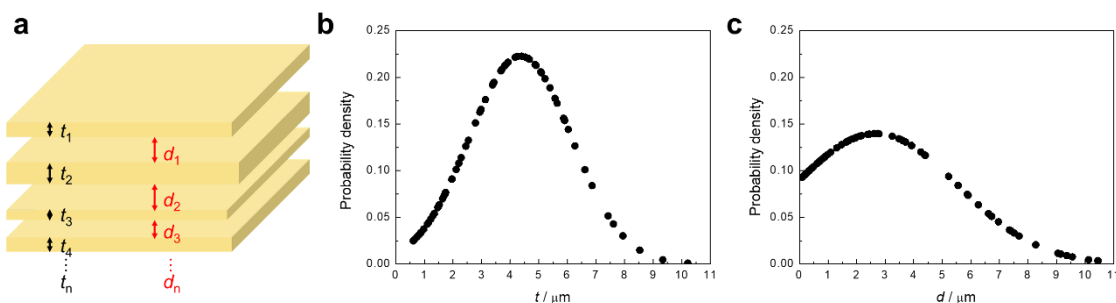
Figure 4.19 (a) Schematic illustration for calculating the thickness of crystals and the distance between crystals of **4.1o-film**. (b) Probability density of crystal thickness of **4.1o-film**. (c) Probability density of the distance between crystals of **4.1o-film**. (b) and (c) were calculated by extracting 100 samples from cross-sectional SEM images of **4.1o-film**.

Then, the **4.1o-film** was grinded to see the effect of crystal stacking on luster. When the **4.1o-film** was ground to a powder in a mortar, the luster was lost (Figure 4.20a). In comparing the XRD patterns of the crystalline film and the powder, the specific diffraction peak intensities were higher in the film than in the powder (Figure 4.20b).

Therefore, the crystal planes were highly oriented in the same direction within the film. Moreover, the reflectance of the powder of **4.1o** in the visible region was about the same as that of **4.1o-film**, but its specular reflectance was lower than that of **4.1o-film** (Figure 4.20c and d). In addition, the amorphous cast film of **4.1o** did not show any lustrous color (Figure 4.21). A detailed clarification of the luster mechanism at the molecular level, still not fully understood, remains a future subject in molecular optical physics. These data strongly suggest that stacking plate-like crystals may be one clue to producing luster (Figure 4.22).
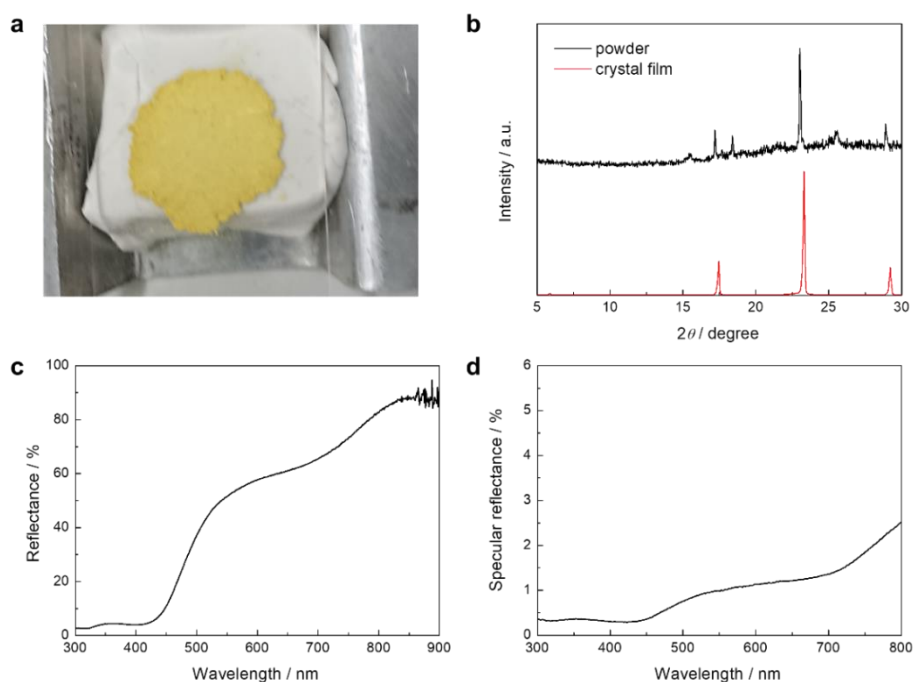
Figure 4.20 (a) Photograph of **4.1o-film** ground into powder. (b) XRD patterns of crystal film (red) and powder (black) of **4.1o**. (c) Reflection spectra of powder of **4.1o**. (d) Specular reflectance spectra of powder of **4.1o**.
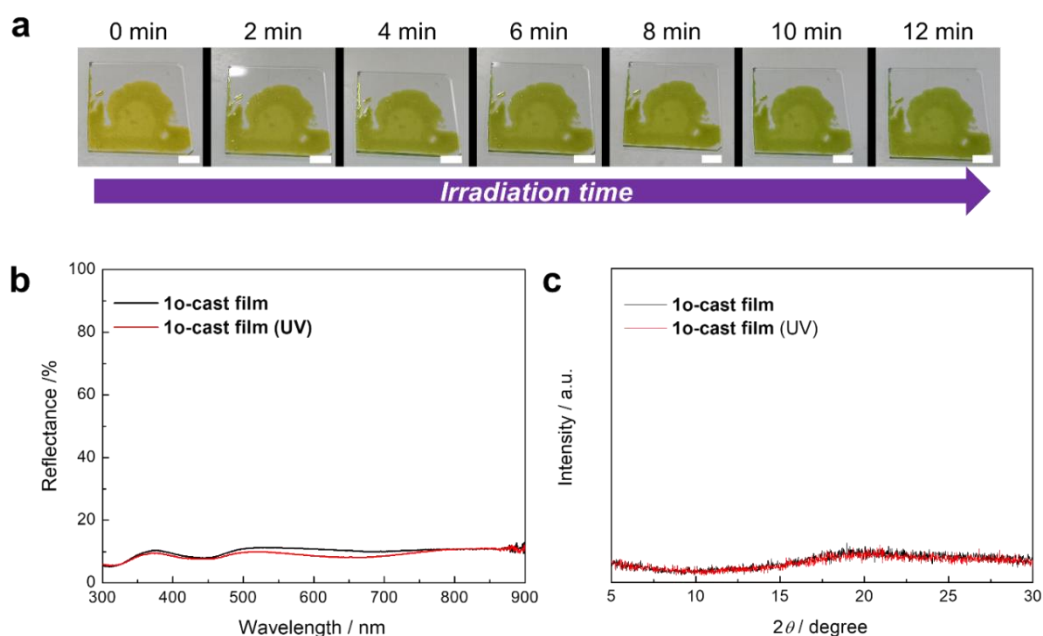
Figure 4.21 (a) Color change of **4.1o-cast film** by UV light irradiation. Scale bars: 0.5 cm. (b) Reflection spectral changes of **4.1o-cast film** by UV-visible light irradiation. (c) XRD patterns of **4.1o-cast film** before (black) and after UV light irradiation (red).
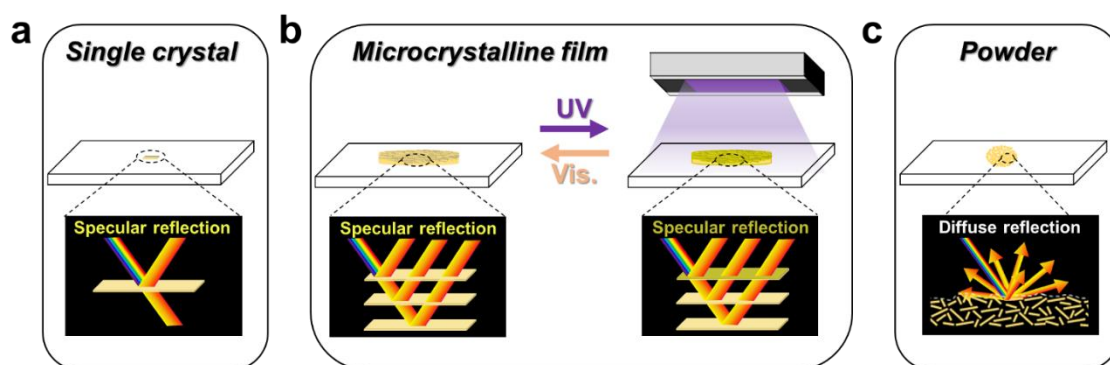
Figure 4.22 Schematic illustration of the reflection properties of the single crystal (a), microcrystalline film (b), and powder (c) of **4.1o**. Stacking of planes causes multiple reflections, resulting in clarity of luster. The change in luster color of **4.1o-film** is caused by the formation of **4.1c** in a thin layer on the surface upon UV light irradiation, which changes the absorption band.

4.4 Conclusion

This study presented a yellowish gold-colored textured surface with plate-like crystals

stacked into a multilayered structure, and it was formed by simple recrystallization and suction filtration of diarylethene **4.1o**. The golden luster was obtained by absorption of incident light due to dyes and multiple specular reflections at each plane of the stacked structure. The film was characterized by its photoresponsivity and reversibility: It changed to a deep gold color when irradiated with UV light and returned to its original color when irradiated with visible light. This photoresponsivity and reversibility is due to the cyclization and cycloreversion reactions of **4.1o**. This result demonstrates for the first time that light can be used to control such a material's luster color. A larger range of color variation is a future challenge. The luster color of materials using photochromic dyes and multilayer structures can be modulated by varying the light, and this offers the potential to provide a variety of luster colors depending on the dye used. This work's results provide useful insights for the fabrication of new kinds of metallic-looking paints.

4.5 References

[1]   E. A. Tice, *J. Air Pollut. Control Assoc.* **1962**, *12*, 553.

[2]   N. Singh, A. Turner, *Mar. Pollut. Bull.* **2009**, *58*, 559.

[3]   C. K. Takahashi, A. Turner, G. E. Millward, G. A. Glegg, *Mar. Pollut. Bull.* **2012**, *64*, 133.

[4]   X. C. Li, H. Sirringhaus, F. Garnier, A. B. Holmes, S. C. Moratti, N. Feeder, W. Clegg, S. J. Teat, R. H. Friend, *J. Am. Chem. Soc.* **1998**, *120*, 2206.

[5]   R. Tagawa, H. Masu, T. Itoh, K. Hoshino, *RSC Adv.* **2014**, *4*, 24053.

[6]   T. Tokuda, K. Hoshino, *Polym. J.* **2016**, *48*, 1141.

[7]   Y. Takashina, T. Mitogawa, K. Saito, K. Hoshino, *Langmuir* **2018**, *34*, 3049.

[8]   D. Takayama, K. Hoshino, *Chem. Lett.* **2018**, *47*, 540.

[9]   M. Tachiki, R. Tagawa, K. Hoshino, *ACS Omega* **2020**, *5*, 24379.

[10]   K. Ogura, R. Zhao, H. Yanai, K. Maeda, R. Tozawa, S. Matsumoto, M. Akazome, *Bull. Chem. Soc. Jpn.* **2002**, *75*, 2359.

[11]   R. Zhao, M. Akazome, S. Matsumoto, K. Ogura, *Tetrahedron* **2002**, *58*, 10225.

[12]   K. Ogura, R. Zhao, M. Jiang, M. Akazome, S. Matsumoto, K. Yamaguchi, *Tetrahedron lett.* **2003**, *44*, 3595.

[13]   K. Ogura, R. Zhao, T. Mizuoka, M. Akazome, S. Matsumoto, *Org. Biomol. Chem.* **2003**, *1*, 3845.

[14]   K. Ogura, K. Ooshima, M. Akazome, S. Matsumoto, *Tetrahedron* **2006**, *62*, 2413.

[15]   K. Ogura, K. Ooshima, M. Akazome, S. Matsumoto, *Tetrahedron* **2006**, *62*, 2484.

[16] M. Kukino, J. Kuwabara, K. Matsuishi, T. Fukuda, T. Kanbara, *Chem. Lett.* **2010**, *39*, 1248.

[17] M. Morisue, Y. Hoshino, M. Shimizu, S. Tomita, S. Sasaki, S. Sakurai, T. Hikima, A. Kawamura, M. Kohri, J. Matsui, T. Yamao, *Chem. Commun.* **2017**, *53*, 10703.

[18] T. Morikita, I. Yamaguchi, T. Yamamoto, *Adv. Mater.* **2001**, *13*, 1862.

[19] N. Saito, M. Ono, H. Komatsubara, K. Fukushima, Y. Takahashi, Y. Kondo, *Dyes Pigm.* **2020**, *179*, 108394.

[20] A. Matsumoto, M. Kawaharazuka, Y. Takahashi, N. Yoshino, T. Kawai, Y. Kondo, *J. Oleo Sci.* **2010**, *59*, 151–156.

[21] Y. Kondo, A. Matsumoto, K. Fukuyasu, K. Nakajima, Y. Takahashi, *Langmuir* **2014**, *30*, 4422.

[22] Y. Kojima, K. Kishimura, S. Ichikawa, J. Matsui, K. Hirai, Y. Kondo, M. Kohri, *ACS Appl. Polym. Mater.* **2021**, *3*, 1819.

[23] N. Saito, K. Yanada, Y. Kondo, *Colloid Surf. A* **2019**, *579*, 123705.

[24] Y. Takeoka, *J. Mater. Chem. C* **2003**, *1*, 6059.

[25] M. Irie, *Chem. Rev.* **2000**, *100*, 1685.

[26] M. Irie, T. Fukaminato, K. Matsuda, S. Kobatake, *Chem. Rev.* **2014**, *114*, 12174.

[27] K. Matsuda, Y. Shinkai, T. Yamaguchi, K. Nomiyama, M. Isayama, M. Irie, *Chem. Lett.* **2003**, *32*, 1178–1179.

[28] http://phonon-spectrum.com

[29] Gaussian 16, Revision C.01, M. J. Frisch, G. W. Trucks, H. B. Schlegel, G. E. Scuseria, M. A. Robb, J. R. Cheeseman, G. Scalmani, V. Barone, G. A. Petersson, H. Nakatsuji, X. Li, M. Caricato, A. V. Marenich, J. Bloino, B. G. Janesko, R. Gomperts, B. Mennucci, H. P. Hratchian, J. V. Ortiz, A. F. Izmaylov, J. L. Sonnenberg, D. Williams-Young, F. Ding, F. Lipparini, F. Egidi, J. Goings, B. Peng, A. Petrone, T. Henderson, D. Ranasinghe, V. G. Zakrzewski, J. Gao, N. Rega, G. Zheng, W. Liang, M. Hada, M. Ehara, K. Toyota, R. Fukuda, J. Hasegawa, M. Ishida, T. Nakajima, Y. Honda, O. Kitao, H. Nakai, T. Vreven, K. Throssell, J. A. Montgomery, Jr., J. E. Peralta, F. Ogliaro, M. J. Bearpark, J. J. Heyd, E. N. Brothers, K. N. Kudin, V. N. Staroverov, T. A. Keith, R. Kobayashi, J. Normand, K. Raghavachari, A. P. Rendell, J. C. Burant, S. S. Iyengar, J. Tomasi, M. Cossi, J. M. Millam, M. Klene, C. Adamo, R. Cammi, J. W. Ochterski, R. L. Martin, K. Morokuma, O. Farkas, J. B. Foresman, and D. J. Fox, Gaussian, Inc., Wallingford CT, **2016**.

[30] P. Hohenberg, W. Kohn, *Phys. Rev. B* **1964**, *136*, 864.

[31] W. Kohn, L. J. Sham, *Phys. Rev.* **1965**, *140*, A1133.

[32] A. D. Becke, *Phys. Rev. A* **1988**, *38*, 3098.

[33] A. D. Becke, *J. Chem. Phys.* **1993**, *98*, 5648.

[34] C. Lee, W. Yang, R. G. Parr, *Phys. Rev. B* **1988**, *37*, 785.

[35] M. D. Hanwell, D. E. Curtis, D. C. Lonie, T. Vandermeersch, E. Zurek, G. R. Hutchison, *J Cheminform.* **2012**, *4*, 17.

[36] J. Schanda, *CIE colorimetry.* In: J. Schanda editor. *Colorimetry: understanding the CIE system.* N. J. Hoboken: John Wiley &Sons, **2007**, pp. 25–76.

[37] W. S. Stiles, J. M. Birch, *Opt. Acta* **1959**, *6*, 1.

[38] N. I. Speranskaya, *Optics Spectrosc.* **1959**, *7*, 424.

[39] S. Kobatake, S. Takami, H. Muto, T. Ishikawa, M. Irie, *Nature* **2007**, *446*, 778.

[40] A. Bravais, *Études Cristallographiques*, Academie des Sciences, Paris, France **1913**.

[41] J. D. H. Donnay, *Am. Min.* **1937**, *22*, 446.

[42] S. Kobatake, K. Uchida, E. Tsuchida, M. Irie, *Chem. Commun.* **2002**, 2804.

[43] M. Morimoto, M. Irie, *J. Am. Chem. Soc.* **2010**, *132*, 14172.

[44] D. Kitagawa, S. Kobatake, *J. Phys. Chem. C* **2013**, *117*, 20887.

[45] D. Kitagawa, S. Kobatake, *Photochem. Photobiol. Sci.* **2014**, *13*, 764.

[46] N. K. Nath, T. Runčevski, C. Y. Lai, M. Chiesa, R. E. Dinnebier, P. Naumov, P. *J. Am. Chem. Soc.* **2015**, *137*, 13866.

Chapter 5

5.1 Conclusions

In this thesis, I described a new photo-operable functional materials based on photochromic diarylethenes. The goal of this research is to provide new examples of functional control by light using diarylethne molecules. Molecular-level changes in photoisomerization of diarylethenes were used to develop selective cell killing, manipulation method of photomechanical behavior by light, and phototunable luster material.

In Chapter 1, the research history of diarylethenes is described. The synthesis of diarylethene was first reported in 1988. Since then, a number of studies have been reported on systems that produce visible macroscopic changes or movements induced by changes at the molecular level and on the control of functions using photoisomerization of diarylethene molecules. Light is an excellent tool for local and remote manipulation. Therefore, photoresponsive materials have the potential to overcome challenges such as localized or remote manipulation that cannot be achieved with conventional materials. We have developed a new functional control system by light, such as selective cell killing, manipulation of photomechanical behavior by light, and phototunable luster material using diarylethene molecules.

In Chapter 2, we evaluated the photoinduced cytotoxicity of diarylethenes in terms of molecular structure and molecular size, and presented a molecular design of a diarylethene with a simple structure to achieve precise control based on a molecular-level switching mechanism. In addition, we have clarified the details of a

phototunable cell killing mechanism using diarylethene molecules and their photoswitching ability.

In Chapter 3, we show the relationship between the photosalient effect of DAE crystals of thiazoyl and thienyl derivatives and the intensity of UV light. In particular, the **3.3o** thin crystal successfully switched between photoinduced bending and photosalient effects by using different intensities of UV light. In addition, efficient surface peeling was achieved by multi-step light irradiation using **3.3o** thin crystals. These results show that the different photomechanical behaviors of diarylethene crystals can be manipulated by light.

In Chapter 4, the combination of absorption and specular reflection from the surface of the stacked diarylethene microcrystals resulted in a yellowish-gold textured film. In addition, we successfully developed a luster material that reversibly changes its luster color with light by using the photochromic reaction of diarylethene.

In conclusion, photoinduced selective cell killing technique, manipulation of photomechanical behavior of crystals by light, and phototunable luster material have been developed using the photochromic reaction of diarylethene derivatives. The development described in this thesis proposed new functions in the photochromic research field and expanded the range of applications for photochromic compounds.

5.2 List of Publications

Publications Described in This Thesis

1. Photoinduced cytotoxicity of photochromic symmetric diarylethene derivatives: the relation of structure and cytotoxicity
   Y. Nakagawa, T. Hishida, E. Hatano, K. Sumaru, K. Morishita, M. Morimoto, S. Yokojima, S. Nakamura, K. Uchida
   Org. Biomol. Chem. **2022**, *20*, 3211−3217.

2. Phototunable cell killing by photochromic diarylethene of thiazoyl and thienyl derivatives
   Y. Nakagawa, T. Hishida, K. Sumaru, K. Morishita, K. Kirito, S. Yokojima, S. Sakamoto, S. Nakamura, K. Uchida
   J. Am. Chem. Soc. **2023**, submitted.

3. Photosalient Effect of Diarylethene Crystals of Thiazoyl and Thienyl Derivatives
   Y. Nakagawa, M. Morimoto, N. Yasuda, K. Hyodo, S. Yokojima, S. Nakamura, K. Uchida
   Chem. Eur. J. **2019**, *25*, 7874−7880.

4. Efficient surface peeling, a photoinduced result of photochromic diarylethene crystal by multi-step light irradiation
   Y. Nakagawa, M. Morimoto, S. Yokojima, S. Nakamura, K. Uchida
   Cryst. Growth Des. **2023**, revision submitted.

5. Phototunable Golden Luster Microcrystalline Film of Photochromic Diarylethene
   Y. Nakagawa, R. Nishimura, M. Morimoto, S. Yokojima, S. Nakamura, K. Uchida
   Bull. Chem. Soc. Jpn. **2022**, *95*, 1438−1444.

Publications Not Described in This Thesis

6. Aggregation-induced emission effect on turn-off fluorescent switching of a photochromic diarylethene

   L. Kono, **Y. Nakagawa**, A. Fujimoto, R. Nishimura, Y. Hattori, T. Mutai, N. Yasuda, K. Koizumi, S. Yokojima, S. Nakamura, K. Uchida

   Beilstein J. Org. Chem. **2019**, *15*, 2204−2212.

7. White light emission generated by two stacking patterns of a single organic molecular crystal

   Y. Nakagawa, K. Kinoshita, M. Kasuno, R. Nishimura, M. Morimoto, S. Yokojima, M. Hatakeyama, Y. Sakamoto, S. Nakamura, K. Uchida

   Mater. Adv. **2022**, *3*, 6466−6473.

5.3 Acknowledgements